SPATIAL VARIABILITY OF LOW PERMEABILITY FAULT ROCK AND ITS IMPLICATIONS FOR FAULT SEAL, NORTH TARANAKI, NEW ZEALAND

A thesis

submitted in partial fulfilment of the requirements for the Degree of

Master of Science in Geology

in the

University of Canterbury

by

Henry Winter

ABSTRACT

A number of factors can influence the hydraulic behaviour of faults including, the rheology and permeability of host and fault rock as well as bulk stress conditions, structural anisotropy, differences in pressure across the fault and the viscosity of the fluids interacting with fault zones. These factors ultimately control whether a fault acts as a barrier to lateral fluid flow and/or a conduit for along fault flow. This thesis examines the architecture of normal faults to improve understanding of their geometric variability and how it may impact fluid flow. I analyse six normal faults with displacements of 0.01-0.30 m from within the Late Miocene (~6.5-11 Ma) Mount Messenger Formation exposed along coastal cliffs in north Taranaki, New Zealand. For each fault the fault-zone and fault-rock thicknesses have been measured at 5 cm or 10 cm intervals and are combined with grain-size analysis of displaced beds and fault rock. In addition, the micro-structure of fault zones has been examined using thin sections and SEM images. Data have been used to help constrain the fault-zone structure and faulting processes together with their implications for fault-seal prediction.

Results indicate that for individual faults both fault-zone and fault-rock thicknesses can vary by more than an order of magnitude over distances of <2 m and may be significantly larger over the entire fault surface. The wavelength of these changes may be partly controlled by bed thicknesses and associated fault segmentation. The narrowest fault zones are often observed where siltstone beds intersect the faults. The thickness of fault rock is positively related to the number of deformation bands, which form by cataclasis of host-rock sandstone. Cataclasis is regularly seen in laboratory analysis and is an important process for low permeability fault rock generation. Smear of siltstone beds is also common but not ubiquitous and in many cases, does not contribute significantly to fault-rock generation. Therefore, fault-rock thicknesses are not strongly correlated with the locations of siltstone beds. These data suggest that the utility of algorithms which primarily use shale smear in order to predict fault seal may require re-examination.

ACKNOWLEDGEMENTS

Firstly, I would like to express my gratitude to my advisor Prof. Andy Nicol for the support of my MSc thesis study and related research. Thanks to Andy field work research was enjoyable and immensely interesting. Andy has been very busy as of late but has always found the time to answer any questions or problems. His knowledge and guidance helped me throughout the research and writing of this thesis.

I would also like to thank the crew in the Geology Department at UC, most importantly Gabby Watson, Chris Grimshaw, Rob Speirs, Rebekah Hunt and Dr Catherine Reid for assisting my research by helping with lab equipment, various questions and their time in general. The Department of Geological Sciences has been extremely busy over the last 6 months due to relocating the department and the recent Kaikoura earthquake, so having staff within the department provide help when needed meant a great deal.

Last but not least, I would like to thank my family and friends for supporting me through this time. There has been a mixed bag of emotions and they have always been there to make things better with ideas, laughter, backrubs and continuous motivation.

CONTENTS

LIST OF TABLES

LIST OF FIGURES

LIST OF KEYWORD DEFINITIONS AND ACRONYMS

Fault-rock: Fragments of crushed or deformed rock that retains no host-rock fabric and formed in response to fault shear displacements along a fault plane. Also, known as fault-core (Childs et al., 2009).

Fault-zone: The volume of rock that includes fault-rock and spatially associated networks of interconnected fractures, and small-scale faults. Also, known as the damage zone (Caine et al., 1996).

Deformation band: A common strain localization feature (small fracture) found in deformed porous sediments commonly less than 2 mm in width comprising fault rock across which shear displacement has occurred (Fossen et al., (2007).

Fault seal: When a fault is a barrier to fluid flow it is considered to be sealing. Fault seal can be generated by many processes including and not limited to, juxtaposition of low permeability facies, fault architecture and fluid type (Childs et al., 2009).

Cataclasis: The processes of crushing and mechanical breakdown of host-rock within fault-zones during fault shear which is commonly accompanied by grain-size reduction (Yielding et al., 1997).

Shale smear: The entrainment or smear of fine-grained host rock into fault-zones which commonly increases fault seal potential. Also, known as shale smear (Yielding et al., 1997).

SGR: Shale Gouge Ratio. A shale-smear algorithm which represents the percentage of fine grained rock within the fault-zone in the displaced interval. This algorithm utilises bed thickness and fault throw (Yielding et al., 1997).

SSF: Shale Smear Factor. A shale-smear algorithm which constrains the likelihood of a shale-smear having a continuous character (i.e. a longer smear length into the fault-zone). This algorithm also utilises fault throw and the thickness of the bed being measured (Yielding et al., 1997).

CSP: Clay Smear Potential. A shale-smear algorithm which represents a certain point along a fault where a relative amount of silt (or clay) has been smeared from individual beds. This algorithms utilises bed thickness and distance from source bed (Yielding et al., 1997).

SEM: Scanning Electron Microscope. A microscope which utilises a beam of high-energy electrons to generate geochemical, structural and textural images or solid specimens in high quality (often at millimetre scales) (LTI, 2017).

LDPSA: Laser Diffraction Particle Size Analyser. A machine utilised for particle sizing which uses laser light scattering to detect the size of individual particles (Micromeritics, 2017).

KEY QUESTIONS AND ANSWERS

Question	Answer	Location
What factors influence fault seal?	Many factors influence fault seal potential including, and not limited to, grain-size reduction in fault zones, fluid properties and host rock properties.	Chapter 2
How variable are fault-rock and fault-zone thicknesses?	Fault-rock and fault-zone thicknesses can vary by several orders of magnitude over small distanced (<5 m).	Chapter 4/5
What processes are responsible for generating fault rock in Northern Taranaki?	Cataclasis and shale-smear are responsible for much of the fault rock observed in Northern Taranaki.	Chapter 4/5
What fault-seal algorithms are used for fault seal prediction and how accurate are they?	SGR, SSF and CSP are common algorithms used for fault-seal prediction, however, there is only a 50/50 chance that they will predict seal.	Chapter 2/5
What sample lengths are required to capture the full range of fault-zone architectural elements?	There is a greater chance of capturing the full range of fault data at outcrop scale for smaller displacement faults (<30 cm), as rising displacement typically decreases proportion of the fault sampled	Chapter 5

List of Appendices

1 INTRODUCTION

1.1 Project Background

Fault zones commonly contain fine grained fault rock that has either been entrained into the zone from surrounding host rock or generated by cataclasis (Figure 1). Fault rock may cause a capillary or permeability seal which is often referred to as fault seal. Fault seal prediction methods attempt to quantify the potential for a fault to produce barriers to fluid flow within the upper crust (Caine et al., 1996; Childs et al., 1996, 2009). Many factors can influence fault-seal potential including and not limited to lithology, fault-zone geometry, fault size, fluid properties and geological history.

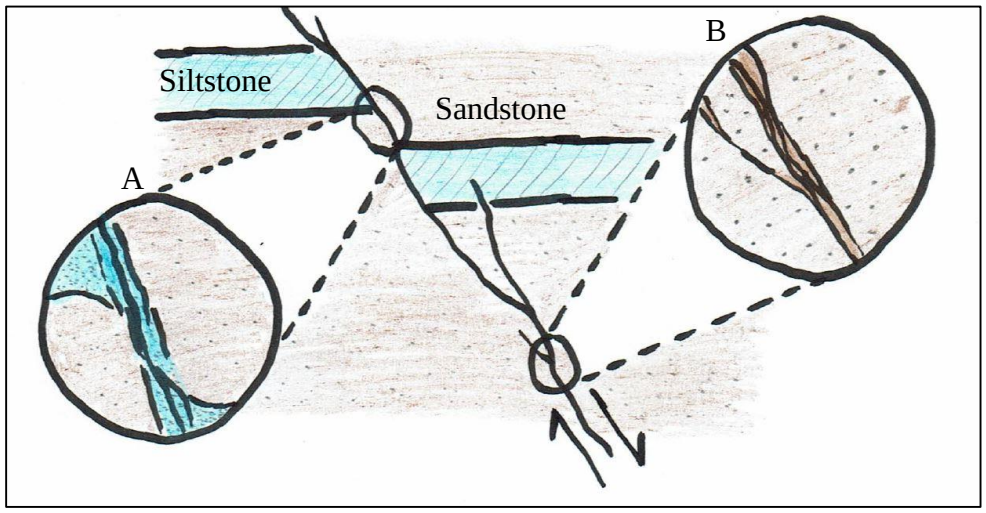

Figure 1: Sketch illustrating a normal fault displacing an interbedded sedimentary sequence. Shale smear, entrained siltstone into fault rock, may occur near displaced siltstone beds (A), while mechanical breakdown of sandstone grains may occur in displaced sandstone fault rock (B) - also known as cataclasis.

A number of algorithms have been developed for predicting fault seal potential of faults that displace interbedded sandstone and siltstone sequences (Yielding, 1992, 2010; Lindsay et al., 1993; Yielding et al., 1997; Manzocchi et al., 1999; Sperrevik et al., 2002; Childs et al., 2007). These algorithms were developed for the petroleum industry and have a wide range of applications from CO_2 sequestration to the safe storage of waste water or nuclear waste. Such algorithms are considered useful approximations that attempt to replicate the spatial variations in fault-zone geometry often observed in outcrop (Childs et al., 2009).

This thesis investigates the spatial variability of fault-zone geometries for six small normal faults with displacements ranging from less than 1 cm to 30 cm that displace thin (typically <0.5 m) turbidite beds within the Mount Messenger Formation, North Taranaki, New Zealand (Figures 2 and 3). The thickness, continuity and spatial distribution of low permeability fault rock controls whether a fault will act as a barrier to lateral fluid flow and therefore is a primary focus of this thesis. The results may have application to industries that are reliant on the extraction of fluid from, or the injection of fluid into, interbedded sandstone and siltstone sequences. In Taranaki, for example, oil and gas is being produced from the Mount Messenger Formation in the onshore Ngatoro and Kaimiro fields. Therefore, the fluid flow properties of faults have economic importance. The results from this study also provide insight into how faults form.

1.1.1 Fault Seal

Current quantitative fault-seal prediction methods utilise bed thickness and displacement to determine the likelihood of a continuous fault seal being formed. However, it has been suggested that these algorithms are overly simplistic and don't take into account the variability and complexity of fault-rock structure observed in outcrops. (James et al., 2004). Fault-zone architecture, lithology and mechanical stratigraphy often display diverse spatial and temporal variations in outcrops. The resulting fault-zone complexity can influence the ability of fluid-flow models to replicate the hydraulic properties of faults. Heterogeneous fault-zone structure is generally not captured by the models and algorithms used to describe fault-rock geometry (e.g. shale-smear geometry) and fault-zone structure. Failure to capture fault-zone heterogeneity means that flow-simulation models may not be representative of reality due to limited understanding of input parameters and their variation (Nicol et al., 2016). Quantification of these input

parameters (e.g. fault-rock thickness and permeability) are required to understand better the utility of fluid-flow models (e.g. Manzocchi et al., 2010).

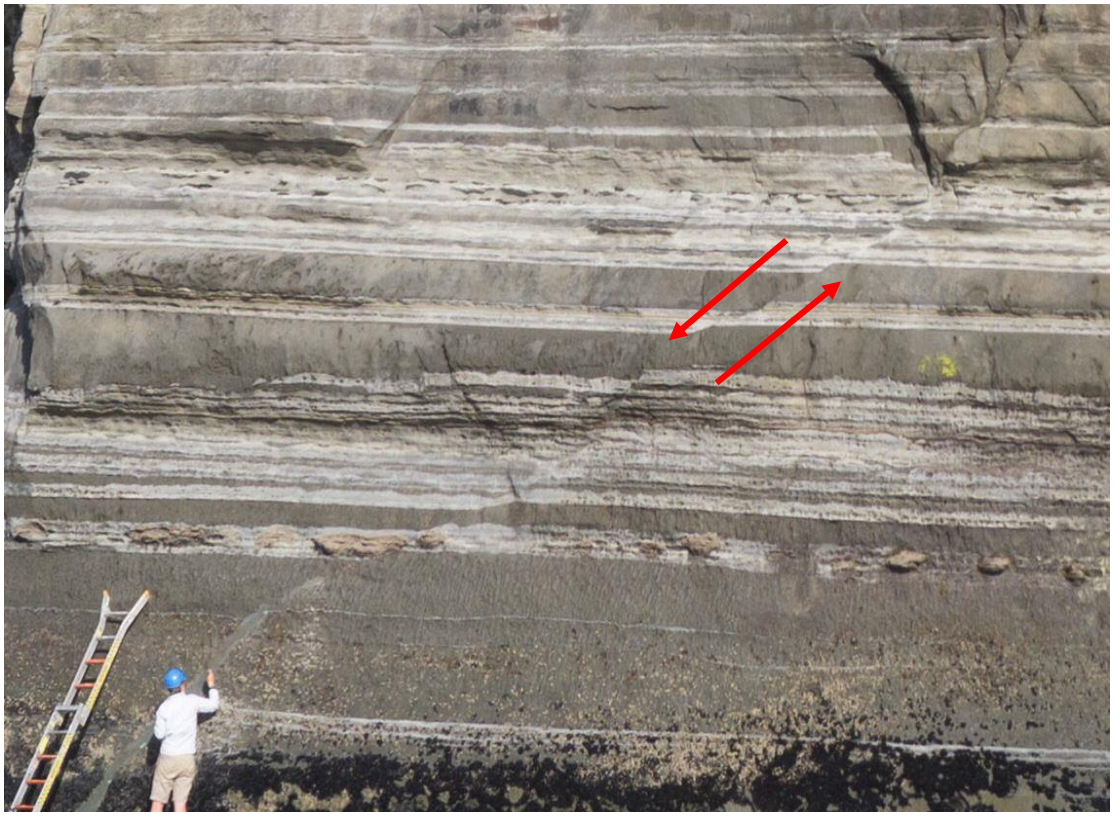

Figure 2: Photograph showing a section of the interbedded Mount Messenger Formation along a coastal cliff located south of Tongaporutu River with a small normal fault (Tongaporutu A) displacing the sequence from top right to bottom left by 16 cm. Darker coloured units are sandstone and lighter units are siltstone. Red arrows indicate sense of movement of fault. Note the person and ladder for scale (total cliff height in the photo is approximately 5 m).

1.1.2 Addressing the Problem

Over the last 40 years extensive research has been completed on the detailed geometry of fault zones (e.g. Chester and Logan, 1986; Wallace and Morris, 1986; Caine et al., 1996; Childs et al., 1996; Shipton et al., 2006; Wibberley et al., 2008; Childs et al., 2009; Faulkner et al., 2010). Many of these publications acknowledge that more data is required to understand better the variability of fault-zone architecture and how it can influence fault-seal predictions.

In order to further refine current understanding on fault seal, and fine-tune models widely utilised in fluid extraction and injection industries, research is required to:

- Quantify the structure, thicknesses and permeability of fault rock and fault zones along faults at a range of scales and in three dimensions (3D).
- Determine how different sequence architectures influence fault structure, permeability and growth.
- Determine if fault-rock architecture and hydraulic properties observed in outcrops can be up-scaled.
- Develop algorithms for predicting the size distribution and spatial frequency of "holes" in low permeability fault rock.

Future research into the complexity and structural variation of fault zones is important for accurately predicting the hydraulic properties of faults/fault zones and producing models that reflect fluid flow processes in faulted stratigraphy. To advance the understanding of fault permeability detailed sampling of the structural components of fault zones is also required. As more fault seal data becomes available, from both outcrop and seismic reflection surveys, the predictive power of models will be improved.

1.2 Thesis Objectives

This thesis is a pilot study designed to quantify the spatial variation of fault rock and fault zone distributions on small outcrop-scale normal faults (N = 6) with variable bed thickness (1-100 cm) and displacement (1-30 cm) in the interbedded Mount Messenger Formation, Taranaki. The overall aim of this study is to use field-based outcrop-scale and micro-scale (i.e. thin section and SEM images) data to understand better the factors that control fluid flow across fault zones. These data constrain the origin of fault rock (e.g., shale smear, cataclasis and/or secondary mineralisation), its permeability structure and the resulting implications for fault-seal prediction. Specific objectives of this thesis are to:

- Quantify the spatial distribution of low permeability (clay rich) fault rock along small normal faults in an interbedded sandstone siltstone sequence,
- Characterise the grain size, shear fabric and permeability of fault rock with respect to host beds,
- Analyse rock samples over a range of scales (e.g. metre to micrometre scale) to determine the processes responsible for generating fault rock (e.g., shale/clay smear or cataclasis),
- Use the data analysed to determine how fault-zone complexity may influence fault-seal potential, and, if appropriate, make recommendations about how these estimates may be improved.

1.3 Study Area

Data were primarily collected from normal faults displacing beds within coastal cliff outcrops of the Mount Messenger Formation sandstone and siltstones on the north Taranaki coast between Awakino and Pukearuhe, New Zealand (Figure 2 and 3, Figure 58: appendix). The units of interest within the Mt Messenger Formation are thinly bedded turbidite sequences exposed within cliffs and sea stacks along the Pukearuhe, Tongaporutu and Rapanui beaches (shown in Figure 4). The lithology of this sequence is dominated by clayey siltstone and silty sandstone. Access to coastal outcrop was primarily through public walkways and/or farmland from which appropriate permission was granted from property owners.

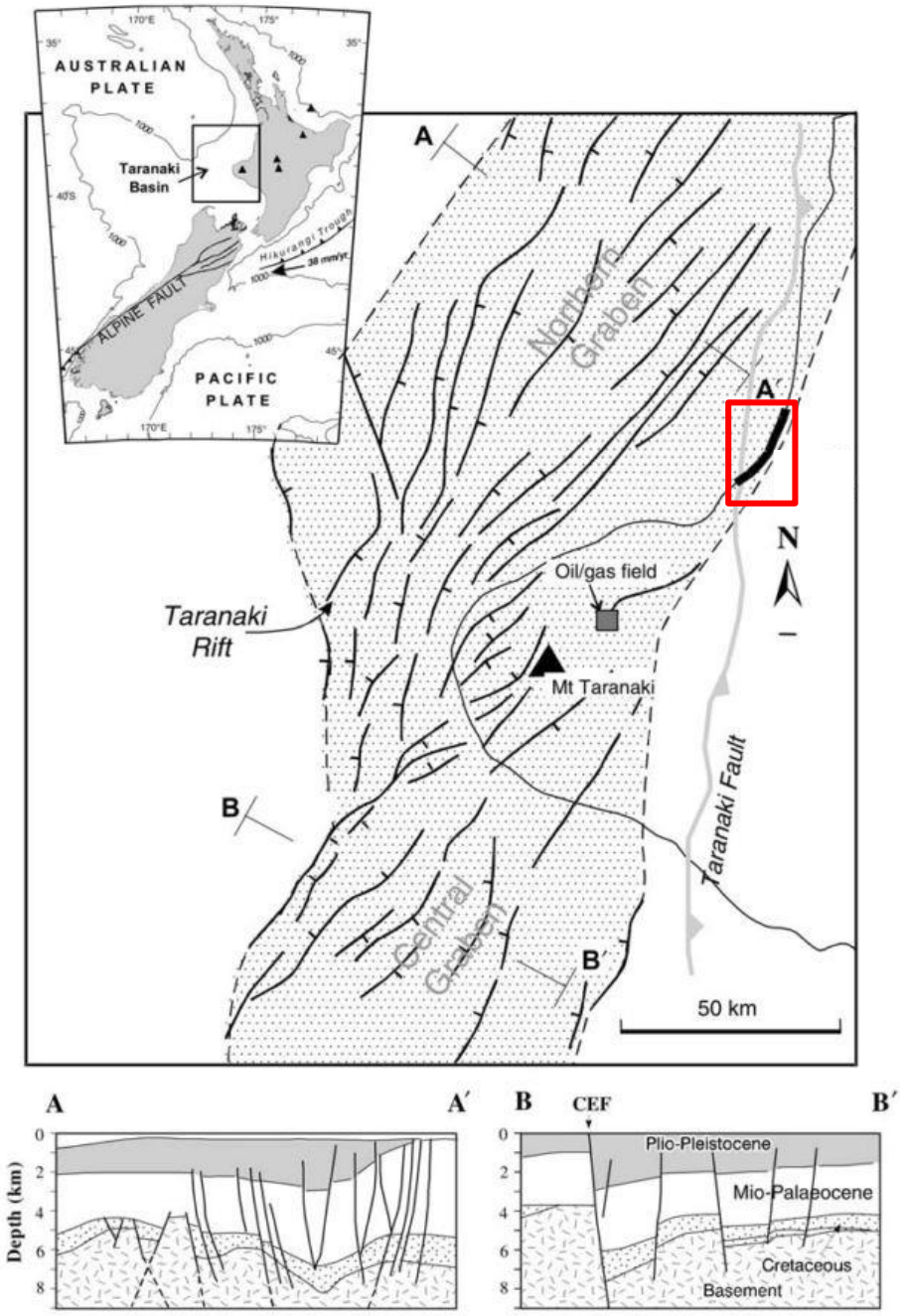

Figure 3: Maps showing the tectonic setting of the study area (shown by the red box; location of Figure 58: appendix). Insert map indicates the New Zealand plate boundary setting. Main map illustrates the Taranaki Rift Basin with associated normal faulting and the northern Taranaki study area. The study area is located close to the southeast margin of the rift system. A-A' and B-B' cross-sections show the structures and stratigraphy observed within the Taranaki Rift Basin (modified from Childs et al., 2007).

1.4 Geological Setting

The Mount Messenger Formation was deposited in the northern Taranaki Basin which contains stratigraphy up to 9km thick with ages ranging from the Mid Cretaceous to Recent (King & Thrasher, 1996). Extensional rifting associated with the opening of the Tasman Sea, and breakup of eastern Gondwana, influenced much of the Taranaki Basin during the Late Cretaceous and Palaeocene (King & Thrasher, 1996). Several post Cretaceous subsidence events driven by relative movement of the Australian and Pacific plate influenced the development of the Taranaki Basin (King & Thrasher, 1996). The first of these events was a period of foreland basin development between ~40 and 5 Ma associated with displacement of the eastern dipping Taranaki Fault System (King & Thrasher, 1996). The Taranaki Fault System defines the eastern margin of the Taranaki Basin and may have formed due to subduction. During the Late Miocene (<~10 Ma) slab roll-back and/or steepening of the subducting Pacific plate beneath the North Island may have resulted in crustal extension (Giba et al., 2010; Seebeck et al., 2014). This extension commenced in the northern basin and migrated southwards with time (King & Thrasher, 1996; Giba et al., 2010). At the latitude of the study area these normal faults extended the shallow basin by 1 – 1.5 km (King & Thrasher, 1996; Nicol et al., 2007; Giba et al., 2010) and produced the faults studied in this thesis oh which formed during the Mio-Pleistocene.

The Upper Miocene Mount Messenger Formation comprises deep-water turbidites (Figure 2) and, in the study area, formed prior to crustal extension (Childs et al., 2007). The Mount Messenger Formation has about 20 km of exposure along NNE-SSW trending beach cliff sections that are up to 200m high and stretch from Mokau in the north to Pukearuhe in the south (Browne et al., 1996). The Mount Messenger Formation located within the north Taranaki study area is between 6.5 – 11 Ma in age, has a stratigraphic thickness of around 850 m and an average dip of 2° – 5° to the SW (King, Scott, & Robinson, 1993) (Figure 4). Lithofacies of the Mount Messenger Formation include thick to medium bedded sandstone units along with interbedded fine sandstone and siltstone/clayey siltstone (King & Thrasher, 1996). The Mount Messenger Formation is made up of a large turbidite system which represents mainly lower-slope depositional environments. Interbedded sandstones, siltstones and siltstones are dominant throughout the formation with frequent occurrences of thin beds (<5 cm) of volcaniclastic material (Browne et al., 1996). Beds sampled throughout the study area are moderately sorted and

normally graded with the siltstone commonly containing coarser silts and the sandstone being primarily fine to very fine.

The Mount Messenger Formation sandstones comprise very fine to fine sands, while the siltstones are primarily coarse silts. Protolith sandstones in the Mount Messenger Formation generally have modal grain sizes of ~90-110 μm with ~55-85% sand-, ~15-40% silt- and ≤5% clay-sized particles (Browne and Slatt, 2002; Browne et al., 2005). These proportions contrast with those of the siltstone beds which have a grain-size mode of 5-10 μm, ~10-30% sand-, ~65-85% silt- and ≤20% clay-sized particles. The sandstones and siltstones are predominantly poorly to moderately sorted (sandstones display more sorting than siltstones) and comprise sub-rounded to sub-angular grains. Sandstone and siltstone porosities are 30-35% and 20-30%, respectively (Browne et al., 2005; this study). Sandstones primarily comprise ~55-80% lithics (mostly of metamorphic and sedimentary origin; Browne et al., 2005), 20-40% quartz, and 10-30% feldspar (<1% muscovite and biotite). Both the lithics and feldspar sand-sized grains are frequently altered, or partly altered, to clays including sericite and montmorillonite (Childs et al., 2007). This alteration is likely to weaken the grains which, together with the general absence of inter-grain cementation and the high porosity, contribute to the low (~3-10 MPa) unconfined compressive strength of the faulted strata (N. Perrin, Pers Comn, unpublished data, 2012).

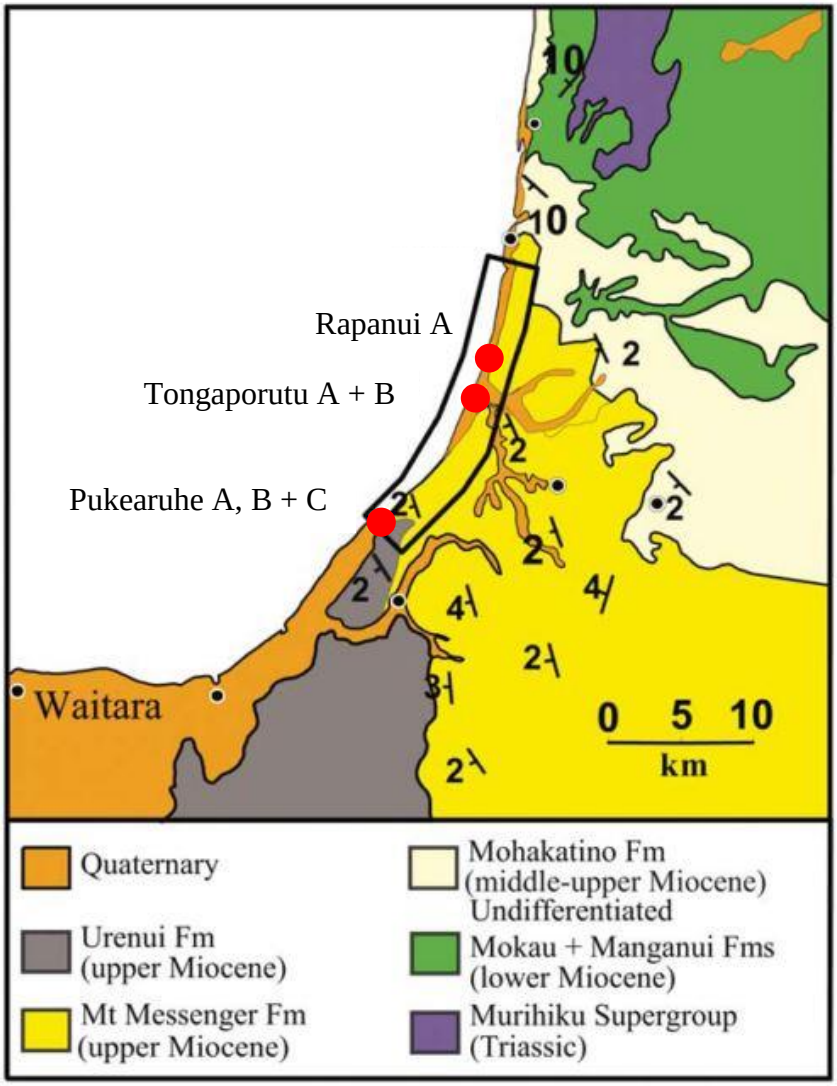

Figure 4: Map showing the geology and location of the faults analysed here (black box) within the northern Taranaki study area (modified from Childs et al., 2007). The locations of the faults studied here are shown. One fault sampled from Rapanui (Rapanui A), two from Tongaporutu (Tongaporutu A + B) and three from Pukearuhe (Pukearuhe A, B + C).

Faulting occurs along the entire 20km coastal section throughout the Mount Messenger Formation. Coastal erosion along the cliffs (up to 1 m/yr) refreshes the faulted outcrops and produces near 100% exposure. Normal faults exposed in outcrop have displacements ranging from <1 mm to >60 m in the study area (Childs et al., 2007). Faulting is mainly 2 – 6 Ma in age and is thought to have formed at burial depths of 1 – 2 km (Childs et al., 2007; Giba et al., 2010). As a result, the faulted sequence is poorly lithified and can be routinely scrapped to produce clean exposures.

1.5 Thesis Structure

The structure of this thesis is as follows:

Chapter two presents the literature review of the current understanding of fault permeability with emphasis on physical properties of fault zones and this influence on fault-sealing processes.

Chapter three describes key concepts and methods used to gather information for this thesis. Numerous methods have been used to analyse the samples collected.

Chapter four presents the field observations from the outcrop data and samples collected.

Chapter five discusses the results and their implications for fault-rock generation and permeability.

Chapter six summarises the observations and results from this thesis, with specific conclusions and recommendations for future work.

2 FAULT ZONES AND PERMEABILITY

2.1 Introduction

This chapter summarises the current understanding of fault zone-structure, hydraulic properties and fault-sealing processes. Fault zones can act as barriers, conduits or dual conduit/barrier systems for fluid flow. Their permeability is strongly influenced by the structure and composition of the fault zone which is primarily controlled by the lithology, and the associated mechanical properties of the host stratigraphy (Ferrill and Morris, 2003). However, there are numerous additional factors that can also influence fault-zone permeability and the interplay of these factors can make prediction of fluid flow near (and within) fault-zones difficult. A number of industries utilise simple geomechanical models and fault-seal algorithms to make predictions on permeability however these rarely take account of fault-zone complexities or are tested using *insitu* fluid flow measurements. Addressing these uncertainties and limitations has been a key theme of the literature surrounding fault permeability (e.g. Wallace and Morris, 1986; Wibberley et al., 2008; Childs et al., 2009).

2.2 Fault-Zone Structure

Over the last 30 years many studies and publications have analysed the structure, growth and hydraulic properties of fault zones (e.g. Chester and Logan, 1986; Wallace and Morris, 1986; Caine et al., 1996; Childs et al., 1996; Shipton et al., 2006; Wibberley et al., 2008; Childs et al., 2009; Faulkner et al., 2010). A relatively simple fault-zone model has been proposed (Figure 5a) and, even with knowledge of the complexity and variation of fault zones (e.g. Childs et al., 2009), is still widely adopted in many recent publications (e.g. Faulkner et al., 2010). The model itself comprises two main elements which accommodate shear displacements. The fault core, also known as fault rock (the term used in this thesis), hosts much of the displacement within the zone and commonly comprises low permeability material that impedes cross-fault fluid flow. The fault damage zone, which encloses the fault core, comprises many small-scale faults and joints

which are commonly inferred to promote fluid flow by increasing permeability along fault zones (e.g. Faulkner et al., 2010). The damage zone model is commonly accepted because it is easily visualised and understood in two-dimensions and has the potential to be numerically modelled. Unfortunately, the fault damage-zone model is rarely observed in outcrop and does not incorporate sufficient variability of fault zone structure to adequately define flow properties of faults (Childs et al., 2009).

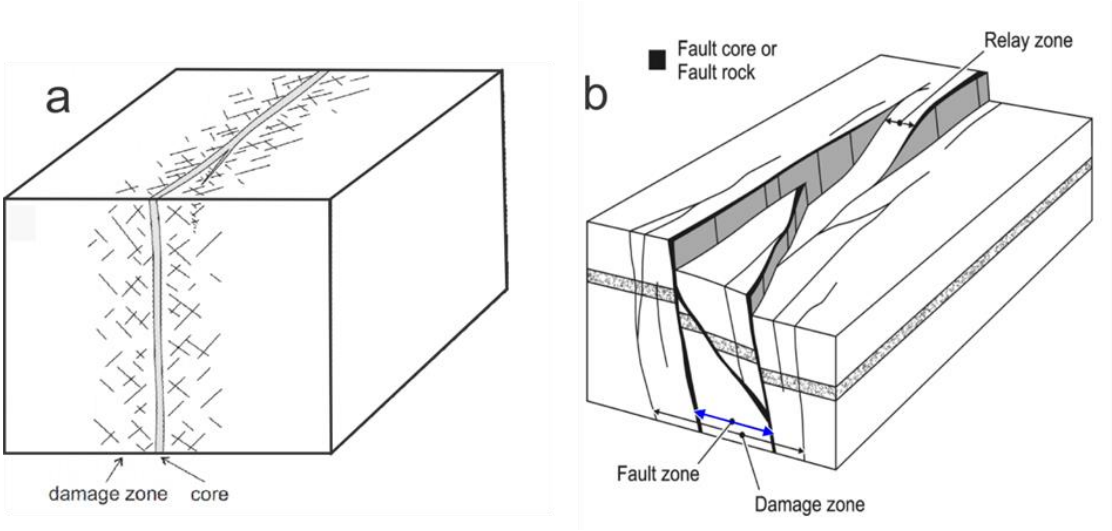

Figure 5: Diagrams illustrating fault-zone models. (a) Fault damage zone – fault core model showing a zone of fracturing which encloses a clay-rich core comprising low permeability fault rock (Chester and Logan, 1986). (b) Fault-zone model which shows how the thickness of clay-rich fault rock and fault zone (dominated by small faults) varies over a fault surface (Childs et al., 2009).

Fault zones are known for their highly variable displacement and internal complexity (Wallace and Morris, 1986; Caine et al., 1996; Childs et al., 1996; Childs et al., 2009; Faulkner et al., 2010). Areas of highest shear displacements are found within or, adjacent to, fault rock that commonly contains clay-rich material (Nicol et al., 2016). This clay-rich/fine grained fault rock can be generated by a number of processes including intense fracturing and crushing of host rock, smearing of clay and siltstone into the fault zone and/or by wall-rock injection into the fault zone. Fault rock commonly forms in spatial association with many small-scale faults and joints (Figure 6b) which together form the fault zone (Childs et al., 2009). Because fault zones include fault rock, (and associated

fractures and joints), the term is not directly comparable to the term damage zone. Furthermore, limited quantitative definitions of these terms (i.e. fault rock, fault core, fault zone, damage zone) produces added uncertainty when relating the geometries and dimensions of fault zones and fault damage zones (Childs et al., 2009).

Areas of variably fractured host rock are commonly (but not always) bounded by slip surfaces and associated fault rock within the fault-zone itself (e.g. Wallace and Morris, 1986; Wibberley et al., 2008; Childs et al., 2009; Faulkner et al., 2010; Nicol et al., 2013). These lenses produce variations in the width of fault zones and fault rock over the fault surface (Childs et al., 2009; Awdal et al., 2014). While fault-zone thickness shows a broad positive relationship with displacement (e.g. thicker fault zones and fault rock are generally associated with higher displacement faults), there can be several orders of magnitude variation in fault zone thickness for a given displacement (Childs et al., 2009; Nicol et al., 2013) (Figure 6 and Figure 7).

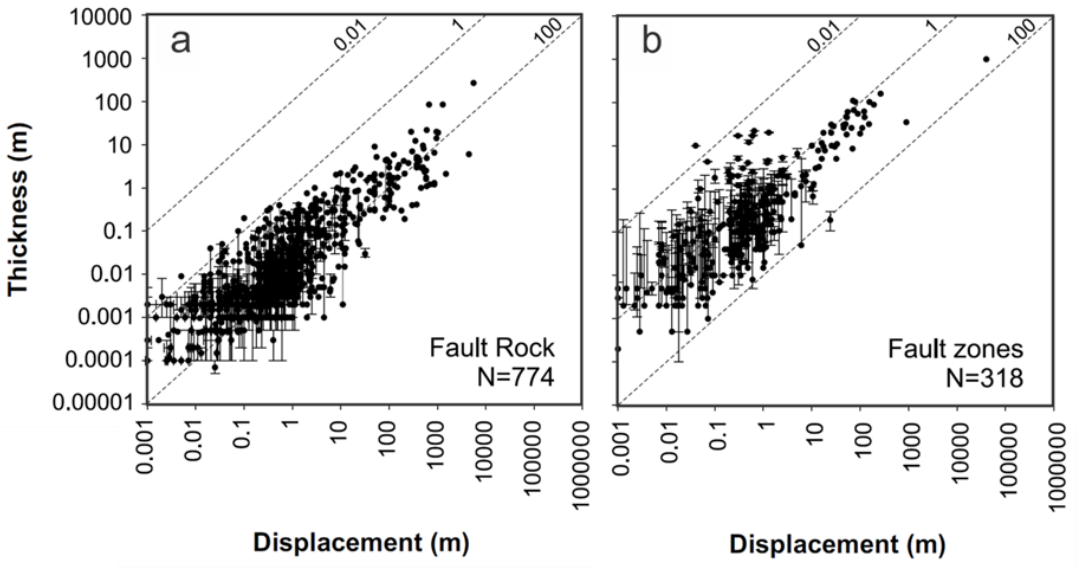

Figure 6: Graphs showing thickness vs. displacement for fault rock (a) and fault zones (b) collated from global data (Childs et al., 2009).

Power-law distributions can be demonstrated for fault length, displacement, width and fault-flow rates (e.g. Walsh et al., 1991; Yielding, 1992; Seebeck et al., 2014). The scaling relationships of these fault attributes are closely coupled with a positive correlation between fault-rock thickness and fault displacement and a number of models have been developed to account for such observations (e.g. Scholz, 1987; Hull, 1988; Power et al., 1988; Faulkner et al., 2003; Childs et al., 2009). In general, the host and fault rock

rheological properties are thought to be a primary control on fault-rock thickness. A geometric model proposed by Childs et al. (2009) describes fault geometry as being a controlling factor for the thickness and distribution of architectural elements. However, given the variability of fault-rock and fault-zone thickness-displacement, and the associated variations between data sets, estimating fault-rock or fault-zone thickness from these models will most likely result in a high level of uncertainty (Nicol et al., 2016).

Wider fault zones are usually associated with increased fault irregularities including segment boundaries (shown as a relay in Figure 5b), fault bends, fault intersections and fault terminations which are all often associated with elevated densities of small-scale faults and joints. Where fault zones are widest their permeability is often greatest (Hermanrud et al., 2014). Information gathered from numerous studies indicates that fluid flow within fault zones can be channelized and heterogeneous (Cox, 1999; Gartrell et al., 2004; Dockrill and Shipton, 2010; Ilg et al., 2012; Hermanrud et al., 2014). The suggestion that fault complexities could represent areas of increased permeability, clay content and channelized fluid flow has been widely published (Caine et al., 1996; Wibberley et al., 2008; Childs et al., 2009; Faulkner et al., 2010), however, there remains uncertainties as to under what conditions (rock rheologies, fault geometries and stresses) fault-zone complexities promote fluid flow and these models have not been robustly tested using *insitu* fluid flow data (Nicol et al., 2016).

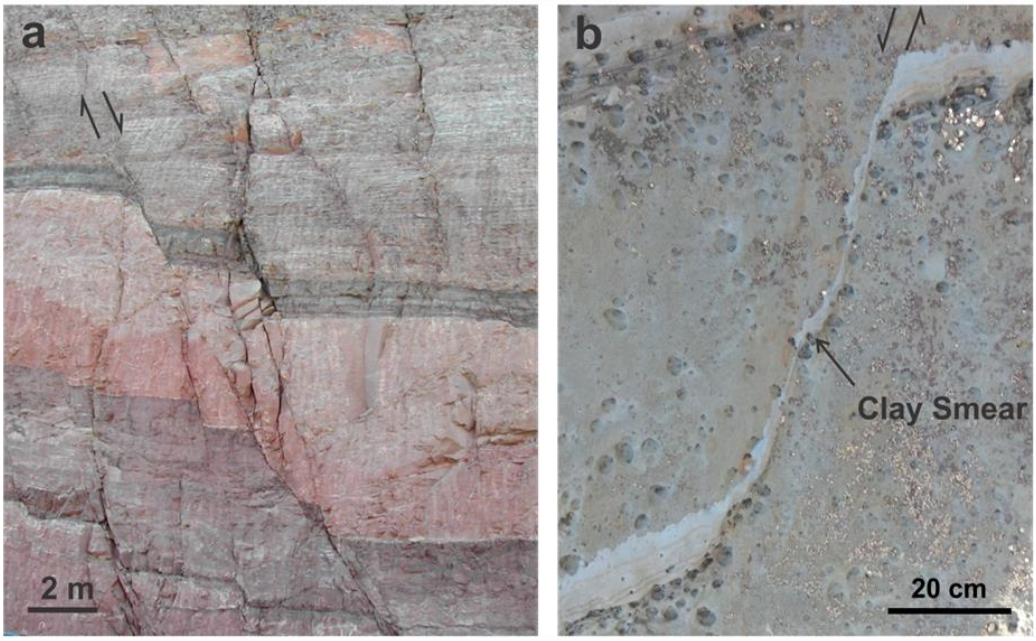

Figure 7: Photographs showing normal faults with varying displacements and degrees of clay smear. a) Fault within the Trail Formation displaying limited shale-smear, Utah, USA, and b) Fault within the Mount Messenger Formation showing extensive shale-smear, Taranaki, New Zealand (Nicol et al., 2016).

A combination of mechanical rock properties and confining stress acting on a volume of rock during deformation ultimately controls the spatial distribution of fault rock products within fault zones (Figure 8; Nicol et al., 2016). The spatial distribution of rock deformation products, such as fractures and fault rock, evolve over time in a three-dimensional sense and are the primary driver for the permeability properties of fault zones (Childs et al., 2009).

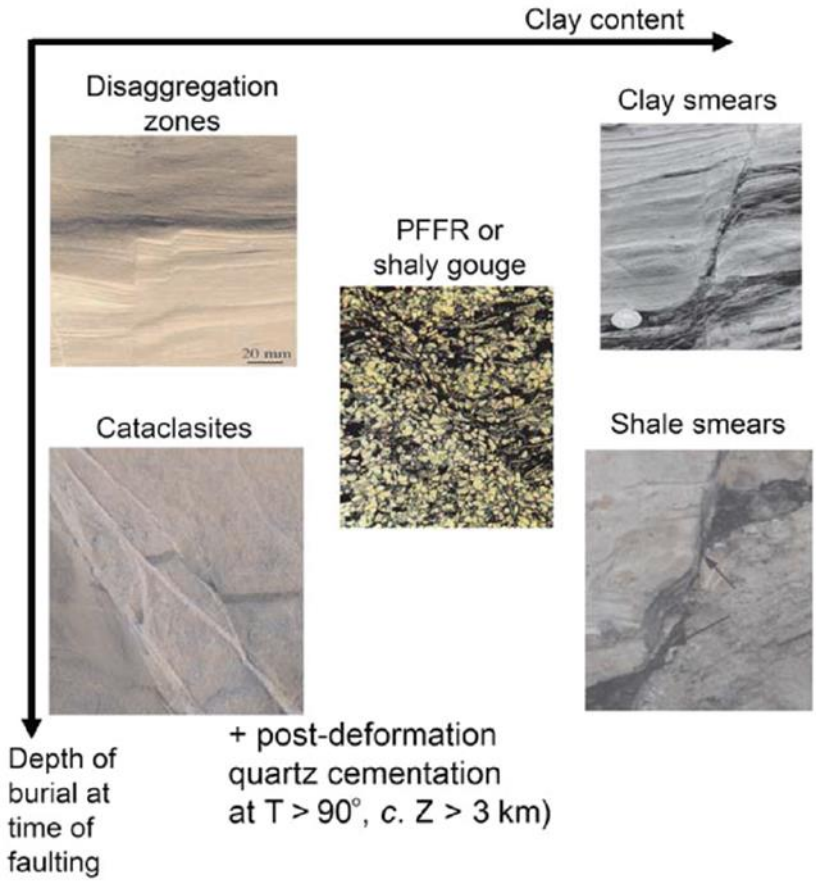

Figure 8: Diagram illustrating the types of fault rock that can be generated in silisiclastic sequences with varying clay content and burial conditions (Yielding et al., 2010).

2.3 Fault Geometries & Mechanical stratigraphy

Sandstone-siltstone sedimentary sequences displaced by normal faults are the primary source for many cross-fault permeability studies (Yielding et al., 1997; Manzocchi et al., 2010). These studies suggest that fault-zone architecture in interbedded sequences is at least partly controlled by the mechanical heterogeneity of the sequence itself, and by confining pressures (Peacock and Zhang, 1994; Childs et al., 1996, 2009; Patton et al., 1998; Schöpfer et al., 2007; Michie et al., 2014). Fault dips often steepen in stronger layers and shallow in weaker layers (e.g. Peacock and Zhang, 1994; Crider and Pollard, 1998; Micarelli et al., 2005; Schöpfer et al., 2006), producing changes in dip as the fault passes through layers of varying mechanical strengths. These changes in dip angle may form during fault propagation (Gross, 1995; Sibson, 1998; Ferrill and Morris, 2003) and can be caused by varying friction angles and failure modes (Figure 9) from one layer to the next.

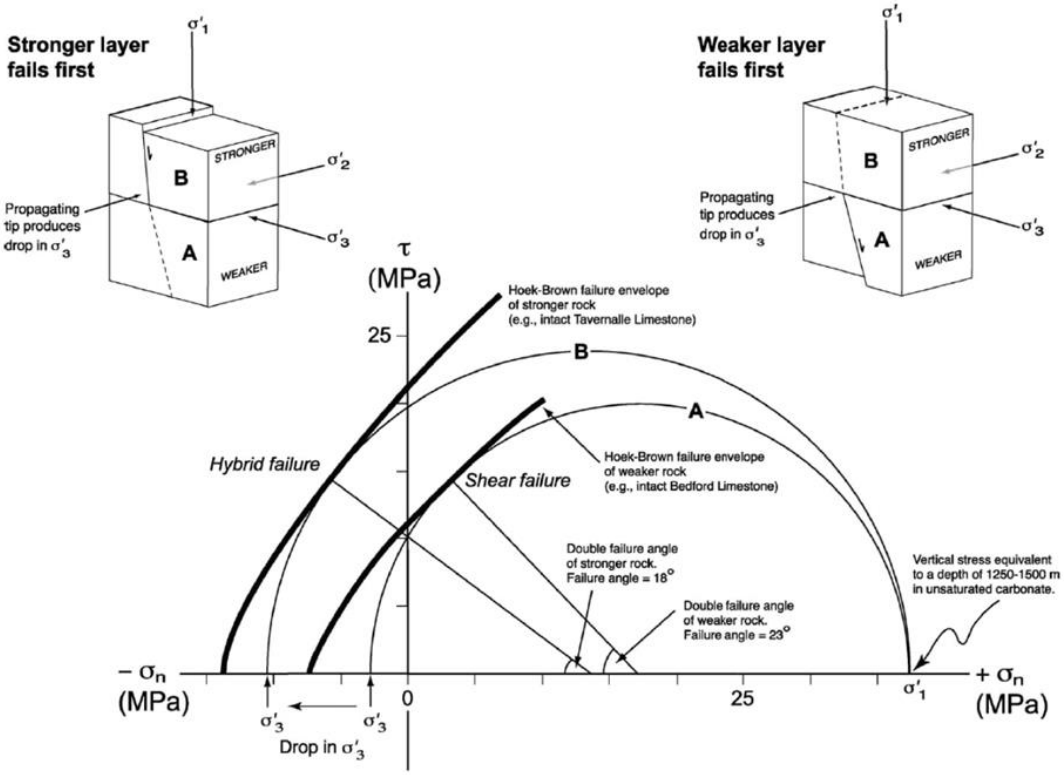

Figure 9: Diagram showing Mohr-circle failure envelopes for different layers varying in strength under normal stress with a weaker rock (B) less likely to fail in hybrid mode than a stronger rock (A) (Ferrill and Morris, 2003).

The greater the variation of mechanical strength between multi-layered sequences, the more likely dip angles will vary up through the sequence (Figure 8) (Sibson, 1996; Ferrill and Morris, 2003). This in turn causes variations in fault linkage during fault growth and has the potential to cause further fault-zone complexities which may include splaying and antithetic fault development (Schöpfer et al., 2007). Complexities in fault geometry related to mechanical stratigraphy can directly influence fluid migration and should be taken into account when characterising faulted reservoir fluid behaviour (Ferrill and Morris, 2003). In layered sedimentary sequences it is common for small-scale faults to be restricted to beds that are stronger mechanically (such as sandstones) (Nicol et al., 1996; Gross et al., 1997; Wilkins and Gross, 2002; Soliva and Benedicto, 2005). Growth of faults from strong beds into surrounding clay layers can also be observed at different scales and whether or not this occurs is primarily dependant on bed rheology, fault displacement and thickness of the clay beds being displaced by the fault (Roche et al., 2012). The degree of fault geometric complexity associated with stratigraphic

heterogeneity influences the variability of fault-zone thickness and geometry (Segall and Pollard, 1980; Peacock and Sanderson, 1991; Cartwright et al., 1995; Childs et al., 1996; Crider and Pollard, 1998; Peacock, 2002; Walsh et al., 2003).

Mechanical properties within individual layers can influence fault-zone architecture as much as mechanical strengths between layers (Soden and Shipton, 2013). Because rock properties directly influence fault growth processes and deformation, accurate prediction of fault-zone structure will not be possible only using displacement-dimension scaling relationships (Shipton et al., 2006). For example, Soden and Shipton (2013) show that more detailed characterisation of mechanical stratigraphy leads to more accurate predictions of fault-zone architecture. Their study demonstrates that host rock mechanical properties, along with burial history, affects fault-deformation processes and understanding these affects will lead to further development of more realistic fault-zone structures for permeability models (Soden and Shipton, 2013).

2.4 Fault Hydraulic Properties.

The hydraulic properties of fault rock and fault zones has been examined for a range of rock types with particular focus on silisiclastic sequences due to their importance for the petroleum industry (Chester and Logan, 1986; Wallace and Morris, 1986; Caine et al., 1996; Childs et al., 1996). The permeability of fault-rock in silisiclastic sequences typically ranges from $< 10^{-19}$ to 10^{-16} m^2 with values typically being highest parallel to the fault slip direction (e.g. Fisher and Knipe, 2001). Fluid flow through a given rock mass is known to be very localised and tortuous, often showing a highly non-linear behaviour with respect to deformation (Sanderson and Zhang, 1999; Tsang et al., 2007). The majority of such flow is often primarily controlled by a small fraction of architectural elements (i.e. fractures) that exist within a fault-zone fracture network (e.g. Seebeck et al., 2014). Damage zones, with associated micro fracturing, are also a focus of recent research (e.g. Faulkner et al. 2010), with studies showing that for siltstone and sandstone lithologies permeability can be 2-4 orders of magnitude higher within damage zones than the surrounding host rock. Increasing fracture density towards a fault can lead to increased permeability parallel to the dominant fracture orientation (e.g. Wibberley and Shimamoto, 2003; Tanikawa et al., 2009). Wibberley and Shimamoto (2003) show the variability of permeability across a large fault zone with the lowest values in the central part of the fault core (Figure 10). The central slip zone is where most of the crushing of host rock and smearing of low permeability fault rock typically occurs and produces clay-

rich material which reduces permeability. Smaller displacement faults (e.g. < 5 m displacement) can also locally influence permeability. Measurements over a 4m wide fault zone from Tanikawa et al. (2009) shows two-orders of magnitude variation in permeability where the highest and lowest permeabilities are proximal to the primary fault surface. Such studies reinforce the idea that the internal components of fault zones can act as low permeability barriers and high permeability conduits dependant on a range of factors including burial depth, fluid pressure and fluid barriers and viscosity.

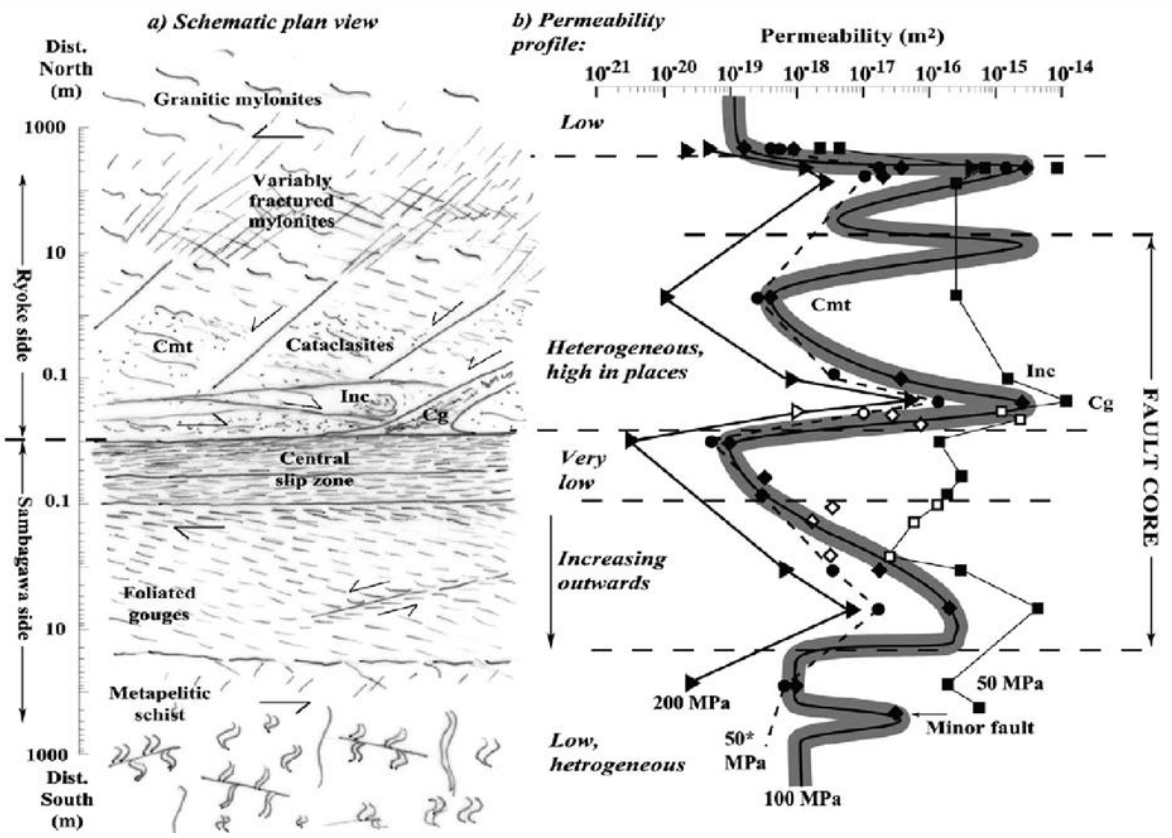

Figure 10: Diagrams showing variations in fault permeability across the Median Tectonic Line (Wibberley and Shimamoto, 2003). a) Main structural zones and b) permeability data. Cmt = cemented, Inc = incohesive and Cg = crenulated gouge.

Although shale smears commonly form in poorly lithified sequences via ductile flow and or injection, they can also form in lithified sequences via abrasion/shearing processes resulting in thin shale veneers along fault planes (Lindsay et al., 1993; Yielding et al., 2010). Shale smears usually become more discontinuous with increasing displacement with breaks in smears assumed to be sites of lower fault seal potential (Childs et al., 2007).

Figure 11 indicates the potential relationships between the clay content of a fault and the associated fault rock permeability (Fisher and Knipe, 2001). Fisher and Knipe (2001) illustrate the considerable amount of variability in permeability for any given clay content within a general trend of decreasing permeability as a function of increased clay content (Figure 11).

In sequences that are sand dominated the most common type of fault rock are disaggregation zones and cataclasites (Figure 11) (Fisher and Knipe, 2001; Sperrevik et al., 2002; Fossen and Gabrielsen, 2005). When slip occurs in sandstones under relatively low confining pressure (< 1 km in depth) dissagregation zones can form (Fossen and Gabrielsen, 2005). Grains within dissagregation zones do not undergo fracturing, instead they are reorganised within the zone and tend to have similar hydraulic properties as their host sandstones (Fossen and Gabrielsen, 2005). By contrast, cataclastic processes due to fragmentation of grains and infilling of pore-spaces associated with diagenetic processes form at higher confining pressures (> 1 km depth) resulting in cataclasites which generally have 2 – 3 orders of magnitude less permeability compared to the host (Fisher and Knipe, 2001). Beyond depths of > 3 km, with increasing geothermal gradient (> 90 °C), post deformation processes such as quartz cementation and clay alteration occur, with disaggregation zones and cataclasites becoming altered (e.g. Fisher et al., 2003; Cavailhes et al., 2013).

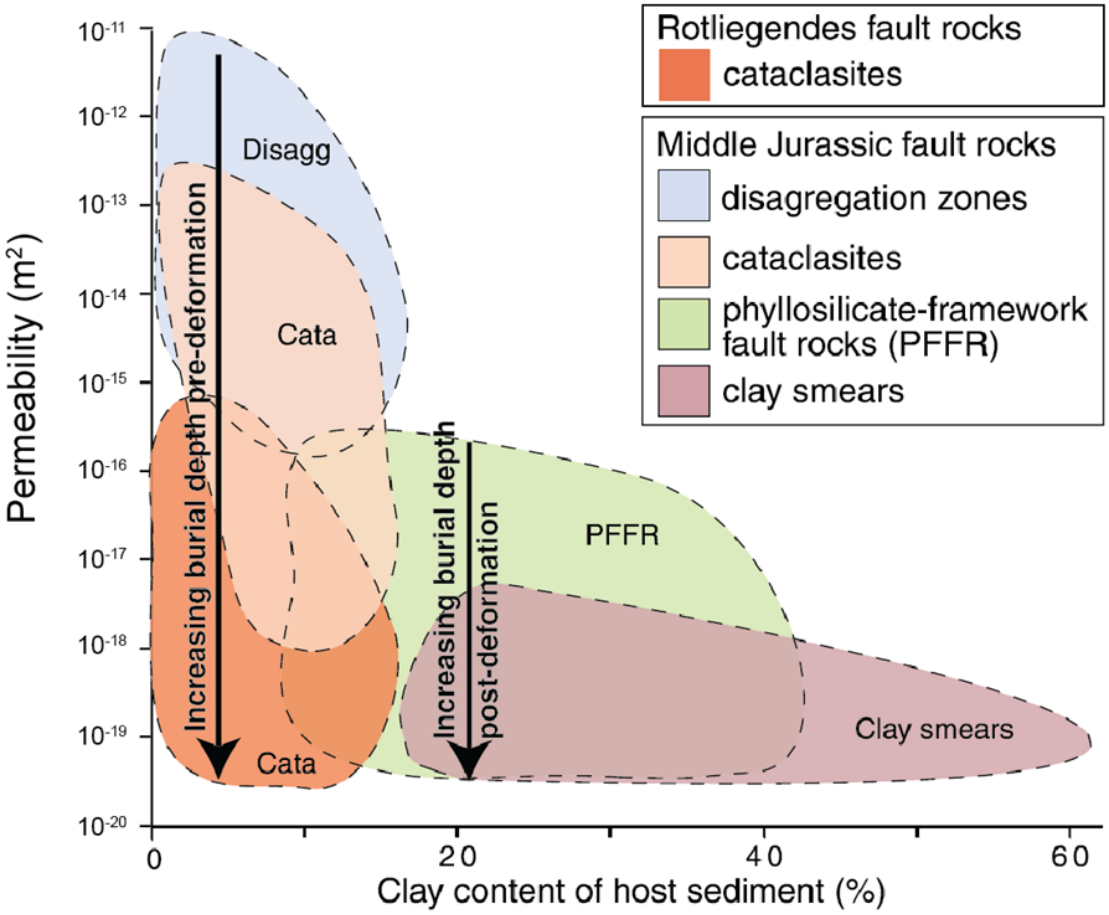

Figure 11: Graph showing permeability plotted against clay content of host rock for different types of fault rock using data from the North Sea and Norwegian Shelf (Fisher and Knipe, 2011).

It is widely accepted that bulk-rock permeability decreases with increasing depth in the crust which is consistent with pore/fracture closure and effective pressure studies (e.g. Wei et al., 1995; Ohman et al., 2005; Ishii et al., 2010). Fault-zone architecture, kinematics and permeability can be strongly influenced by the depth at which the fault formed (Ishii et al., 2010). Fluid migration potential within siltstones is known to change with different principal modes of failure, which is directly related to the depth at which a fault formed (Ishii et al., 2010). At depths of <400 m fault growth is mainly driven by linkage of tensile fractures which is known to generate fault zones of increased permeability, whereas at depths exceeding 400 m it is common for shear failure to form faults leading to increased fault-rock generation (Ishii et al., 2010).

Studies of fault-rock and fault-zone architecture suggest an inverse relationship between the fault-rock permeability and the burial depth (Tanikawa et al., 2009; Morrow et al., 2014), but this relationship does not always hold as fault-rock permeability, like other fault zone characteristics, displays a significant amount of variability (shown in Figure 12). For example, both shale smear and cataclastic fault rock display up to 2 – 3 orders of magnitude variation in permeability at a given depth (Fisher and Knipe, 2001) (Figure 12 B).

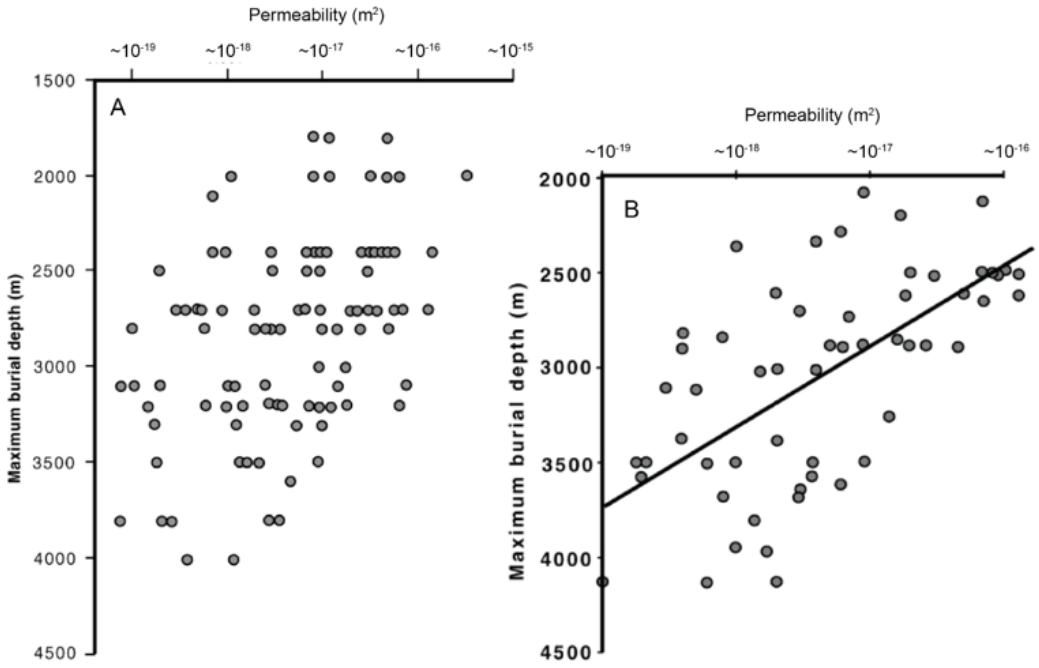

Figure 12: Graphs showing the relationship between permeability and maximum burial depth for cataclastic fault rock (A) and clay rich (shale smear) fault rock (B) from faults in the North Sea (from Fisher and Knipe, 2001).

2.4.1 Fault Permeability

Fault zones can be understood in a 4-D context as deformed volumes of rock with highly heterogeneous and anisotropic properties that change and evolve over time within the crust (Nicol et al., 2016). While only constituting a small fraction of the crust, faults can strongly influence its mechanical and hydraulic properties. Faults comprise numerous components (e.g. relay ramps, dilatational jogs, reidel shears) across one or more slip planes (e.g. within the fault zone) accommodating a large variability in strain (Caine et al., 1996; Childs et al., 1996; Shipton and Cowie, 2001; Faulkner et al., 2003; Childs et al., 2009; Faulkner et al., 2010; Michie et al., 2014). The interaction of these factors leads

to structural variations along strike and down dip that can occur over relatively short distances (Childs et al., 1996; Shipton and Cowie, 2001; Lunn et al., 2008; Faulkner et al., 2010; Seebeck et al., 2014). Fluid flow through a volume of rock is usually governed by pressure gradients, structural permeability (such as faults, fractures and folds) and host rock anisotropy (such as foliation and bedding) (Nicol et al., 2016). Such parameters can lead to localised high-volume flow associated with economic mineral deposits within fault zones (Sibson, 1996; Cox, 1999; Rowland and Simmons, 2012). The hydraulic properties, structure, mechanical behaviour and composition of fault rock can be influenced by four main factors which include:

- Host rock composition and rheology, with emphasis on fine grain clay mineral content.
- Stress conditions during faulting including burial depth, tectonic setting and fluid movements.
- Temperatures post-faulting, relating to burial depth and associated geothermal gradients.
- Syn- and post-kinematic fluid interaction including composition and reaction products.

Permeability, rock mechanics and the structure of fault zones have significant temporal and spatial variability which in turn has the potential to impact or modify crustal fluid flow and migration (Obeahon et al., 2014). The analysis of the sealing potential of faulted low permeability cap rocks and the resultant impact on hydrocarbon migration and CO_2 sequestration make predicting the hydraulic properties of faults important for practical reasons.

At larger scales faults control uplift and subsidence which in turn influences fluid pressure gradients, temperature and fluid migration (Hooper, 1991). Smaller scale fault zones control flow pathways of fluid during migration through a volume of rock (Barr, 2007; Van Hulten, 2010). The structure, fluid flow properties and internal mechanics of fault zones are closely coupled and should not be considered or analysed separately from one another as this could generate inconsistencies within potential permeability modelling and prediction (Faulkner et al., 2010).

Along fault fluid flow has generally been inferred to be facilitated by open fractures, but there is limited data to support this idea and the mechanisms that are associated with fracture opening and flow localisation (Cartwright et al., 2007). Along fault permeability

can be sufficiently promoted by one or two orders of magnitude between the unfaulted seal and fault zone (Cox, 1999; Seebeck et al., 2014). Some studies indicate that along-fault fluid migration can be up to nine times higher than surrounding host rocks with a $10^{-13}/10^{-11}$ m^2 increase in permeability (Ingebritsen and Manning, 2010). Several in-situ studies have displayed the extreme complexity of fluid flow through fractured host material (e.g. Tsang and Neretnieks, 1998; Cox, 1999). One example includes a ground water flow study which indicated that the majority of flow was confined to specific points within highly fractured zones of larger faults (Seebeck et al., 2014). Such channelized flow is also generally inferred to reflect the heterogeneous structure of fault zones, particularly with regards to variations in clusters of joints and in the thickness of low-permeability fault rock (shown in Figure 13) (Nicol et al., 2016). Numerical models support results from in-situ permeability measurements and detailed fault studies. Models generated show highly non-linear fluid behaviour and flow localisation for a wide range of natural fracture networks which are well connected and critically stressed (Zhang and Sanderson, 1998; Sanderson and Zhang, 1999; Tsang et al., 2007). Distribution and flow rate variability for such fracture systems can be accounted for within the system if it is close to the percolation threshold (e.g. Cox, 1999; Sanderson and Zhang, 1999).

2.4.2 Connectivity of Faults

When analysing fluid migration through fault zones it is important to take account of connectivity within the fault zone or rock mass as fractures typically control bulk permeability. Percolation threshold theory can be used to describe how such networks influence fluid flow. Percolation theory incorporates three main network elements which includes, i) backbone - connections within the system that are responsible for much of the associated fluid flow through the fracture network (usually from one side of the system to the other), ii) dead-end - smaller connections that branch off from backbone fracture networks, and iii) isolated - networks that are not associated with fluid flow and are often disconnected from the main system (Balberg et al., 1991; Cox, 1999; Odling et al., 1999). Percolation thresholds are defined by the point where enough elements connect over a fault system to allow fluid flow across the width of the zone, thus the reservoir or seal becomes permeable (Stauffer, 1987; Zhang and Sanderson, 1998; Berkowitz et al., 2000). As a fracture network crosses the percolation threshold large permeability changes are achieved by small changes in fracture length (Tsang et al., 2007).

The orientation and size distribution of fractures, which relates to the density and spatial distribution of fracture networks, contribute to fracture connectivity (Odling et al., 1999). As fracture density increases so does the proportion of fracture area within a fracture cluster/network. Fracture orientation has a large influence on permeability as fractures with similar orientations do not intersect until fracture density becomes high enough, whereas fractures at high angles to each other are more likely to intersect and influence connectivity. Size and distribution of fractures can also have an important influence on connectivity as clusters of shorter fractures will more often than not have less connections than clusters of longer fractures (Balberg et al., 1991; Odling et al., 1999).

A study from Bour & Davy (1997) analysed random fracture patterns in 2D and concluded that the exponent of the power-law distribution (cumulative frequency length distribution) can be used to quantitatively describe the connectivity within a fracture network as it describes the abundance of fractures with varying sizes (Bour & Davy, 1997). Exponents larger than -1.0 indicate that overall connectivity, and therefore fluid flow, is controlled by larger fractures while exponents less than -2.0 are indicative of smaller fractures controlling connectivity, and anything falling between these exponents suggests that both large and small fractures are contributing to overall connectivity (Bour and Davy, 1997; Odling et al., 1999).

Different types of fault rock in silisiclastic sequences may form due to changes in the ratio of coarse grain to fine grained material (sand to clay/shale), to depth of burial, amount of displacement, and/or the degree of lithification (Lehner and Pilaar, 1997; Aydin and Eyal, 2002). Shale smears can occur over a fault plane (see Figures 6 and 7) and are often assumed to thin with increasing distance from the source bed (e.g. Lehner and Pilaar, 1997; Aydin and Eyal, 2002; Eichhubl et al., 2005; van der Zee and Urai, 2005; Yielding et al., 2010).

2.4.3 Fluid Migration

Faulting within the earth's crust strongly influences the migration of subsurface fluids and gas (Wade, 1913; Hooper, 1991; Caine et al., 1996; Wibberley et al., 2008; Faulkner et al., 2010). A number of factors can influence the hydraulic behaviour of faults and these include the rheology and permeability of host and fault rock as well as bulk stress conditions, structural anisotropy, differences in pressure across the fault and viscosity of the fluids interacting with a fault zone can influences its permeability (Caine et al., 1996; Evans et al., 1997; Edlmann et al., 2013).

Different fluids are influenced by different forces, e.g. hydrocarbons will flow and interact with rock and associated fractures differently to water due to varying physical properties such as viscosity (Nicol et al., 2016). Hydrocarbon generation and migration (or flow) is commonly driven by burial and sediment compaction; however, hydrocarbons can also become mobile in a water saturated system due to displacement pressures, which can retard hydrocarbon flow and modify buoyancy potential allowing fluids to rise vertically (Nicol et al., 2016). Displacement potential describes the capillary entry pressure required to drive fluids, such as water, out of pore spaces by hydrocarbons. Capillary entry pressures can also retard the flow of oil through rock (more commonly for fine-grained material) even when there is well established flow of water through the same rock mass (Hooper, 1991).

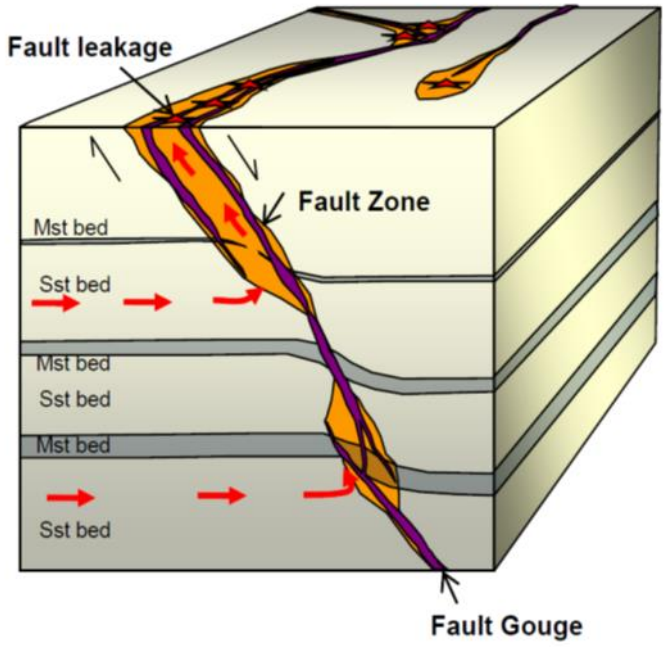

Figure 13: Block model indicating zone of permeability (red stars) and potential fluid migration along a fault zone (Nicol et al., 2016).

Elevated stresses in the crust and fluid pressure gradients have also been thought to generate fluid flow pathways (Sibson, 1996; Cox, 1999; Tsang et al., 2007). Several geomechanical techniques can be used to predict along-fault fluid migration by utilising location and fault geometry, along with estimated stress tensors, from which critically stressed points along the fault (which are inferred to promote fluid flow) can be identified

(see Figure 13) (e.g. Morris et al., 1996; Ferrill and Morris, 2003). Although the theory behind such techniques has been widely accepted, the predictions that have been made remain unsubstantiated in many cases (Nicol et al., 2016). With limited detailed analysis and understanding of mechanisms that lead to along-fault fluid flow, the potential for some faults to the integrity of regional seals compartmentalise reservoirs can be difficult to assess.

2.5 Fault Seal Prediction

2.5.1 Evidence for Fault-seal

Fault zones comprise anastomosing systems of interacting slip surfaces and fault rock which are irregular over scales from millimetres to kilometres (Caine et al., 1996; Childs et al., 1996; Evans et al., 1997; Faulkner et al., 2010). Faults can act as both barriers and conduits for sub-surface fluid flow, and recent studies suggest that the permeability of fault zones may be greater during deformation than after (Ballas et al., 2015). Evidence that low permeability fault zones influence fluid-flow include reservoir compartmentalisation, across-fault pressure changes, differential subsidence, and the accumulation of large volumes of hydrocarbons against fault planes (Hooper, 1991; Van Hulten, 2010). Faults have been observed to produce thermal, salinity, seismic and gas flux anomalies as well as to induce mineralisation within surrounding host rocks suggesting that they can also act as conduits for fluid flow under the right conditions (Hooper, 1991; Annunziatellis et al., 2008; Faulkner et al., 2010; Seebeck et al., 2014). For example, active faults may cause the permeability of faults zones to increase while inactive faults could reduce fault zone permeability, thus suggesting that processes such as fault creep may cause fault zones to both act as a conduit and barrier to fluid flow during their lifetime (Miller et al., 2004; Leclère et al., 2015).

Fault seal prediction analyses emphasises the importance of fine-grained fault rock associated with local permeability reductions and have primarily been developed for the petroleum industry (Yielding et al., 2010; Noorsalehi-Garakani et al., 2013). Fault seal analysis is based on the idea that faults form capillary seals (Jennings, 1987; Watts, 1987; Yielding et al., 1997; Brown, 2003; Manzocchi et al., 2010; Bretan et al., 2011). Hydrocarbon flow and migration is usually locally driven by buoyancy and retarded by capillary properties associated with the rock mass from which migration is occurring (Carruthers and Ringrose, 1998; Bretan et al., 2011). Fluid migration can be prevented by

such capillary forces causing a seal to occur. Seals are likely to remain established until buoyancy forces of trapped hydrocarbons exceed capillary threshold pressures associated with the rock initially generating the capillary seal (Nicol et al., 2016). Pore throat size is the main factor which controls capillary threshold pressures as the smaller the pore throat size the more likely the seal will be able to withstand higher capillary threshold pressures, and therefore larger hydrocarbon column, before leaking occurs through the fault zone (Yielding et al., 1997; Manzocchi et al., 2010; Bretan et al., 2011). This is important as siltstone in interbedded sequences have smaller pore sizes than the sandstones, and when smeared, may cause the fault rock to develop higher capillary thresholds and reduced permeability meaning the fault is acting as a seal.

2.5.2 Juxtaposition

Where a reservoir is faulted against siltstone, in sandstone-siltstone sequences, it is likely that a seal will occur via juxtaposition. Where sandstone units are in contact across a fault it could be sealing or leaking to cross-fault fluid flow, while it is also possible that the fault may be sealing at one location while leaking at the other at any given point of time (Nicol et al., 2016). Stratigraphic unit juxtaposition can be visualised by creating Allan diagrams which display the hanging wall and footwall, cutoffs of key stratigraphic units, over the mapped extent of the fault surface (Allan, 1989). Allan diagrams are commonly utilised for both petroleum industry studies and CO_2 storage assessment (Bretan et al., 2011). Cross-fault permeability studies can be regarded as static on production timescales, even though displacement evolution and back stripping is incorporated, as they do not take into account changes in fault seal during fluid injection (Nicol et al., 2016).

2.5.3 Fault Seal Models and Algorithms

Many studies on fault-rock and fault-seal prediction infer that the generation of fault rock is formed from smearing and mixing of clay-rich host rock beds into the fault zone (Nicol et al., 2016). Various algorithms have been created for predicting and estimating flow properties of faults and analysing their implications for fluid migration. Algorithms used for fault permeability predictions are based on conceptual models that incorporate shale smear and mixing processes. Shale-smear algorithms assume source bed are progressively sheared with increasing displacement and include Clay Smear Potential (CSP) and Shale Smear Factor (SSF) methods (Figure 14) (Lindsay et al., 1993; Manzocchi et al., 1999; Sperrevik et al., 2002).

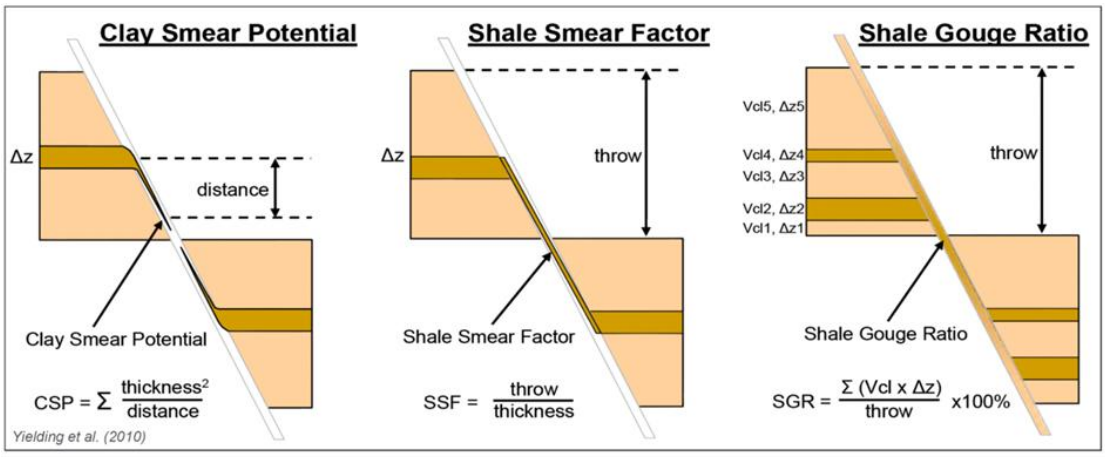

Figure 14: Diagrams illustrating the three main types of fault seal models used in industry for permeability predictions within fault zones. Each conceptual model has an associated algorithm used for prediction calculations (Yielding et al., 2010).

CSP and SSF contrast with the Shale Gouge Ratio (SGR) which is the most commonly utilised method for predicting fault seal. SGR is an algorithm that calculates the shale to sand ratio at a specific point on a fault based upon the ratio of shale:sand that has gone passed that point (Figure 14, Table 1) (Sperrevik et al., 2002). Calculations for SGR can be made along a fault profile using displacement and a measure of the faulted stratigraphy. Mapping and modelling of mudstone or siltstone beds from outcrop and well logs (such as gamma ray) allows for content of clay to be estimated for SGR and further manipulated to generate fault-rock threshold pressures or permeability estimates which can be used in fault-seal analyses (Nicol et al., 2016). SGR values and associated relationships between both threshold pressure and permeability commonly vary between different fault rock studies which is most likely due to a combination of varying burial, diagenetic and/or fault-rock generation processes (Childs et al., 2007; Manzocchi et al., 2010).

Table 1: Summary of potential algorithms used for shale-smear and permeability predictions of fault zones associated with shale beds Giger et al., 2013).

Algorithm	Formula*	Predictive Application	Mechanisms	References
Clay smear potential (CSP)	$CSP = c \times \sum t_{sh}^{n}/d^{m}$ $c = 1, m = 1, n = 2$	Thickness of clay smear	Injection, flow	Bouvier et al., 1989; Lehner and Pilaar, 1997
	Variations: Calibration factor $c \neq 1$ to account for rheology and stress dependency			Fulljames et al., 1997
	Smear factor (SF = CSP, but where $c = 1$, $m \neq 1$, $n \neq 2$)[1], also referred to as generalized smear potential (GSP) by[2]			[1]Yielding et al., 1997 [2]Doughty, 2003
Shale smear factor (SSF)	$SSF_{[c]} = S_{t[c]}/t_{sh}$**	Continuity of clay smear, seal breakdown for $SSF = SSF_c$	Abrasion, shear/drag, injection/flow	Lindsay et al., 1993
	Variation: Probabilistic shale smear factor (PSSF)			Childs et al., 2007
Shale gouge ratio (SGR)	$SGR = \sum[V_{sh(i)} \times t_{sh(i)}]/S_t$	Distribution of phyllosilicates along fault zone, seal strength when calibrated	Abrasion, wear, grain-scale mixing	Fristad et al., 1997; Yielding et al., 1997
	Variation: Effective shale gouge ratio (ESGR) with weighting factor, essentially a hybrid of CSP and SGR			Knipe et al., 2004; Freeman et al., 2010

*c = constant to calibrate for rheology and stress; d = distance between the shale/clay source layer and a point in the fault zone; m and n = scaling exponents; S_t = cumulative or total slip; t_{sh} = thickness of phyllosilicate-rich (clay/shale) layer; V_{sh} = volumetric fraction of phyllosilicates.
**The subscript $_{[c]}$ denotes the critical S_t at which clay smears become discontinuous (seal breakdown).

SSF is an alternative method to SGR which assumes fault zone structure is acting as a perfect shear zone, the smear being continuous until a critical point is reached (SSFc) where the bed becomes discontinuous (Figure 14). A Probabilistic Shale Smear Factor (PSSF) can be applied when SSF > SSFc and the discontinuous smear is randomly placed between the shale bed cut offs. A fault is inferred to be sealing when multiple smeared siltstone beds form an unbroken seal across the fault zone (Childs et al., 2007; Yielding, 2012). The PSSF method is stochastic and multiple models can be run with, or without, varying parameters to test the stability of the results (Childs et al., 2007).

2.5.4 Validation of Models and Algorithms

Validation of SGR and SSF methods is limited with only a small number of studies comparing SGR/SSF estimates with capillary threshold and trapped column height information (Yielding, 2012). The most commonly applied fault-seal prediction methods rely on correlations between clay content (usually from lab samples) and threshold pressures, which are coupled together with the assumption that SGR provides a proxy for fault-rock clay content (Bretan et al., 2011). The basis for this idea is illustrated in Figure 14 which shows that heterogeneity of reservoir rocks can generate variable SGR profiles and calculated capillary threshold pressures linked exponentially to SGR using industry standards (Manzocchi et al., 2010; Bretan et al., 2011). Accumulations of hydrocarbons

against sealing faults increases the column height which in turn leads to an increase in capillary pressures at the seal-reservoir interface (shown as dotted lines, Figure 15C) (Manzocchi et al., 2010). At some point the capillary pressure will match the capillary threshold of the fault rock, allowing the migration of fluids across the fault zone. Figure 15 illustrates that the point at which the seal is breached can vary as it does not always occur at; a) the top of the accumulation, b) the hydrocarbon-water contact, or, c) the location of lowest SGR (Manzocchi et al., 2010).

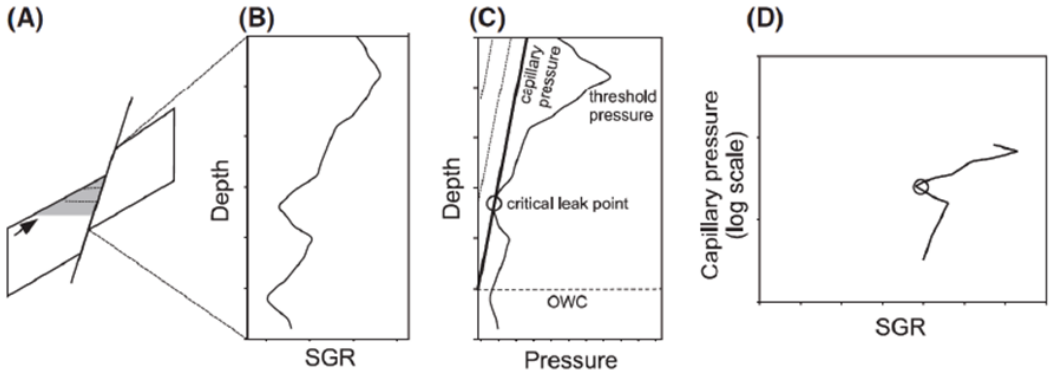

Figure 15: Diagrams illustrating the use of the Shale Gouge Ratio (SGR) method. A) Idealized hydrocarbon column (grey) with arrow indicating migration direction. B) SGR readings along the zone of sand-on-sand offset. C) Capillary threshold pressure estimated from SGR information. Black circle indicates seal capacity of the fault as the capillary threshold pressure of the reservoir has reached the capillary threshold pressure of the fault rock. D) Reservoir capillary pressure plotted against SGR with indication of potential leak point (circle) (Bretan et al., 2011).

One study from (Bretan et al., 2011) describes the relationship between SGR to capillary threshold pressure data from fault-bounded reservoirs using empirical fault seal envelopes (Figure 15). The seal envelopes are calibrated by associated capillary pressure and depth data of studied hydrocarbon-water contacts. If a particular fault is controlling hydrocarbon column height a defined critical leak point can be established from the distribution or spread of capillary pressure vs. SGR data (Figure 15). Specific SGR values can be further constrained using multiple sets of capillary pressure/SGR data from numerous faults from combined field studies. Figure 15 represents a compilation of

known normal faults active at < 2 km depth with assumed across-fault pressures equal to capillary pressures (Yielding, 2002). The faults analysed suggest that burial depths can influence fault-seal envelopes.

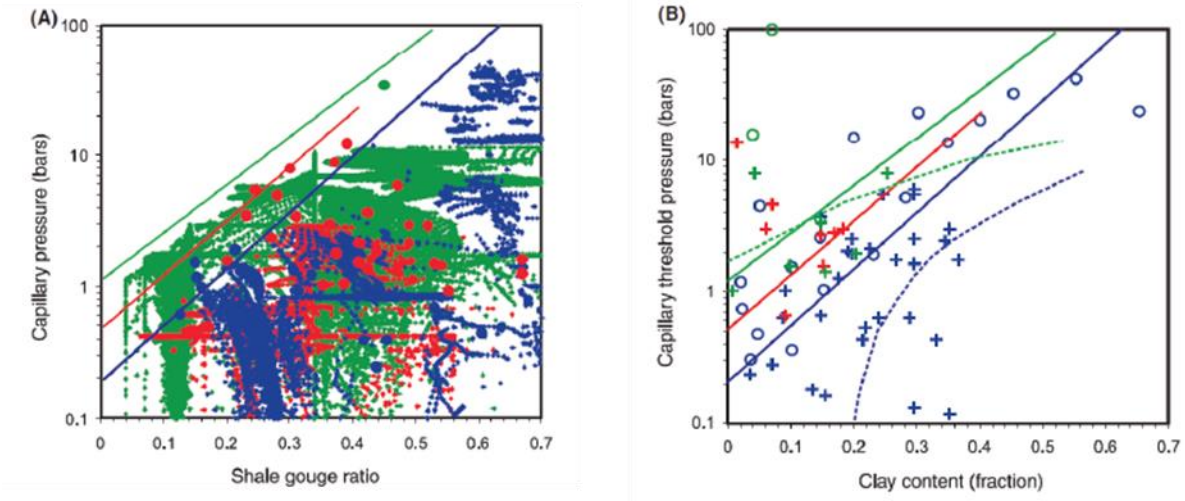

Figure 16: Graphs showing SGR calibrations (Manzocchi et al., 2010). A) Global normal fault data with SGR values vs. capillary pressures associated with analysed faults. Small groups of circles represent all data for individual faults (as shown in Figure 15D), while large circles represent "critical leak points" (circle in Figure 15C/D). Colour represents depth of fault burial with blue corresponding to < 3 km depth, red 3 – 3.5 km depth, and green being 3.5 – 5 km depth. B) Fault seal failure envelopes generated from (A) and further compared with capillary threshold measurements from laboratory studies (Gibson, 1998; Sperrevik et al., 2002) based on a hydrocarbon-water interface tension of 40mN/m at 30 °. Dashed lines represent seal failure envelopes for shallowest and deepest depth classes (Yielding et al., 2010).

2.5.5 Uncertainties of Fault Seal prediction

Calibrations of fault seal methods using empirical reservoir pressures and hydrocarbon column height/flow data, along with predictions and application to the field/other fault systems, still carries a high level of uncertainty (James et al., 2004). Such uncertainties are listed below:

- Quality or quantity of input parameters are insufficient. This includes displacement measurements, fault-rock content and fault-zone geometries. These

parameters are key for producing representative flow simulations which are non-unique (James et al., 2004).

- Definitions for shale-smear geometry and fault-zone structure are limited/not detailed enough for models which introduces further uncertainty as heterogeneous structure of fault zones may not be fully captured (James et al., 2004).
- Unmapped, sub-seismic, faults may alter clay smear geometries on a local scale (Nicol et al., 2016).
- Defining clay content of fault zones from gamma ray logs varies significantly and is often model dependant, and fault-seal prediction may also vary depending on where the sand/mud dominated rock type change is delineated (Nicol et al., 2016).
- Physical properties and geometries of clay smear has potential to be altered by mineralogy and diagenesis which are not explicitly accounted for in the algorithms currently in use (Nicol et al., 2016).
- Capillary threshold pressure data and/or column height information is rarely utilised for fault-seal prediction with little validation of fault seal for a given basin or reservoir containing the faults of interest. There are still uncertainties whether using global input parameters/calibration for local application is correct (Nicol et al., 2016).

Though fault seal predictions are common practice throughout CO_2 and petroleum industries, such uncertainties suggest that fault seal prediction models and results may be interpreted differently from one person to the next which has broad implications for fault seal model utilisation. There are doubts within the petroleum industry whether faults seal on geological timescales (Vrolijk et al., 2012; Hermanrud et al., 2014). On the other hand there is increasing evidence to suggest that fault seal can be effective on production timescales (Manzocchi et al., 2010). Both the CO_2 and petroleum industries provide insights into how faults control and influence reservoir compartmentalisation. To test fault-seal methods, and ultimately improve the predictive power of fault analysis, a clearer understanding of the heterogeneites and processes that produce low permeable fault rock is required. Up to date knowledge and fault seal datasets are held by large petroleum companies which either unpublished or not inaccessible to the public and these data are required to facilitate further advances in fault seal prediction modelling (Nicol et al., 2016).

2.6 Summary

Examining how faults interact with reservoirs and influence fluid flow is important for many industries including petroleum, CO_2 storage, geothermal and nuclear. Fault zones are complex and vary both spatially and temporally. Knowledge of the interactions between hydrocarbons and faults provides information on fault-sealing and migration processes. Numerical flow simulations, algorithms and geomechanical models are useful for understanding fluid flow (i.e. CSP, SSF and SGR methods). Information obtained from these models can be used to constrain hydrocarbon migration processes and, with technological advances, can allow testing and validation of results gained from models with fine-tuning of structural and stratigraphic input parameters (Manzocchi et al., 2010; Vrolijk et al., 2012; Hermanrud et al., 2014). However, in order to interpret the models there is a need to better understand of the input parameters and associated uncertainties. Key areas of future focus that arise from these studies includes; a) further defining, improving and quantifying the geometries and hydraulic properties associated with fault zones, b) advancing flow simulations and geomechanical flow predictions coupled with sensitivity testing, and c) validation and further testing of such models using information gathered from empirical fluid flow observations from various fault zones (Nicol et al., 2016). This thesis focuses on improving our understanding of fault-zone geometry and its spatial variation.

3 DATA AND METHODS

3.1 Introduction

This chapter provides an overview of how the research objectives set out in the previous chapter 1 will be achieved. It presents data collection and analysis methods, and discusses the limitations of the data. The data were mainly sourced from outcrop-scale observations coupled with laboratory based analysis designed to provide micro-scale information of the faulting. Descriptions of the observations and interpretation of the results are presented in chapters 4 and 5, respectively.

3.2 Field-data Collection

A large amount of fault data have been collected from the Mount Messenger Formation (e.g. Childs et al., 2005; Childs et al., 2007; Giba et al., 2010; Nicol et al., 2013). These studies present information on the geometries, kinematics, fault-zone architecture and permeability of faults. Of particular relevance to this study Childs et al., (2007) developed the probabilistic shale smear factor (PSSF) methodology using fault observation and analysis from the Mount Messenger Formation. This thesis builds on Childs et al., (2007) by measuring and analysing dip-parallel variations in fault attributes (e.g. fault displacement, fault-zone width, and fault-rock thickness and grain size distribution).

Data were primarily gathered from small normal faults (< 0.3 m displacement) exposed in sea cliffs of the Mount Messenger Formation along the Northern Taranaki coast (Figure 2 and Figure 58). These data have been collected to help quantify the geometric complexity and variations of hydraulic properties along fault zones. Observations can be used to produce models and algorithms that reflect fault-seal processes. All faults analysed displace interbedded fine – very fine sandstone to coarse – very coarse siltstone sequences with varying thickness from 2 to 60 cm for the sandstones and 0.9 to 29 cm for the siltstones (e.g. Figures Figure 65 – 71). The Mount Messenger Formation was subject to burial depths of less than 1.5 km during faulting with little mineralization in fault zones. The faults studied have 100% exposure at scales of 1 mm or greater.

For the purpose of this thesis six faults were studied in detail. Summaries of the fault locations, geometries and sample measurements are presented in Tables 2 and 3, respectively. The data collected from each fault includes measurements of fault-zone thickness, fault-rock thickness, bed displacement (i.e. throw) and number of deformation bands (Tables 13 – 19: appendix). These measurements were accompanied by grain-size analysis of individual sandstone and siltstone beds and fault rock derived from the host rock (Tables 21 – 26: appendix). In addition, a limited number of samples were subject to Scanning Electron Microscope (SEM) and thin section analysis to examine fault microstructure. Data were collected from a restricted range of fault types, fault sizes and sample lengths to limit the scope of this study. This information may apply to faults of several tens of metre displacement, however upscaling of results from this thesis have not been specifically examined. In all cases the distance over which a fault could be sampled was constrained by vertical reach (i.e. ladder height and personal reach). Cleaning and preparation of outcrops was carried out using a flat-head scraper to smooth the rock surface and a compressed water sprayer was utilised to remove loose sediment and expose finer structural details within the fault zones.

Table 2: Summary of the locations, displacements, lengths and measurement spacings for the six faults studied.

Fault Name	Location		Maximum Displacement (mm)	Average Displacement (mm)	Fault Sample Length (cm)	*Measurement Spacings (cm)*
	Latitude	Longitude				
Rapanui A	*-38.799244*	174.590538	26	22.8	683	10
Pukearuhe A	*-38.893687*	174.51652	130	119.0	360	5
Pukearuhe B	-38.890111	174.520283	290	270	305	5
Pukearuhe C	*-38.893745*	174.516445	165	153.8	445	5
Tongaporutu A	*-38.825025*	174.578631	160	128.6	340	5
Tongaporutu B	*-38.827298*	174.577788	5	4.5	265	5

Table 3: Summary of the quantity of samples and measurements for the six faults studied.

Fault Name	Number of Samples and Measurements						
	Samples taken for grain-size analysis			Number of fault-zone architecture measurements			
	Sandstone Host Rock	*Siltstone Host Rock*	Fault Rock	*Fault Rock Thickness*	*Fault Zone Thickness*	*Schmidt Hammer*	*Deformation Bands*
Rapanui A	13	12	4*	80	80	80	80
Pukearuhe A	9	8	4	73	73	158	73
Pukearuhe B	9	8	1	61	61	170	61
Pukearuhe C	21	20	5	89	89	399	89
Tongaporutu A	12	11	5	68	68	220	68
Tongaporutu B	7	6	0	54	54	75	54
TOTAL	***71***	***65***	***15***	***425***	***425***	***1102***	***425***

* Sample taken for thin section and/or SEM images

3.2.1 Field Measurements

The following measurements were collected along each fault in the field and are described below. General descriptions of the faults and the data collected for each are given in Tables 2 and 3 (for definitions of terms and abbreviations refer to page xvi). All data are two dimensional (2D) and were collected from line samples usually approximately parallel to the dip of the fault plane. The samples are of limited extent and in most cases likely only record data from a small proportion (<5 %) of the dip-parallel dimension of the fault surface. Data were analysed in Excel and have been compared to data from the literature.

3.2.1.1 Fault-zone thickness

Fault-zone thicknesses were measured at uniform spacings of 5 cm for 5 faults and 10 cm for one fault (Table 2). In each case fault-zone thickness was measured normal to the fault zone between the outermost synthetic deformation bands or minor faults. As the faults studied are generally isolated from other faults these measurements were generally unambiguous with little uncertainty in identifying which synthetic structures form part of the fault zone. Fault-zone thicknesses range from 0.5 to 55 mm. The lower bound of this range is defined by what is considered to be the smallest reliable measurement observed at outcrop scale.

3.2.1.2 Fault-rock thickness

Fault rock includes material and fragments of host rock that have been dragged into the fault zone and/or crushed during faulting for which the original sedimentary fabric cannot be recognised. Fault-rock was predominantly recorded in deformation bands and fault rock thicknesses of individual bands have been summed across fault zones, and normal to the deformation bands (Figure 17). Where fault rock is represented by a single deformation band with a thickness <1 mm its width is assumed to be 0.5 mm. For the purpose of this thesis total deformation band thickness has been calculated by multiplying the number of bands with an average thickness of 0.7 mm (Fossen et al., 2007). Data on fault-rock thickness were measured at 5 cm intervals for (Pukearuhe A, B and C, and Tongaporutu A and B) and every 10 cm for Rapanui A (refer to Table 2). Fault-rock thicknesses range between 0.5 mm and 13 mm, and as with fault-zone measurements, the lower bound of this range is defined by what can reliably be observed at outcrop scale. Smearing and slicing fault-rock geometries (shown in Figure 17) have also been noted for all beds that have been fully displaced.

3.2.1.3 Deformation bands

Deformation bands range up to several mm in thickness and contain cataclastic material generated by displacements which are typically <5 cm (Fossen et al., 2007). Information on deformation bands has been gathered by counting the number of synthetic bands within the fault zone every 5 cm or 10 cm (refer to Table 3) along the fault profile. In the Mount Messenger Formation deformation bands vary from 0.5 mm to 2 mm in thickness with an average of 3 deformation bands at each sample location; the number of bands generally increases with rising displacement (Nicol et al., 2013).

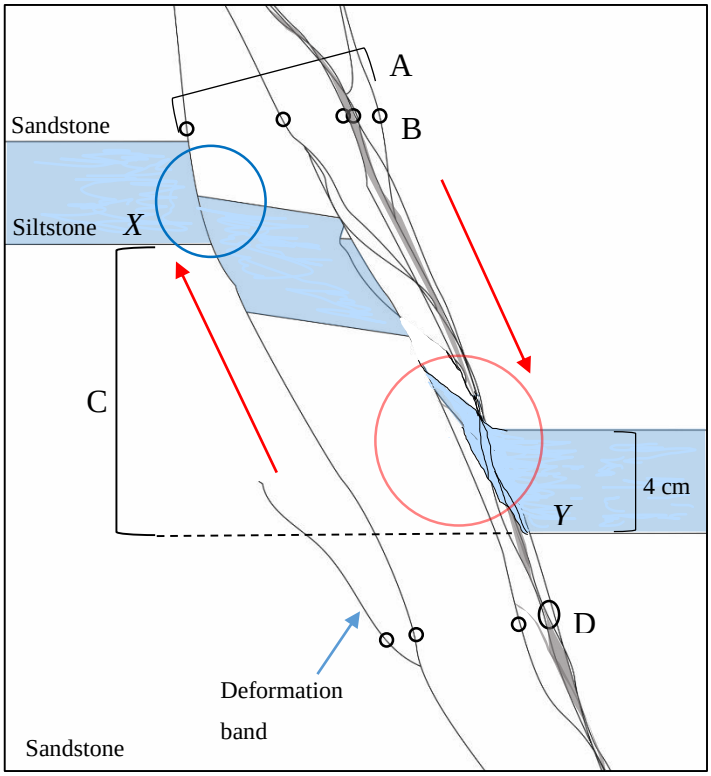

Figure 17: Schematic cross section illustrating a displaced siltstone bed (blue polygon) for a normal fault with both discrete displacement (blue circle) and smearing (red circle) of the siltstone bed. Fault-zone thickness (A), Deformation band (B), displacement (C) and fault-rock thickness (D: comprising the sum of the fault rock and all synthetic deformation bands) are shown. Red arrows indicate sense of slip on the fault.

3.2.1.4 Displacement

Fault displacement has been determined by measuring the vertical separation (i.e. throw) between displaced beds which, prior to faulting, were continuous and approximately horizontal. Unlike the other fault parameters described above, which were measured at 5 cm or 10 cm intervals, displacement was measured on all bed boundaries that could be confidently correlated across the fault plane. In cases where beds were dragged or smeared into faults (e.g. siltstone bed in the hanging wall of the fault in Figure 17), the bed rotations were considered as part of the displacement field (i.e. bed rotations are incorporated into the displacements by measuring where between near-horizontal parts of the beds). Displacements ranged from 1 mm to 290 mm. The throw has been used to calculate shale smear factor (SSF), shale gouge ratio (SGR) and clay smear potential (CSP) values using each of the siltstone beds sampled. The high densities of measurements provide high fidelity information on fault displacement variations.

3.3 Laboratory Analysis

All sample preparation and analysis was completed in laboratory facilities at the University of Canterbury (UC), Christchurch, New Zealand. Grain-size and thin section analysis was conducted the Department of Geological Sciences and SEM in the Department of Mechanical Engineering.

3.3.1 Grain-size Distribution (GSD)

Particle sizing analysis was conducted on over 150 samples of fault and host rock using a Saturn DigiSizer II Laser Diffraction Particle Size Analyser (LDPSA). The LDPSA instrument uses light scattering analysis to capture a high resolution, digital representation of the grain-size distribution pattern produced from each sample analysed (Micromeritics, 2017). Data collected was binned into appropriate grain-size ranges which fall within the instruments range detection of 0.04 – 2500 µm (Tables 21 – 26: appendix). An example LDPSA output graph can be found in the appendix (Figure 71).

Sample preparation was carried out by mixing 1 cm^3 volumes of sand or mud samples per beaker containing 50 mL of sodium hexametaphosphate (referred to here as calgon) at a concentration of 25 mg/L, an anticoagulant and deflocculant, which promoted breakdown of the samples into individual grains. This method of chemical dispersion is widely used (Ryzak and Bieganowski, 2011) and verified as an effective method under international standards (ISO 11277, 2009). This process of anticoagulation was conducted on individual samples for time intervals ranging from approximately 1 day to more than 2 months. Once broken down, the sample is then mixed using a laboratory magnetic stirrer (IKA C-Mag MS 4; Figure 18) until all sediment is suspended within the beaker. This method has been adopted due to the reduced amount of human induced mechanical breakdown of the sample that it causes. Samples are then transferred to the LDPSA sample handling unit using a pipette until an adequate sample load was reached within the particle-sizer (between 8 % – 10 % obscuration). Finally, the LDPSA scans the sample 3 times (to assure statistically significant results) with a chamber flow velocity of 600 rpm. Grain-size distribution graphs are generated on a PC connected to the LDPSA and an excel file produced.

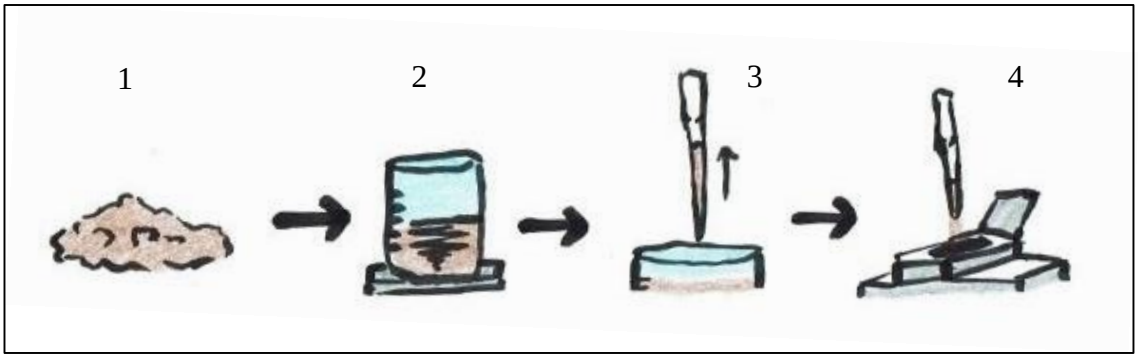

Figure 18: Sketch showing step by step sample preparation for sample extraction before grain-size analysis. 1) raw sample, 2) mixing atop magnetic stirrer, 3) sample extraction using pipette during mixing, and 4) sample placement inside sediment handling unit of the LDPSA.

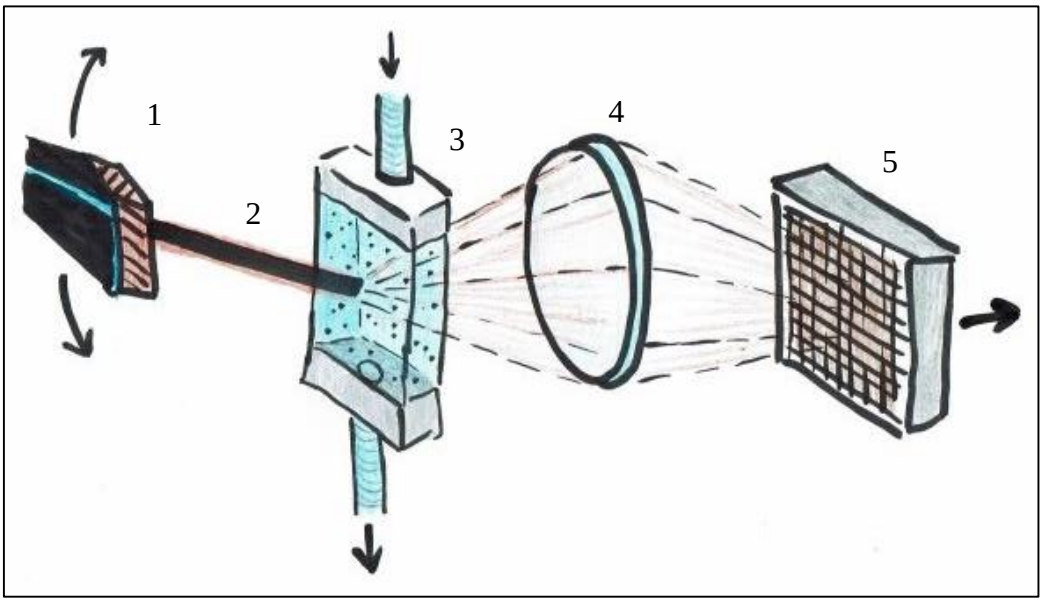

Figure 19: Sketch showing process of grain-size analysis inside Saturn Digisizer II laser diffraction particle size analyser (LDPSA). 1) Moving laser source, 2) laser beam, 3) cell holding circulating sample, 4) lens and, 5) element detector (modified from Micromeritics, 2017).

The grain-size analysis method adopted has a number of limitations. The LDPSA used has a lower-detection limit of <0.04 µm (does not routinely detect grains below this value), however, all samples were above this limit. Sample extraction and representative sample issues have been minimised by unbiased sample extraction using the magnetic stirrer with three individual five-minute particle-sizer scans to reduce the influence of particle orientation disrupting the measurements. Contamination issues were minimised by rinsing the LDPSA after each sample scan and thoroughly cleaning sampling equipment between each sample. One time use pipettes were utilised to ensure uncontaminated sample preparation.

Fault rock was often difficult to sample for grain-size analysis without contamination from host rock which was particularly true for shale smear samples as they were typically thin (<1 cm). Extra care was taken when preparing fault-rock samples to minimise contamination by host rock.

3.3.2 Scanning Electron Microscope (SEM)

A scanning electron microscope (SEM) has been utilized to observe the micro-structure of fault-zones at the scale of individual grains (conducted by Gabby Watson). High resolution SEM images of host and fault rock provided a wide range of information including grain-sizes, grain alignment, grain disaggregation and chemical composition. These data help constrain the processes that might influence grain-size distribution and overall fault structure. SEM analysis also permits comparison of micrometre-scale processes, to cm and mm scale processes observed in outcrop. Such comparisons could lead to insights on the scaling of structures and how feasible it may be to upscale observations made here to faults with displacements of metres or kilometres.

Preparation of SEM samples includes selecting areas of interest from the sample (i.e. fault rock such as shale smears or deformation bands), cleaning (with an uncontaminated small-scale scraper followed by compressed air to remove lose grains) and mounting individual levelled samples of interest onto small plates using epoxy glue which is painted in gold to allow sample discharge onto base plates (LTI, 2017). Once secured samples were coated in liquid carbon to assure conductivity and placed inside a vacuum to check for loose particles and to remove air before being inserted inside the SEM for scanning. Samples of both host and fault rock have been analysed and high resolution topographic and chemical composition images were generated (this thesis examines the topographic images only).

3.3.3 Thin Section Analysis

Thin sections for a limited number of samples were created by Rob Spiers (a lab technician within the Geological Sciences Department at UC) for the faults (**Error! eference source not found.**) and analysed. Fault and host rock thin sections have been observed using a petrographic optical microscope. Thin section analysis has allowed further insight into how individual grains may be interacting with each other during faulting processes within interbedded sandstone and siltstone lithologies.

Cementation of sampled outcrops was mainly absent which aided in sample extraction but meant that sample preservation (such as for SEM and thin section analysis) was not ideal as samples would fracture and disintegrate along shear planes and deformation bands during preparation.

3.4 Schmidt Hammer Testing

The Schmidt Hammer was used during fieldwork to provide an indication of the relative strengths of sandstone, siltstone and fault rock within the faulted Mount Messenger Formation. Where possible Schmidt Hammer measurements of fault rock and host rock (including sandstone and siltstone beds), were repeated 5 times and averaged (Table 20: appendix). Instrument sensitivity was an issue for some lithologies and outcrops within the study area. The available Schmidt Hammer utilised for this study was an analogue instrument and where the rock was weak in some cases failed to record a value >0. Schmidt Hammer results are presented here and have not been converted to unconfined compressive strength (UCS) as no density measurements have been acquired to enable strengths to be calculated. Weathering and/or salt precipitation could increase the apparent strength of the samples and to reduce the possible impact of these processes outcrops subject to Schmidt Hammer were scrapped back 1 – 5 cm.

3.5 Summary

Methods outlined here and data collected for this thesis were derived from field work measurements and sample collection together with laboratory analysis. All laboratory and data analysis were conducted at the University of Canterbury. Where possible biases and limitations of data collection have been minimised to increase the utility of the results. Six small normal faults have been studied in detail. To facilitate analysis 151 samples and 2377 measurements were collected. Samples were used for grain-size, thin section and SEM analysis. Measurements were used to quantify fault-zone geometries, displacements and relative strengths.

4 FIELD AND LABORATORY OBSERVATIONS

4.1 Introduction

Chapter 4 details observations and data gathered during field and laboratory work for this thesis. The contents of this chapter follow the progression of field work sampling and description of individual faults, through to laboratory analysis. Results include: fault-zone thickness, fault-rock thickness, deformation band, displacement, and strength data together with laboratory-derived observation including grain-size distributions, SEM imaging and available thin-section results. Information presented here is interpreted in the Chapter 5.

4.2 Outcrop Analysis

Insitu observations and measurements of fault-zone architecture for six faults are presented in (Figure 20 - Figure 22). Photographs of each fault stitched together using CorelDRAW software can be found in the Appendix of the theis (Figure 65 - Figure 67). Further information on the number of samples gathered for each fault has been outlined in Tables 2 and 3. Detailed photographs and descriptions of each fault are presented from north to south in sections 4.2.1 to 4.2.6. Data collected for each fault has been tabled and are presented in Tables 13 – 19 in the appendix.

4.2.1 Rapanui A

Fault Rapanui A displaces 12 siltstone beds and 13 sandstone beds by an average of 2.3 cm over a fault length of 6.8 m (e.g. Figure 20 and Figure 65: appendix). The majority of sandstone beds have 50 – 120 µm diameter (very fine – fine sand) and the siltstones 8 – 105 µm grains (medium silt – very fine sand). Rapanui A has an average of 3 deformation bands, 2.4 mm of fault-rock and 4.6 mm in fault-zone thickness over the length of the sampled fault. Two - three deformation bands host the majority of fault rock along this fault with displacement commonly confined to a single band at each siltstone bed intersection. Deformation bands commonly splay out and form clusters in the sandstone beds. Smearing of siltstone beds into the fault zone is not common along this fault with discrete displacement of beds dominating. The fault itself comprises several bends which are usually located near siltstone beds. The fault shows little evidence of segmentation.

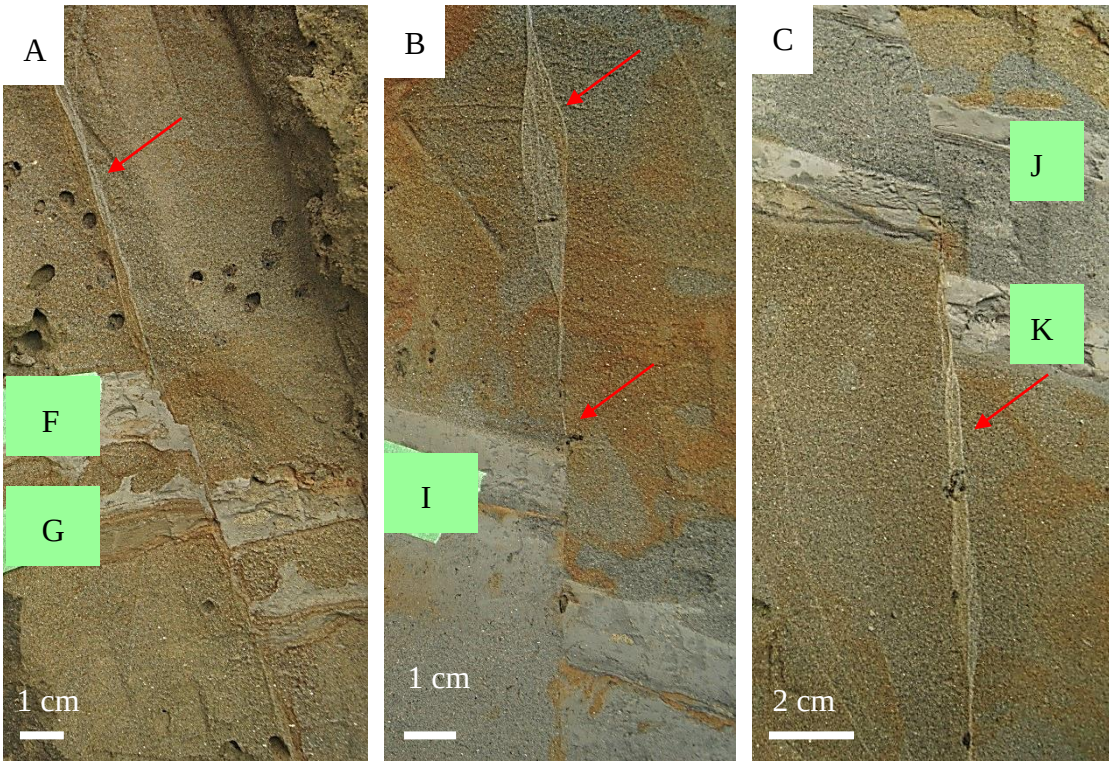

Figure 20: Photographs showing sections of Rapanui A fault where it displaces siltstone beds F and G (A), I (B), and J and K (C). Red arrows indicate deformation bands. Fault is located located 300m along Rapanui Beach north of the Rapanui stream (approximately 1.5 km drive north of Tongaporutu River). See Table 2 for details of the fault and Figure 58 for its location.

4.2.2 Tongaporutu A

Fault Tongaporutu A displaces 11 siltstone beds and 12 sandstone beds with an average displacement of 12.9 cm over a fault length of 3.4 m (e.g. Figure 21 and Figure 66: appendix). The majority of sandstone beds have grain-sizes of 90 – 120 µm (very fine – fine sand) and the siltstones 5 – 60 µm (fine silt – very fine sand). Tongaporutu A has an average of 2.5 deformation bands, 3.4 mm of fault-rock and 12.5 mm in fault-zone Thickness over the length of the fault profile sampled at 5 cm intervals. Bends and steps within the fault zone are common along this fault, usually occurring near siltstone beds. Displacements are commonly contained within two - three primary deformation bands which all produce fault rock of varying thicknesses along the fault. Displaced siltstone beds are commonly subjected to confined or discrete displacement, although some smearing and distributed shear of siltstone and sandstone beds also occurs.

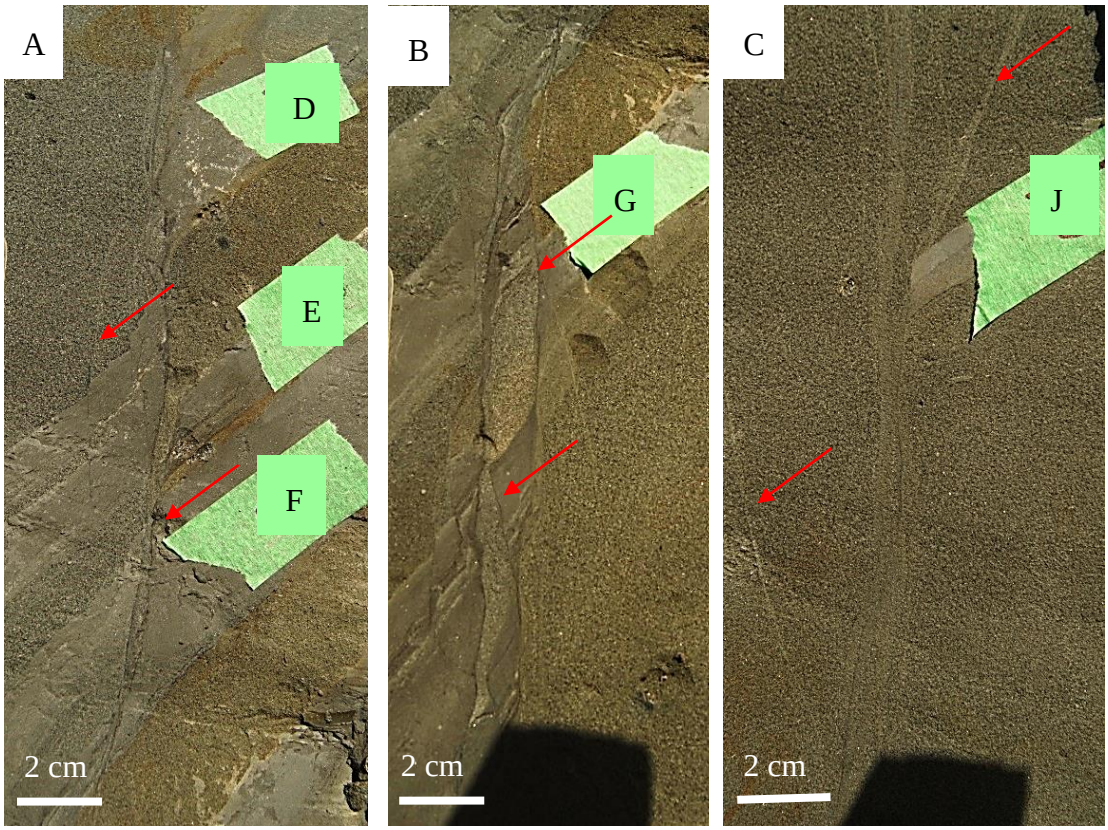

Figure 21: Photographs showing sections of Tongaporutu A fault where it displaces siltstone beds D, E and F (A), G (B), and J (C). Red arrows indicate deformation bands. Fault is located 600m south of the Tongaporutu River mouth on the coastal cliff. See Table 2 for details of the fault and Figure 58 for its location.

4.2.3 Tongaporutu B

Fault Tongaporutu B displaces 7 siltstone beds and 8 sandstone beds with an average displacement of 0.5 cm over a fault length of 2.7 m (Figure 22 and Figure 67: appendix). The majority of sandstone beds have grain-sizes of 100 – 120 µm (fine sand) and the siltstones beds 5 – 60 µm (fine silt – very fine sand). Tongaporutu B has an average of 1.2 deformation bands, 0.88 mm of fault-rock and a 1.08 mm fault-zone thickness over the length of the fault sample. Displacement is primarily confined to a single deformation band apart from a small splay near the top of the fault. The fault is almost straight with limited bends or steps, and no clear evidence of smearing. No fault rock was sampled from this fault as the fault-rock was too thin.

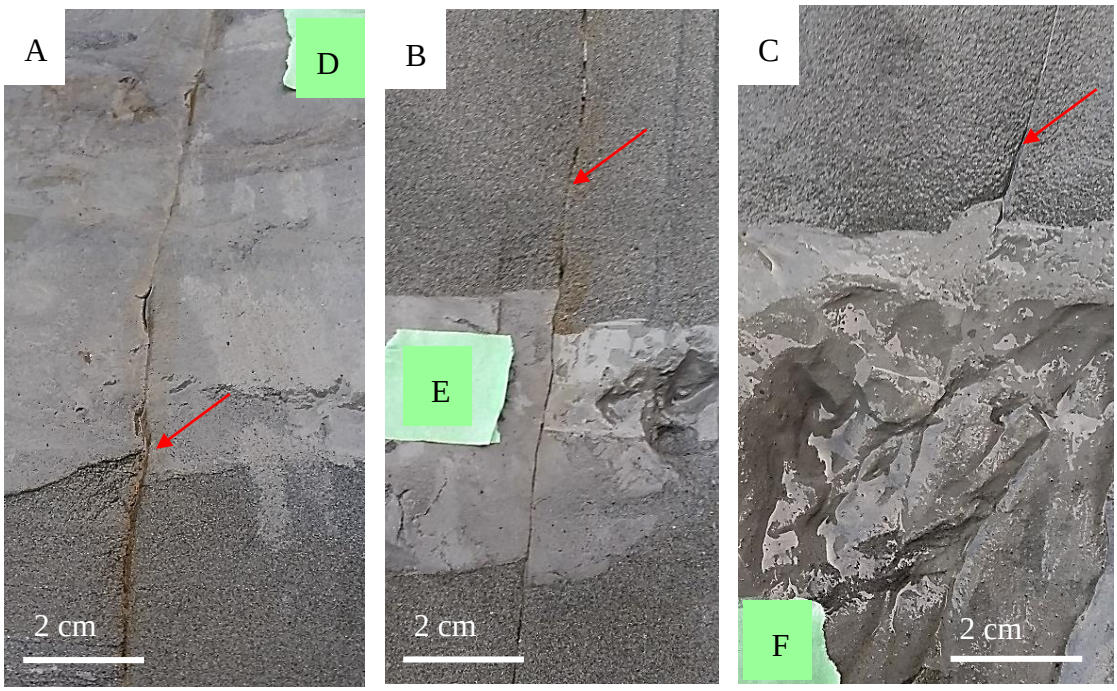

Figure 22: Photographs showing sections of Tongaporutu B fault displaces siltstone beds D (A), E (B), and F (C). Red arrows indicate deformation bands. Fault is located 1 km along the beach south of the Tongaporutu River-mouth. See Table 2 for details of the fault and Figure 58 for its location.

4.2.4 Pukearuhe A

Fault Pukearuhe A displaces 8 siltstone beds and 9 sandstone beds with an average displacement of 12 cm over a fault length of 3.6 m (Figure 23 and Figure 68: appendix). The majority of sandstone beds have grain-sizes of 40 – 115 µm (very coarse silt – fine sand) and the silts 8 – 100 µm (medium silt – very fine sand). Pukearuhe A has an average of 2.8 deformation bands, 3 mm of fault-rock and 8.2 mm in fault-zone thickness over the length of the fault sample. This fault offsets a predominantly silt rich fine sandstone interbedded with coarse siltstone beds. Signs of cross-bedding are present usually at sandstone/siltstone horizons. One - two deformation bands generate the majority of fault-rock seen along this fault profile with displacement commonly confined to one deformation band. Several very thin deformation bands are observed in some parts of the sandstone beds usually at the tops of siltstone beds. This fault is relatively straight with small bends and little evidence of steps. Slicing of siltstone beds is a common feature of this fault with limited evidence of shale-smearing.

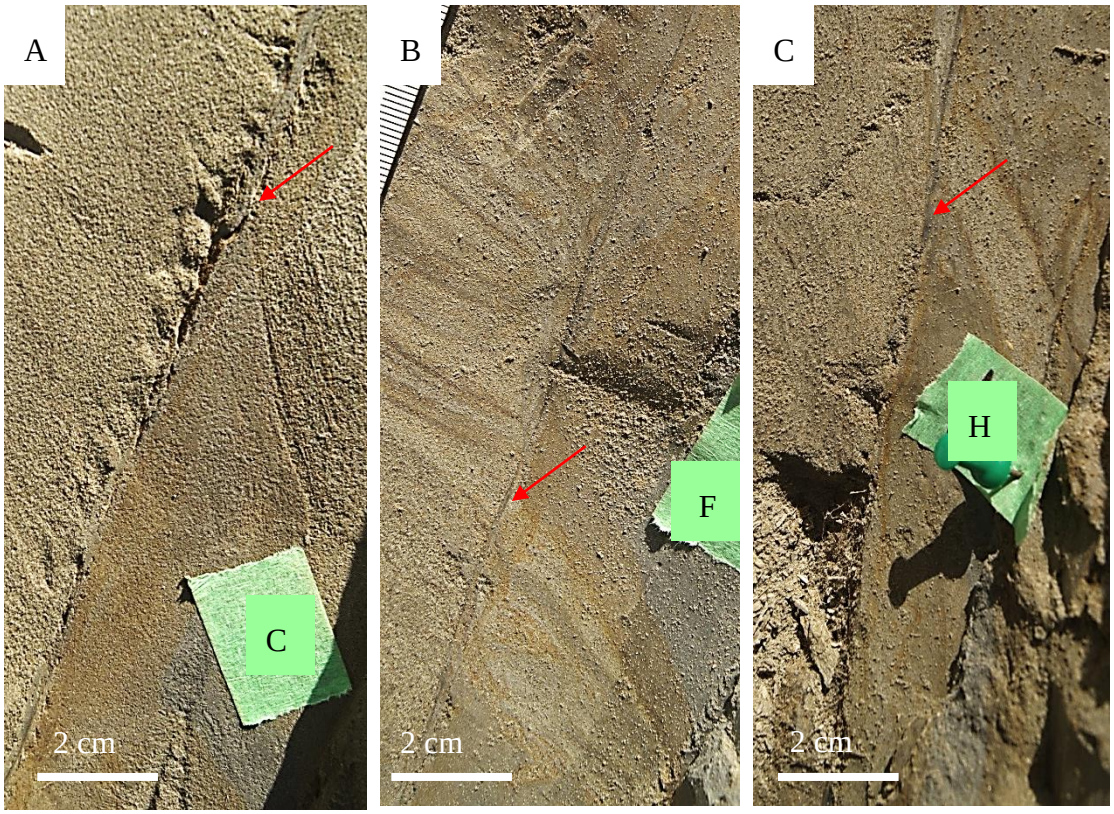

Figure 23: Photographs showing sections of Pukearuhe A fault displacing siltstone bed C (A), siltstone bed F (B), and siltstone bed H (C). Blue circles indicate deformation bands. Fault is located on a cliff face 5 m from the Pukearuhe beach front/Whitecliffs walkway car park. See Table 2 for details of the fault and Figure 58 for its location.

4.2.5 Pukearuhe B

Fault Pukearuhe B displaces 8 siltstone beds and 9 sandstone beds with an average displacement of 27 cm over a fault length of 3.05 m (Figure 24 and Figure 69: appendix). The majority of sandstone beds have grain-sizes of 20 – 110 µm (coarse silt – fine sand) and the siltstone beds 6 – 100 µm (fine silt – very fine sand). Pukearuhe B has an average of 3.8 deformation bands, 4.7 mm of fault-rock and 19.7 mm in fault-zone thickness over the length of the fault sample. Several small deformation bands responcible for the majority of displacements along this fault with 1-2 deformation bands generating the majority of fault rock. Faulting and smearing of the siltstone beds is common along this fault. Siltstone beds are generally laminated and often host coarser lithics similar to those in the adjacent sandstone beds. Bending of the fault plane occurs proximal to siltstone beds. Fault rock sampling from this fault was limited as the fault could not be reached (due to beach-sand erosion) when sampling was conducted.

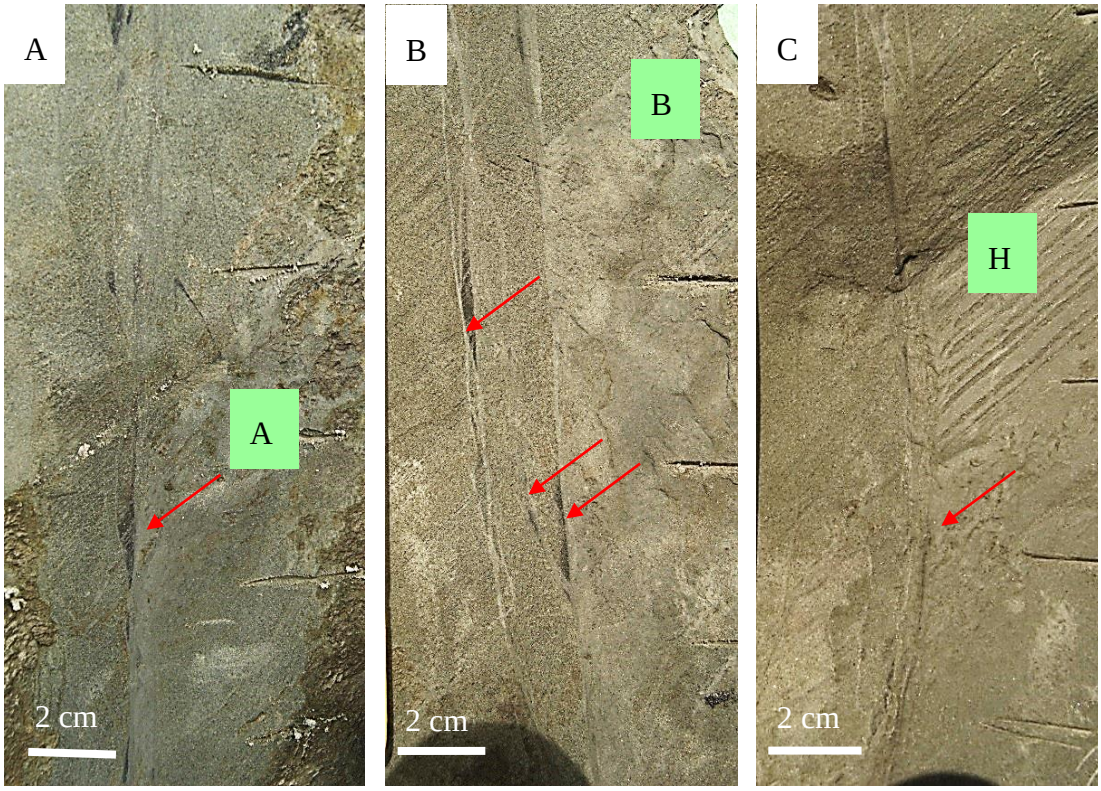

Figure 24: Photographs showing sections of Pukearuhe B fault displacing siltstone bed A (A), siltstone bed B (B), and siltstone bed H (C). Blue circles indicate deformation bands. Fault is located 900m along the beach north of the Whitecliffs car park. See Table 2 for details of the fault and Figure 58 for its location.

4.2.6 Pukearuhe C

Fault Pukearuhe C displaces 20 siltstone beds and 21 sandstone beds with an average displacement of 15.4 cm over a fault length of 4.5 m (Figure 25 and Figure 70: appendix). The majority of sandstone beds have grain-sizes of 60 – 110 µm (very fine – fine sand) and the siltstone beds 7 – 90 µm (fine silt – very fine sand). Pukearuhe C has an average of 3.4 deformation bands, 2.4 mm of fault-rock and 9.6 mm in fault-zone thickness over the length of the fault sample. Displacements on this fault are primarily confined within two – four anastomosing deformation bands which generate the majority of fault rock. Smearing and discrete faulting of the siltstone beds is common.

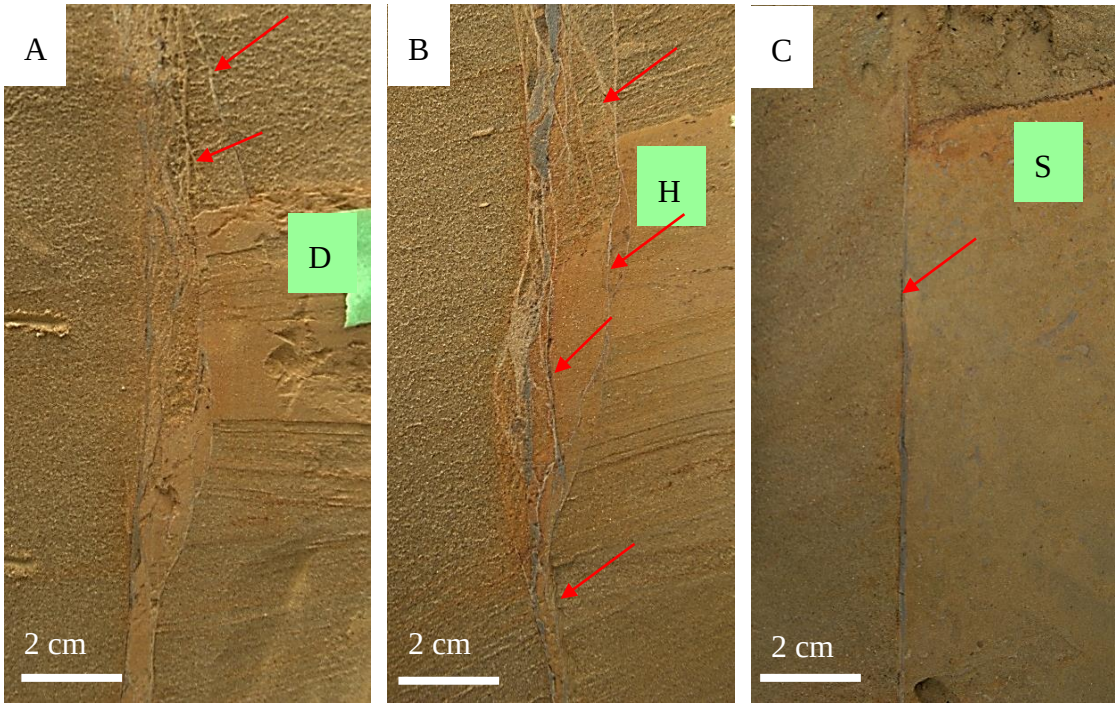

Figure 25: Photographs showing sections of Pukearuhe C fault displacing siltstone bed D (A), siltstone bed H (B), and siltstone bed S (C). Blue circles indicate deformation bands. Fault is located on a cliff face 10m from the Whitecliffs walkway carpark (5m from Pukearuhe A fault). See Table 2 for details of the fault and Figure 58 for its location.

4.3 Fault-zone Architecture

Fault-zone architecture has been analysed with the aid of distance-dimension graphs (Figure 32 - Figure 31). The resulting graphs plot a range of variables including host-rock bed location (measured from foot-wall), displacement, fault-rock and fault-zone thicknesses, deformation band count and calculated smear predictions (SSF, SGR and CSP).

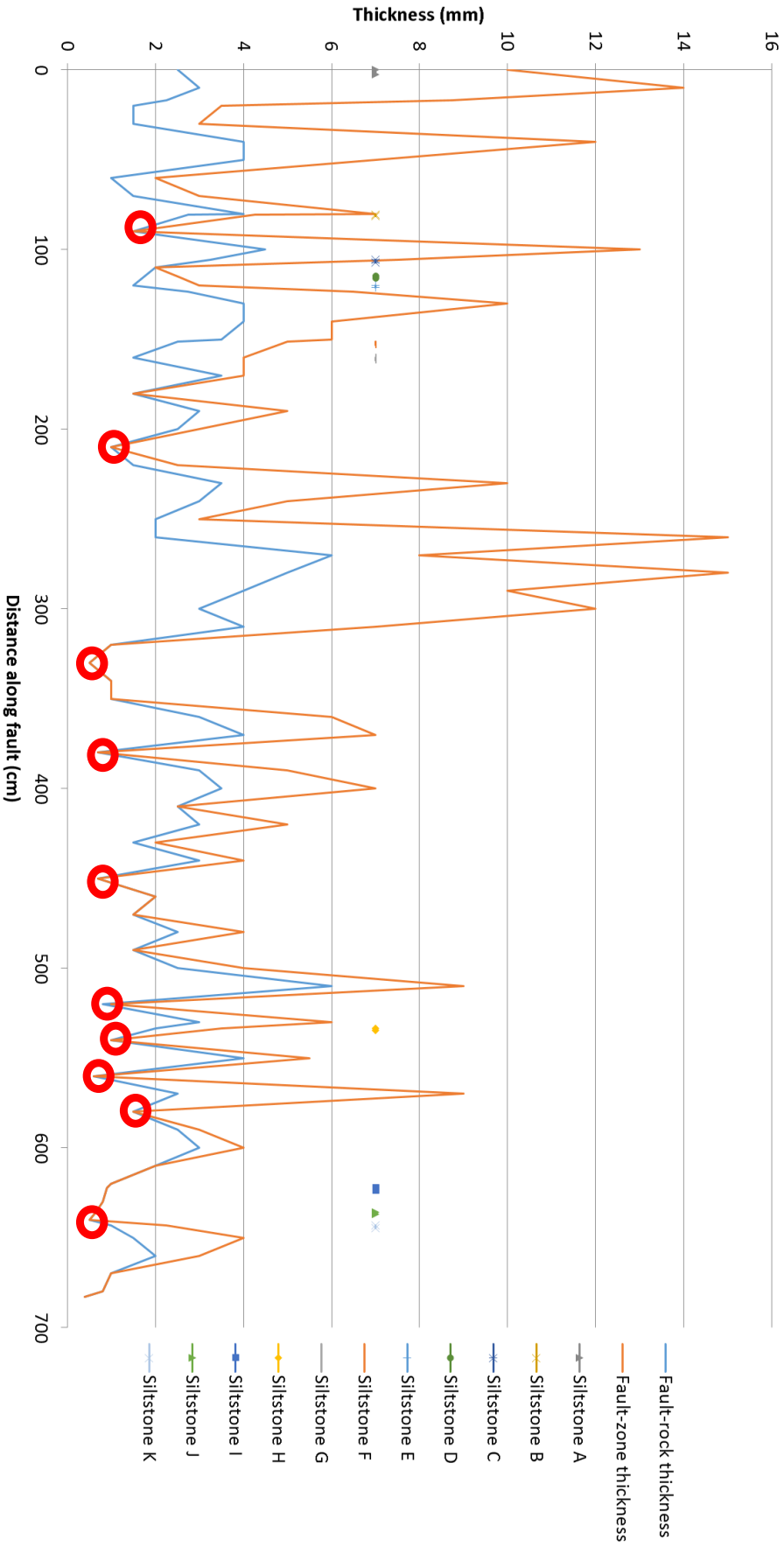

Figure 26: Graph showing fault-rock and fault-zone thickness variations, and location of siltstone beds along the length of the Rapanui A fault.

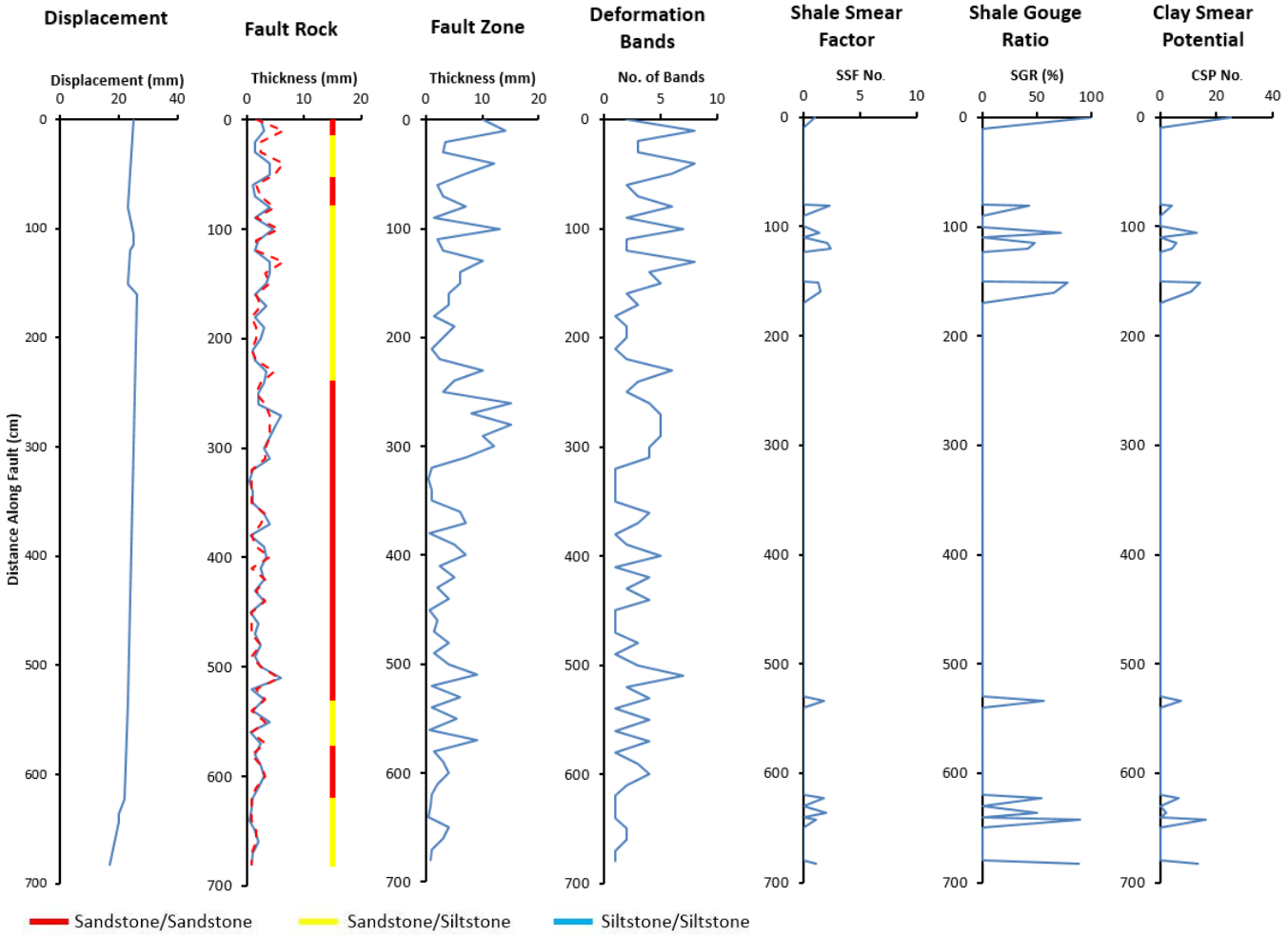

Figure 27: Graphs showing displacement, fault-rock thickness, fault-zone thickness and deformation band count along the Rapanui A fault together with distance versus shale smear predictions (SSF, SGR and CSP) along the length of the fault.

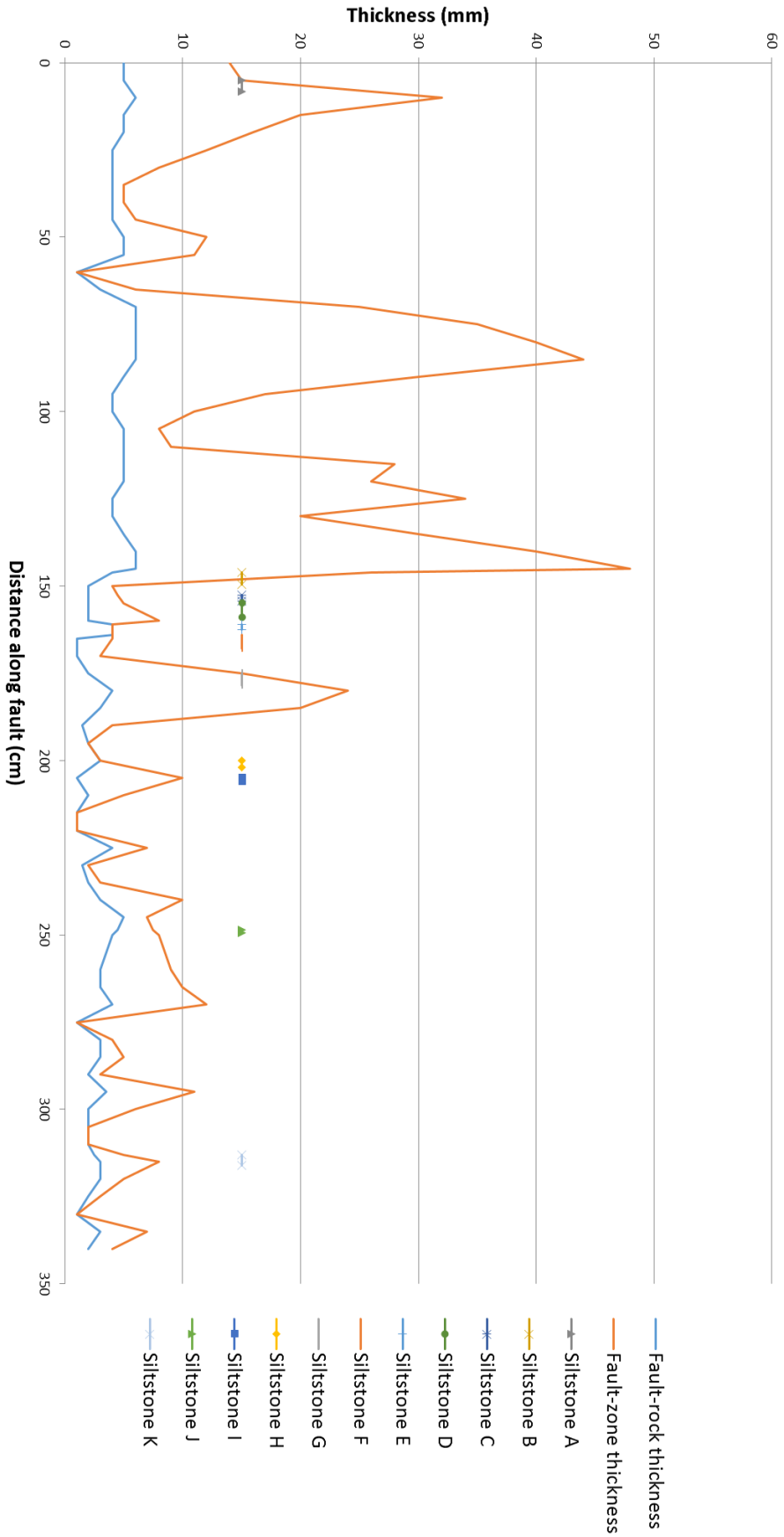

Figure 28: Graph showing fault-rock and fault-zone thickness variations, and location of siltstone beds along the length of the Tongaporutu A fault.

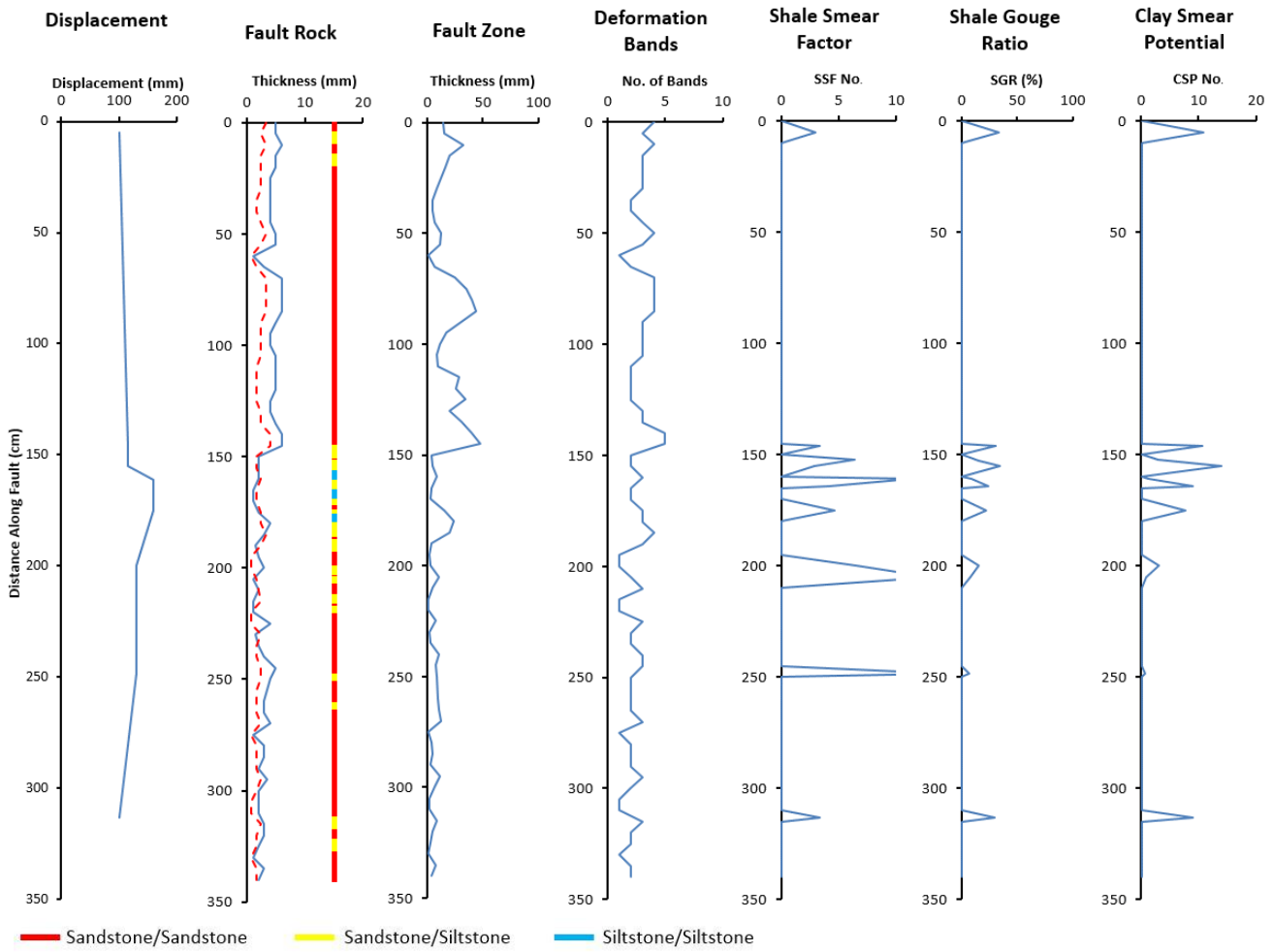

Figure 29: Graphs showing displacement, fault-rock thickness, fault-zone thickness and deformation band count along the Tongaporutu A fault together with distance versus shale smear predictions (SSF, SGR and CSP) along the length of the fault.

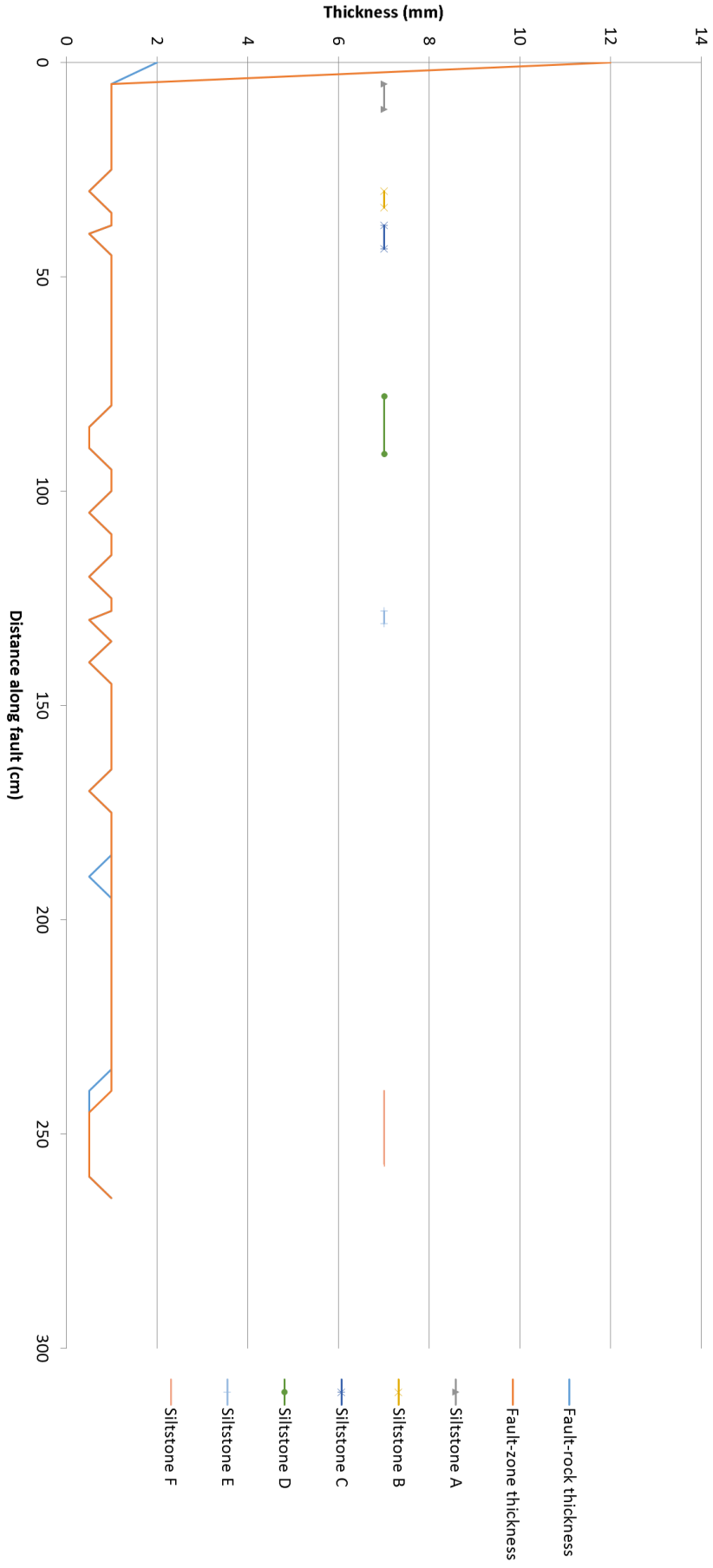

Figure 30: Graph showing fault-rock and fault-zone thickness variations, and location of siltstone beds along the length of the Tongaporutu B fault.

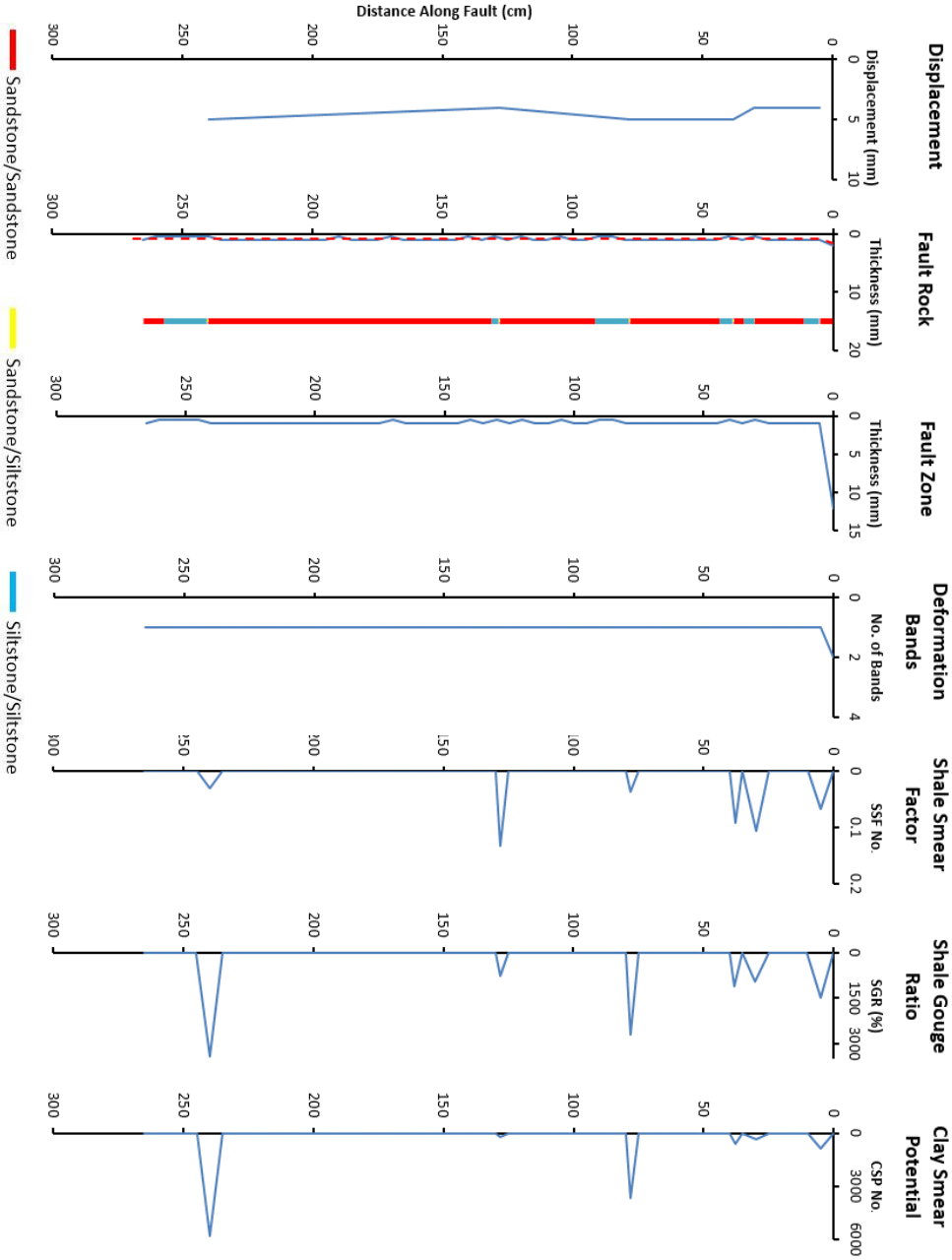

Figure 31: Graphs showing displacement, fault-rock thickness, fault-zone thickness and deformation band count along the Tongaporutu B fault together with distance versus shale smear predictions (SSF, SGR and CSP) along the length of the fault.

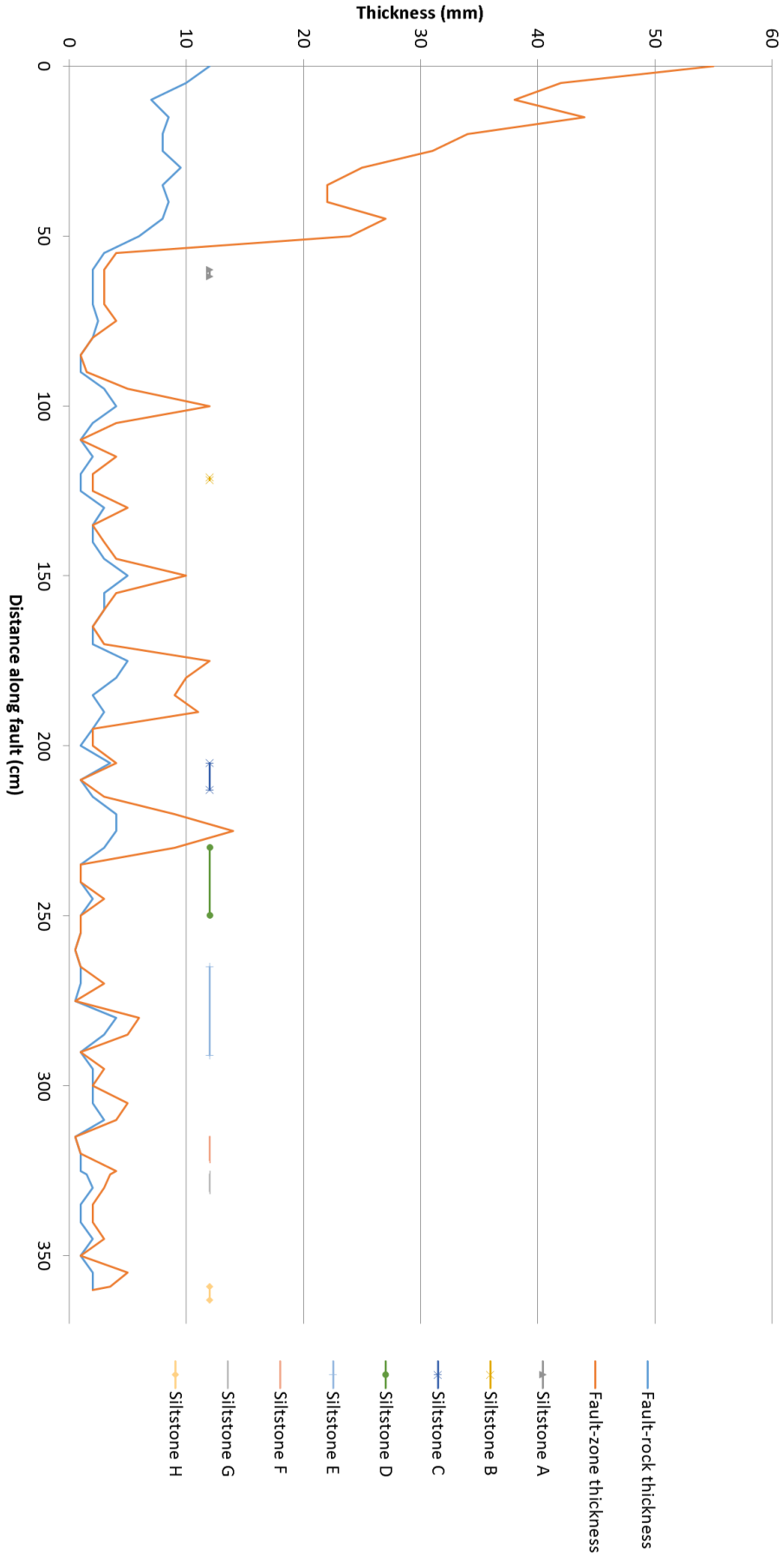

Figure 32: Graph showing fault-rock and fault-zone thickness variations, and location of siltstone beds along the length of Pukearuhe A.

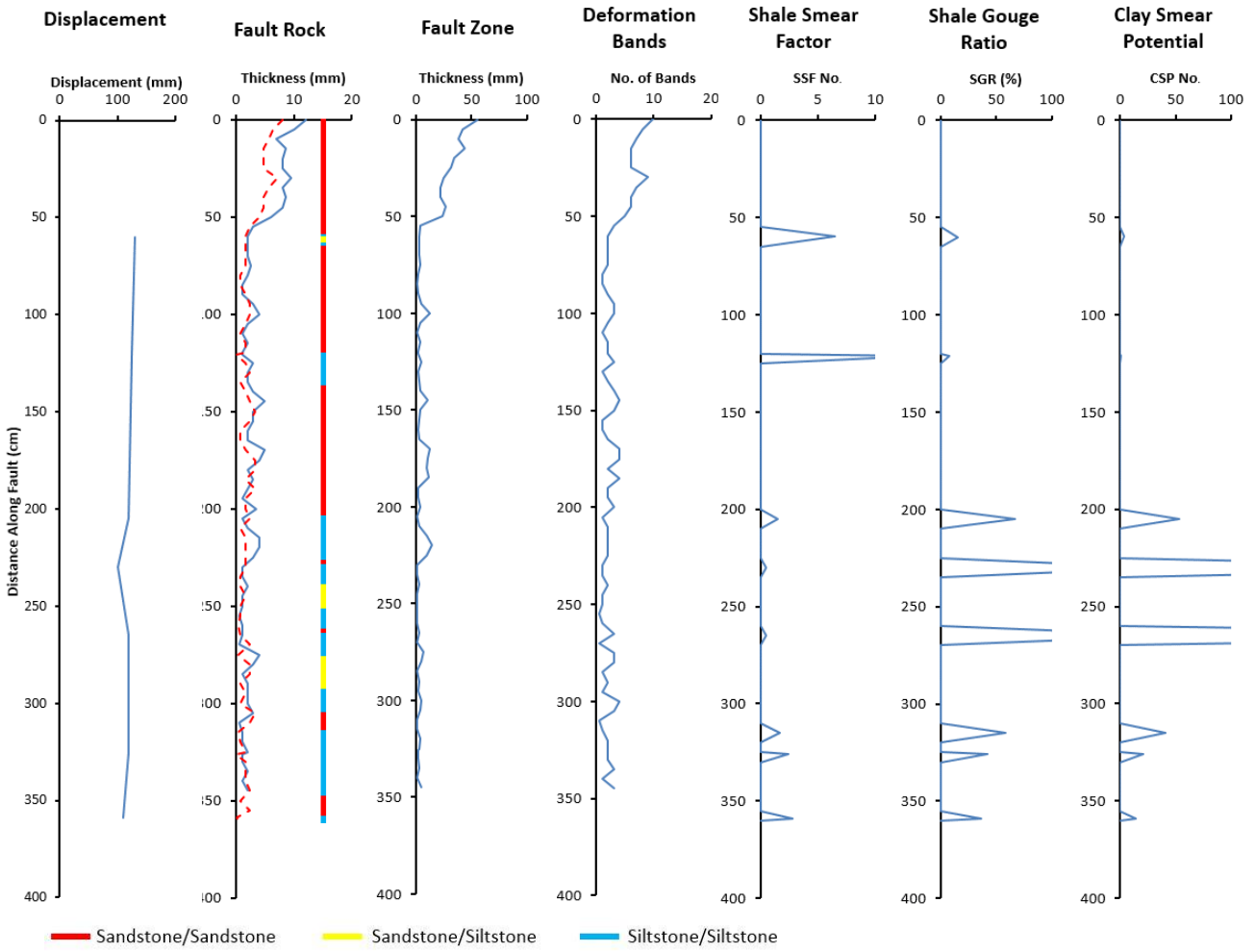

Figure 33: Graphs showing displacement, fault-rock thickness, fault-zone thickness and deformation band count along the length of Pukearuhe A fault together with distance versus shale smear predictions (SSF, SGR and CSP) along the length of the fault.

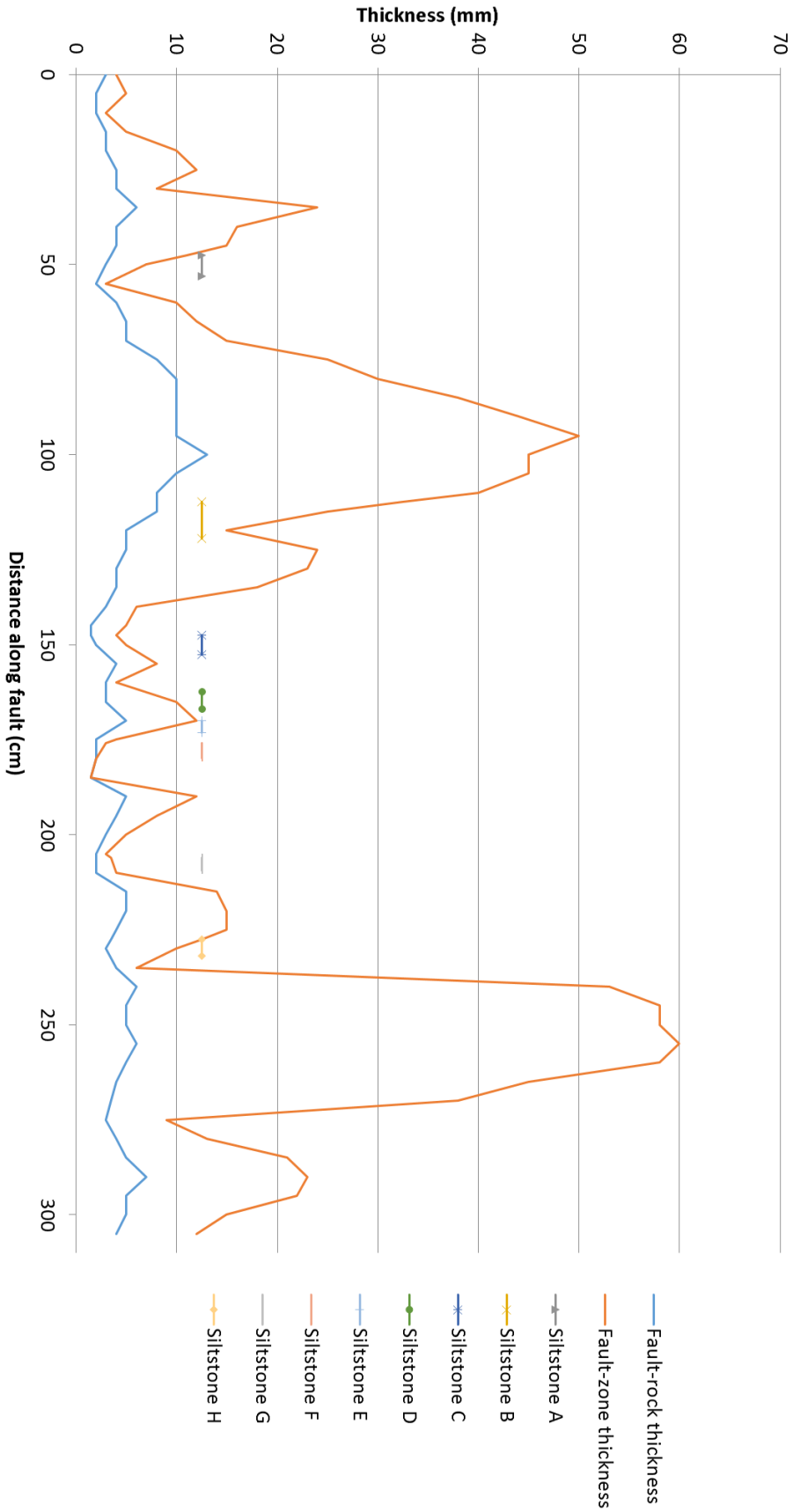

Figure 34: Graph showing fault-rock and fault-zone thickness variations, and location of siltstone beds along the length of Pukearuhe B.

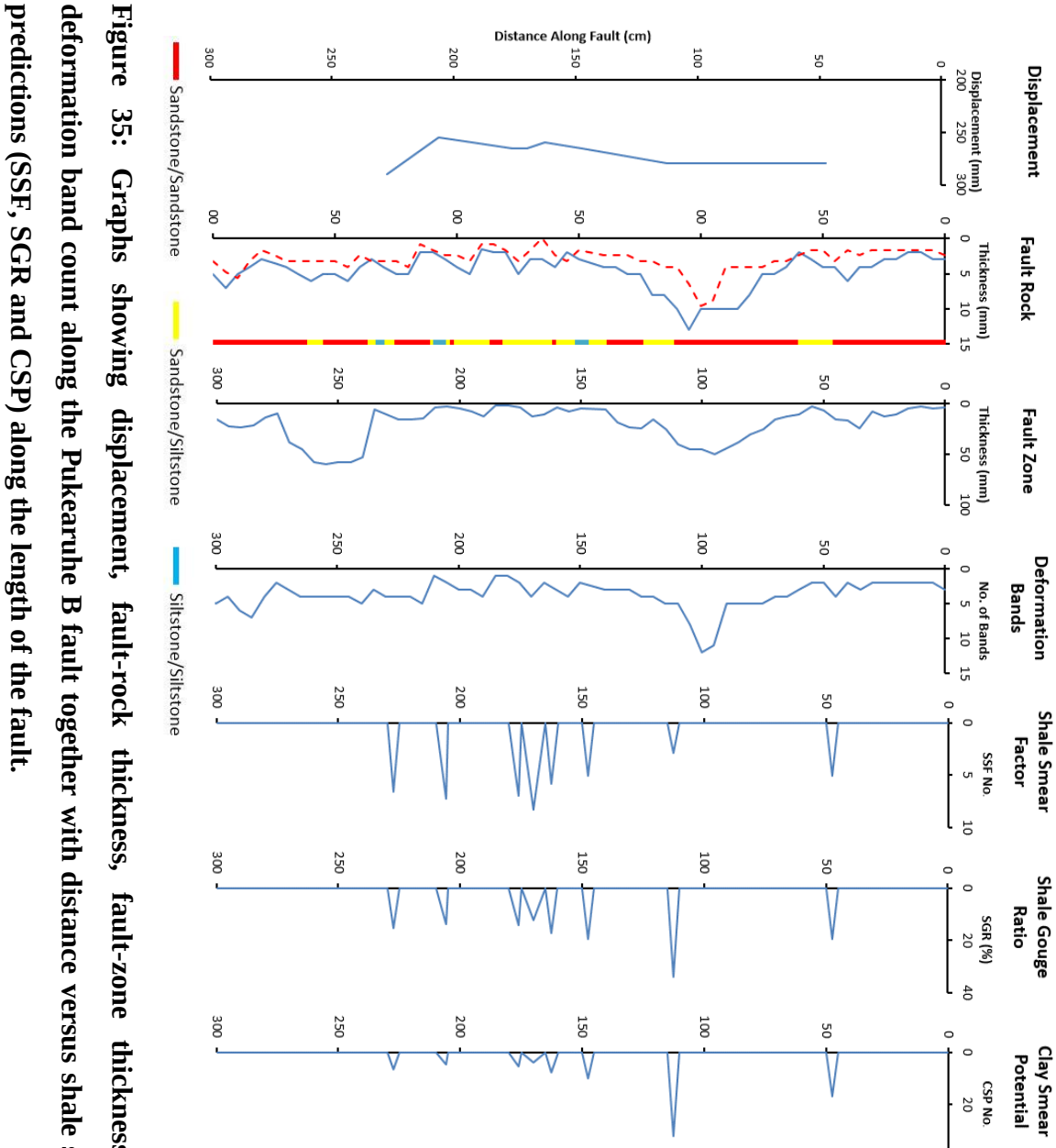

Figure 35: Graphs showing displacement, fault-rock thickness, fault-zone thickness and deformation band count along the Pukearuhe B fault together with distance versus shale smear predictions (SSF, SGR and CSP) along the length of the fault.

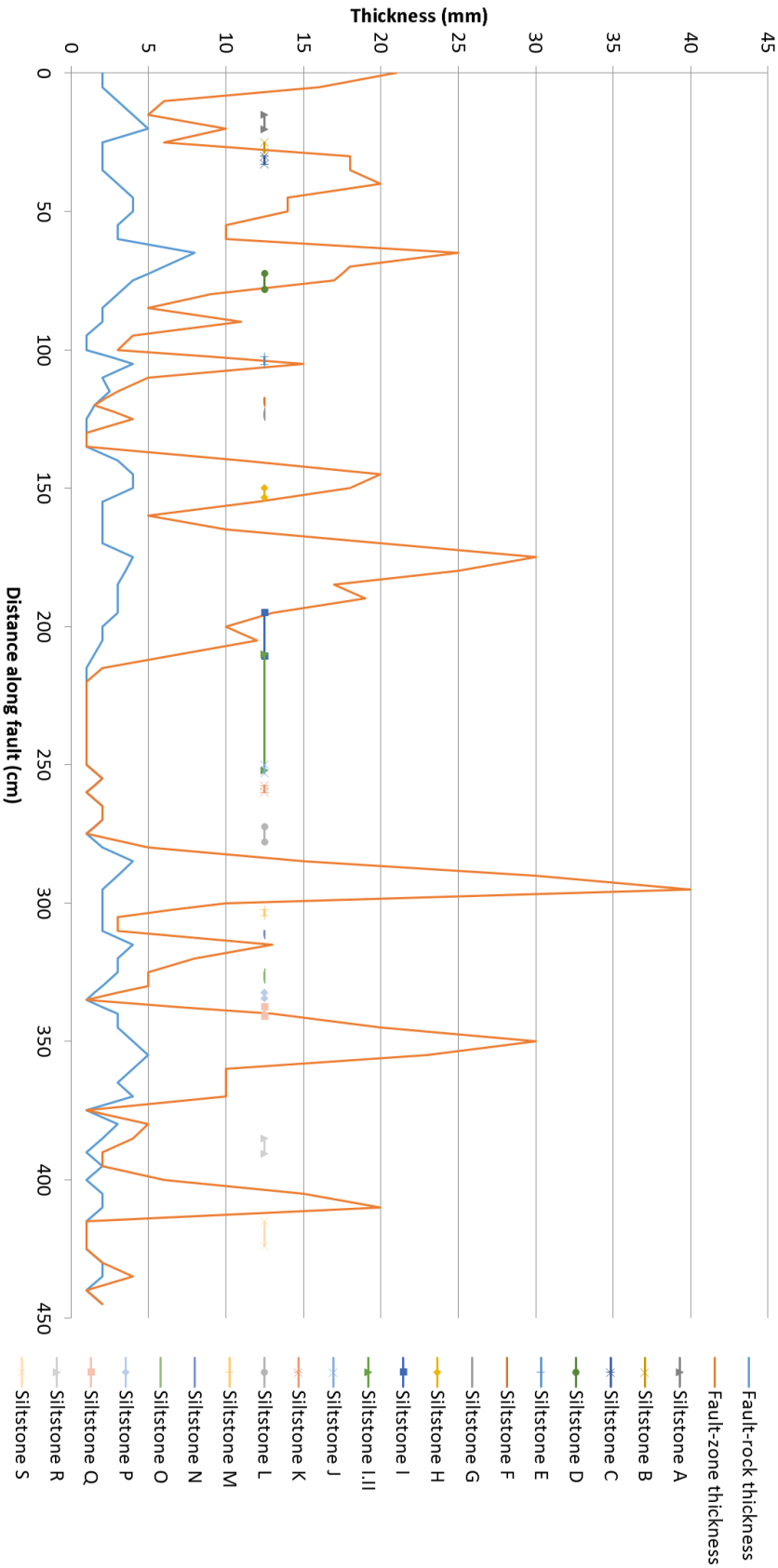

Figure 36: Graph showing fault-rock and fault-zone thickness variations, and location of siltstone beds along the length of Pukearuhe C.

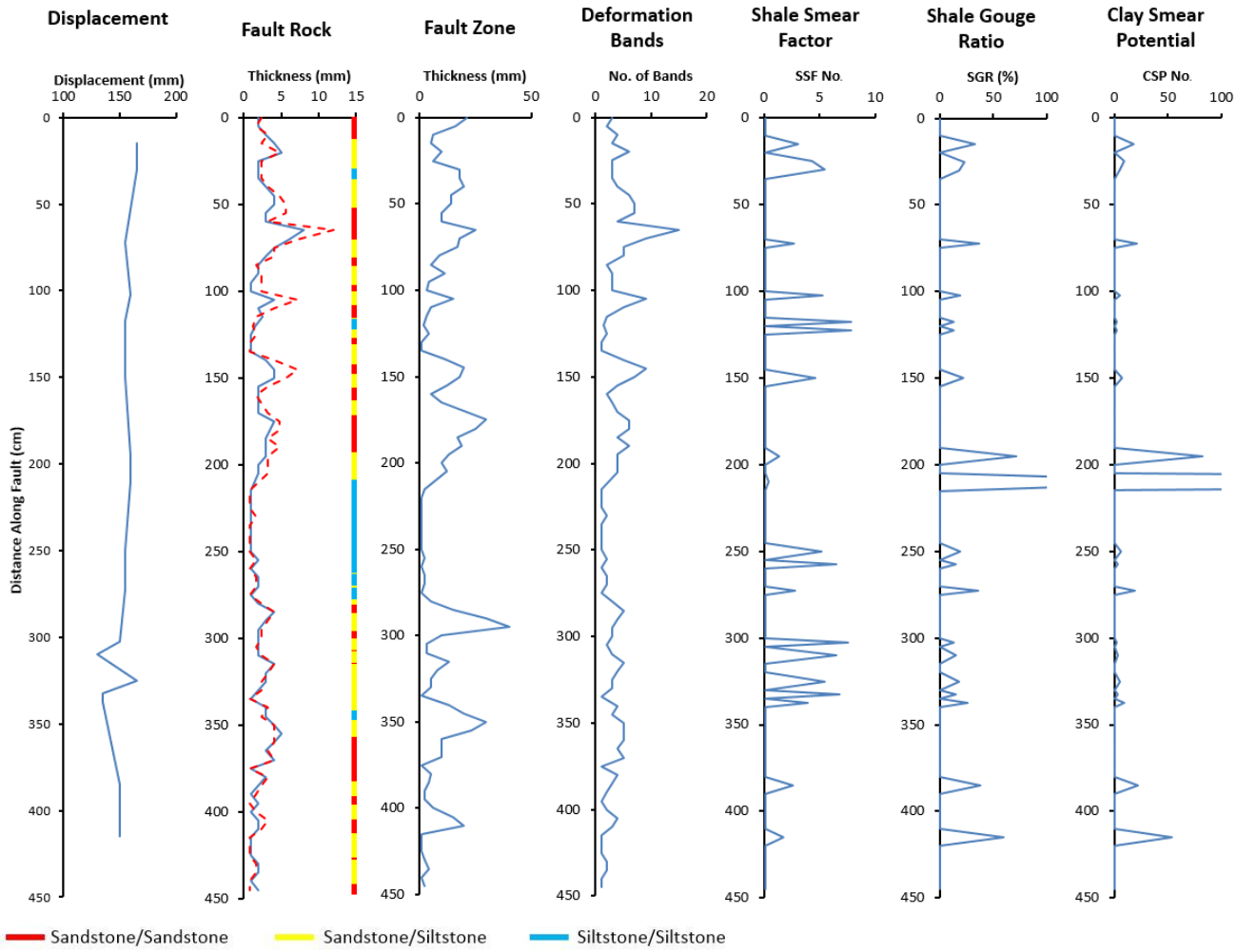

Figure 37: Graphs showing displacement, fault-rock thickness, fault-zone thickness and deformation band count along the Pukearuhe C fault together with distance versus shale smear predictions (SSF, SGR and CSP) along the length of the fault.

4.3.1 Fault-rock and Fault-zone Thickness Variations

The graphs in Figures 26-37 show that both fault-rock and fault-zone thicknesses vary along each of the faults sampled. These variations primarily reflect changes in the upper bounds of the thicknesses with the lower bounds typically being 0.5 to 1 mm and defined by the observational limits of the data. Fault-rock thicknesses along each fault sampled generally range by about an order of magnitude with changes as low as a factor of three. By contrast variations in fault-zone thickness generally exceed a factor of 20. Thickness variations for both fault rock and fault zones are positively related, with the thickest and thinnest values for each measurement commonly being at similar locations along each fault. In part this correlation occurs because fault-rock and fault-zone thicknesses are the same at numerous points on each fault (see filled circles on Figs 27). On individual faults thicknesses appear to show a weak correlation with bed lithology. Many of the thinnest measurements occur where the faults displace siltstone beds. In addition, there are differences in the thickness populations between faults, with higher displacements generally being associated with greater ranges of thickness and larger mean values. Such increases in fault-rock and fault-zone thicknesses with rising displacement is consistent with previous work on the Mount Messenger Formation and also for faults in other siliciclastic sequences (e.g. Childs et al., 2007, 2009; Nicol et al., 2013).

4.3.2 Deformation-bands

Much of the fault-rock thickness measured was generated by one or more deformation bands. The number of deformation bands varies along each fault from a minimum of 1 to maximums of 2-20 (Figures 26, 28, 30, 32, 34 & 36). The lower and upper limits of these maximums are defined by faults with the smallest and largest displacements (see Figures 27 and 31). A positive correlation between displacement and maximum number of bands has been proposed by Nicol et al. (2013), however more data are required to confidently draw this conclusion from the present study. On individual faults variations in the number of bands appears to be positively related to fault-rock and fault-zone thicknesses (Figures 27, 29, 31, 33, 35 & 37). The positive relationship between number of bands and fault-rock thickness is to be expected given that the range of band thicknesses is relatively small (i.e., 0.5 to 2 mm). The positive relationship between the number of bands and fault-zone thickness arises because these variables are both greatest at locations where the bands form clusters or bundles (for further discussion of these clusters see Nicol et al., 2013). Between these clusters the bands pinch together and decrease in number, in many

cases reducing to a single band. The separation between clusters on each fault (i.e. the distance between peaks in the number of deformation bands in (Figures 27, 29, 31, 33, 35 & 37), is typically <1 m and does not appear to be strongly related to displacement. The locations of clusters are however related to stratigraphy with clusters being generally confined to sandstone beds.

4.3.3 Displacement and Smear

Observations in this thesis suggest that displacement and smear show a moderate to poor relationship as shale-smear predictions (i.e. SSF, SGR, and CSP) in part because siltstone beds are not always smeared along faults. As a consequence, smearing of siltstone beds are not always positively related to fault-rock or fault-zone thickness as suggested by the results in Figure 32- Figure 31 which show significant disparity between fault-rock thickness and expected smear location (consistent with outcrop information on smear summarised in Table 12). Shale smears have been defined as any visibly displaced siltstone that has been entrained into the fault zone (dragged or sliced) with a clear connection from one siltstone slice to the next. For no smear the siltstone bed displays no visible entrainment of siltstone into the fault zone. For the faults studied in this thesis, smear and no smear were observed on each individual fault with limited correlation to siltstone bed thickness. A variety of smear geometries were observed from 100% continuous smear to only small smear (i.e. evidence of a limited amount of drag of siltstone bed into the fault-zone). A total of 55 siltstone beds were measured for shale smears with 31 observations of smear (56%) and 24 observations of non-smeared beds. Given that just over half of the siltstone beds measured showed evidence for shale-smear over varying displacements and bed thicknesses means there is high uncertainty when assessing when a siltstone bed will and wont smear.

4.4 Fault-rock Grain-size

A digital particle sizer has been utilised to produce grain-size distribution graphs of siltstone and sandstone beds adjacent to each fault and from fault rock along each fault (Figures 40 - 45). Furthermore, SEM and thin-section analysis has been conducted on available samples to investigate grain-size reduction processes within fault zones.

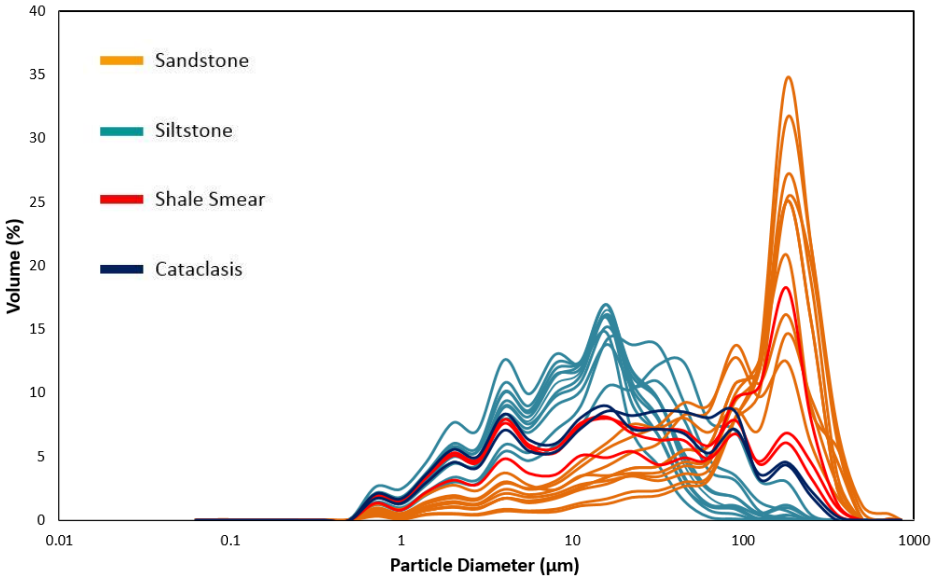

Figure 38: Graph showing all sandstone and siltstone beds, and fault-rock grain-size distributions sampled next to, and within, fault Rapanui A

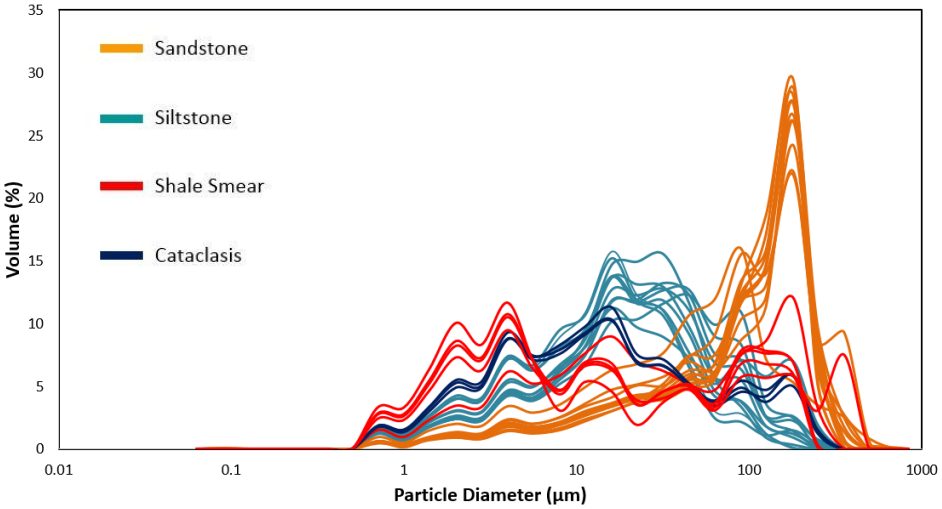

Figure 39: Graph showing all sandstone and siltstone beds, and fault-rock grain-size distributions sampled next to, and within, fault Tongaporutu A.

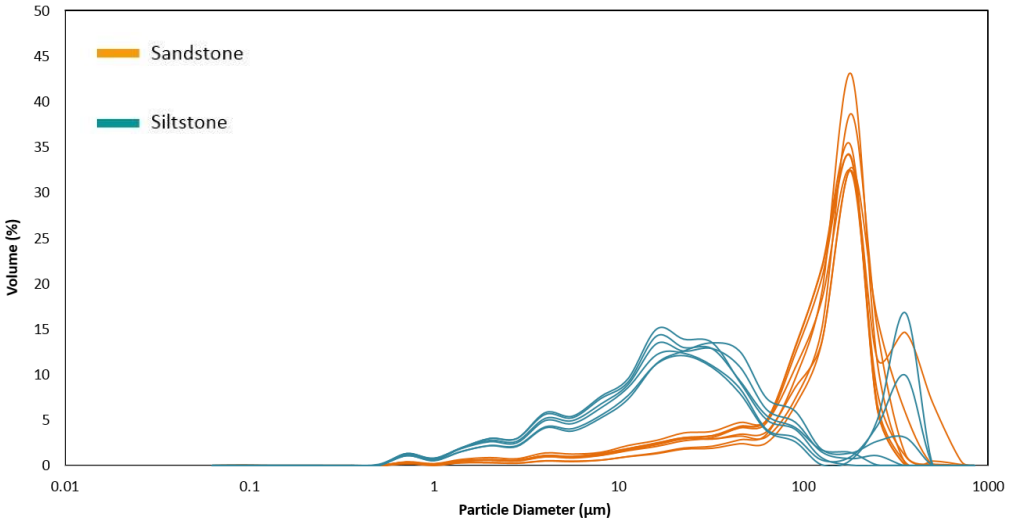

Figure 40: Graph showing all grain-size distributions for sandstone and siltstone beds sampled next to fault Tongaporutu B. No fault rock was sampled due sampling issues arising because beds were not completely displaced and fault-rock was too thin to reliably sample.

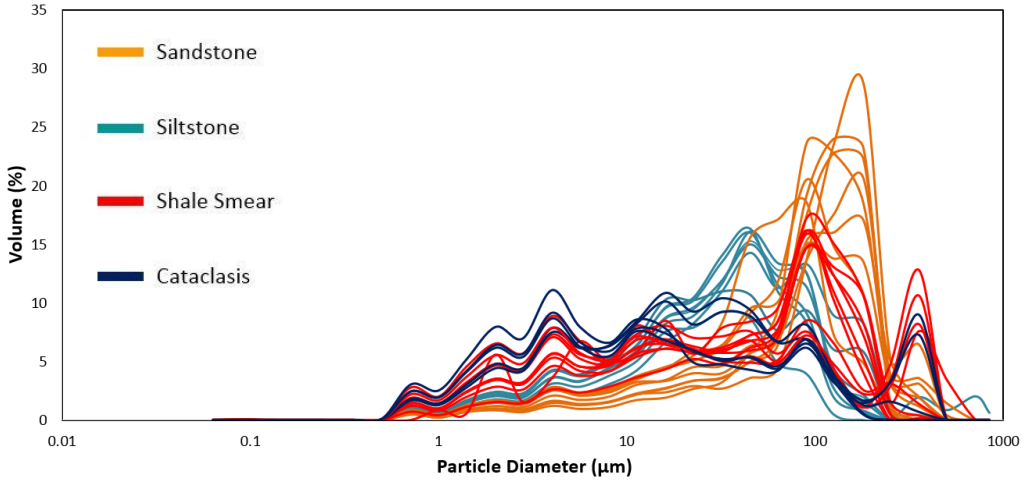

Figure 41: Graph showing all sandstone and siltstone beds, and fault-rock grain size distributions sampled next to, and within, fault Pukearuhe A.

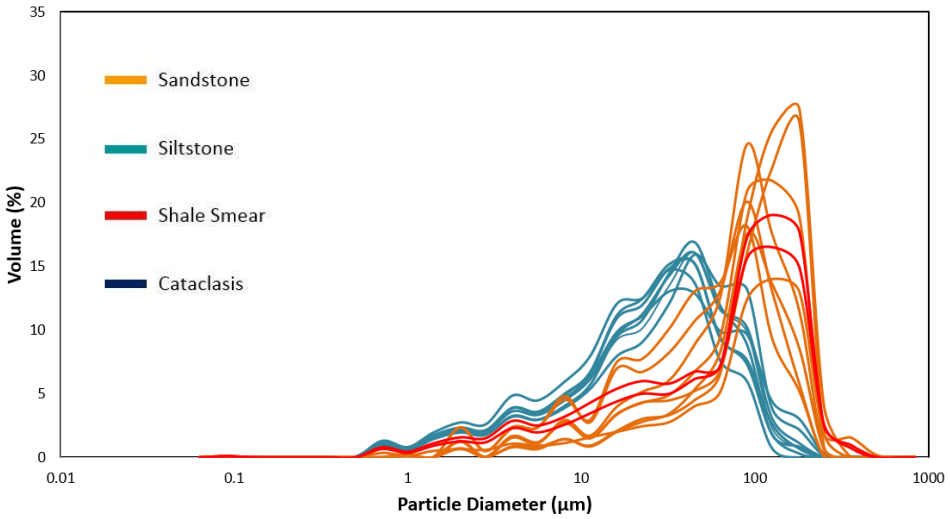

Figure 42: Graph showing all sandstone and siltstone beds, and fault-rock grain size distributions sampled next to, and within, fault Pukearuhe B.

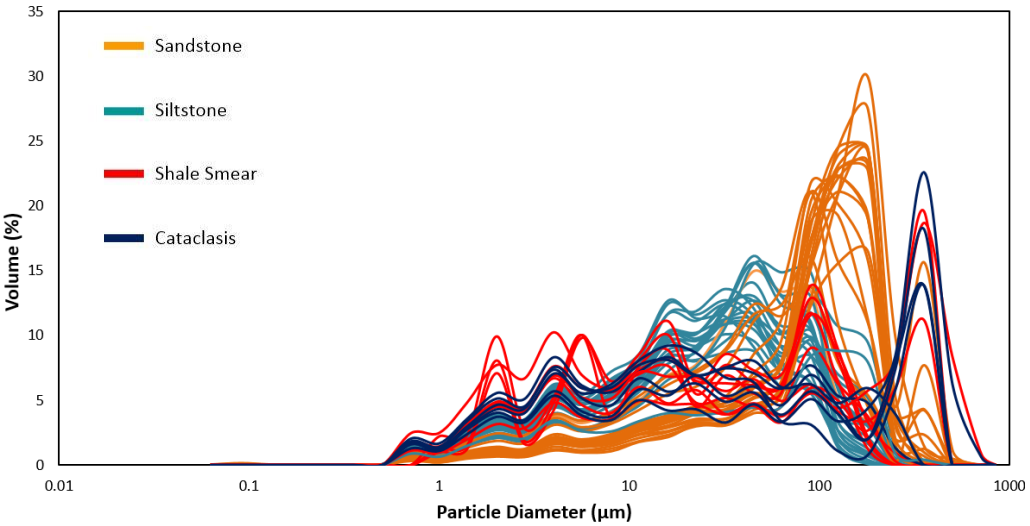

Figure 43: Graph showing all sandstone and siltstone beds, and fault-rock grain size distributions sampled next to, and within, fault Pukearuhe C.

Results for all sample grain-size analysis from individual faults show that within the sampled region of North Taranaki the sandstone samples comprise an average of 69% sand (840 – 45.1 µm), 29% silt (45 - 1.5 µm), and 2% clay (1.4 - 0.04 µm), while siltstone samples contain an average of 20% sand (840 – 45.1 µm), 75% silt (45 - 1.5 µm), and 5% clay (1.4 - 0.04 µm). Grain-size distributions for sandstone beds are usually dominated by a single mode from 90 – 300 µm with a long tail of silt and clay sized particles. By contrast the grain-size distribution for siltstone beds is generally spread across a broad modal peak. In addition, some siltstone beds contain a small medium to coarse sand fraction which provides a second mode (e.g. Figure 41).

Grain-size analysis of sandstone and siltstone beds deformed by faulting suggest that they respond differently to shear strains. Cataclasis and smearing are common within the study area. Faulted siltstone host rock generally does not show significant grain-size reduction while sandstone host rock can experience appreciable grain-size reduction. Cataclasis of sandstone beds can produce reductions in grain-size that create fault rock with similar grain-size distributions to host siltstone (Figures 40, 41, 43, 44 and 45). Bulk average grain size change for fault-rock derived from siltstone shows a slight increase in both the sand (3.6%) and clay (2.1%) portion of the sample, with a small decrease in the silts. The average grain-size reduction for sandstone beds produces an average decrease in the sand-sized particles of 42%, an increase in the silt-sized particles of 36.7%, and a 5.6% increase of the clay-sized fraction.

4.5 Relative Rock Strength

Siltstone beds within the Mount Messenger Formation generally protrude further than sandstones in outcrop, which suggests siltstone beds are eroding at a slower rate than sandstone and may be stronger. Previous UCS measurements suggest that the Mount Messenger Formation is relatively weak (UCS <12 MPa, Perrin pers com., 2012). Schmidt Hammer measurements are, on average, greater for siltstones than sandstone in the source outcrops (Table 20: appendix). If the Schmidt Hammer data provide a proxy for rock strength, then these observations support the hypothesis that siltstones are the slightly stronger of the two lithologies. However, at outcrop scale there was evidence that siltstones have deformed in a more brittle fashion. Fault rock displaced a wide range of Schmidt Hammer measurements and could be both stronger and weaker than the host rock.

4.6 SEM and Thin Section Analysis

SEM analysis of sandstone host rock and fault rock from a deformation band associated with the host sandstone (Figure 44) indicates grain-size reduction consistent with cataclasis. Host rock sandstone shows larger irregular angled grains (section A) compared to the fault rock. Within the fault rock there are finer grains/groundmass (section B) which have most likely formed due to cataclasis. Larger grains from the host rock have been rounded and reduced in size to form a more regular sub-rounded pattern throughout the fault rock supporting the cataclasis model. The transition from host rock to fault rock is also visible as fine grained ground mass and rounding of grains increases away from the host rock (section C).

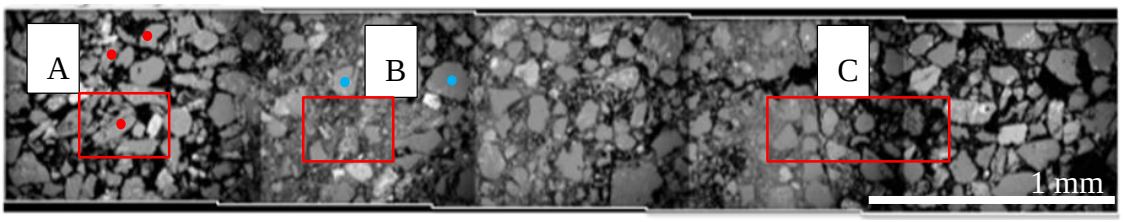

Figure 44: Photographs produced from SEM along a faulted sandstone from the study area showing cataclastic processes. The host rock (A), deformation band (B) and the transition zone from unfaulted host rock to faulted host rock and fault rock (C) are visible in high detail. Unfaulted host rock grains are much more angular and elongated (red dots) than the faulted host rock grains which are notticably rounder (blue dots).

Thin section of a shale smear (Figure 45) shows a discontinuous shale smear with unevenly distributed slices of siltstone/siltstone along the length of the sheared sample. The shale smear does not display a characteristic tapering which may be due to the large number of small slip surfaces encompassing the smear. Such complexities may make it difficult to predict shale smear and its potential to impede fluid flow. Figure 48, a small individual section from Figure 47, shows micro-fracturing/slip surfaces and smearing of clay into the fault zone together with entrainment of sand grains from host rock sandstone adjacent the siltstone bed and into the fault rock.

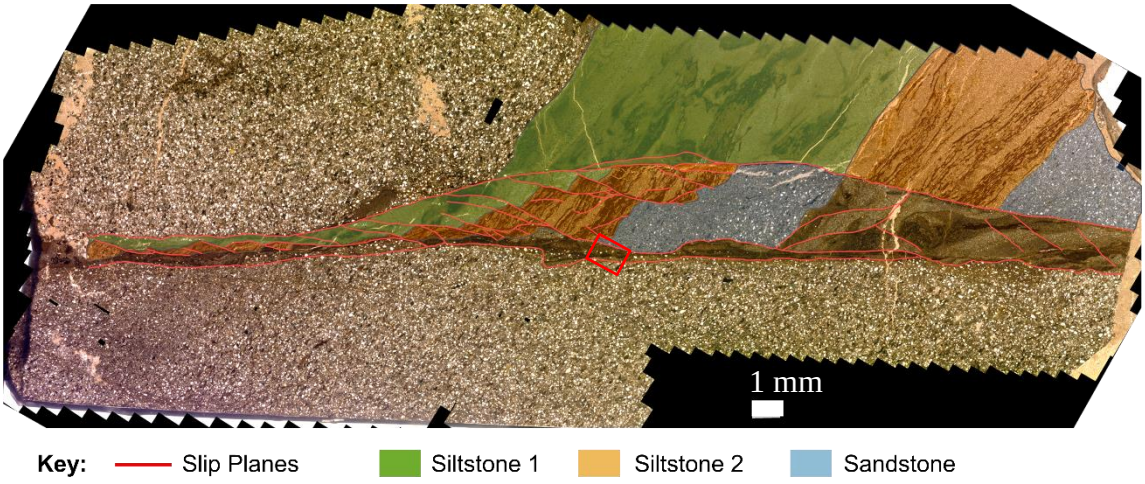

Figure 45: Photograph showing stitched images of thin section from an offset siltstone bed sampled from Rapanui within the Mount Messenger Formation. Individual units and slip surfaces have been annotated.

In Figure 47 and 48 complex micro-fracturing has occurred within the fault rock of the smeared siltstone bed. Slight variations in fracture length and density between changes in lithology can be observed between sandstone and siltstone beds. This may be due to mechanical strength variations between the beds. Here shale smear, though brittle in deformation, shows signs of ductile flow and grain incorporation whereas cataclasis is primarily due to crushing and grinding individual grains. The sedimentary fabric is still visible within the shale-smear (Figure 47 and 48) however there are small rotations of individual faulted sections related to shear. At outcrop scale shale smears may look dominantly ductile in deformation, however, at micro-scale many micro-fractures accommodated strain within the shale smear and control the smear geometries.

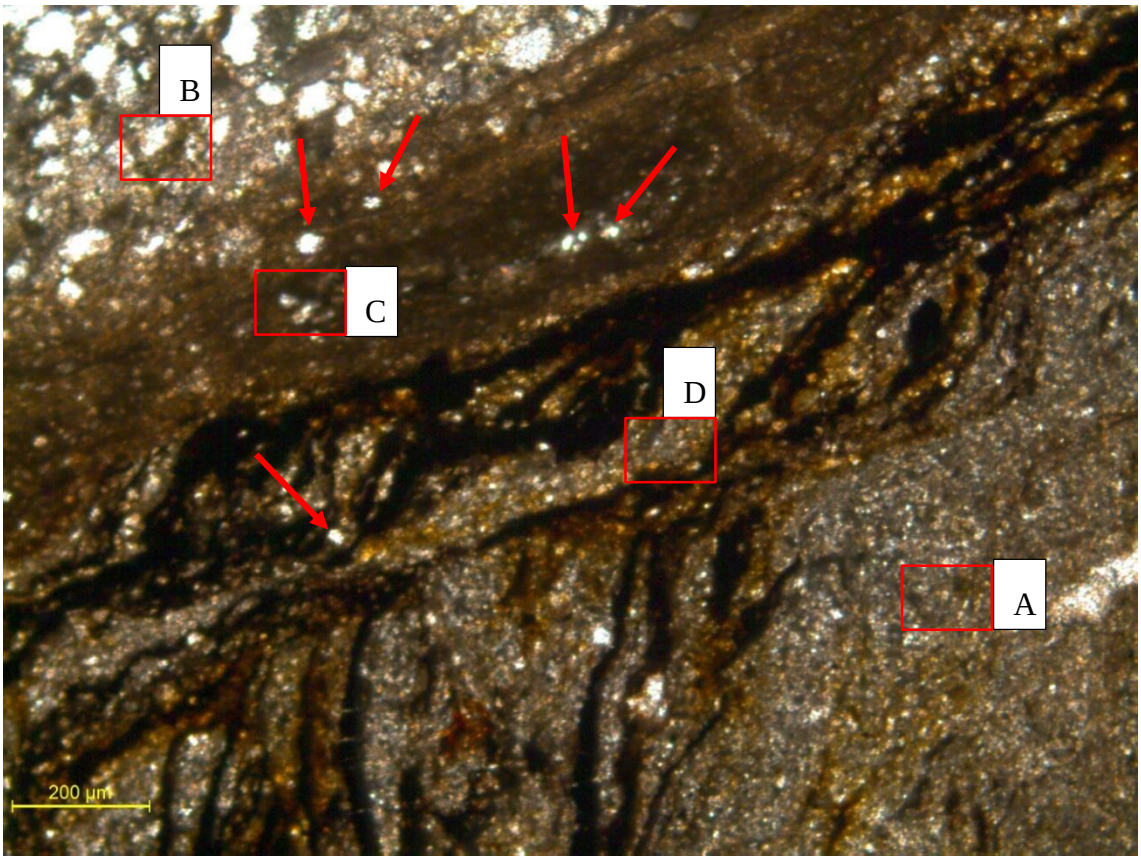

Figure 46: Photograph showing a faulted siltsone bed (A) adjacent host rock sandstone (B) and shale smear processes in detail. Sandstone grains can be seen entrained in the fault rock (C/red arrows) and siltstone is being smeared into the fault zone (D). Image from Figure 50 (red box).

4.7 Summary

The observations outlined in this chapter provide insight into the variability of fault-zone architecture (e.g. fault rock thickness, fault zone width, deformation bands and displacement), strength properties and generation of fault rock within the north Taranaki study area. Fault-zone architecture is highly variable between faults and over small distances (<100 mm) within individual fault zones. Grain-size reduction in sandstone fault-rock (compared to the source beds) is more prominent in than reductions in siltstone fault-rock. Micro-fracturing is also evident within shale-smears which may play a large role in the evolution and geometries of shale smears. These data are discussed in chapter 5 to determine how important this information is for quantifying fault-seal predictions and the hydraulic properties of fault zones.

5 Interpretation of Data and Implications for Fault Permeability

5.1 Introduction

This chapter explores fault-rock generation processes and the impacts of fault rock on bulk permeability using the data presented in chapter 4. Unlike chapter 4 which comprises observations only, chapter 5 is interpretive and examines the implications of the available data for fault-zone growth and fault-seal predictions.

Quantifying the spatial variation of low permeability fault rock has been achieved by mapping six faults at millimetre to centimetre scales, measuring the dimensions of the fault-zone and its displacement, analysing the strength of host beds and fault rock, and collecting samples for micro-scale analysis. The resulting detailed graphs display spatial variations in fault dimensions which are 1 – 3 orders of magnitude. Observations from Taranaki are consistent with previous work (e.g. Childs et al., 2007, 2009) in suggesting that fault-zone architecture is complex and predicting fluid-flow properties of fault zones (without direct outcrop data) may be challenging. Effective fault-seal prediction requires quantification of the variability of fault-rock dimensions and properties at outcrop scale. In conducting this research, it is assumed that results from outcrop studies can be upscaled to larger faults. This upscaling has been assumed for many previous studies and is rarely tested; it has not been tested in the current thesis.

Fault rock observed in the Taranaki region formed via cataclasis and shale smear. In some cases, these processes may be one in the same and which processes are observed might be scale dependent. For example, shale-smearing at outcrop scale may be accommodated by secondary fracturing at the micro-scale. The processes responsible for generating fault rock may strongly influence fault permeability (as suggested by grain-size reduction) and possibly fault thicknesses, two parameters that have been used to estimate fault transmissibility (e.g. Manzocchi et al., 2010). The following section examines Mount

Messenger Formation strength, cataclasis and shale smear, fault-zone architectural elements, and displacements as a means of quantifying fault-zone variability.

5.2 Rock and Fault Strength

The strength of individual host-rock beds (e.g. siltstone and sandstone) and associated fault rock has the potential to influence the style of deformation within fault zones. For example, weak beds are more likely to deform in a ductile fashion, while stronger beds are more often fractured. Data collected and analysed here is displayed as three frequency histograms (Figure 47).

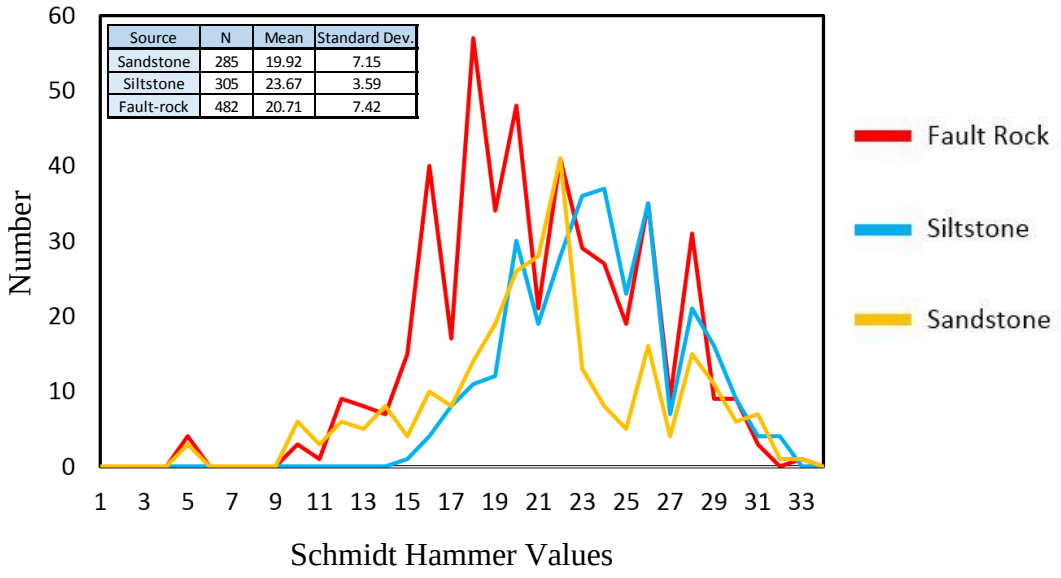

Figure 47: Frequency histograms showing the relative strength of host sandstone and siltstone beds, and fault rock from all six faults analysed in this thesis. Strength proxy measurements were collected using a manual Schmidt Hammer with nil values being excluded.

From the histograms, it is possible to draw the following conclusions. a) The ranges of Schmidt Hammer values are similar for sandstone and fault rock; these ranges are greater than for siltstone. b) The mean and mode Schmidt Hammer values for the sandstones (19.92/22) are, on average, 12% lower than siltstones (23.67/24) (i.e. siltstones may, on average, be slightly stronger than sandstones). c) The mean and mode Schmidt Hammer values for fault rock (20.71/18) are, on average, 14% lower than host rock strength. Given the wide range of values for each of the three histograms (standard deviations: siltstone = 3.59; sandstone = 7.15; and fault rock = 7.42) it remains possible that the average

strength relationships for the entire population do not apply for all outcrops. However, all outcrops studied here suggest that host-rock generally appears to be stronger than fault-rock.

5.3 Cataclasis and Shale Smear

The occurrence of shale smears and cataclasites within fault zones ultimately influences the permeability of individual faults and bulk fluid flow within faulted host rock. shale smears are known to generate fluid-flow barriers or baffles as fine grained material is dragged along the fault plane, while cataclasis produces grain-size reduction of coarser grained material leading to reduced pore-throat size and increased capillary entry pressures (Hooper, 1991). The Mount Messenger Formation has an average net to gross of approximately 0.6, although this value varies from about 0.2 to 0.9 between different facies. On average, the formation contains more sandstone (than siltstone) with sand on sand contacts along across faults dominating. Sandstone vs. sandstone contacts are generally more likely (than sandstone – siltstone fault contacts) to permit across fault fluid flow. The likelihood of across fault flow is examined in the following text using data from laboratory analysis of host-rock and fault-rock samples within the Taranaki study.

5.3.1 Grain-size Distribution Changes

In Taranaki cataclasis of sandstone due to faulting is common, leading to grain-size reduction that can produce fault rock as fine grained as siltstone beds in the host-rock (Figure 42 - Figure 40). By contrast, grain-size changes in the siltstone beds are relatively minor and suggest only slight cataclasis in some cases (Table 4: Pukearuhe A), while other siltstones are characterised by increases in grain-size (Table 4: Rapanui A, Pukearuhe C) which is consistent with some entrainment of sand into smears (Figure 46). The changes in host-rock grain-size due to faulting are quantified in Tables 5 – 6. These tables display the % volume grain-size changes due to faulting of siltstone (Table 5) and sandstone (Table 6) host rock.

Table 4: Summary of siltstone bed grain-size changes from for fault-rock formed by shale smear. Average values are plotted on Figure 48. Green indicates increase in volume and light brown a decrease.

Fault	Siltstone Bed	Average Displacement (cm)	Grain-size Change (%)		
			Sandstone (840 - 45 µm)	*Siltstone (45 - 1.4 µm)*	*Clay (1.4 - 0.04 µm)*
Rapanui A	*I*	2.28	23.5	-22.4	-1.1
	K		17.3	-18.8	1.5
Pukearuhe A	*D*	11.9	-23.3	19.4	3.9
	E		-11.1	3.7	7.3
Tongaporutu A	*K*	12.85	0.6	-3.5	2.9
	H		-1.6	-0.8	2.3
Pukearuhe C	*I*	15.38	13.8	-16.0	2.1
	J		3.5	-4.9	1.4
	S		9.4	-12.0	2.5
Average	-	-	*3.6*	*-6.1*	*2.5*

Table 5: Summary of sandstone bed grain-size changes for fault-rock formed by cataclasis of sandstone beds. Average values are plotted on Figure 48. Green indicates increase in volume and light brown a decrease.

Fault	Sandstone Bed	Average Displacement (cm)	Grain-size Change (%)		
			Sandstone (840 - 45 µm)	*Siltstone (45 - 1.4 µm)*	*Clay (1.4 - 0.04 µm)*
Rapanui A	*G-H*	2.28	-59.0	53.3	5.9
	H-I		-55.2	50.7	6.1
Pukearuhe A	*C-D*	11.9	-45.8	41.5	4.7
	E-F		-13.9	10.0	3.9
Tongaporutu A	*J-K*	12.85	-45.6	36.9	8.8
	G-H		-45.7	36.4	9.3
	Base		-42.9	34.3	8.7
Pukearuhe C	*H-I*	15.38	-50.0	48.6	1.5
	Q-R		-44.2	40.1	4.6
Pukearuhe B	*Base*	27	-17.7	15.7	1.9
Average	-	-	*-42.0*	*36.7*	*5.5*

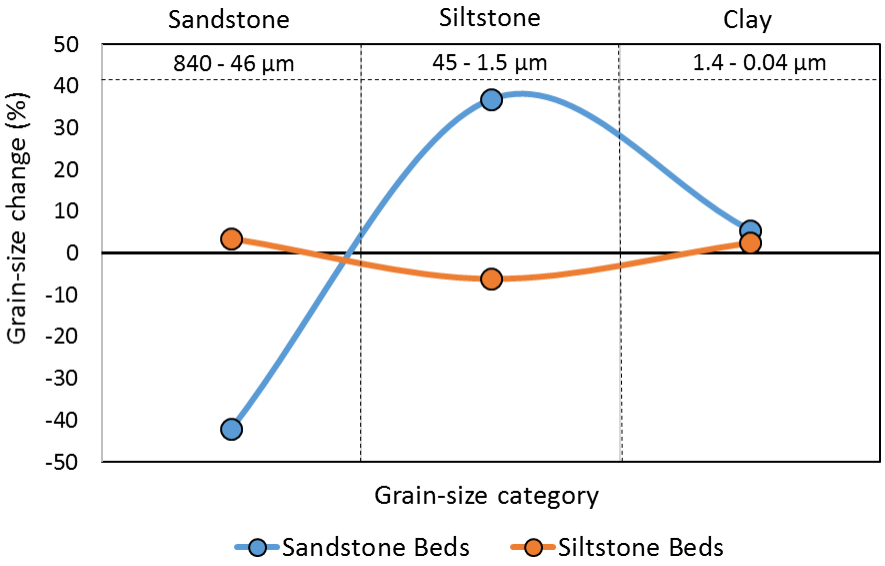

Figure 48: Graph showing average grain-size changes for sand-, silt-, and clay-sized grains in fault rock produced by shearing of sandstone and siltstone beds.

The amount of grain-size change varies for sandstone and siltstone beds. Minor grainsize reduction is generally observed for smeared siltstone beds, however, inspection of the individual beds suggests that grain-size reduction of sand paticles can be up to 23%. (e.g. Table 5: Pukearuhe A, bed D). These observations can be interpreted to indicate that siltstone beds generally experience very little cataclasis during faulting. Some siltstone beds appear to show a minor increase in the sand-sized fraction (e.g. Table 5: Rapanui A - bed I, and Pukearuhe C), which is consistent with some entrainment of sand grains from nearby sandstone beds during smearing (Figure 46: red arrows). Such entrainment requires mixing of grains from separate beds at bed boundaries. Sandstone beds typically display an average of over 40% grain-size reduction of sand-sized particles. Reduction in the size of sand grains is accompanied by an average increase of silt- and clay-sized particles of almost 40% and 5%, respectively. Given the approximate equivalence of the sand decrease and the silt/clay increase it is possible that crushing of sand grains produces both silt and clay. Irrespective of whether the new clay-sized particles were produced from silt or sand it is clear that cataclasis of sandstone beds within fault-zones primarily produces new silt-sized grains. Further examination of shear failure processes, the mechanical strength of beds/different areas of individual beds, the temperature regime during burial/faulting, mineral precipitation and diagenic processes are imperative for

improving understanding of how cataclasis and shale smears evolve over space and time under different conditions.

The cataclastic processes observed in the Mount Messenger Formation occurred at shallow depths (<1500 m) and in weakly lithified strata. The available data support previous work on unlithified Quaternary sediments (e.g. Cashman and Cashman, 2000; Kristensen et al., 2013) in suggesting that brittle processes can deform strata at shallow depths and low confining pressures. In Taranaki cataclasis does not appear to have been accompanied by secondary mineralisation and unlike deformation bands in the quartz-rich sands of Utah (e.g. Aydin, 1978; Aydin and Johnson, 1983) there is no evidence that the faults are significantly stronger than the host-rocks (section 5.2 Rock and Fault Strength), which could promote local brittle failure. Instead brittle failure of sand grains may be promoted by presence of a significant proportion of weak lithic sand-sized grains, which can be disaggregated at low shear strains. Thin sections indicate that some quartz grains, which are likely to have been relatively strong, are also fractured and crushed, from which it can be inferred that grain strength (i.e. the presence of weak grains) cannot completely account for the observed cataclasis in the Mount Messenger Formation.

5.3.2 Shale Smear

Shale smear observed in the Mount Messenger Formation, occurred in the same geological conditions as for cataclasis, shows signs of both brittle and ductile deformation. Like the cataclastic processes brittle deformation may influence the formation and geometries of smears during faulting. Though displaying ductile deformation at outcrop scale many shale smears observed in Taranaki show signs of micro-fracturing in thin scetions (Figure 45) which can controll sand-sized grain entrainment as well as smear geometries. Micro-faults may also be responsible for the small grain-size reductions observed some shale-smears.

Using information gathered from outcrop on all faults analysed (Table 27: appendix), it is possible to assess the accuracy of SSF, SGR and CSP predictions. These predictions dominantly rely on bed thickness and displacement. Observed smearing and non-smearing of siltstone beds has been counted for each fault along with the number of counts for where smear calculations predict or don't predict shale smear accurately (Table 12: Appendix). Results show that out of the 55 siltstone beds sampled 56% smeared (). All calculations have relied on numbers to define smear potential using bed/fault characteristics. For SSF < 5 = likely continuous smear, 5- 7 = possible continuous smear

and > 7 = no continuous smear; for SGR > 30 = likely continuous smear, 20 – 30 = possible continuous smear and < 20 = no continuous smear; for CSP > 30 = likely continuous smear, 15- 30 = possible continuous smear and < 15 = no continuous smear (Yielding et al., 1997; Lindsay et al., 1993). Only beds that have been fully displaced have been recorded and analysed due to full displacement being required to determine smear predictions of algorithms. Tongaporutu B fault has not been accounted for here as none of the beds were fully offset due to the small displacement along the fault.

Table 6: Summary of shale smear observations and predictive accuracy of SGR, CSP and SSF algorithms for shale smear on displaced siltstone beds.

Fault Name	Number of Siltstone Beds	Correct Smear Predictions					
		SGR	*%*	*CSP*	*%*	*SSF*	*%*
Rapanui A	11	6	55%	5	45%	6	55%
Pukearuhe A	6	4	67%	3	50%	3	50%
Pukearuhe B	8	3	38%	3	38%	2	25%
Pukearuhe C	19	10	53%	9	47%	9	47%
Tongaporutu A	11	6	55%	2	18%	8	73%
TOTAL	55	29	53%	22	40%	28	51%
Average Accuracy		53%		40%		50%	
Minimum		38%		18%		25%	
Maximum		67%		50%		73%	

Information gathered here suggests that these algorithms have variable reliability between individual faults and different techniques. SGR and SSF have an overall average predictive accuracy (i.e. averaged between individual faults measured) of about 50%. While CSP accuracy is similar at 40%. The highest predictive accuracy recorded was for SSF on Tongaporutu A where it was 73% while the lowest recorded predictive accuracy was a low 18% for CSP (also on Tongaporutu A). Given that SGR, CSP and SSF calculations are, on average, accurate about half of the time the predictive power of these algorithms might be called into question.

Strength of individual siltstone beds along the same fault produce comparable Schmidt Hammer values, suggesting that the beds may have similar strength, and yet beds of similar strength maybe both smeared and not smeared. This suggests that strength is not a key controlling factor for why some siltstone beds produce smears and others do not. In addition, given that sandstone beds appear to be similar in strength, and perhaps slightly weaker than, siltstone beds it is expected that sandstone will also smear. Although not the focus of this thesis such sandstone smears have been observed and are implicit in the mixing of siltstone and sand grains.

5.4 Fault Zone Architecture

Observations made in chapter 4 shows that fault-rock and fault-zone thickness are complex and spatially variable on individual faults (e.g. Figure 28). These variations are here quantified for individual faults and compared between faults to derive generic conclusions that may apply beyond the Mount Messenger Formation. These conclusions are required to quantify better the structural and lithological variations across and along fault zones which are essential for predicting fault fluid-flow properties.

Figure 49 illustrates the small portion of faults that are typically observable or measurable in the outcrops compared to the total dip length. Quantifying the variation of fault-zone architecture over the entire, often un-sampled, fault surface is key for understanding faulting and how they influence hydraulic properties. Trying to determine and quantify the spatial variation and variability of architectural elements of faults is important for modelling and fluid flow simulations as normalized data from many faults may be used as a proxy for determining the spread of different architectural and hydraulic elements along various fault lengths for individual faults.

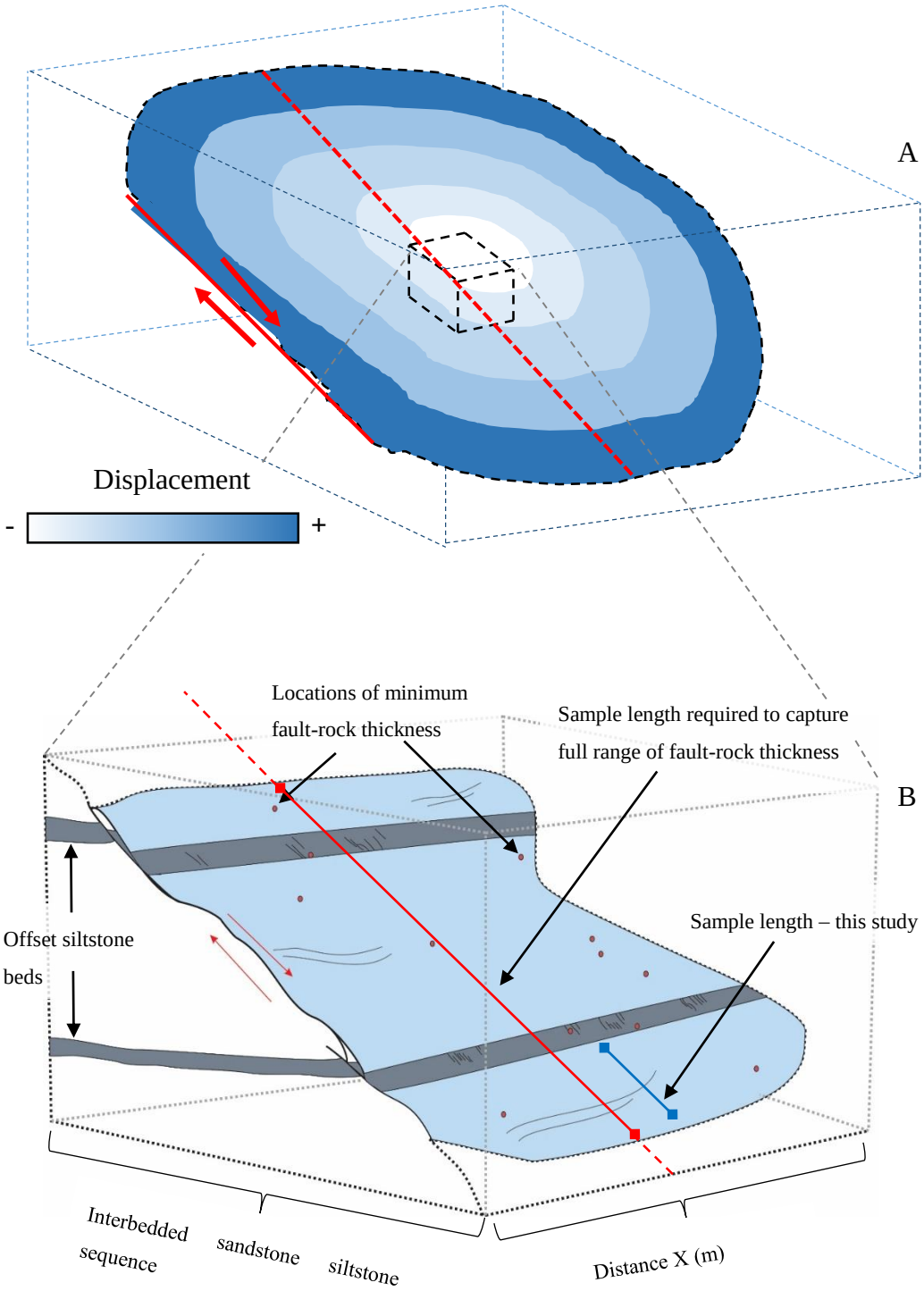

Figure 49: Schematic diagrams illustrating three-dimensional fault plane (A) and a zoomed in section of the plane (B) with measured sample lengths (blue line) with limited observations of fault-zone architecture and a sample line (red line- see also A) the entire dip-length of the fault. Red line increases in length for individual faults as displacement increases and as a consequence the sample line length (blue line) represents a decreasing portion of the total length (because sample line lengths are approximately fixed).

5.4.1 Quantifying Variability

Individual architectural elements (i.e. fault-rock and fault-zone thickness) have been analysed to define better the predictability of each element with increasing displacement and over different sample lengths. To facilitate comparison of results between faults each fault element, including fault-rock thickness (Figure 50), fault-zone thickness (Figure 51) and deformation band count (Figure 52) (425 samples each) has been normalized to 1. Fault-rock thickness ranges from 0.5 mm (the resolution limit of the data) to 13 mm. Fault-rock thickness has a broad positive relationship with displacement, however, fault-rock and fault-zone thickness may vary within and between individual faults by up to 1.5 orders of magnitude (Figure 50 and Figure 51).

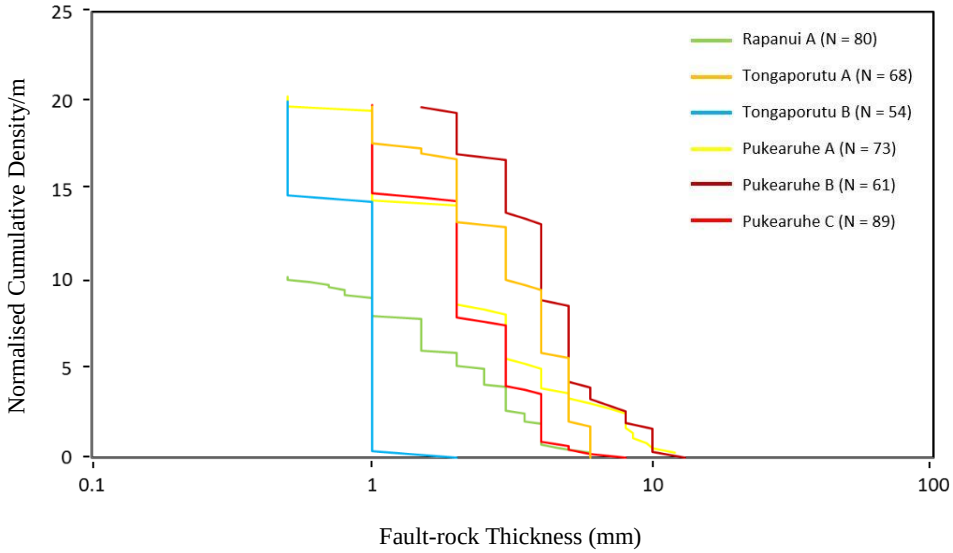

Figure 50: Normalised frequency per m of sample-line length for fault-rock thickness. Each coloured line shows data for an individual fault (see key for fault names).

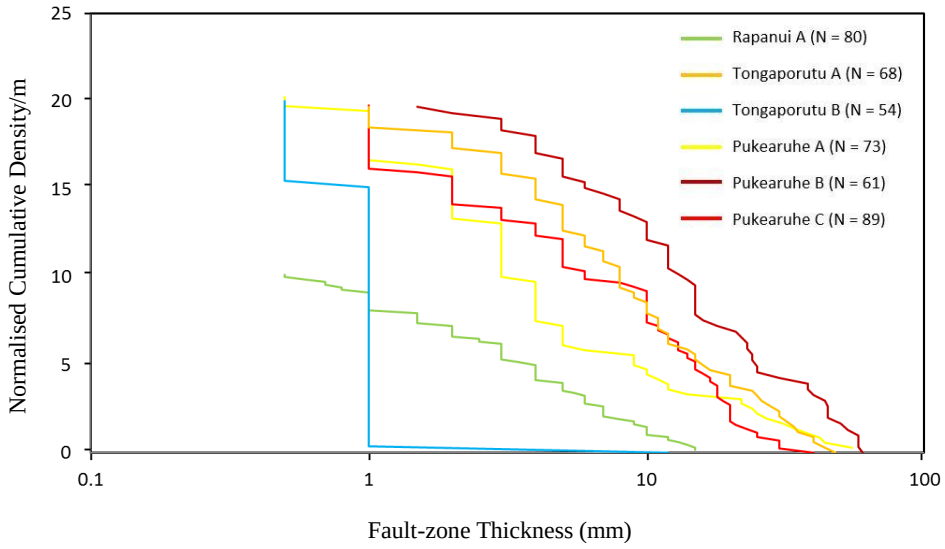

Figure 51: Normalised frequency per m of sample-line length for fault-zone thickness. Each coloured line shows data for an individual fault (see key for fault names).

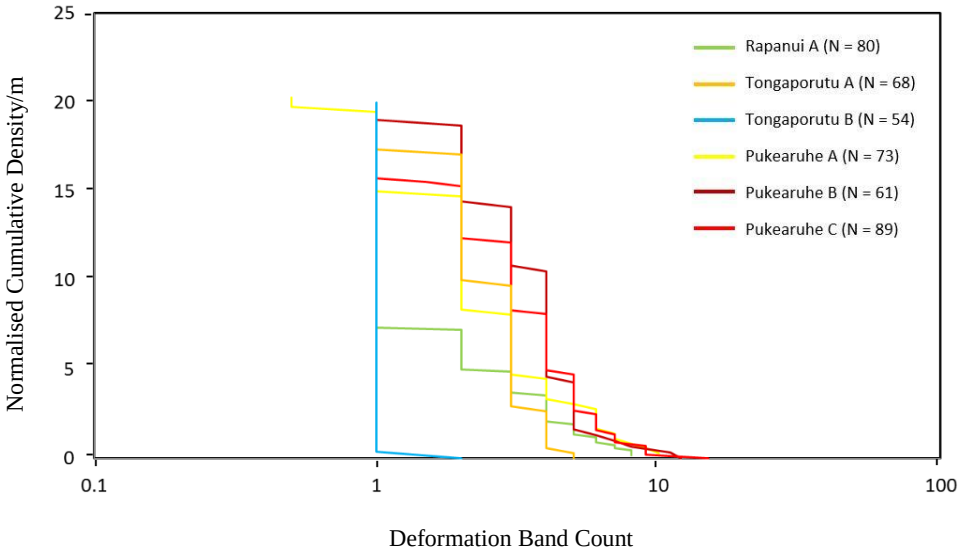

Figure 52: Normalised frequency per m of sample-line lengths for deformation band count. Each coloured line shows data for an individual fault (see key for fault names).

The maximum fault-rock thickness ranges from 2 – 13 mm with each of the individual faults displaying an increase in normalised density at small thicknesses. Despite the fact that fault-rock curves in Figure 50 are all stepped (primarily because thicknesses were measured at millimetre increments), each curve can be approximately fit by a straight line on the linear-log graphs. The slopes of the curves for each fault are controlled by the range of the thickness and the density of measurements. Given that neither the lower resolution limit of the measurements nor the density of measurements changes significantly between faults (excluding Rapanui A which had 10 cm sample spacing), it is expected that the slopes will decrease with increasing displacement and maximum thickness. While such a decrease can be observed between the smallest displacement fault (Figure 53) and the rest of the faults studied, too few data are presently available to adequately test the predicted relationship.

The cumulative density plot for fault-zone thickness in Figure 51 show similar results to fault-rock thicknesses (i.e. cumulative density increases linearly with decreasing thickness). The primary difference between the cumulative density plots for fault-rock and fault-zone data is that the later curves have lower slopes due to their greater range of values. Despite these differences in slope both Figure 50 and Figure 51 suggest a factor of three decrease in thickness results in a two-fold increase in cumulative density. These data are broadly consistent with a negative exponential relationship for which the number of thinner thicknesses are greater than the thicker values (Figure 54). For example, fault-zone thicknesses from 1 – 3 mm and 3 – 10 mm for the Pukearuhe C fault have cumulative densities of 3.5/m and 1/m, respectively.

The cumulative density plot for deformation-band count (Figure 52) also shows similar results to Figure 50 and Figure 51 with cumulative density increasing linearly with decreasing count. Deformation-band counts vary from ½ count (or half where only displacement is observed), to 12 counts. Each curve varies in shape depending on the number of deformation bands counted at each sampling location (i.e. only a single deformation band was counted for the majority of the sample line for Tongaporutu B, thus the blue line is steep). All curves are stepped as only integer values are possible with curves steepening as displacement increases because new deformation bands a generally added as fault zones evolve (Nicol et al., 2013).

Fault-rock and fault-zone thicknesses analysed here have been combined with thickness data from throughout the Mount Messenger Formation in Childs et al. (2009). The minimum and maximum values for fault-rock and fault-zone thickness are shown by

dashed blue and red lines, respectively. The black dashed line shows the resolution limit of observations and it is possible that some thicknesses extend below this line especially at low displacements (e.g. <10 cm). Fault rock thickness, fault zone width and deformation band count measurements have been normalised and graphed (Figure 54).

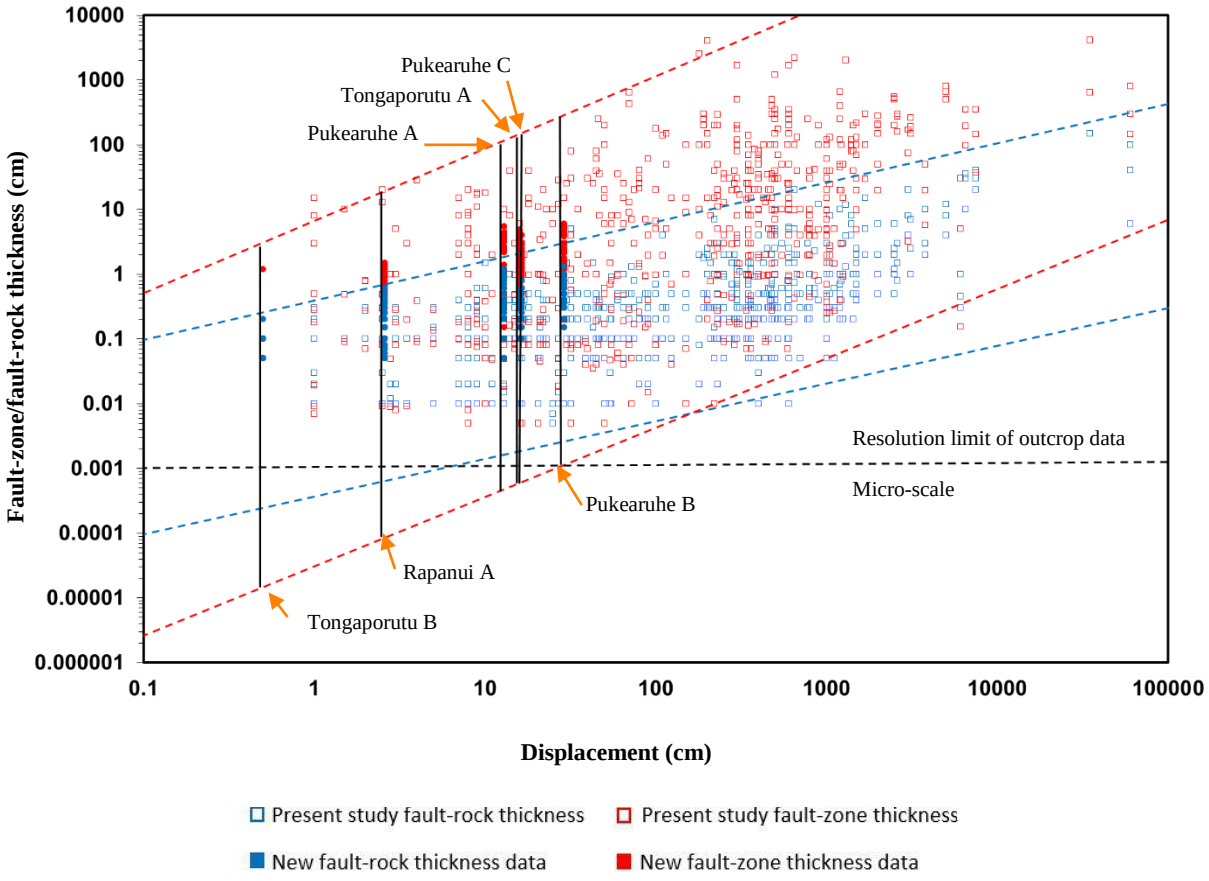

Figure 53: Graph showing new data sampled for this study (and data sources) combined with data from Childs et al., (2009) with upper and lower estimated boundaries for fault-rock and fault-zone thickness. Black dashed line denotes resolution limits below which thicknesses typically cannot be measured.

Upper and lower limits for fault-rock and fault-zone thickness have been positioned by eye and are assumed to encompass at least 95% of the total spread that can be observed in outcrop within the Mount Messenger Formation. Observations made in this thesis are consistent with previous measurements in suggesting that there is a broad positive relationship between thickness and displacement, although fault-rock and fault-zone thicknesses can vary significantly (3 – 4 orders of magnitude) for a given displacement (e.g. Childs et al., 2009). New measurements collected from individual faults (added to

the dataset) also display a large spread in thickness for a given displacement, although this spread is much smaller than for the entire dataset of Childs et al. (2009).

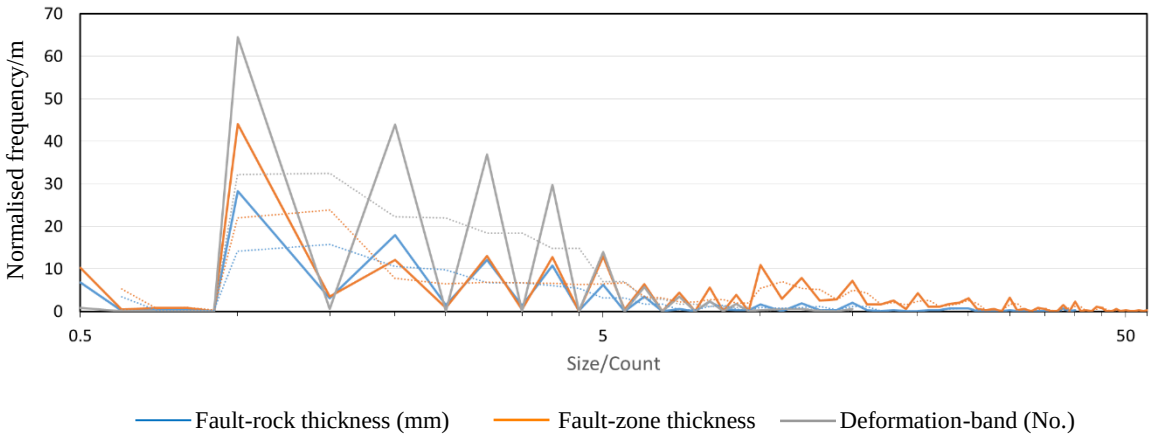

Figure 54: Graph showing normalized frequency per m of sample-line length for fault rock thickness, fault zone thickness and deformation band count (logarithmically scaled).

These measurements suggest that data falling between 0 – 5 is far more frequent than data above 5. Deformation band frequency drops off significantly as the count increase, while fault-rock and fault-zone thickness gradually drop off into 35 – 50 mm range with fault-zone thickness occurring more frequently in the higher ranges than fault-rock thickness. Normalized frequency measurements of fault-rock thickness, fault-zone thickness and deformation-band count show that in general there is a gradual decrease is these elements as the thickness of fault zone/rock and deformation-band count increases.

Table 7: Summary of minimum and maximum fault-rock thickness ranges and calculated range of data from this study relative to the range of data from Childs et al. (2009).

Fault Name	Average Displacement (cm)	Fault-rock Thickness (cm) - this study			Fault-rock Thickness (cm) - Childs et al. (2009)			Ratio	
		Min	*Max*	*Range*	*Min*	*Max*	*Range*		
Rapanui A	2.60	0.05	0.60	0.55	0.0006	0.60	0.60	0.918	91.8%
Pukearuhe A	13.00	0.05	1.20	1.15	0.0015	2.00	2.00	0.575	57.5%
Pukearuhe B	29.00	0.15	1.30	1.15	0.0020	4.00	4.00	0.288	28.8%
Pukearuhe C	16.50	0.10	0.80	0.70	0.0010	2.55	2.55	0.275	27.5%
Tongaporutu A	16.00	0.10	0.60	0.50	0.0010	2.50	2.50	0.200	20.0%
Tongaporutu B	0.50	0.05	0.20	0.15	0.0003	0.25	0.25	0.601	60.1%

Table 8: Summary of minimum and maximum fault-zone thickness ranges and calculated range of data from this study relative to the range of data from Childs et al. (2009).

Fault Name	Average Displacement (cm)	Fault-zone Thickness (cm) - this study			Fault-zone Thickness (cm) - Childs et al. (2009)			Ratio	
		Min	*Max*	*Range*	*Min*	*Max*	*Range*		
Rapanui A	2.60	0.05	1.5	1.45	0.0001	20.00	20.00	0.073	7.3%
Pukearuhe A	13.00	0.05	5.5	5.45	0.0005	100.00	100.00	0.055	5.5%
Pukearuhe B	29.00	0.15	6	5.85	0.0015	300.00	300.00	0.020	2.0%
Pukearuhe C	16.50	0.1	4	3.9	0.0008	175	175.00	0.022	2.2%
Tongaporutu A	16.00	0.1	4.8	4.7	0.0007	150	150.00	0.031	3.1%
Tongaporutu B	0.50	0.05	1.2	1.15	0.0000	3	3.00	0.383	38.3%

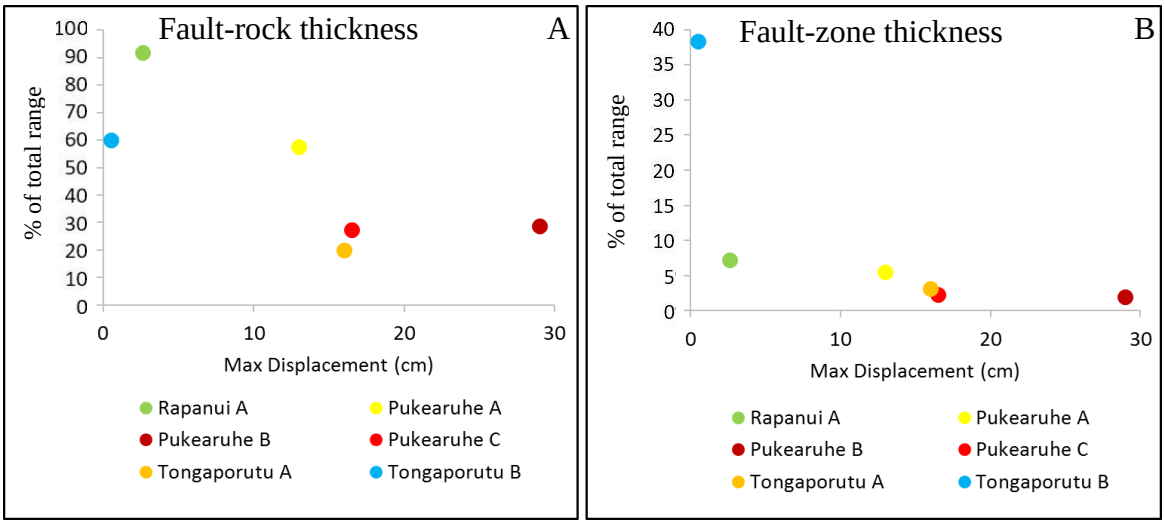

Figure 55: Graphs showing the range of fault-rock (A) and fault-zone (B) thickness data in this thesis compared to total range of data in Childs et al. (2009) versus displacement.

The range of fault-rock and fault-zone thickness measurements for this thesis is smaller than that for the entire dataset. The comparison of these datasets provides a basis for beginning to assess how much variability of fault-zone architecture is possible on individual faults (Table 7, Table 8, Figure 55 and Figure 55). The results here indicate that the smaller the fault displacement the greater the proportion of total range in thickness is captured for all faults (Childs et al., 2009). This negative relationship is most clearly demonstrated in Figure 55 A where up to 90% of the total range (i.e. for all data) in thickness was sampled in this study by a short line sample on an individual fault. To explore this negative relationship further and to examine what the range in thickness may indicate about fault-zone architecture, sample length and displacement these data are plotted on Figure 56 and Figure 57 . The portion of the total dip length represented by each sample has been estimated by using the equation $D = cL^n$ to estimate the total dip length, where D is maximum displacement, c is a constant related to rock properties, L is length and n is an exponent (e.g. Cowie and Scholz, 1992). Parameters for this displacement-length scaling equation have were adopted from FIFT (2005) where $D = 0.001L^{1.35}$. Measured maximum displacements have been used to calculate the dip length for the sampled faults in the Mount Messenger Formation and length is assumed to be dip length (assuming that fault dip length and strike length are equal is consistent with observations).

The sample line length is divided by the total dip length of the fault surface (see Table 11) The resulting modified calculation for fault dip length is:

$$L= (D/0.001)^{1/1.35}$$

The range % is the range of thickness for each fault in this study divided by the range in thickness for all faults in the Mount Messenger Formation with displacements equal to those of the sampled faults. The sample range divided by the total range is multiplied by 100 to produce a percentage. The resulting percentage is then divided by the sample line length to normalise for different line lengths.

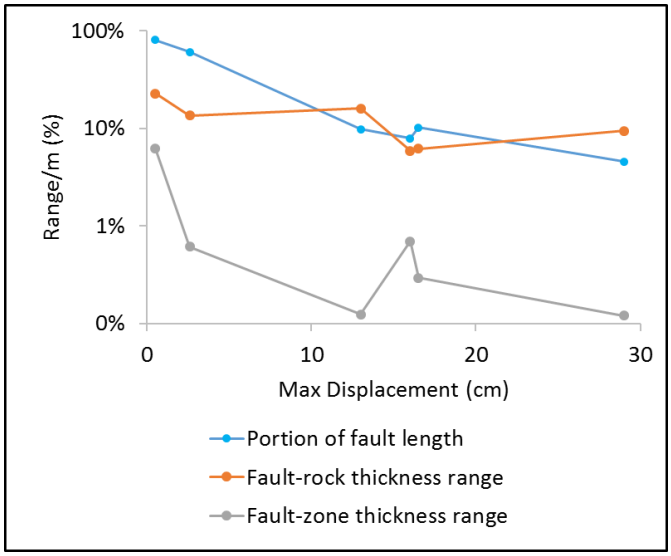

Figure 56: Graph showing normalized range (%) per m of sample-line length for fault-rock thickness and fault-zone thickness versus maximum displacement accompanied with calculated sample portion. Note logarithmic y-axis. Normalised data has been calculated from the information present in Table 9 and Table 10.

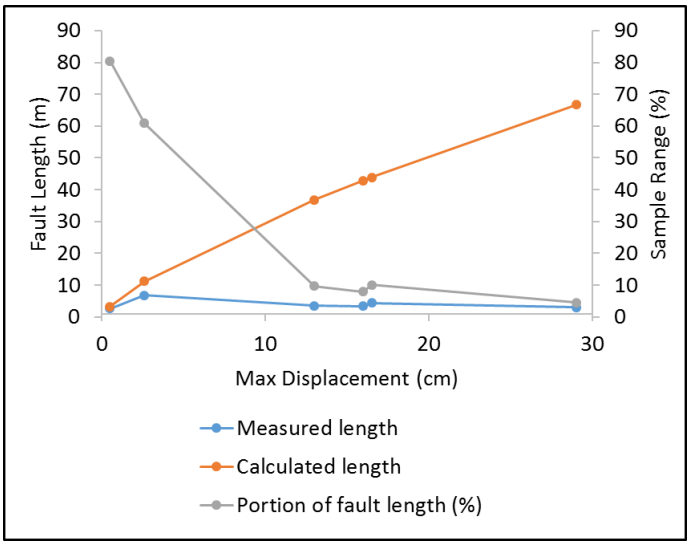

Figure 57: Graph showing measured sample-line length, calculated fault length and portion of fault surface (%) data for faults sampled. Normalised data has been calculated from this information in Table 9 and Table 10.

Results indicate that the range/m sample-line length for fault-rock and fault-zone thickness, and the portion of the fault sampled, decrease as displacement increases (Figure 56). These relationships are expected given that the sample lengths have been normalised and likely record less of the fault with increasing displacement. The data suggest that longer sample lines are required to capture the full range of fault-zone thickness than for fault-rock thickness (shown in Table 9 and Table 10). For example, Tongaporutu B fault has a calculated total length of 3.29 m, and samples 80% of the total range in fault-rock thickness and 80% of the total dip length. As displacement increases the fault sample length required to obtain 100% of fault-rock thickness range decreases. For example, Pukearuhe B is calculated to be 67 m in dip length, however, based on the available data an 11 m sampling length may be required to capture the full (100%) range of possible fault-rock thicknesses for this fault. This suggests that the minimum and maximum fault-rock thickness may be obtainable without needing to sample a large portion of the fault length (e.g. ~16% of Pukearuhe B's fault length may contain the full range of fault-rock thickness information).

Normalized range per m of fault-zone thickness is lower than that of fault-rock data which suggests a much longer sample-line length is required to sample the full range of thicknesses. It is worth noting, however, that calculating sample length required to sample the full range of fault-zone thicknesses can be problematic. For example, fault Pukearuhe C has a calculated length of 44 m, however, a sample length of 200 m can be calculated to obtain the full range (minimum and maximum thicknesses) of data. Ideally the full range of thicknesses should be sampled within the calculated fault length, but fault-zone thickness is highly variable (1 – 2 orders of magnitude) on all sampled faults and the range of thicknesses sampled may be strongly dependant on the sample locations. Additional uncertainties in the present range analysis include errors on the minimum and maximum values in the ranges; upper and lower boundaries for fault-rock and fault-zone thickness may change with new data.

The proportion of the total dip length sampled decreases as displacement increases, in part because the calculated length of each fault significantly increases with rising displacement. This information coupled with frequency distribution curves of fault-rock thickness, fault-zone thickness and deformation bands (Figure 54) permits modelling of fault-zone architecture over the fault surface for faults with a range of displacement. Collectively these data can be used to generate virtual fault settings for modelling and permeability predictions. These predictions can be constrained by thickness frequency distribution curves, which help to characterise fault-zone architecture for a range of displacements. This may help with improving the predictability of individual elements within faults to generate more meaningful models and algorithms that reflect fault-zone and fluid-flow properties in the subsurface.

5.5 Implications for Permeability Predictions

Observed shale smears within fault-zones correlate poorly with SSF, SGR and CSP models which are used to predict the sealing properties of fault zones (Table 4 and Table 12: appendix). The apparent poor correlation between fault-seal said and shale smearing suggests that measurements of displacement and bed thickness, which underpin the models, may not be sufficient to provide insights into the permeability of fault zones. A number of fault-zone architectural parameters (such as, and not limited to, fault-zone thickness, grain-size reduction processes, displacement or lithology) are most likely controlling the occurrence and extent of fault-seal. Results from this study may have implications for structure and permeability predictions of fault zones.

There is significant variability of fault-zone architecture for both smeared and non-smeared siltstone beds. Analysis of siltstone bed smear (Table 4) indicates that current models are on average, only 50% accurate at predicting where smear will occur which means there is a high level of uncertainty in the utility of the models. Quantifying the impacts of fault zone architecture of smearing processes is an important step towards refining fault-seal models for more accurate fault seal predictions. Quantifying where smear will and won't occur relies on more than just bed thicknesses and displacement. Complex interactions between different processes within fault zones control smear geometries, including mechanical strengths between host beds and phyllosilicate content of host siltstone beds. Models require an understanding of these processes to more accurately predict smearing processes. Study of the processes that control shale smear is beyond the scope of this study.

Cataclasis may be an important phenomenon to take into account when analysing fault-seal potential. Consideration should be given to how cataclasitic and shale-smear processes interact with each other and what this interaction might mean for permeability. Cataclastic processes have been observed here to generate fault-rock material as fine as shale-smears and may produce barriers to fluid flow, comparable to what might be predicted from shale-smear analysis. Therefore, re-evaluation of the role of cataclasis for fault-seal is warranted and requires detailed analysis which again is beyond the scope of this thesis.

5.6 Summary

The results of this chapter have implications for quantifying fault-zone architecture, fault-rock generation, and permeability predictions. Outcrop analysis shows that the structural elements of fault-zones are variable and characterising fault permeability structure challenging. Laboratory analysis suggests that cataclasis is important for generating low permeability fault rock. Cataclasis could influence fault-zone permeability in the Taranaki study area at sand on sand contacts within interbedded sequences and consideration should be given to when incorporating cataclasis into fault-seal models and algorithms (i.e. when it is important to focus on cataclasis and shale smear). Sampling of fault zones and scaling of their variability has been analysed and shows that with increasing displacement the range of fault-zone and fault-rock thickness data becomes more difficult to capture at outcrop scale. Sampling over larger fault-dip lengths is required to obtain higher quality data that represents the full range of individual elements/processes occurring within a fault zone. There remains uncertainty in the fault-sealing properties of fault-rock and how they would be affected by variations in fault-zone thickness. Fault-zone permeability has the potential to vary spatially within fault zones and using simplistic fault-seal models (e.g. SGR, CSP, and SSF) for calculating fluid flow may need to be re-examined.

6 SUMMARY AND RECOMMENDATIONS

6.1 Summary

In this study, six normal faults within the interbedded Mount Messenger Formation, Taranaki, have been sampled in detail and analysed to characterise the structure and is variation within fault zones. The data have been used to help constrain the origin of fault rock and its implications for fault-seal prediction.

A literature review identified a range of uncertainties associated with the definition and quantification of fault-zone geometries and hydraulic properties. Many of the uncertainties associated with numerical fluid-flow simulations and permeability algorithms are related to input parameters directly linked to fault-zone structure. Three ways to improve understanding of fluid-flow at faults have been identified. These are; A) more clearly define and quantify hydraulic properties with fault zones, B) enhance fluid-flow models and simulation with associated sensitivity testing, and C) validate and further test models using insitu empirical fluid-flow data from fault zones (Nicol et al., 2016).

In this thesis outcrop and laboratory analysis was undertaken for six individual faults within the Mount Messenger Formation. Outcrop analysis included measuring displacement, deformation-band count, fault-rock thickness, fault-zone thickness and relative strength of host beds and fault-rock. In addition, the grain-size distributions of host-rock and fault-rock were analysed using a digital particle-sizer with supplementary thin section and SEM imaging used to examine micro-structure. All laboratory and data analysis were conducted at the University of Canterbury. Where possible biases and limitations of data collection have been minimised to increase the utility of the results. To facilitate analysis 151 samples and 2377 measurements were collected for the six faults studied.

The observations in this thesis provide insight into the variability of fault-zone architecture (e.g. fault-rock thickness, fault-zone width, deformation band count and displacement), strength properties and generation of fault rock within the north Taranaki study area. Fault-zone architecture is highly variable between faults and over small

distances (<100 mm) within individual fault zones. Grain-size reduction in sandstone-derived fault-rock (compared to the source beds) is more prominent than reductions in siltstone-derived fault-rock. Micro-fracturing is also evident within shale-smears which may play an important role in the evolution and geometries of shale smears.

The results of this thesis have implications for quantifying fault-zone architecture, fault-rock generation, and permeability predictions. Outcrop analysis shows that the structural elements of fault-zones are variable and characterising fault permeability structure challenging. Laboratory analysis suggests that cataclasis is important for generating low permeability fault rock. Cataclasis could influence fault-zone permeability in the Taranaki study area at sand on sand contacts within interbedded sequences and consideration should be given to determining under what cirucmstances cataclasis should be incorporated into fault-seal models and algorithms (i.e. when is it important to focus on cataclasis and shale smear). Sampling of fault zones and scaling of their variability has been analysed and shows that with increasing displacement the range of fault-zone and fault-rock thicknesses becomes more difficult to capture at outcrop scale. Sampling over larger fault-dip lengths is required to obtain higher quality data that represents the full range of individual elements/processes occurring within a fault zone. There remains uncertainty in the fault-sealing properties of fault-rock and how they would be affected by variations in fault-zone thickness. Fault-zone permeability has the potential to vary spatially within fault zones and using simplistic fault-seal models (e.g. SGR, CSP, and SSF) for calculating fluid flow may need to be re-examined.

6.2 Future work and recommendations

Given the time and resources constraints placed on MSc projects they are often unable to explore many facets of research related to the thesis. The present thesis is no exception and has generated as many questions as answers. Below I discuss four areas of possible future work that may help illuminate the variability of fault-zone structure and how it could influence fluid flow.

1) Some attempt has been made in this thesis to describe scaling properties of fault-rock and fault-zone thicknesses. Due to the limited scope of MSc thesis's this study focused on six faults with fault-zone properties measured over relatively short sample-line lengths along faults (<7 m). To test the results of this thesis a larger sample of faults and longer sample-line lengths are essential. A larger sample population should be used to define better the variability of fault-rock and fault-zone thicknesses. In particular, future

quantification of fault-zone structure could be used to place constraints on the spatial distribution of holes in fault rock or areas of minimum fault-rock thicknesses over fault surfaces. Sites of minimum fault-rock thickness are the points where across-fault hydrocarbon flow is most likely and may be especially important for fault-seal (or more specifically non-fault-seal).

2) This thesis highlights the importance of cataclasis in the development of low-permeability fault rock. While acknowledged in the literature as being important cataclasis is not explicitly incorporated into fault-seal algorithms. Further investigation is required to determine if the cataclasis observed in the Mount Messenger Formation significantly impacts the thickness and permeability of fault rock. Future research should include measurement of permeabilities for cataclastic fault rock and for fault-rock generated via smear of host siltstones. In addition, further work is required to determine under what geological conditions cataclasis has the potential to generate significant quantities of fault rock.

3) Shale smear has not been a significant focus of this thesis; however, it is clear from the available data that shale smear is not ubiquitous for all shale beds. This raises a number of questions that should be addressed by future research. These include; can we quantify the likelihood that individual siltstone beds will smear and what factors influence the occurrence of shale smear?

4) Based on observations in this thesis it seems that the fault-seal algorithms employed by the petroleum industry neither make it possible to predict the variations of fault-rock thickness nor are closely related to the occurrence of shale smear. Given that smear is implicit in the algorithms questions remain about their utility. Future development of these algorithms requires more data from a wide range of lithologies to test the results of this thesis.

7 REFERENCES

Allan, U. S. (1989), Model for Hydrocarbon Migration and Entrapment within Faulted Structures, AAPG Bulletin, 73(7), 803–811.

Annunziatellis, A., S. E. Beaubien, S. Bigi, G. Ciotoli, M. Coltella, and S. Lombardi (2008), Gas migration along fault systems and through the vadose zone in the Latera caldera (central Italy): Implications for CO2 geological storage, International Journal of Greenhouse Gas Control, 2(3), 353–372.

Awdal, A., D. Healy, and G. I. Alsop (2014), Geometrical analysis of deformation band lozenges and their scaling relationships to fault lenses, Journal of Structural Geology, 66, 11–23.

Aydin, A., and Y. Eyal (2002), Anatomy of a normal fault with shale smear: Implications for fault seal, AAPG Bulletin, 86(8), 1367–1381.

Aydin, A., Johnson, A.M., 1983. Analysis of faulting in porous sandstones. Journal of Structural Geology 5, 19–31.

Aydin, A., 1978. Small faults formed as deformation bands in sandstone. Pure and Applied Geophysics 116, 913–930.

Balberg, I., B. Berkowitz, and G. E. Drachsler (1991), Application of a Percolation Model to Flow in Fractured Hard Rocks, Journal of Geophysical Research-Solid Earth and Planets, 96(B6), 10015–10021.

Ballas, G., H. Fossen, and R. Soliva (2015), Factors controlling permeability of cataclastic deformation bands and faults in porous sandstone reservoirs, Journal of Structural Geology, 76, 1–21.

Barr, D. (2007), Conductive faults and sealing fractures in the West Sole gas fields, southern North Sea, in Structurally Complex Reservoirs, edited by S. J. Jolley, D. Barr, J. J. Walsh and R. J. Knipe, pp. 431–451, Geological Society, London, Special Publications,292.

Berkowitz, B., O. Bour, P. Davy, and N. Odling (2000), Scaling of fracture connectivity in geological formations, Geophysical Research Letters, 27(14), 2061–2064.

Boles, J. R., P. Eichhubl, G. Garven, and J. Chen (2004), Evolution of a hydrocarbon migration pathway along basin-bounding faults: Evidence from fault cement, AAPG Bulletin, 88(7), 947–970.

Bour, O., and P. Davy (1997), Connectivity of random fault networks following a power law fault length distribution, Water Resources Research, 33(7), 1567–1583.

Bretan, P., G. Yielding, O. M. Mathiassen, and T. Thorsnes (2011), Fault-seal analysis for CO2 storage: an example from the Troll area, Norwegian Continental Shelf, Petroleum Geoscience, 17(2), 181–192.

Browne, G.H., King, P.R., Higgs, K.E., Slatt, R.M., 2005. Grain size characteristics for distinguishing basin floor fan and slope fan depositional settings: outcrop and subsurface examples from the late Miocene Mount Messenger Formation, New Zealand. New Zealand Journal of Geology & Geophysics 48, 213-227.

Browne, G.H., Slatt, R.M. 2002. Outcrop and behind-outcrop characterization of a late Miocene slope fan system, Mt. Messenger Formation, New Zealand. American Association of Petroleum Geologists Bulletin 86, 841–862.

Browne, G. H., McAlpine, A. &King, P. R. 1996. An outcrop study of bed thickness, continuity and per- meability in reservoir facies of the Mt. Messenger Formation, North Taranaki. New Zealand Petroleum Conference Proceedings, 10-13 March 1996, Volume 1. Ministry of Economic Development, Wellington, 154–163.

Brown, A. (2003), Capillary effects on fault-fill sealing, AAPG Bulletin, 87(3), 381–395.

Caine, J. S., J. P. Evans, and C. B. Forster (1996), Fault zone architecture and permeability structure, Geology, 24(11), 1025–1028.

Canet, C., R. M. Prol-Ledesma, E. Escobar-Briones, C. Mortera-Gutierrez, R. L. S. Cruz, C. Linares, E. Cienfuegos, and P. Morales-Puente (2006), Mineralogical and geochemical characterization of hydrocarbon seep sediments from the Gulf of Mexico, Marine and Petroleum Geology, 23(5), 605–619.

Canet, C., R. M. Prol-Ledesma, P. R. Dando, V. Vazquez-Figueroa, E. Shumilin, E. Birosta, A. Sanchez, C. J. Robinson, A. Camprubi, and E. Tauler (2010),

Discovery of massive seafloor gas seepage along the Wagner Fault, northern Gulf of California, Sedimentary Geology, 228(3-4), 292–303.

Carruthers, D., and P. S. Ringrose (1998), Secondary oil migration: oil-rock contact volumes, flow behaviour and rates, in Dating and Duration of Fluid Flow and Fluid-Rock Interaction, edited by J. Parnell, pp. 205–220, Geological Society, London, Special Publication,144.

Cartwright, J., M. Huuse, and A. Aplin (2007), Seal bypass systems, AAPG Bulletin, 91(8), 1141-1166.

Cartwright, J. A., B. D. Trudgill, and C. S. Mansfield (1995), Fault Growth by Segment Linkage - an Explanation for Scatter in Maximum Displacement and Trace Length Data from the Canyonlands Grabens of Se Utah, Journal of Structural Geology, 17(9), 1319-1326.

Cashman, S., Cashman, K., 2000. Cataclasis and deformation-band formation in unconsolidated marine terrace sand, Humboldt County, California. Geology 28, 111–114.

Cavailhes, T., R. Soliva, P. Labaume, C. Wibberley, J. P. Sizun, C. Gout, D. Charpentier, A. Chauvet, B. Scalabrino, and M. Buatier (2013), Phyllosilicates formation in faults rocks: Implications for dormant fault-sealing potential and fault strength in the upper crust, Geophysical Research Letters, 40(16), 4272-4278.

Chester, F. M., and J. M. Logan (1986), Implications for Mechanical-Properties of Brittle Faults from Observations of the Punchbowl Fault Zone, California, Pure and Applied Geophysics, 124(1–2), 79–106.

Childs, C., J. Watterson, and J. J. Walsh (1996), A model for the structure and development of fault zones, Journal of the Geological Society, 153, 337–340.

Childs, C., Haughton, P.D.W., King, P.R., Manzocchi, T., Nicol, A., Schopfer, M., Strand, J., Sweeney, E., Tomasso, M., Walsh, J.J. 2005. Quantitative characteristics of Faults and fault zones and their impact on flow within deep water turbidites, onshore New Zealand. Final Client Report FIFT Consortium Project. FIFT project final report May 2005. 1 v., 5 apps

Childs, C., T. Manzocchi, J. J. Walsh, C. G. Bonson, A. Nicol, and M. P. J. Schopfer (2009), A geometric model of fault zone and fault rock thickness variations, Journal of Structural Geology, 31(2), 117–127.

Childs, C., J. J. Walsh, T. Manzocchi, J. Strand, A. Nicol, M. Tomasso, M. P. J. Schopfer, and A. Aplin (2007), Definition of a fault permeability predictor from outcrop studies of a faulted turbidite sequence, Taranaki, New Zealand, in Structurally Complex Reservoirs, edited by S. J. Jolley, D. Barr, J. J. Walsh and R. J. Knipe, pp. 235–258, Geological Society, London, Special Publication 292.

Cowie, P. A., and Scholz, C. H., 1992a, Displacement-length scaling relationship for faults: Data synthesis and discussion: Journal of Structural Geology, v. 14, p. 1149–1156.

Cox, S. F. (1999), Deformational controls on the dynamics of fluid flow in mesothermal gold systems., in Fractures, Fluid Flow and Mineralisation, edited by K. McCaffrey, L. Lonergan and J. J. Wilkinson, pp. 123–140, Geological Society, London, Special Publications,155.

Crider, J. G., and D. D. Pollard (1998), Fault Linkage: Three-dimensional mechanical interaction between echelon normal faults, Journal of Geophysical Research-Solid Earth, 103(B10), 24373–24391.

Dewhurst, D. N., and A. L. Hennig (2003), Geomechanical properties related to top seal leakage in the Carnarvon Basin, Northwest Shelf, Australia, Petroleum Geoscience, 9(3), 255–263.

Dockrill, B., and Z. K. Shipton (2010), Structural controls on leakage from a natural CO2 geologic storage site: Central Utah, U.S.A, Journal of Structural Geology, 32(11), 1768–1782.

Edlmann, K., S. Haszeldine, and C. I. McDermott (2013), Experimental investigation into the sealing capability of naturally fractured shale caprocks to supercritical carbon dioxide flow, Environmental Earth Sciences, 70(7), 3393–3409.

Eichhubl, P., N. C. Davatzes, and S. P. Becker (2009), Structural and diagenetic control of fluid migration and cementation along the Moab fault, Utah, AAPG Bulletin, 93(5), 653-681.

Eichhubl, P., P. S. D'Onfro, A. Aydin, A. Waters, and D. K. McCarty (2005), Structure, petrophysics, and diagenesis of shale entrained along a normal fault at Black Diamond Mines, California - Implications for fault seal, AAPG Bulletin, 89(9), 1113–1137.

Evans, J. P., C. B. Forster, and J. V. Goddard (1997), Permeability of fault-related rocks, and implications for hydraulic structure of fault zones, Journal of Structural Geology, 19(11), 1393–1404.

Faulkner, D. R., A. C. Lewis, and E. H. Rutter (2003), On the internal structure and mechanics of large strike-slip fault zones: field observations of the Carboneras fault in southeastem Spain, Tectonophysics, 367(3-4), 235–251.

Faulkner, D. R., C. A. L. Jackson, R. J. Lunn, R. W. Schlische, Z. K. Shipton, C. A. J. Wibberley, and M. O. Withjack (2010), A review of recent developments concerning the structure, mechanics and fluid flow properties of fault zones, Journal of Structural Geology, 32(11), 1557–1575.

Ferrill, D. A., and A. P. Morris (2003), Dilational normal faults, Journal of Structural Geology, 25(2), 183–196.

Ferrill, D. A., and A. P. Morris (2008), Fault zone deformation controlled by carbonate mechanical stratigraphy, Balcones fault system, Texas, AAPG Bulletin, 92(3), 359–380.

Ferrill, D. A., A. P. Morris, R. N. McGinnis, K. J. Smart, and W. C. Ward (2011), Fault zone deformation and displacement partitioning in mechanically layered carbonates: The Hidden Valley fault, central Texas, AAPG Bulletin, 95(8), 1383–1397.

Fisher, Q. J., and R. J. Knipe (2001), The permeability of faults within siliciclastic petroleum reservoirs of the North Sea and Norwegian Continental Shelf, Marine and Petroleum Geology, 18(10), 1063–1081.

Fisher, Q. J., M. Casey, S. D. Harris, and R. J. Knipe (2003), Fluid-flow properties of faults in sandstone: The importance of temperature history, Geology, 31(11), 965–968.

Fossen, H., Schultz, R. A., Shipton, Z. K., & Mair, K. (2007). Deformation Bands in Sandstone: A Review. Journal of the Geological Society, London, 755-769.

Gartrell, A., Y. H. Zhang, M. Lisk, and D. Dewhurst (2004), Fault intersections as critical hydrocarbon leakage zones: integrated field study and numerical modelling of an example from the Timor Sea, Australia, Marine and Petroleum Geology, 21(9), 1165–1179.

Giba, M., J. J. Walsh, and A. Nicol (2012), Segmentation and growth of an obliquely reactivated normal fault, Journal of Structural Geology, 39, 253–267.

Giba, M., Nicol, A., Walsh, J. J. (2010), Evolution of faulting and volcanism in backarc basin and its implications for subduction processes. Tectonics 29, TC4020, doi:10.1029/2009TC002634,2010.

Gross, M. R. (1995), Fracture Partitioning - Failure Mode as a Function of Lithology in the Monterey Formation of Coastal California, Geological Society of America Bulletin, 107(7), 779–792.

Gross, M. R., G. GutierrezAlonso, T. X. Bai, M. A. Wacker, K. B. Collinsworth, and R. J. Behl (1997), Influence of mechanical stratigraphy and kinematics on fault scaling relations, Journal of Structural Geology, 19(2), 171–183.

Hermanrud, C., M. E. Halkjelsvik, K. Kristiansen, A. Bernal, and A. C. Strömbäck (2014), Petroleum column-height controls in the western Hammerfest Basin, Barents Sea, Petroleum Geoscience, 20(3), 227–240.

Hooper, E. C. D. (1991), Fluid Migration Along Growth Faults in Compacting Sediments, Journal of Petroleum Geology, 14(2), 161–180.

Ilg, B. R., S. Hemmings-Sykes, A. Nicol, J. Baur, M. Fohrmann, R. Funnell, and M. Milner (2012), Normal faults and gas migration in an active plate boundary, southern Taranaki Basin, offshore New Zealand, AAPG Bulletin, 96(9), 1733–1756.

Ingebritsen, S. E., and C. E. Manning (2010), Permeability of the continental crust: dynamic variations inferred from seismicity and metamorphism, Geofluids, 10(1-2), 193–205.

Ishii, E., H. Funaki, T. Tokiwa, and K. Ota (2010), Relationship between fault growth mechanism and permeability variations with depth of siliceous siltstones in northern Hokkaido, Japan, Journal of Structural Geology, 32(11), 1792–1805.

ISO. (2009). Soil quality — Determination of particle size distribution in mineral soil material — Method by sieving and sedimentation. International Organization for Standardization.

James, W. R., L. H. Fairchild, G. P. Nakayama, S. J. Hippler, and P. J. Vrolijk (2004), Fault-seal analysis using a stochastic multifault approach, AAPG Bulletin, 88(7), 885–904.

Jennings, J. B. (1987), Capillary-Pressure Techniques - Application to Exploration and Development Geology, AAPG Bulletin, 71(10), 1196–1209.

King, P. R., Scott, G. H., & Robinson, P. H. (1993). Description, correlation and depositional history of Miocene sediments outcropping along the north Taranaki coast. Institute of Geological and Nuclear Sciences Monograph, Wellington, 5.

King, P. R., & Thrasher, G. P. (1996). Cretaceous– Cenozoic geology and petroleum systems of the Taranaki Basin, New Zealand. Institute of Geological and Nuclear Sciences Monograph, 13.

Kristensen, M.B., Childs, C., Olesen, N.Ø., Korstgård, J.A., 2013. The microstructure and internal architecture of shear bands in sand-clay sequences. Journal of Structural Geology 46, 129-141.

Laubach, S. E., P. Eichhubl, P. Hargrove, M. A. Ellis, and J. N. Hooker (2014), Fault core and damage zone fracture attributes vary along strike owing to interaction of fracture growth, quartz accumulation, and differing sandstone composition, Journal of Structural Geology, 68, 207–226.

Leclère, H., F. Cappa, D. Faulkner, O. Fabbri, P. Armitage, and O. Blake (2015), Development and maintenance of fluid overpressures in crustal fault zones by elastic compaction and implications for earthquake swarms, Journal of Geophysical Research-Solid Earth, 120(6), 4450–4473.

Lehner, F., and W. Pilaar (1997), The emplacement of clay smears in syn-sedimentary normal faults: inference from field observations near Frechen, Germany, in Hydrocarbon Seals: Importance for Exploration and Production, edited by P. Moller-Pederson and A. G. Koestler, pp. 39–50, Norwegian Petroleum Society (NSF) Special Publication,7.

Lindsay, N. G., F. C. Murphy, J. J. Walsh, and J. Watterson (1993), Outcrop studies of shale smears on fault surfaces, in The Geological Modelling of Hydrocarbon Reservoirs and Outcrop Analogues, edited by S. S. Flint and I. D. Bryant, pp. 113–123, Special Publication of the International Association of Sedimentologists,15.

LTI. (2017). Metallurgical Sample Preparation: Microscopy and SEM Sample Preparation. Retrieved from Laboratory Testing Inc:

https://www.labtesting.com/services/materials-testing/metallurgical-testing/sample-preparation/

Lunn, R. J., J. P. Willson, Z. K. Shipton, and H. Moir (2008), Simulating brittle fault growth from linkage of preexisting structures, Journal of Geophysical Research-Solid Earth, 113(B7).

Manzocchi, T., C. Childs, and J. J. Walsh (2010), Faults and fault properties in hydrocarbon flow models, Geofluids, 10(1-2), 94–113.

Manzocchi, T., J. J. Walsh, P. Nell, and G. Yielding (1999), Fault transmissibility multipliers for flow simulation models, Petroleum Geoscience, 5(1), 53–63.

Micarelli, L., A. Benedicto, C. Invernizzi, B. Saint-Bezar, J. L. Michelot, and P. Vergely (2005), Influence of P/T conditions on the style of normal fault initiation and growth in limestones from the SE-Basin, France, Journal of Structural Geology, 27(9), 1577–1598.

Michie, E. A. H., T. J. Haines, D. Healy, J. E. Neilson, N. E. Timms, and C. A. J. Wibberley (2014), Influence of carbonate facies on fault zone architecture, Journal of Structural Geology, 65, 82–99.

Micromeritics. (2017). Saturn DigiSizer II. Retrieved from Micromeritics Product Showcase:http://www.micromeritics.com/Product-Showcase/Saturn-DigiSizer-II.aspx

Miller, S. A., C. Collettini, L. Chiaraluce, M. Cocco, M. Barchi, and B. J. P. Kaus (2004), Aftershocks driven by a high-pressure CO2 source at depth, Nature, 427(6976), 724–727.

Morris, A., D. A. Ferrill, and D. B. Henderson (1996), Slip-tendency analysis and fault reactivation, Geology, 24(3), 275–278.

Morrow, C. A., D. A. Lockner, D. E. Moore, and S. Hickman (2014), Deep permeability of the San Andreas Fault from San Andreas Fault Observatory at Depth (SAFOD) core samples, Journal of Structural Geology, 64, 99–114.

Nicol, A., J. Watterson, J. J. Walsh, and C. Childs (1996), The shapes, major axis orientations and displacement patterns of fault surfaces, Journal of Structural Geology, 18(2–3), 235–248.

Nicol, A., C. Childs, J. J. Walsh, and K. W. Schafer (2013), A geometric model for the formation of deformation band clusters, Journal of Structural Geology, 55, 21–33.

Nicol A.; Seebeck H.; Field B.; McNamara D. 2016. Fault Permeability Study IEA/CON/15/230, GNS Science Consultancy Report 2015/206. 135 p.

Noorsalehi-Garakani, S., G. J. K. Vennekate, P. Vrolijk, and J. L. Urai (2013), Clay-smear continuity and normal fault zone geometry - First results from excavated sandbox models, Journal of Structural Geology, 57, 58–80.

O'Brien, G. W., M. Lisk, I. R. Duddy, J. Hamilton, P. Woods, and R. Cowley (1999), Plate convergence, foreland development and fault reactivation: primary controls on brine migration, thermal histories and trap breach in the Timor Sea, Australia, Marine and Petroleum Geology, 16(6), 533–560.

Obeahon, P. P., G. Ypma, and U. O. Onyeagoro (2014), Dynamic Fault Seal Breakdown Investigation -A Study of Egret Field in the North Sea, paper presented at SPE Annual Technical Conference and Exhibition, Society of Petroleum Engineers, Amsterdam, 27–29 October.

Odling, N. E., et al. (1999), Variations in fracture system geometry and their implications for fluid flow in fractured hydrocarbon reservoirs, Petroleum Geoscience, 5(4), 373–384.

Ohman, J., A. Niemi, and C. F. Tsang (2005), Probabilistic estimation of fracture transmissivity from Wellbore hydraulic data accounting for depth-dependent anisotropic rock stress, International Journal of Rock Mechanics and Mining Sciences, 42(5-6), 793–804.

Patton, T. L., J. M. Logan, and M. Friedman (1998), Experimentally generated normal faults in single-layer and multilayer limestone specimens at confining pressure, Tectonophysics, 295(1-2), 53–77.

Peacock, D. C. P. (2002), Propagation, interaction and linkage in normal fault systems, Earth-Science Reviews, 58(1-2), 121–142.

Peacock, D. C. P., and D. J. Sanderson (1991), Displacements, Segment Linkage and Relay Ramps in Normal-Fault Zones, Journal of Structural Geology, 13(6), 721–&.

Peacock, D. C. P., and X. Zhang (1994), Field Examples and Numerical Modeling of Oversteps and Bends Along Normal Faults in Cross-Section, Tectonophysics, 234(1-2), 147–167.

Philip, Z. G., J. W. Jennings, J. E. Olson, S. E. Laubach, and J. Holder (2005), Modeling coupled fracture-matrix fluid flow in geomechanically simulated fracture networks, Spe Reservoir Evaluation & Engineering, 8(4), 300–309.

Power, W. L., T. E. Tullis, and J. D. Weeks (1988), Roughness and Wear during Brittle Faulting, Journal of Geophysical Research-Solid Earth and Planets, 93(B12), 15268–15278.

Roche, V., C. Homberg, and M. Rocher (2012), Architecture and growth of normal fault zones in multilayer systems: A 3D field analysis in the South-Eastern Basin, France, Journal of Structural Geology, 37, 19–35.

Rowland, J. V., and S. F. Simmons (2012), Hydrologic, Magmatic, and Tectonic Controls on Hydrothermal Flow, Taupo Volcanic Zone, New Zealand: Implications for the Formation of Epithermal Vein Deposits, Economic Geology, 107(3), 427–457.

Ryzak, M., & Bieganowski, A. (2011). Methodological Aspects of Determining Soil Particle Size Distribution using the Laser Diffraction Method. Journal of Plant Nutrition, 624-633.

Sager, W. W., I. R. MacDonald, and R. S. Hou (2004), Side-scan sonar imaging of hydrocarbon seeps on the Louisiana continental slope, AAPG Bulletin, 88(6), 725–746.

Sanderson, D. J., and X. Zhang (1999), Critical stress localization of flow associated with deformation of well-fractured rock masses, with implications for mineral deposits, in Fractures, Fluid Flow and Mineralization, edited by K. McCaffrey, L. Lonergan and J. J. Wilkinson, pp. 69–81, Geological Society, London, Special Publications,155.

Scholz, C. H. (1987), Wear and Gouge Formation in Brittle Faulting, Geology, 15(6), 493–495.

Schöpfer, M. P. J., C. Childs, and J. J. Walsh (2006), Localisation of normal faults in multilayer sequences, Journal of Structural Geology, 28(5), 816–833.

Schöpfer, M. P. J., C. Childs, and J. J. Walsh (2007), Two-dimensional distinct element modeling of the structure and growth of normal faults in multilayer sequences: 2. Impact of confining pressure and strength contrast on fault zone geometry and growth, Journal of Geophysical Research-Solid Earth, 112(B10).

Seebeck, H., A. Nicol, J. J. Walsh, C. Childs, R. D. Beetham, and J. Pettinga (2014), Fluid flow in fault zones from an active rift, Journal of Structural Geology, 62, 52–64.

Segall, P., and D. D. Pollard (1980), Mechanics of Discontinuous Faults, Journal of Geophysical Research, 85(Nb8), 4337–4350.

Shipton, Z. K., and P. A. Cowie (2001), Damage zone and slip-surface evolution over mu m to km scales in high-porosity Navajo sandstone, Utah, Journal of Structural Geology, 23(12), 1825–1844.

Shipton, Z. K., A. M. Soden, J. D. Kirkpatrick, A. M. Bright, and R. J. Lunn (2006), How thick is a fault? Fault displacement-thickness scaling revisited, Earthquakes: Radiated Energy and the Physics of Faulting, 170, 193–198.

Sibson, R. H. (1996), Structural permeability of fluid-driven fault-fracture meshes, Journal of Structural Geology, 18(8), 1031–1042.

Sibson, R. H. (1998), Brittle failure mode plots for compressional and extensional tectonic regimes, Journal of Structural Geology, 20(5), 655–660.

Soden, A. M., and Z. K. Shipton (2013), Dilational fault zone architecture in a welded ignimbrite: The importance of mechanical stratigraphy, Journal of Structural Geology, 51, 156–166.

Soliva, R., and A. Benedicto (2005), Geometry, scaling relations and spacing of vertically restricted normal faults, Journal of Structural Geology, 27(2), 317–325.

Sperrevik, S., P. A. Gillespie, Q. J. Fisher, T. Halvorsen, and R. J. Knipe (2002), Empirical estimation of fault rock properties, in Hydrocarbon Seal Quantification, edited by A. G. Koestler and R. Hunsdale, pp. 109–126, Norwegian Petroleum Society (NPF) Special Publication,11.

Stauffer, D. (1987), Introduction to Percolation Theory, Taylor and Francis Ltd, London.

Tanikawa, W., M. Sakaguchi, T. Hirono, W. Lin, W. Soh, and S. R. Song (2009), Transport properties and dynamic processes in a fault zone from samples

recovered from TCDP Hole B of the Taiwan Chelungpu Fault Drilling Project, Geochemistry Geophysics Geosystems, 10.

Tsang, C. F., and I. Neretnieks (1998), Flow channeling in heterogeneous fractured rocks, Reviews of Geophysics, 36(2), 275–298.

Tsang, C. F., J. Rutqvist, and K. B. Min (2007), Fractured rock hydromechanics: from borehole testing to solute transport and CO(2) storage, Rock Physics and Geomechanics in the Study of Reservoirs and Repositories, 284, 15–34.

van der Zee, W., and J. L. Urai (2005), Processes of normal fault evolution in a siliciclastic sequence: a case study from Miri, Sarawak, Malaysia, Journal of Structural Geology, 27(12), 2281–2300.

Van Hulten, F. F. N. (2010), Geological factors effecting compartmentalization of Rotliegend gas fields in the Netherlands, in Reservoir Compartmentalization, edited by S. J. Jolley, Q. J. Fisher, R. B. Ainsworth, P. J. Vrolijk and S. Delisle, pp. 301–315, Geological Society, London, Special Publications,347.

Vrolijk, P. J., R. Skelly, S. E. Bradley, A. C. Ostridge, N. MacCallum , and J. Wood (2012), Methods to Evaluate and Predict the Effects of Extreme Reservoir Compartmentalization, BNA Reservoir, Canada, in 3rd EAGE International Conference on Fault and Top Seals edited, Montpellier, France

Wade, A. (1913), The natural history of petroleum, Proceedings of the Geologists' Association, 24(1), 1–13.

Wallace, R. E., and H. T. Morris (1986), Characteristics of faults and shear zones in deep mines, Pure & Applied Geophysics, 124(1/2), 105–125.

Walsh, J., J. Watterson, and G. Yielding (1991), The Importance of Small-Scale Faulting in Regional Extension, Nature, 351(6325), 391–393.

Walsh, J. J., W. R. Bailey, C. Childs, A. Nicol, and C. G. Bonson (2003), Formation of segmented normal faults: a 3-D perspective, Journal of Structural Geology, 25(8), 1251–1262.

Wei, Z. Q., P. Egger, and F. Descoeudres (1995), Permeability Predictions for Jointed Rock Masses, International Journal of Rock Mechanics and Mining Sciences & Geomechanics Abstracts, 32(3), 251–261.

Wibberley, C. A. J., and T. Shimamoto (2003), Internal structure and permeability of major strike-slip fault zones: the Median Tectonic Line in Mie Prefecture, Southwest Japan, Journal of Structural Geology, 25(1), 59–78.

Wibberley, C. A. J., G. Yielding, and G. Di Toro (2008), Recent advances in the understanding of fault zone internal structure: a review, in The Internal Structure of Fault Zones: Implications for Mechanical and Fluid Flow Properties, edited by C. A. J. Wibberley, W. Kurtz, J. Imber, R. E. Holdsworth and C. Collettini, pp. 5–33, Geological Society, London, Special Publications,299.

Wilkins, S. J., and M. R. Gross (2002), Normal fault growth in layered rocks at Split Mountain, Utah: influence of mechanical stratigraphy on dip linkage, fault restriction and fault scaling, Journal of Structural Geology, 24(9), 1413–1429.

Wilson, J. E., J. S. Chester, and F. M. Chester (2003), Microfracture analysis of fault growth and wear processes, Punchbowl Fault, San Andreas System, California, Journal of Structural Geology, 25(11), 1855–1873.

Yielding, G. (1992), The prediction of small-scale faulting in reservoirs, First Break, 10, 449–460.

Yielding, G. (2002), Shale Gouge Ratio — calibration by geohistory, in Hydrocarbon Seal Quantification, edited by A. G. Koestler and R. Hunsdale, pp. 1–15, Norwegian Petroleum Society (NSF) Special Publications,11.

Yielding, G. (2012), Using probabilistic shale smear modelling to relate SGR predictions of column height to fault-zone heterogeneity, Petroleum Geoscience, 18(1), 33–42.

Yielding, G., B. Freeman, and D. T. Needham (1997), Quantitative fault seal prediction, AAPG Bulletin, 81(6), 897-917.

Yielding, G., P. Bretan, and B. Freeman (2010), Fault seal calibration: a brief review, in Reservoir Compartmentalization, edited by S. J. Jolley, Q. J. Fisher, R. B. Ainsworth, P. J. Vrolijk and S. Delisle, pp. 243–255, Geological Society, London, Special Publications,347.

Zhang, X., and D. J. Sanderson (1998), Numerical study of critical behaviour of deformation and permeability of fractured rock masses, Marine and Petroleum Geology, 15(6), 535–548.

8 APPENDICES

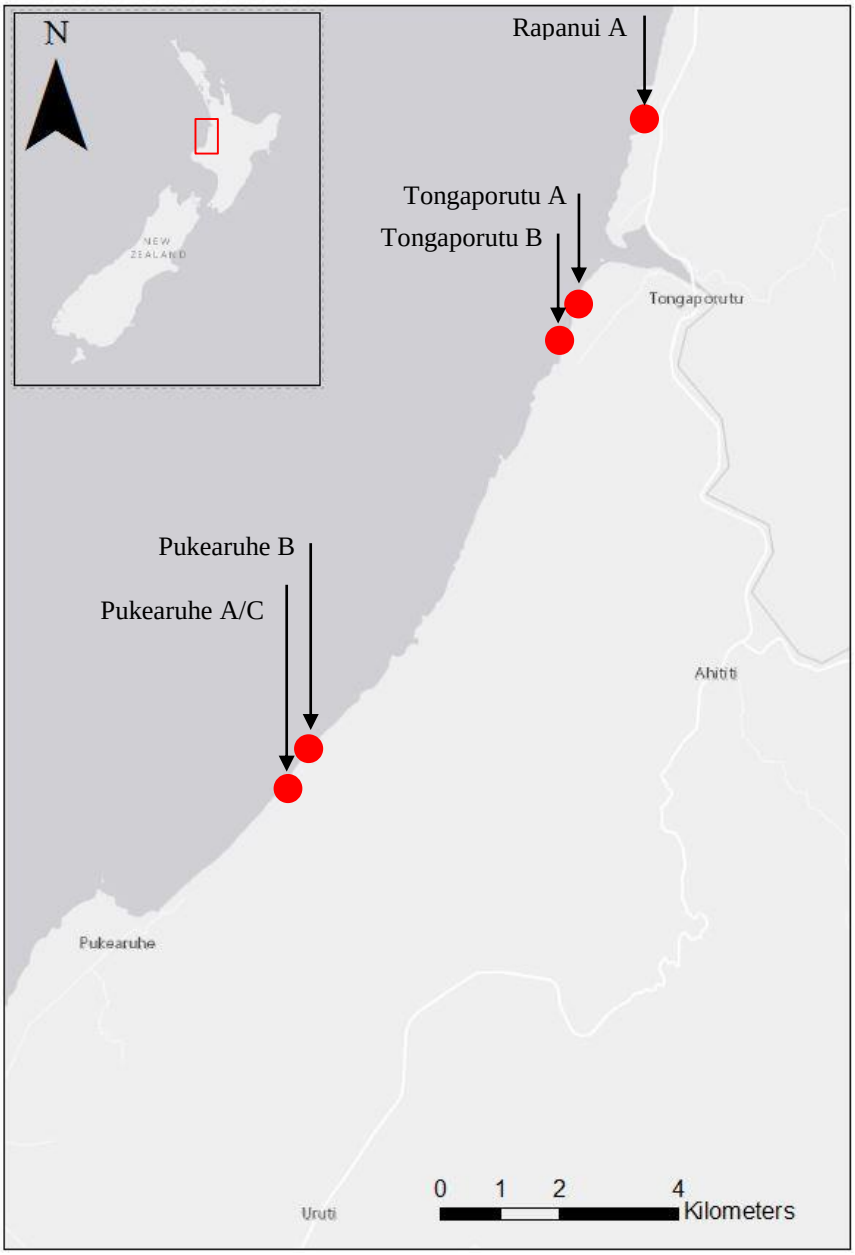

Figure 58: Map showing locations of individual faults sampled for this study along the coast of northern Taranaki. Insert map shows the study area location on the West Coast of the North Island, New Zealand.

TABLE 9: SUMMARY OF NORMALIZED FAULT ROCK THICKNESS SPREAD FOR EACH SAMPLED FAULT FOR THIS STUDY.

Fault Name	Original Spread (%)	Length of Fault (m)	Normalized Spread per m (%)
Rapanui A	91.8%	6.8	13.5%
Pukearuhe A	57.5%	3.6	16.0%
Pukearuhe B	28.8%	3.05	9.4%
Pukearuhe C	27.5%	4.45	6.2%
Tongaporutu A	20.0%	3.4	5.9%
Tongaporutu B	60.1%	2.65	22.7%

TABLE 10: SUMMARY OF NORMALIZED FAULT ROCK THICKNESS SPREAD FOR EACH SAMPLED FAULT FOR THIS STUDY.

Fault Name	Original Spread (%)	Length of Fault (m)	Normalized Spread per m (%)
Rapanui A	7.3%	6.8	1.1%
Pukearuhe A	5.5%	3.6	1.5%
Pukearuhe B	2.0%	3.05	0.6%
Pukearuhe C	2.2%	4.45	0.5%
Tongaporutu A	3.1%	3.4	0.9%
Tongaporutu B	38.3%	2.65	14.5%

TABLE 11: SUMMARY OF CALCULATED FAULT LENGTHS AND SAMPLE PORTIONS FOR EACH FAULT SAMPLED FOR THIS STUDY ORDERED FROM MINIMUM TO MAXIMUM DISPLACEMENT.

Fault	Fault Sample Length (m)	Max Displacement (m)	Observed Fault Length (m)	Calculated Fault Length (m)	Sample Portion (%)
Tongaporutu B	2.65	0.005	3	3.29	80.4%
Rapanui A	6.8	0.026	8	11.17	60.9%
Pukearuhe A	3.6	0.13	10+	36.80	9.8%
Tongaporutu A	3.4	0.16	10+	42.92	7.9%
Pukearuhe C	4.45	0.165	10+	43.91	10.1%
Pukearuhe B	3.05	0.29	10+	66.68	4.6%

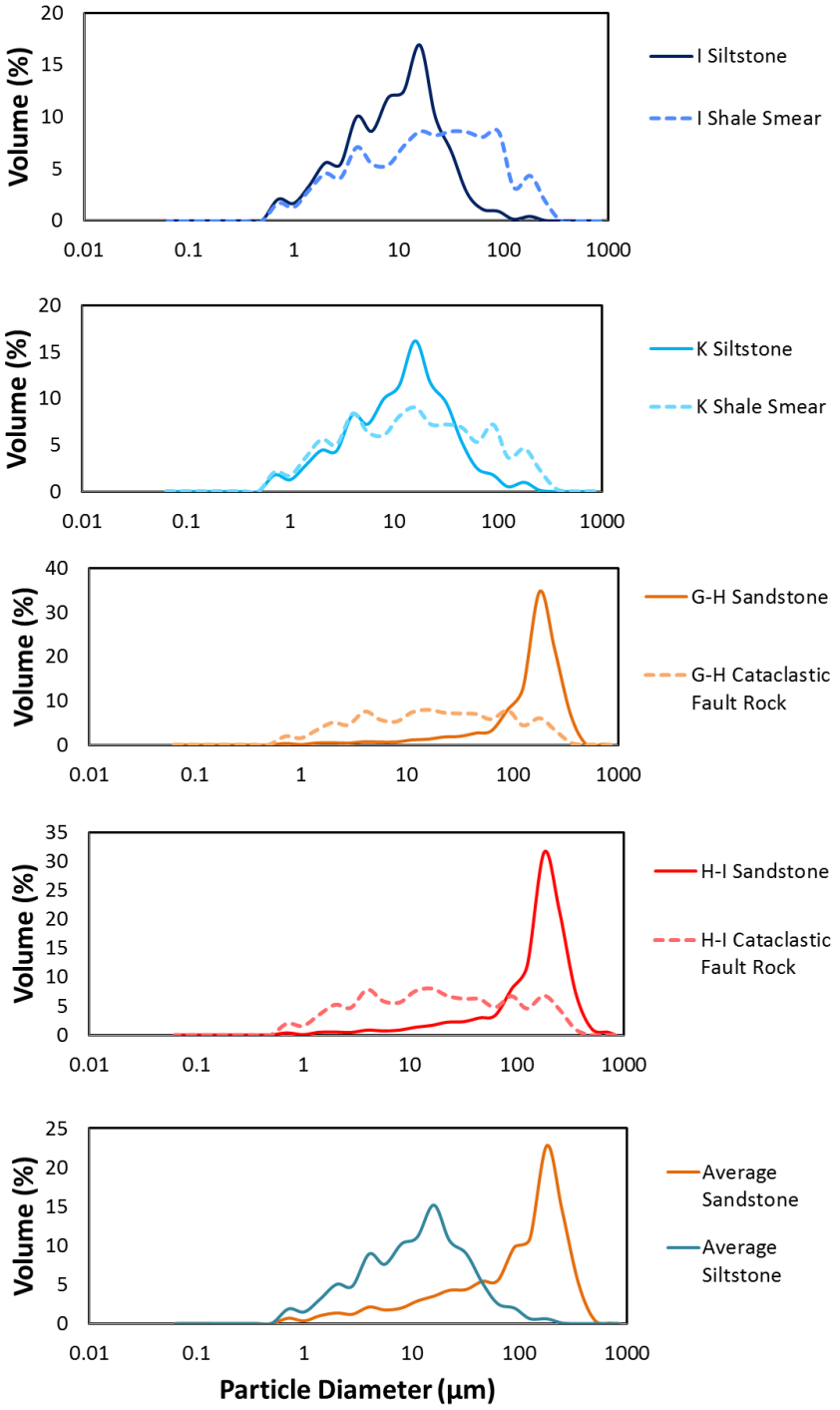

FIGURE 59: GRAPHS SHOWING GRAIN-SIZE DISTRIBUTION OF HOST ROCK AND FAULT ROCK SAMPLES TAKEN FROM RAPANUI A.

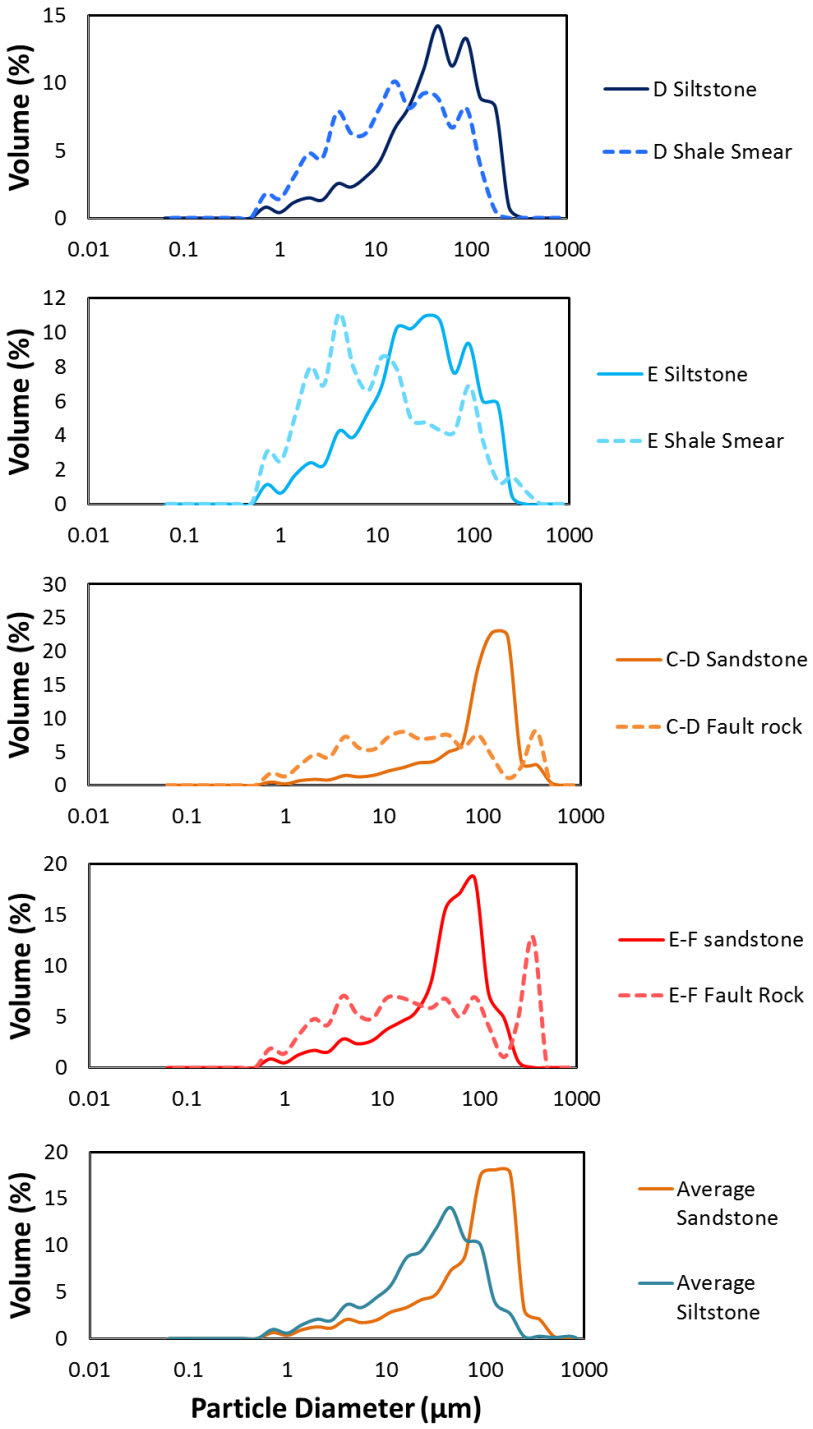

FIGURE 60: GRAPHS SHOWING GRAIN-SIZE DISTRIBUTION OF HOST ROCK AND FAULT ROCK SAMPLES TAKEN FROM PUKEARUHE A.

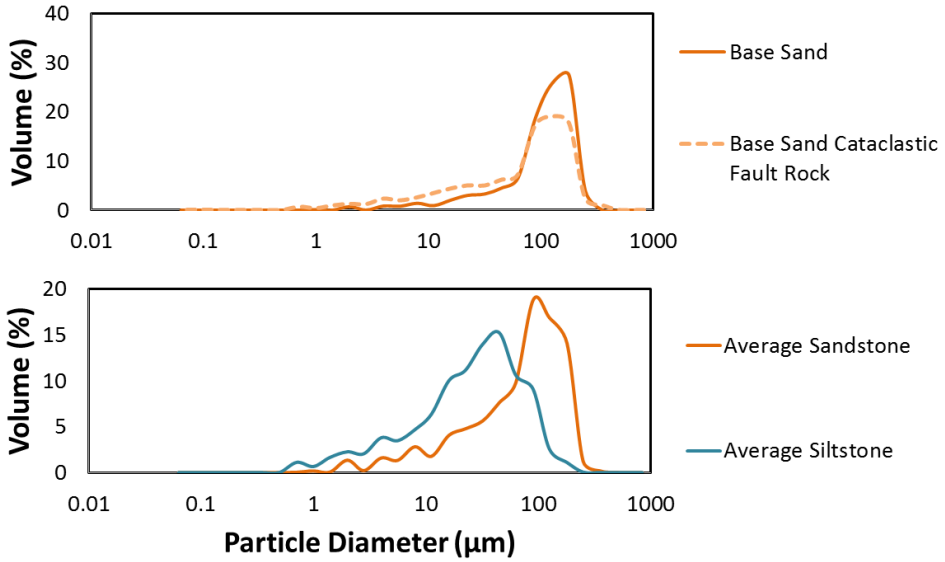

FIGURE 61: GRAPHS SHOWING GRAIN-SIZE DISTRIBUTION OF HOST ROCK AND FAULT ROCK SAMPLES TAKEN FROM PUKEARUHE B.

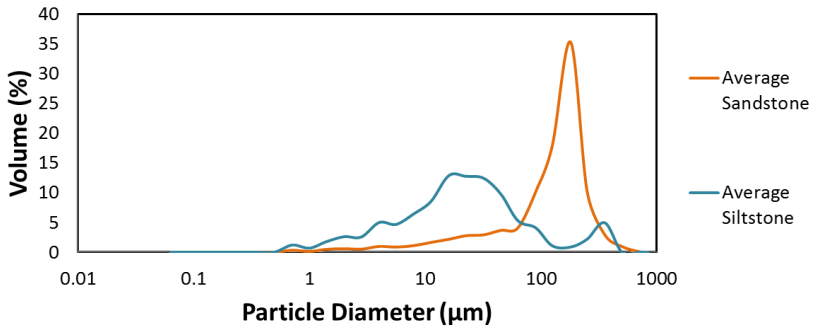

FIGURE 62: GRAPH SHOWING AVERAGE GRAIN-SIZE DISTRIBUTION OF HOST ROCK SAMPLES TAKEN FROM TONGAPORUTU B.

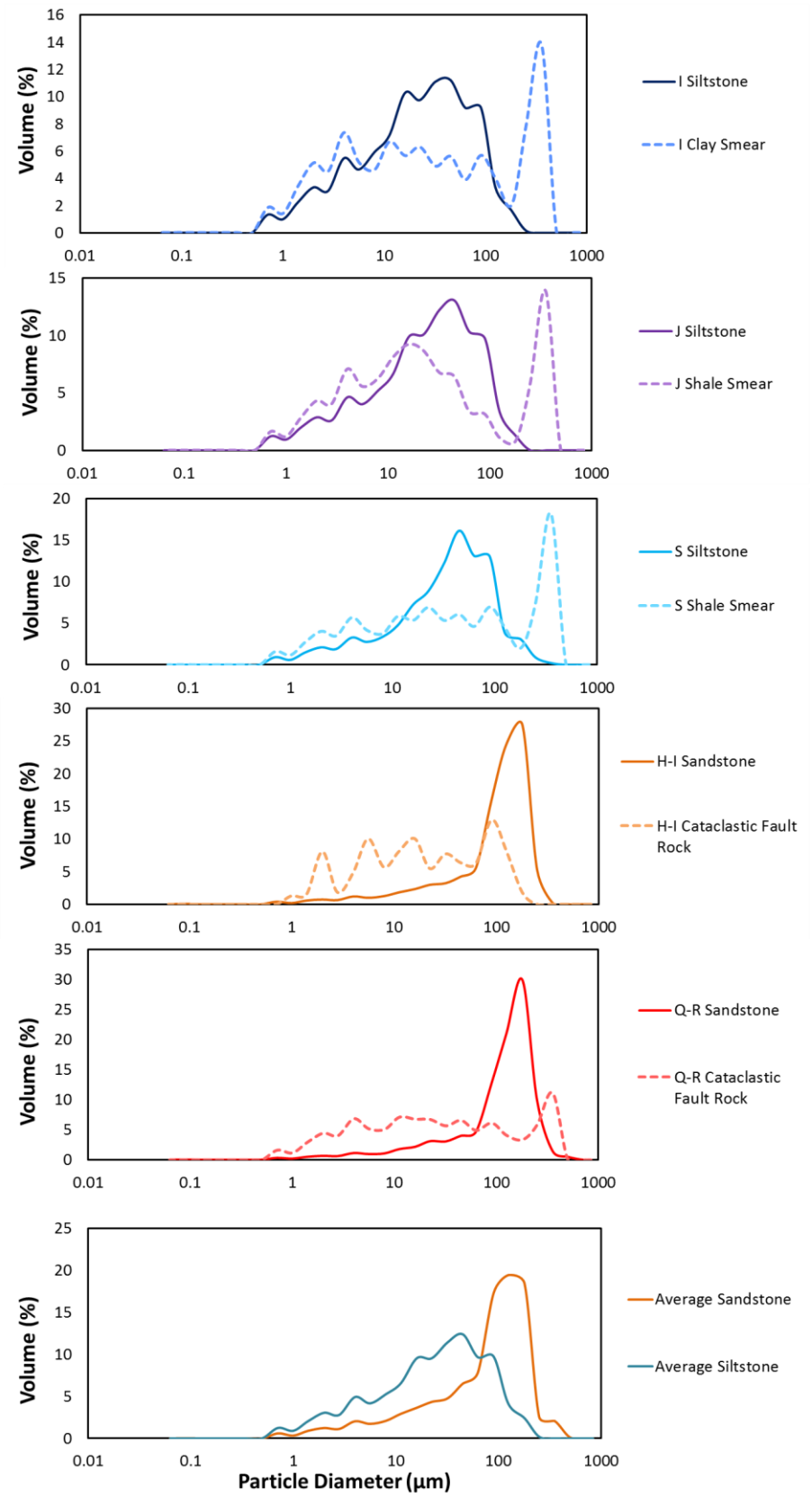

FIGURE 63: GRAPHS SHOWING GRAIN-SIZE DISTRIBUTION OF HOST ROCK AND FAULT ROCK SAMPLES TAKEN FROM PUKEARUHE C.

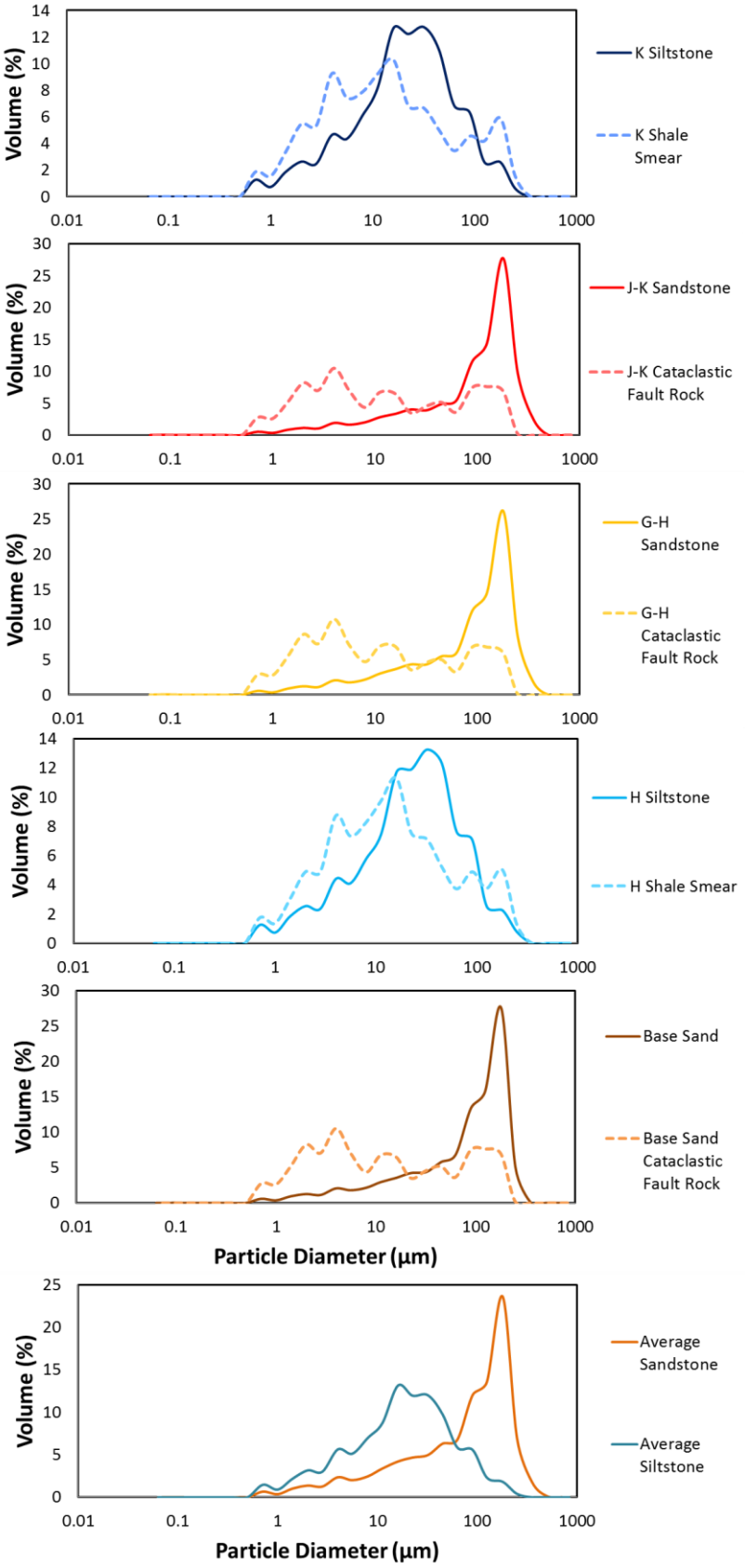

FIGURE 64: GRAPHS SHOWING GRAIN-SIZE DISTRIBUTION OF HOST ROCK AND FAULT ROCK SAMPLES TAKEN FROM TONGAPORUTU A.

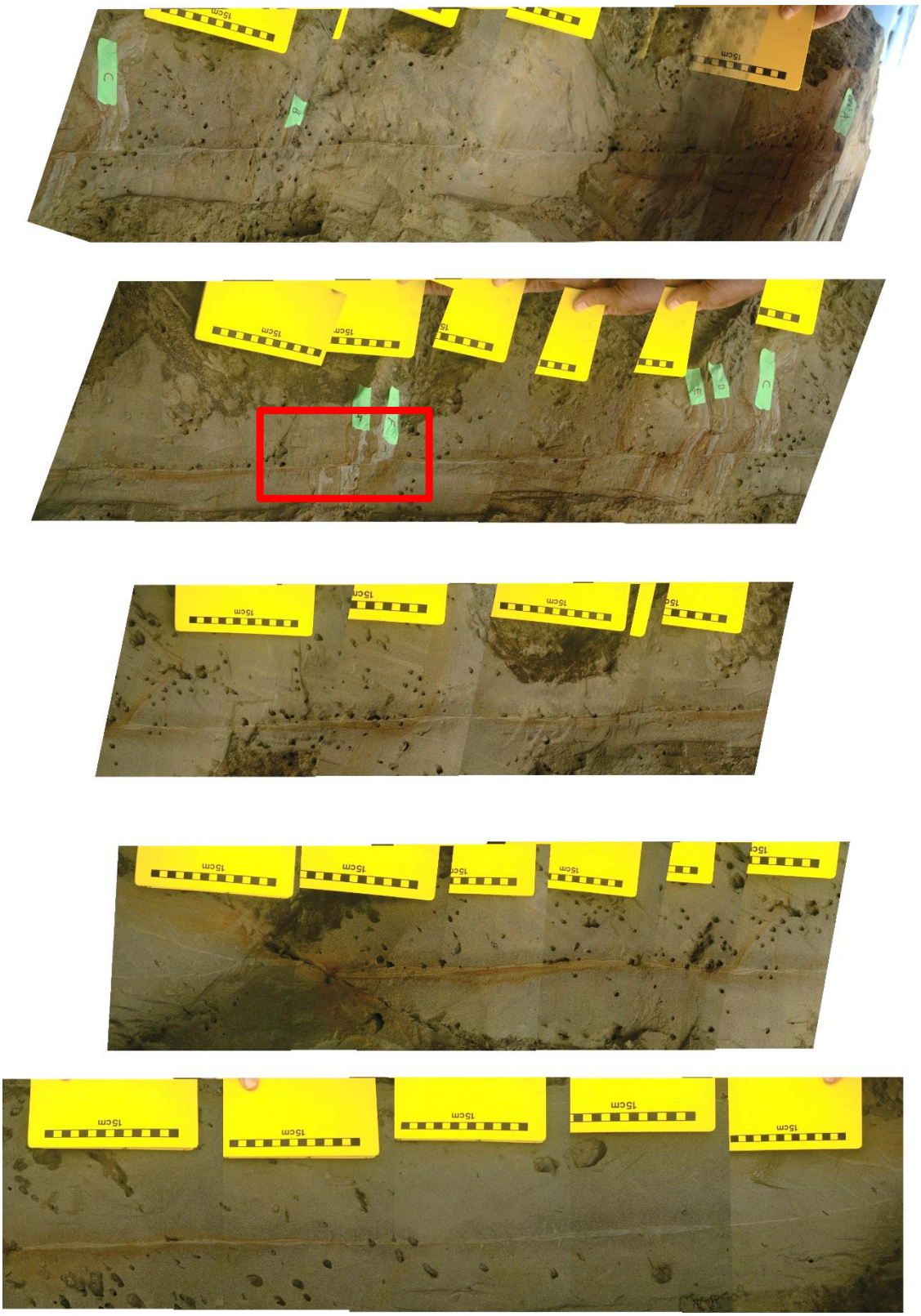

FIGURE 65: STACKED PHOTOGRAPHS OF RAPANUI A FAULT FROM TOP (TOP LEFT) TO BASE (BOTTOM RIGHT; CONTINUED ON NEXT PAGE)

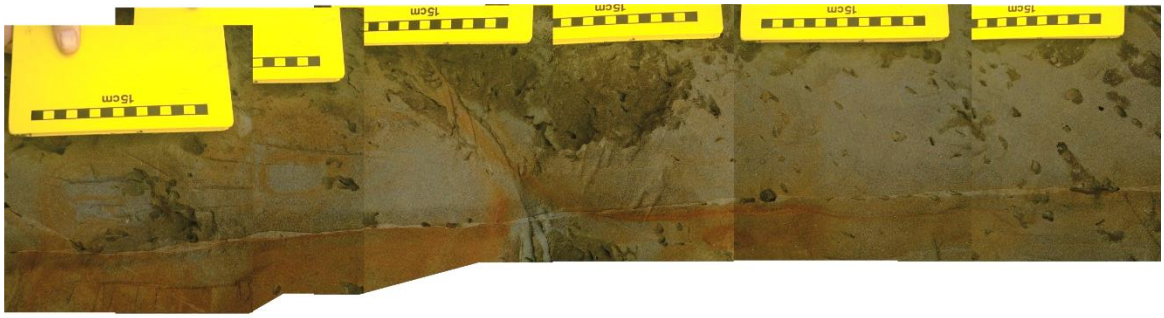
15cm


15cm
H

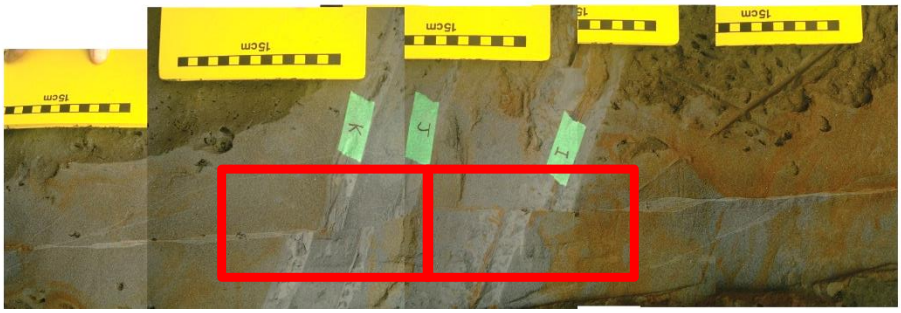
15cm
K
J
I

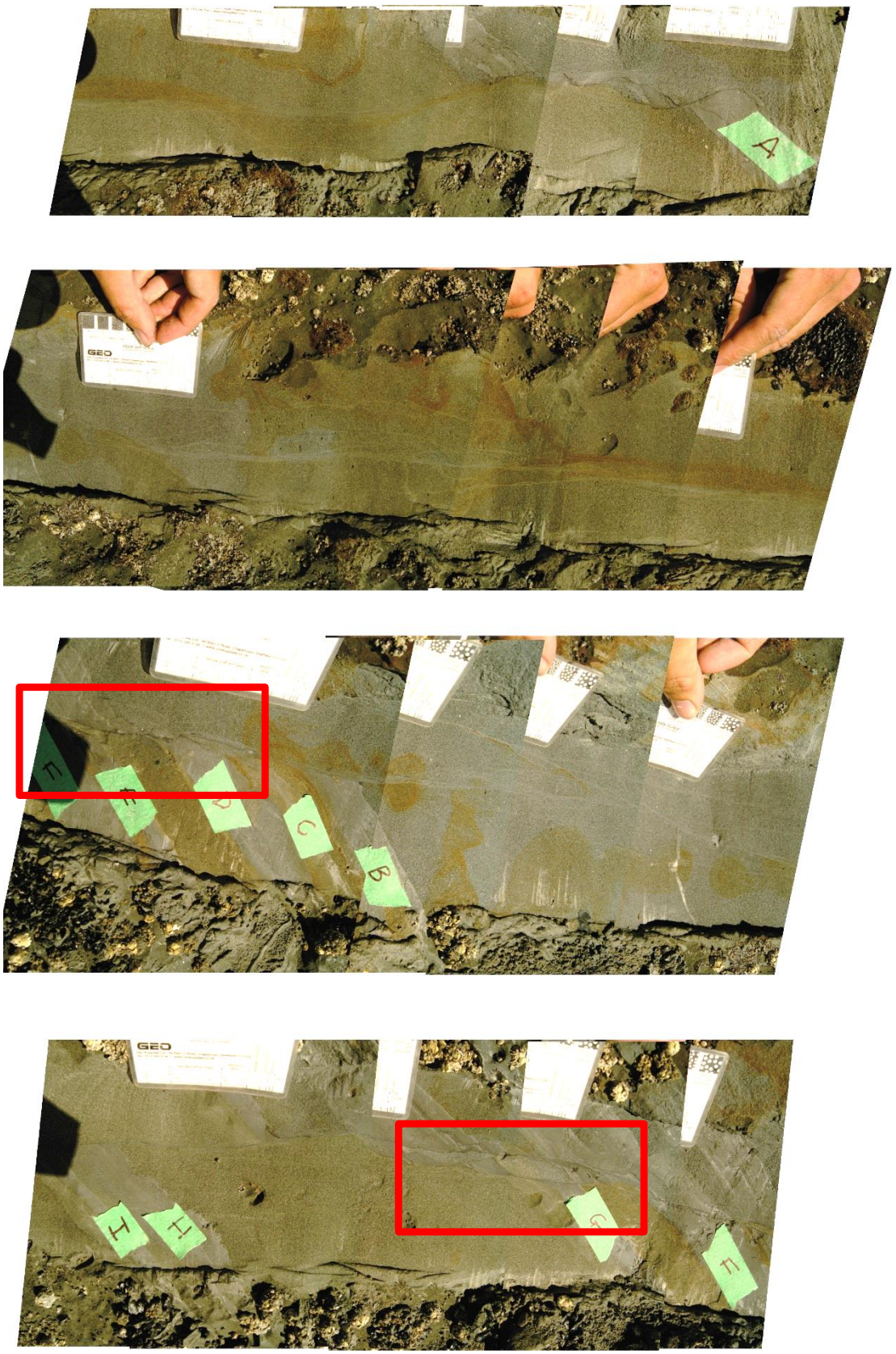

FIGURE 66: STACKED PHOTOGRAPHS SHOWING TONGAPORUTU A FAULT FROM TOP (TOP LEFT) TO BASE (BOTTOM RIGHT: CONTINUED ON NEXT PAGE).


GEO
1

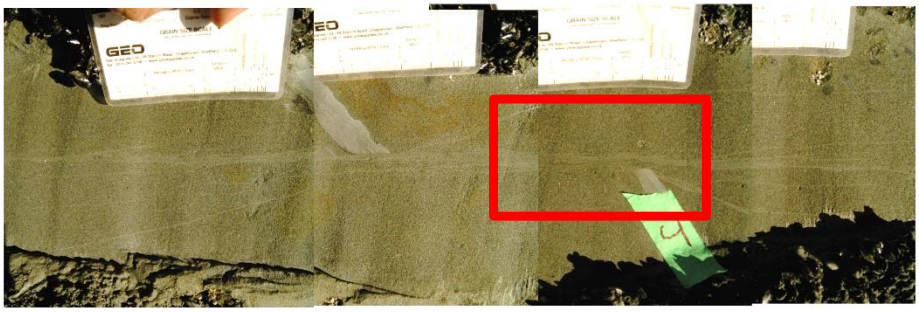
GEO
3

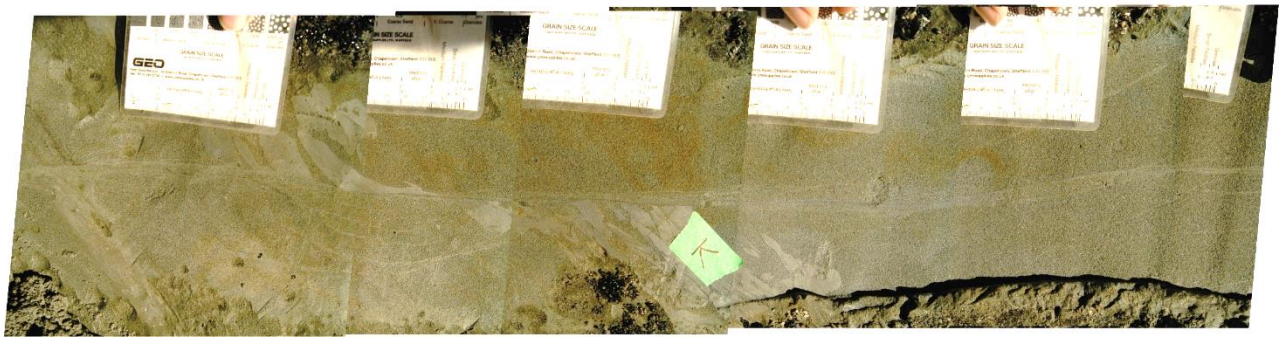
GEO
K

FIGURE 67: STACKED PHOTOGRAPHS SHOWING TONGAPORUTU B FAULT FROM TOP (TOP LEFT) TO BASE (BOTTOM RIGHT). NOTE BED G WAS NOT ACCESSIBLE DURING PHOTOGRAPHING AS BASE OF FAULT WAS COVERED DUE TO HEAVY BEACH SAND ACCRETION.

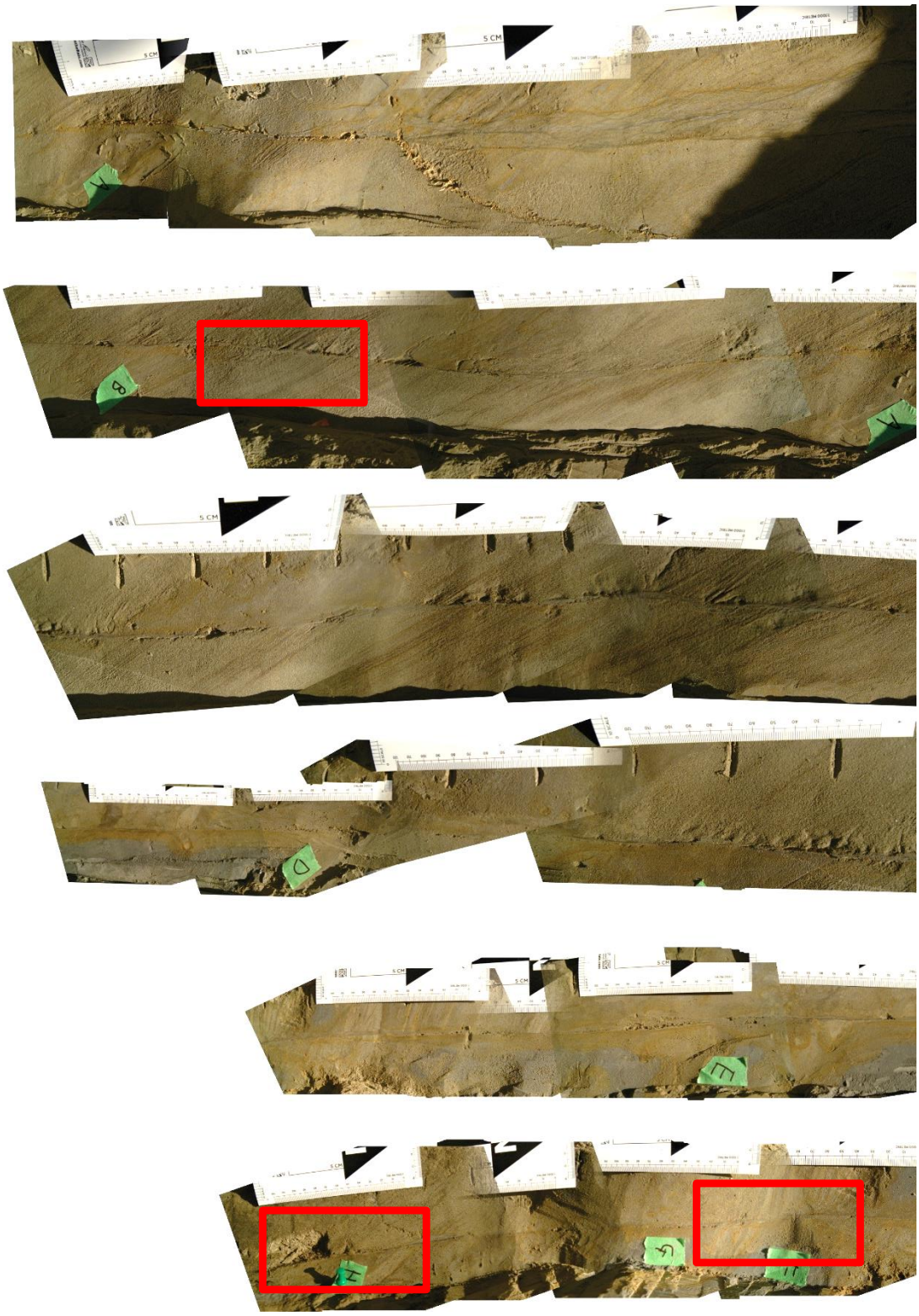

FIGURE 68: STACKED PHOTOGRAPHS SHOWING PUKEARUHE A FAULT FROM TOP (TOP LEFT) TO BASE (BOTTOM RIGHT).

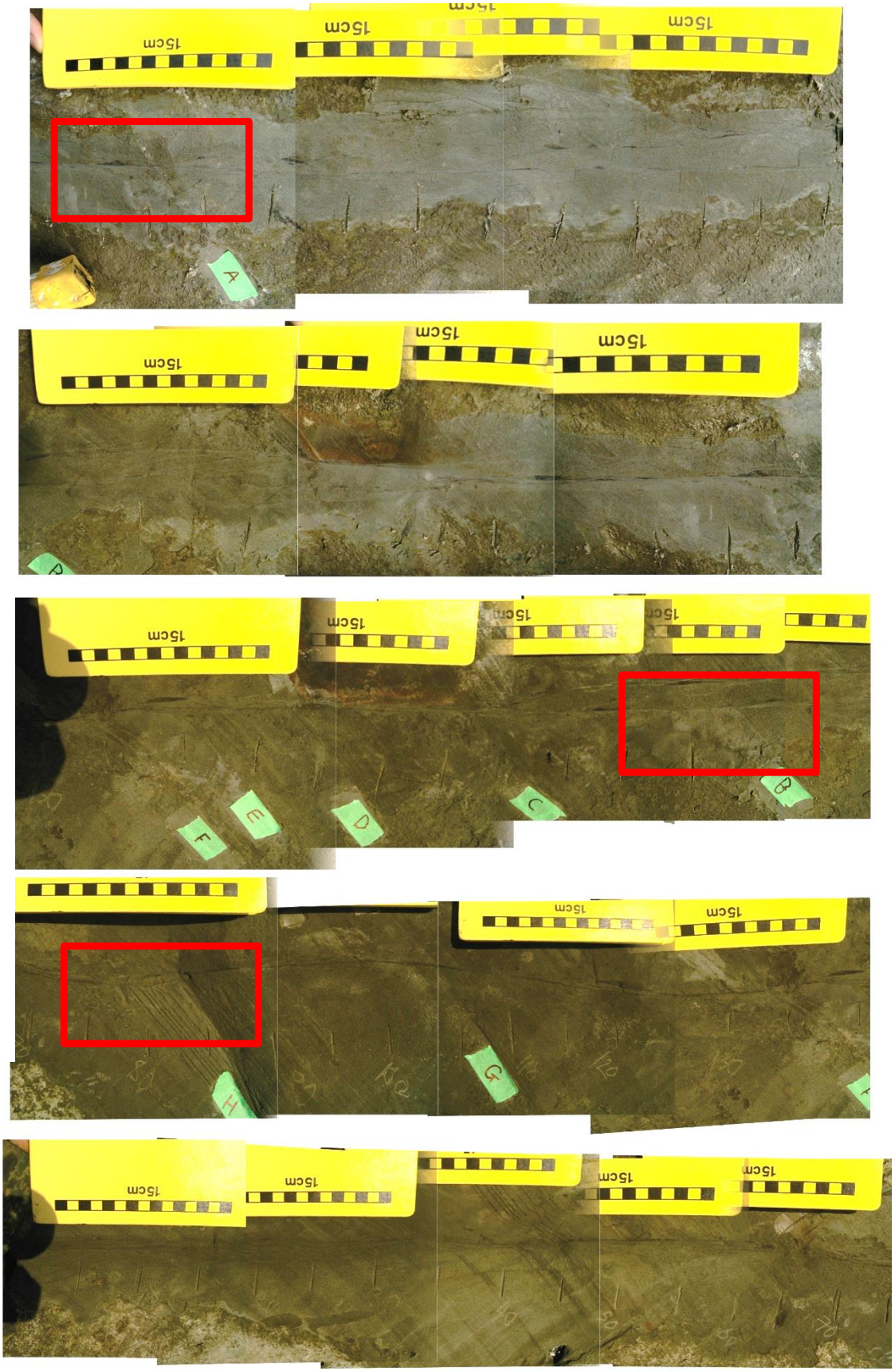

FIGURE 69: STACKED PHOTOGRAPHS SHOWING PUKEARUHE B FAULT FROM TOP (TOP LEFT) TO BASE (BOTTOM RIGHT.

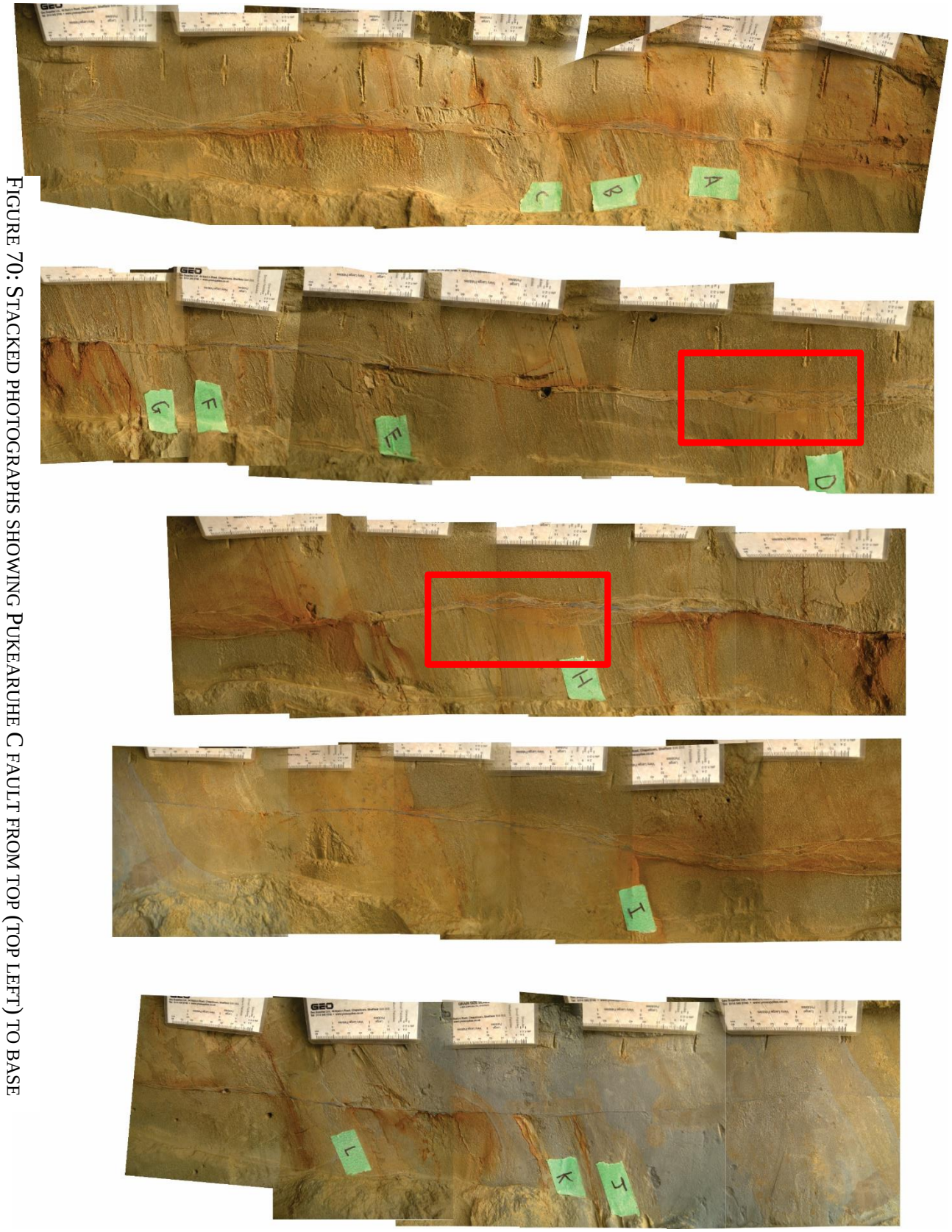

FIGURE 70: STACKED PHOTOGRAPHS SHOWING PUKEARUHE C FAULT FROM TOP (TOP LEFT) TO BASE (BOTTOM RIGHT: CONTINUED ON NEXT PAGE.

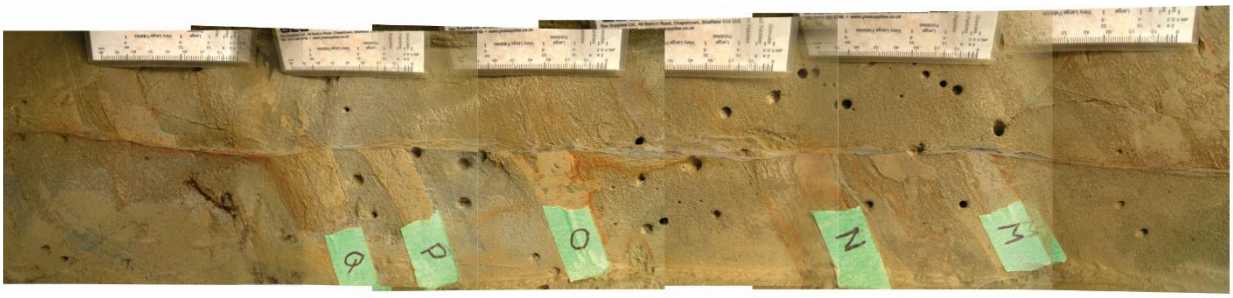
Q
P
O
N
M


S
R

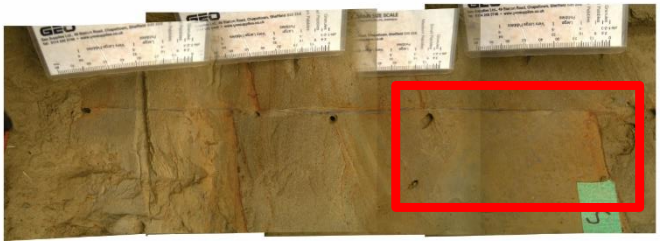

TABLE 12: OUTCROP READINGS OF SMEARED AND NON-SMEARED BEDS COMPARED WITH PREDICTIVE ACCURACY OF SHALE SMEAR FACTOR (SSF), SHALE GOUGE RATIO (SGR) AND CLAY SMEAR POTENTIAL (CSP) CALCULATIONS. POTENTIAL SMEAR HAS BEEN COMBINED WITH SMEAR FOR SSF, SGR AND CSP PREDICTIONS.

Fault Name	Bed	Recorded Smear		SGR		CSP		SSF	
		Smear	No smear	Smear/Potential Smear	No Smear	Smear/Potential Smear	No Smear	Smear/Potential Smear	No Smear
Rapanui A	a	1	0	1	0	1	0	1	0
	b	1	0	1	0	0	1	1	0
	c	1	0	1	0	0	1	1	0
	d	1	0	1	0	0	1	1	0
	e	1	0	1	0	0	1	1	0
	f	1	0	1	0	0	1	1	0
	g	0	1	1	0	0	1	1	0
	h	0	1	1	0	0	1	1	0
	i	0	1	1	0	0	1	1	0
	j	0	1	1	0	0	1	1	0
	k	0	1	1	0	1	0	1	0
Total	*11*	*6*	*5*	*11*	*0*	*2*	*9*	*11*	*0*
Predictive Accuracy				**55%**		**45%**		**55%**	
Pukearuhe A	a	0	1	0	1	0	1	1	0
	b	0	1	0	1	0	1	0	1
	c	0	1	1	0	1	0	1	0
	d	0	1	1	0	1	0	1	0
	e	1	0	1	0	1	0	1	0
	f	1	0	1	0	0	1	1	0
Total	*6*	*2*	*4*	*4*	*2*	*3*	*3*	*5*	*1*
Predictive Accuracy				**67%**		**50%**		**50%**	
Pukearuhe B	a	1	0	0	1	0	1	1	0
	b	0	1	1	0	1	0	1	0
	c	0	1	0	1	0	1	1	0
	d	0	1	0	1	0	1	1	0
	e	1	0	0	1	0	1	0	1
	f	0	1	0	1	0	1	1	0
	g	1	0	0	1	0	1	0	1
	h	1	0	0	1	0	1	1	0
Total	*8*	*4*	*4*	*1*	*7*	*1*	*7*	*6*	*2*
Predictive Accuracy				**38%**		**38%**		**25%**	
Pukearuhe C	a	1	0	1	0	1	0	1	0
	b	0	1	1	0	0	1	1	0
	c	0	1	0	1	0	1	1	0
	d	1	0	1	0	1	0	1	0
	e	0	1	0	1	0	1	1	0
	f	1	0	0	1	0	1	0	1
	g	0	1	0	1	0	1	0	1
	h	1	0	1	0	0	1	1	0
	i	0	1	1	0	1	0	1	0
	j	0	1	0	1	0	1	1	0
	k	1	0	0	1	0	1	1	0
	l	0	1	1	0	1	0	1	0
	m	1	0	0	1	0	1	0	1
	n	0	1	0	1	0	1	1	0
	o	1	0	0	1	0	1	1	0
	p	1	0	0	1	0	1	1	0
	q	1	0	1	0	0	1	1	0
	r	1	0	1	0	1	0	1	0
	s	0	1	1	0	1	0	1	0
Total	*19*	*10*	*9*	*9*	*10*	*6*	*13*	*16*	*3*
Predictive Accuracy				**53%**		**47%**		**47%**	
Tongaporutu A	a	1	0	1	0	0	1	1	0
	b	1	0	1	0	0	1	1	0
	c	1	0	0	1	0	1	1	0
	d	1	0	1	0	0	1	1	0
	e	1	0	0	1	0	1	0	1
	f	0	1	1	0	0	1	1	0
	g	1	0	1	0	0	1	1	0
	h	1	0	0	1	0	1	1	0
	i	1	0	0	1	0	1	0	1
	j	0	1	0	1	0	1	0	1
	k	1	0	1	0	0	1	1	0
Total	*11*	*9*	*2*	*6*	*5*	*0*	*11*	*8*	*3*
Predictive Accuracy				**55%**		**18%**		**73%**	

micromeritics®

Micromeritics Instrument Corporation - a

Saturn DigiSizer II 5205 V1.01 Saturn DigiSizer II 5205 V1.01 5200 LSHU V3.00 S/N 123 Page 1

Sample: PUKE99 A CLAY
Operator:
Submitter:
File: C:\...\WINTER\PUKE99A.SMP

Test Number: Avg of 1
Analyzed: 30/06/2016 14:24:17p.m.
Reported: 30/06/2016 14:24:25p.m.
Background: 30/06/2016 10:34:32p.m.

Model: Fraunhofer, 1.331
Material: Fraunhofer / Water
Background: Water RI 1.331
Smoothing: Medium

Combined Report

Incremental Volume Percent vs. Particle Diameter Graph

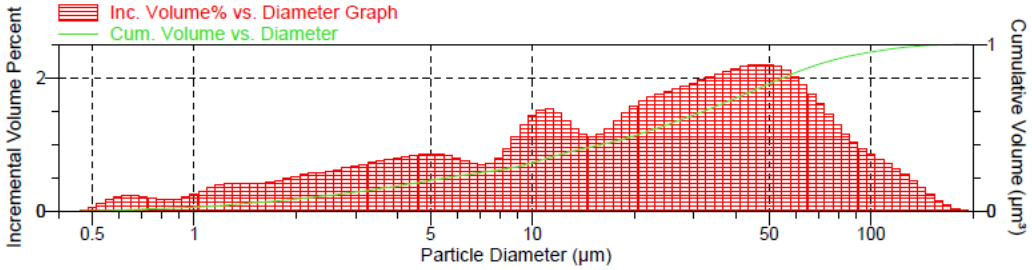

Summary Report

Sample

Sample Concentration: 0.00418 %
Obscuration: 8.6 %

Weighted Statistics (Volume Distribution)

		Std Dev of 1			Std Dev of 1
Mean	32.547	0.000	Mode	47.322	0.000
Median	23.511	0.000			

Peaks: Weighted Statistics (Volume Distribution)

Peak Number	Percent of Dist.*	Percent of Dist. Std Dev of 1	Mean	Mean Std Dev of 1	Median	Median Std Dev of 1	Mode
1	5.0	0.0	1.519	0.000	1.500	0.000	1.996

FIGURE 71: EXAMPLE GRAPH AND ASSOCIATED DATA GENERATED FROM PARTICLE-SIZER ANALYSIS (FROM PUKEARUHE C).

TABLE 13: SUMMARY OF FAULT ZONE ARCHITECTURE (BED LOCATIONS, SAMPLE LOCATIONS, FAULT-ROCK AND FAULT-ZONE THICKNESSES, DEFORMATION BAND COUNT, PSEUDO FAULT-ROCK THICKNESS AND SMEAR VALUES) FOR RAPANUI A FAULT.

Fault Zone Architecture Info								
Bed	Distance Along Fault (cm)	Fault-rock Thickness (mm)	Fault-zone Thickness (mm)	No. Deformation Bands	Pseudo Fault-rock	SSF	SGR	CSP
Top A	0	2.5	10	2	1.6	1	100	25
	10	3	14	8	6.4			
	17	2.25	8.75	5.5	4.4			
	20	1.5	3.5	3	2.4			
	30	1.5	3	3	2.4			
	40	4	12	8	6.4			
	50	4	7	6	4.8			
	60	1	2	2	1.6			
	70	1.5	3	3	2.4			
	80	4	7	6	4.8			
Top B	80.5	2.75	4.25	4	3.2	2.3	43	4.35
	90	1.5	1.5	2	1.6			
	100	4.5	13	7	5.6			
Top C	105.5	3.25	7.5	4.5	3.6	1.4	72	12.96
	110	2	2	2	1.6			
Top D	115	1.75	2.5	2	1.6	2.08	48	5.76
Top E	120	1.5	3	2	1.6	2.4	41.7	4.17
	123.5	2.75	6.5	5	4			
	130	4	10	8	6.4			
	140	4	6	4	3.2			
	150	3.5	6	5	4			
Top F	151.2	2.5	5	3.5	2.8	1.28	78.3	14.1
Top G	160	1.5	4	2	1.6	1.53	65.4	11.1
	170	3.5	4	3	2.4			
	180	1.5	1.5	1	0.8			
	190	3	5	2	1.6			
	200	2.5	3	2	1.6			
	210	1	1	1	0.8			
	220	1.5	2.5	2	1.6			
	230	3.5	10	6	4.8			
	240	3	5	3	2.4			
	250	2	3	2	1.6			
	260	2	15	4	3.2			
	270	6	8	5	4			
	280	5	15	5	4			
	290	4	10	5	4			
	300	3	12	4	3.2			
	310	4	7	4	3.2			
	320	1	1	1	0.8			
	330	0.5	0.5	1	0.8			
	340	1	1	1	0.8			
	350	1	1	1	0.8			
	360	3	6	4	3.2			
	370	4	7	3	2.4			
	380	0.7	0.7	1	0.8			
	390	3	5	2	1.6			
	400	3.5	7	5	4			
	410	2.5	2.5	1	0.8			
	420	3	5	4	3.2			
	430	1.5	2	2	1.6			
	440	3	4	4	3.2			
	450	0.7	0.7	1	0.8			
	460	2	2	1	0.8			
	470	1.5	1.5	1	0.8			
	480	2.5	4	3	2.4			
	490	1.5	1.5	1	0.8			
	500	2.5	4	3	2.4			
	510	6	9	7	5.6			
	520	0.8	1	2	1.6			
	530	3	6	4	3.2			
Top H	533.5	2	3.5	2.5	2	1.77	56.5	7.35
	540	1	1	1	0.8			
	550	4	5.5	4	3.2			
	560	0.6	0.6	1	0.8			
	570	2.5	9	4	3.2			
	580	1.5	1.5	1	0.8			
	590	2.5	3	3	2.4			
	600	3	4	4	3.2			
	610	2	2	2	1.6			
	620	1	1	1	0.8			
Top I	622.5	0.9	0.9	1	0.8	1.83	54.55	6.55
	630	0.8	0.8	1	0.8			
Top J	636	0.65	0.65	1	0.8	2	50	2
	640	0.5	0.5	1	0.8			
Top K	643	1	2.25	1.5	1.2	1.11	90	16.2
	650	1.5	4	2	1.6			
	660	2	3	2	1.6			
	670	1	1	1	0.8			
	680	0.8	0.8	1	0.8			

TABLE 14: SUMMARY OF FAULT ZONE ARCHITECTURE (BED LOCATIONS, SAMPLE LOCATIONS, FAULT-ROCK AND FAULT-ZONE THICKNESSES, DEFORMATION BAND COUNT, PSEUDO FAULT-ROCK THICKNESS AND SMEAR VALUES) FOR TONGAPORUTU A FAULT.

Fault Zone Architecture Info								
Bed	Distance Along Fault (cm)	Fault-rock Thickness (mm)	Fault-zone Thickness (mm)	No. Deformation Bands	Pseudo Fault-rock	SSF	SGR	CSP
	0	5	14	4	3.2			
Top A	5	5	15	3	2.4	3	33	10.9
	10	6	32	4	3.2			
	15	5	20	3	2.4			
	20	5	16	3	2.4			
	25	4	12	3	2.4			
	30	4	8	3	2.4			
	35	4	5	2	1.6			
	40	4	5	2	1.6			
	45	4	6	3	2.4			
	50	5	12	4	3.2			
	55	5	11	3	2.4			
	60	1	1	1	0.8			
	65	3	6	2	1.6			
	70	6	25	4	3.2			
	75	6	35	4	3.2			
	80	6	40	4	3.2			
	85	6	44	4	3.2			
	90	5	30	3	2.4			
	95	4	17	3	2.4			
	100	4	11	3	2.4			
	105	5	8	3	2.4			
	110	5	9	2	1.6			
	115	5	28	2	1.6			
	120	5	26	2	1.6			
	125	4	34	2	1.6			
	130	4	20	3	2.4			
	135	5	30	3	2.4			
	140	6	40	5	4			
	145	6	48	5	4			
Top B	146	4	26	3.5	2.8	3.3	30.4	10.7
	150	2	4	2	1.6			
Top C	152.5	2	4.5	2	1.6	6.4	15.7	2.8
Top D	155	2	5	2	1.6	2.9	34.8	13.9
	160	2	8	3	2.4			
Top E	161	4	4	4	0	11.4	8.8	1.2
Top F	164	4	4	4	0	4.2	23.8	9
	165	1	4	2	1.6			
	170	1	3	2	1.6			
Top G	175	2	15	3	2.4	4.6	21.9	7.7
	180	4	24	3	2.4			
	185	3	20	4	3.2			
	190	1.5	4	3	2.4			
	195	2	2	1	0.8			
Top H	200	3	3	1	0.8	6.5	15.4	3.1
Top I	205	1	10	2	1.6	13	7.7	0.8
	210	2	5	3	2.4			
	215	1	1	1	0.8			
	220	1	1	1	0.8			
	225	4	7	3	2.4			
	230	1.5	2	2	1.6			
	235	2	3	2	1.6			
	240	3	10	3	2.4			
	245	5	7	3	2.4			
Top J	248.5	4.5	7.5	2.5	2	14.4	6.9	0.6
	250	4	8	2	1.6			
	260	3	9	2	1.6			
	265	3	10	2	1.6			
	270	4	12	3	2.4			
	275	1	1	1	0.8			
	280	3	4	2	1.6			
	285	3	5	2	1.6			
	290	2	3	2	1.6			
	295	3.5	11	3	2.4			
	300	2	6	2	1.6			
	305	2	2	1	0.8			
	310	2	2	1	0.8			
Top K	313	2.5	5	2	1.6	3.3	30	9
	315	3	8	3	2.4			
	320	3	5	2	1.6			
	325	2	3	2	1.6			
	330	1	1	1	0.8			
	335	3	7	2	1.6			
	340	2	4	2	1.6			

TABLE 15: SUMMARY OF FAULT ZONE ARCHITECTURE (BED LOCATIONS, SAMPLE LOCATIONS, FAULT-ROCK AND FAULT-ZONE THICKNESSES, DEFORMATION BAND COUNT, PSEUDO FAULT-ROCK THICKNESS AND SMEAR VALUES) FOR TONGAPORUTU B FAULT.

Fault Zone Architecture Info								
Bed	Distance Along Fault (cm)	Fault-rock Thickness (mm)	Fault-zone Thickness (mm)	No. Deformation Bands	Pseudo Fault-rock	SSF	SGR	CSP
	0	2	12	2	1.6			
Top A	5	1	1	1	0.8	0.066666667	1500	900
	10	1	1	1	0.8			
	15	1	1	1	0.8			
	20	1	1	1	0.8			
	25	1	1	1	0.8			
Top B	30	0.5	0.5	1	0.8	0.105263158	950	361
	35	1	1	1	0.8	0		
Top C	38	1	1	1	0.8	0.090909091	1100	605
	40	0.5	0.5	1	0.8			
	45	1	1	1	0.8			
	50	1	1	1	0.8			
	55	1	1	1	0.8			
	60	1	1	1	0.8			
	65	1	1	1	0.8			
	70	1	1	1	0.8			
	75	1	1	1	0.8			
Top D	78	1	1	1	0.8	0.037037037	2700	3645
	80	1	1	1	0.8			
	85	0.5	0.5	1	0.8			
	90	0.5	0.5	1	0.8			
	95	1	1	1	0.8			
	100	1	1	1	0.8			
	105	0.5	0.5	1	0.8			
	110	1	1	1	0.8			
	115	1	1	1	0.8			
	120	0.5	0.5	1	0.8			
	125	1	1	1	0.8			
Top E	128	1	1	1	0.8	0.133333333	750	225
	130	0.5	0.5	1	0.8			
	135	1	1	1	0.8			
	140	0.5	0.5	1	0.8			
	145	1	1	1	0.8			
	150	1	1	1	0.8			
	155	1	1	1	0.8			
	160	1	1	1	0.8			
	165	1	1	1	0.8			
	170	0.5	0.5	1	0.8			
	175	1	1	1	0.8			
	180	1	1	1	0.8			
	185	1	1	1	0.8			
	190	0.5	1	1	0.8			
	195	1	1	1	0.8			
	200	1	1	1	0.8			
	205	1	1	1	0.8			
	210	1	1	1	0.8			
	215	1	1	1	0.8			
	220	1	1	1	0.8			
	225	1	1	1	0.8			
	230	1	1	1	0.8			
	235	1	1	1	0.8			
Top F	240	0.5	1	1	0.8	0.029411765	3400	5780
	245	0.5	0.5	1	0.8			
	250	0.5	0.5	1	0.8			
	255	0.5	0.5	1	0.8			
	260	0.5	0.5	1	0.8			
	265	1	1	1	0.8			

TABLE 16: SUMMARY OF FAULT ZONE ARCHITECTURE (BED LOCATIONS, SAMPLE LOCATIONS, FAULT-ROCK AND FAULT-ZONE THICKNESSES, DEFORMATION BAND COUNT, PSEUDO FAULT-ROCK THICKNESS AND SMEAR VALUES) FOR PUKEARUHE A FAULT.

Fault Zone Architecture Info								
Bed	Distance Along Fault (cm)	Fault-rock Thickness (mm)	Fault-zone Thickness (mm)	No. Deformation Bands	Pseudo Fault-rock	SSF	SGR	CSP
	0	12	55	10	8			
	5	10	42	8	6.4			
	10	7	38	7	5.6			
	15	8.5	44	6	4.8			
	20	8	34	6	4.8			
	25	8	31	6	4.8			
	30	9.5	25	9	7.2			
	35	8	22	7	5.6			
	40	8.5	22	6	4.8			
	45	8	27	6	4.8			
	50	6	24	5	4			
	55	3	4	3	2.4			
Top A	60	2	3	2	1.6	6.5	15.4	3.08
	65	2	3	2	1.6			
	70	2	3	2	1.6			
	75	2.5	4	2	1.6			
	80	2	2	1	0.8			
	85	1	1	1	0.8			
	90	1	1.5	2	1.6			
	95	3	5	3	2.4			
	100	4	12	3	2.4			
	105	2	4	2	1.6			
	110	1	1	1	0.8			
	115	2	4	2	1.6			
	120	1	2	2	1.6			
Top B	121	1	2	2	1.6	13.9	7.2	0.65
	125	1	2	2	1.6			
	130	3	5	3	2.4			
	135	2	2	1	0.8			
	140	2	3	2	1.6			
	145	3	4	3	2.4			
	150	5	10	4	3.2			
	155	3	4	3	2.4			
	160	3	3	1	0.8			
	165	2	2	1	0.8			
	170	2	3	2	1.6			
	175	5	12	4	3.2			
	180	4	10	4	3.2			
	185	2	9	2	1.6			
	190	3	11	4	3.2			
	195	2	2	2	1.6			
	200	1	2	2	1.6			
Top C	205	3.5	4	3	2.4	1.5	66.67	53.3
	210	1	1	1	0.8			
	215	2	3	2	1.6			
	220	4	9	2	1.6			
	225	4	14	2	1.6			
Top D	230	3	9	2	1.6	0.5	200	400
	235	1	1	1	0.8			
	240	1	1	1	0.8			
	245	2	3	2	1.6			
	250	1	1	1	0.8			
	255	1	1	1	0.8			
	260	0.5	0.5	0.5	0.4			
Top E	265	1	1	1	0.8	0.46	216.7	563
	270	1	3	3	2.4			
	275	0.5	0.5	0.5	0.4			
	280	4	6	3	2.4			
	285	3	5	3	2.4			
	290	1	1	1	0.8			
	295	2	3	2	1.6			
	300	2	2	1	0.8			
	305	2	5	4	3.2			
	310	3	4	3	2.4			
Top F	315	0.5	0.5	0.5	0.4	1.71	58.33	40.83
	320	1	1	1	0.8			
	325	1	4	2	1.6			
Top G	326	1.5	3.5	2	1.6	2.4	41.7	20.8
	330	2	3	2	1.6			
	335	1	2	2	1.6			
	340	1	2	2	1.6			
	345	2	3	3	2.4			
	350	1	1	1	0.8			
	355	2	5	3	2.4			
Top H	359	2	3.5	2	1.6	2.75	36.4	14.4
	360	2	2	1	0.8			

TABLE 17: SUMMARY OF FAULT ZONE ARCHITECTURE (BED LOCATIONS, SAMPLE LOCATIONS, FAULT-ROCK AND FAULT-ZONE THICKNESSES, DEFORMATION BAND COUNT, PSEUDO FAULT-ROCK THICKNESS AND SMEAR VALUES) FOR PUKEARUHE B FAULT.

Fault Zone Architecture Info								
Bed	Distance Along Fault (cm)	Fault-rock Thickness (mm)	Fault-zone Thickness (mm)	No. Deformation Bands	Pseudo Fault-rock	SSF	SGR	CSP
	0	3	4	3	2.4			
	5	2	5	2	1.6			
	10	2	3	2	1.6			
	15	3	5	2	1.6			
	20	3	10	2	1.6			
	25	4	12	2	1.6			
	30	4	8	2	1.6			
	35	6	24	3	2.4			
	40	4	16	2	1.6			
	45	4	15	4	3.2			
Top A	47.5	3.5	11	3	2.4	5.1	19.6	16.8
	50	3	7	2	1.6			
	55	2	3	2	1.6			
	60	4	10	3	2.4			
	65	5	12	4	3.2			
	70	5	15	4	3.2			
	75	8	25	5	4			
	80	10	30	5	4			
	85	10	38	5	4			
	90	10	44	5	4			
	95	10	50	11	8.8			
	100	13	45	12	9.6			
	105	10	45	8	6.4			
	110	8	40	5	4			
Top B	112.5	8	32.5	5	4	2.9	33.9	32.2
	115	8	25	5	4			
	120	5	15	4	3.2			
	125	5	24	4	3.2			
	130	4	23	3	2.4			
	135	4	18	3	2.4			
	140	3	6	3	2.4			
	145	1.5	5	1.5	1.2			
Top C	147.5	1.5	4	0	0	5.1	19.6	10.2
	150	2	5	2	1.6			
	155	4	8	4	3.2			
	160	3	4	3	2.4			
Top D	162.5	3	7	2.5	2	5.8	17.3	7.8
	165	3	10	2	1.6			
Top E	170	5	12	4	3.2	8.3	12.1	3.9
	175	2	4	2	1.6			
Top F	176	2	3	1.5	1.2	7	14.3	5.4
	180	2	2	1	0.8			
	185	1.5	1.5	1	0.8			
	190	5	12	4	3.2			
	195	4	8	3	2.4			
	200	3	5	3	2.4			
	205	2	3	2	1.6			
Top G	206	2	3.5	1.5	1.2	7.3	13.7	4.8
	210	2	4	1	0.8			
	215	5	14	5	4			
	220	5	15	4	3.2			
	225	4	15	4	3.2			
Top H	227.5	3.5	12.5	4	3.2	6.6	15.2	6.7
	230	3	10	4	3.2			
	235	4	6	3	2.4			
	240	6	53	5	4			
	245	5	58	4	3.2			
	250	5	58	4	3.2			
	255	6	60	4	3.2			
	260	5	58	4	3.2			
	265	4	45	4	3.2			
	270	3.5	38	3	2.4			
	275	3	9	2	1.6			
	280	4	13	4	3.2			
	285	5	21	7	5.6			
	290	7	23	6	4.8			
	295	5	22	4	3.2			
	300	5	15	5	4			
	305	4	12	4	3.2			

TABLE 18: SUMMARY OF FAULT ZONE ARCHITECTURE (BED LOCATIONS, SAMPLE LOCATIONS, FAULT-ROCK AND FAULT-ZONE THICKNESSES, DEFORMATION BAND COUNT, PSEUDO FAULT-ROCK THICKNESS AND SMEAR VALUES) FOR PUKEARUHE C FAULT. CONTINUED ON FOLLOWING PAGE.

Fault Zone Architecture Info								
Bed	Distance Along Fault (cm)	Fault-rock Thickness (mm)	Fault-zone Thickness (mm)	No. Deformation Bands	Pseudo Fault-rock	SSF	SGR	CSP
	0	2	21	3	2.4			
	5	2	16	2	1.6			
	10	3	6	4	3.2			
Top A	15	4	5	3	2.4	3.1	32.7	17.7
	20	5	10	6	4.8			
Top B	25	2	6	3	2.4	4.3	23	8.8
Top C	30	2	18	3	2.4	5.5	18.2	5.5
	35	2	18	3	2.4			
	40	3	20	4	3.2			
	45	4	14	6	4.8			
	50	4	14	7	5.6			
	55	3	10	7	5.6			
	60	3	10	4	3.2			
	65	8	25	15	12			
	70	6	18	9	7.2			
Top D	72.5	5	17.5	7	5.6	2.7	37.1	21.3
	75	4	17	5	4			
	80	3	9	5	4			
	85	2	5	2	1.6			
	90	2	11	3	2.4			
	95	1	4	3	2.4			
	100	1	3	3	2.4			
Top E	102.5	2.5	9	6	4.8	5.3	18.8	5.6
	105	4	15	9	7.2			
	110	2	5	5	4			
	115	2.5	3	2	1.6			
Top F	117.5	2	2.25	1.75	1.4	7.8	12.9	2.6
	120	1.5	1.5	1.5	1.2			
Top G	122.5	1.25	2.75	1.75	1.4	7.8	12.9	2.6
	125	1	4	2	1.6			
	130	1	1	1	0.8			
	135	1	1	1	0.8			
	140	3	11	5	4			
	145	4	20	9	7.2			
Top H	150	4	18	7	5.6	4.6	21.9	7.5
	155	2	12	4	3.2			
	160	2	5	2	1.6			
	165	2	10	3	2.4			
	170	2	20	4	3.2			
	175	4	30	6	4.8			
	180	3.5	25	6	4.8			
	185	3	17	4	3.2			
	190	3	19	6	4.8			
Top I	195	3	13	4	3.2	1.4	71.8	82.7
	200	2	10	4	3.2			
	205	2	12	4	3.2			
Top I.II	210	1.5	7	2.5	2	0.4	256.3	1050.6
	215	1	2	1	0.8			
	220	1	1	1	0.8			
	225	1	1	1	0.8			
	230	1	1	2	1.6			
	235	1	1	1	0.8			
	240	1	1	1	0.8			
	245	1	1	1	0.8			
Top J	250	1	1	1	0.8	5.2	19.4	5.8
	255	2	2	2	1.6			
Top K	257.5	1.5	1.5	1.5	1.2	6.5	15.5	3.7
	260	1	1	1	0.8			
	265	2	2	2	1.6			
	270	2	2	2	1.6			
Top L	272.5	1.5	1.5	1.5	1.2	2.8	35.5	19.5
	275	1	1	1	0.8			
	280	2	5	3	2.4			
	285	4	15	5	4			
	290	3	30	4	3.2			
	295	2	40	3	2.4			
	300	2	10	3	2.4			

Top M	302.5	2	6.5	2.5	2	7.5	13.3	2.7
	305	2	3	2	1.6			
Top N	310	2	3	3	2.4	6.5	15.4	3.1
	315	4	13	5	4			
	320	3	8	4	3.2			
Top O	325	3	5	3	2.4	5.5	18.2	5.5
	330	2	5	3	2.4			
Top P	332.5	1.5	3	2	1.6	6.8	14.8	3
	335	1	1	1	0.8			
Top Q	337.5	2	7	2.5	2	3.9	25.9	9.1
	340	3	13	4	3.2			
	345	3	20	3	2.4			
	350	4	30	5	4			
	355	5	23	5	4			
	360	4	10	5	4			
	365	3	10	4	3.2			
	370	4	10	5	4			
	375	1	1	1	0.8			
	380	3	5	4	3.2			
Top R	385	2	4	3	2.4	2.6	38	21.7
	390	1	2	2	1.6			
	395	2	2	1	0.8			
	400	1	6	2	1.6			
	405	2	15	4	3.2			
	410	2	20	3	2.4			
Top S	415	1	1	1	0.8	1.7	60	54
	420	1	1	1	0.8			
	425	1	1	1	0.8			
	430	2	2	2	1.6			
	435	2	4	2	1.6			
	440	1	1	1	0.8			
	445	2	2	1	0.8			

TABLE 19: SUMMARY OF SILTSTONE BED THICKNESSES AND MAXIMUM DISPLACEMENTS FOR ALL SILTSTONE BEDS SAMPLED ALONG RAPANUI A, TONGAPORUTU A AND B, AND PUKEARUHE A, B AND C FAULTS.

Rapanui A		
Siltstone Bed Info		
Bed	Thickness (mm)	Displacement (mm)
A	25	25
B	10	23
C	18	25
D	12	25
E	10	24
F	18	23
G	17	26
H	13	23
I	12	22
J	10	20
K	18	20

Tongaporutu A		
Siltstone Bed Info		
Bed	Thickness (mm)	Displacement (mm)
A	33	100
B	35	115
C	18	115
D	40	115
E	14	160
F	38	160
G	35	160
H	20	130
I	10	130
J	9	130
K	30	100

Pukearuhe C		
Siltstone Bed Info		
Bed	Thickness (mm)	Displacement (mm)
A	54	165
B	38	165
C	30	165
D	57.5	155
E	30	160
F	20	155
G	20	155
H	34	155
I	115	160
I.II	410	160
J	30	155
K	24	155
L	55	155
M	20	150
N	20	130
O	30	165
P	20	135
Q	35	135
R	57	150
S	90	150

Tongaporutu B		
Siltstone Bed Info		
Bed	Thickness (mm)	Displacement (mm)
A	60	4
B	38	4
C	55	5
D	135	5
E	30	4
F	170	5
G	60	0

Pukearuhe A		
Siltstone Bed Info		
Bed	Thickness (mm)	Displacement (mm)
A	20	130
B	9	125
C	80	120
D	200	100
E	260	120
F	70	120
G	50	120
H	40	110

Pukearuhe C		
Siltstone Bed Info		
Bed	Thickness (mm)	Displacement (mm)
A	55	280
B	95	280
C	52	265
D	45	260
E	32	265
F	38	265
G	35	255
H	44	290

TABLE 20 SUMMARY OF RELATIVE STRENGTH VALUES AND ASSOCIATED AVERAGES FOR INDIVIDUAL SILTSTONE AND SANDSTONE BEDS SAMPLED ALONG RAPANUI A, TONGAPORUTU A AND B, AND PUKEARUHE A, B AND C FAULTS.

Rapanui A

Strength Info

Bed	Strength reading 1	2	3	4	5	Average Hardness
Top Sand						
A	14	14	14	14	14	14
A - B Sand	12	14	12	10	11	11.8
B	11	12	13	13	11	12
B - C Sand	13	12	11	12	13	12.2
C	17	17	16	15	17	16.4
C - D Sand	17	17	17	16	16	16.6
D	15	13	14	13	15	14
D - E Sand	14	14	14	14	13	13.8
E	15	14	14	14	14	14.2
E - F Sand	11	12	12	13	13	12.2
F	12	12	12	13	14	12.6
F - G Sand	16	17	15	16	18	16.4
G	15	16	15	15	14	15
G - H Sand	10	10	5	5	5	7
H	0	0	0	0	0	0
H - I Sand	0	0	0	0	0	0
I	12	12	12	12	12	12
I - J Sand	0	0	0	0	0	0
J	0	5	5	0	0	2
J - K Sand	0	10	10	10	0	6
K	0	0	0	0	0	0
Base Sand	0	0	0	0	0	0

Tongaporutu B

Strength Info

Bed	Strength reading 1	2	3	4	5	Average Hardness
Top Sand	20	18	22	18	21	19.8
A	20	25	23	23	23	22.8
A-B	18	19	20	20	20	19.4
B	21	25	26	24	25	24.2
B-C	22	19	20	20	20	20.2
C	26	27	28	24	26	26.2
C-D	18	19	19	21	18	19
D	19	27	26	26	22	24
D-E	19	18	19	19	18	18.6
E	23	26	25	24	23	24.2
E-F	22	21	22	20	22	21.4
F	28	26	27	26	26	26.6
F-G	20	22	23	23	21	21.8
G	28	26	28	28	26	27.2
Base Sand	28	26	28	26	26	26.8

Pukearuhe A

Strength Info

Bed	Strength reading 1	2	3	4	5	Average Hardness (Mpa)
Top Sand	23	25	24	16	15	20.6
A	23	23	23	23	24	23.2
A - B Sand	21	20	22	22	20	21
B	21	23	24	24	22	22.8
B - C Sand	21	21	22	22	22	21.6
C	24	22	25	24	24	23.8
C - D Sand	22	21	21	19	19	20.4
D	22	22	22	20	22	21.6
D - E Sand	19	19	19	19	20	19.2
E	24	24	20	22	24	22.8
E - F Sand	20	19	19	20	19	19.4
F	28	26	26	20	22	24.4
F - G Sand	22	26	21	20	22	22.2
G	24	26	24	24	22	24
G - H Sand	18	16	16	14	14	15.6
H	17	18	18	18	22	18.6
Base Sand	na	na	na	na	na	na

Fault rock

Distance Along Fault (cm)	Strength reading 1	2	3	4	5	Average Hardness (Mpa)
25	0	13	0	10	10	6.6
60 (Top A)	15	20	12	20	15	16.4
101	17	19	16	16	16	16.8
121 (Top B)	16	20	19	18	18	18.2
156	20	22	24	26	22	22.8
205 (Top C)	16	22	24	26	22	22
225	13	20	19	15	20	17.4
230 (Top D)	16	22	18	20	18	18.8
255	18	20	21	22	20	20.2
265 (Top E)	20	20	20	20	18	19.6
285	10	15	16	16	16	14.6
315 (Top F)	20	18	18	16	20	18.4
320	20	22	18	16	21	19.4
326 (Top G)	16	18	18	16	15	16.6
346	18	20	19	19	19	19
359 (Top H)	16	12	15	20	21	16.8

Tongaporutu A

Strength Info

Bed	Strength reading 1	2	3	4	5	Average Hardness
Top Sand	26	27	26	26	26	26.2
A	26	28	26	28	28	27.2
A-B	28	29	30	28	30	29
B	28	29	32	29	29	29.4
B-C	29	28	31	29	31	29.6
C	26	25	21	26	25	24.6
C-D	26	29	28	28	29	28
D	29	29	28	28	28	28.4
D-E	29	28	28	23	28	27.2
E	29	30	31	31	30	30.2
E-F	N/A	N/A	N/A	N/A	N/A	N/A
F	31	30	29	30	30	30
F-G	31	26	29	29	28	28.6
G	26	30	29	29	29	28.6
G-H	28	27	26	25	30	27.2
H	30	30	29	29	29	29.4
H-I	31	26	27	25	29	27.6
I	26	26	26	27	32	27.4
I-J	27	30	26	28	29	28
J	28	29	28	29	28	28.4
J-K	32	31	30	30	31	30.8
K	31	32	32	29	30	30.8
Base Sand	28	31	33	28	29	29.8

Fault Rock

Top Sand	30	29	26	27	28	28
A	30	30	28	28	28	28.8
A-B	25	26	26	30	28	27
B	31	29	28	28	30	29.2
B-C	26	28	28	29	28	27.8
C	25	26	24	25	26	25.2
C-D	27	24	24	25	25	25
D	28	26	26	26	25	26.2
D-E	26	26	27	26	26	26.2
E	28	26	26	27	28	27
E-F	N/A	N/A	N/A	N/A	N/A	N/A
F	26	25	26	28	28	26.6
F-G	28	28	28	28	26	27.6
G	31	30	29	28	30	29.6
G-H	25	25	26	29	28	26.6
H	25	27	25	24	25	25.2
H-I	25	25	26	24	23	24.6
I	26	26	26	26	27	26.2
I-J	26	27	28	28	26	27
J	28	28	28	28	28	28
J-K	28	28	27	26	29	27.6
K	28	31	30	30	29	29.6
Base Sand	26	27	33	29	29	28.8

Pukearuhe B

Strength Info

Bed	Strength reading 1	2	3	4	5	Average Hardness
Top Sand	21	20	17	18	17	18.6
A	24	25	25	26	25	25
A - B Sand	23	22	21	22	21	21.8
B	22	23	21	22	23	22.2
B - C Sand	23	23	24	22	24	23.2
C	25	25	24	25	25	24.8
C - D Sand	21	22	21	24	23	22.2
D	25	23	25	24	24	24.2
D - E Sand	26	26	23	26	24	25
E	22	22	23	25	23	23
E - F Sand	22	22	22	22	21	21.8
F	24	24	23	23	23	23.4
F - G Sand	21	22	22	22	22	21.8
G	21	22	24	25	24	23.2
G - H Sand	22	22	22	25	24	23
H	23	23	22	25	24	23.4
Base Sand	23	22	24	25	24	23.6

Fault Rock

Top Sand	21	23	23	22	22	22.2
A	24	23	22	24	26	23.8
A - B Sand	20	22	20	20	22	20.8
B	22	23	21	23	22	22.2
B - C Sand	19	22	19	20	20	20
C	21	21	21	25	24	22.4
C - D Sand	22	20	24	20	23	21.8
D	23	23	23	24	24	23.4
D - E Sand	22	23	23	23	24	23
E	22	23	23	23	24	23
E - F Sand	21	22	22	22	23	22
F	23	23	22	22	24	22.8
F - G Sand	24	22	24	24	22	23.2
G	26	26	26	26	25	25.8
G - H Sand	22	22	24	24	22	22.8
H	21	22	22	22	23	22
Base Sand	21	21	21	21	21	21

Pukearuhe C

Strength Info

Bed	Strength reading 1	2	3	4	5	Average Hardness
Top Sand	20	21	22	22	21	21.2
A	19	21	20	22	22	20.8
A-B	14	16	20	20	18	17.6
B	20	20	21	21	22	20.8
B-C	21	21	21	21	22	21.2
C	22	22	21	21	21	21.4
C-D	20	20	20	18	18	19.2
D	21	20	18	19	20	19.6
D-E	19	19	19	15	18	18
E	15	16	18	17	17	16.6
E-F	20	22	21	20	21	20.8
F	18	23	23	24	26	22.8
F-G	16	17	15	16	17	16.2
G	17	17	16	20	20	18
G-H	22	22	20	23	22	21.8
H	24	24	24	24	24	24
H-I	21	22	23	23	20	21.8
I	23	22	23	23	20	22.2
I-I.II	22	22	21	21	22	21.6
I.II	22	24	24	23	23	23.2
J	19	18	16	17	23	18.6
J-K	20	21	21	21	20	20.6
K	21	22	23	24	20	22
K-L	22	23	25	27	24	24.2
L	22	19	18	20	19	19.6
L-M	20	19	18	20	19	19.2
M	24	23	23	20	19	21.8
M-N	17	20	17	20	19	18.6
N	20	21	20	20	21	20.4
N-O	21	21	21	22	22	21.4
O	19	21	22	19	21	20.4
O-P	18	21	21	20	22	20.4
P	17	20	20	17	20	18.8
P-Q	15	16	15	15	16	15.4
Q	16	18	18	18	19	17.8
Q-R	22	23	23	21	23	22.4
R	20	20	19	21	20	20
R-S	19	19	20	20	19	19.4
S	20	20	20	20	20	20
Base Sand	20	20	19	19	17	19

Fault Rock

Top Sand	18	18	18	17	18	17.8
A	18	19	18	18	18	18.2
A-B	14	15	15	15	15	14.8
B	16	15	16	16	16	15.8
B-C	0	12	14	16	16	11.6
C	15	16	15	18	18	16.4
C-D	18	18	17	17	17	17.4
D	16	16	18	18	20	17.6
D-E	16	16	16	16	17	16.2
E	19	19	18	17	17	18
E-F	12	13	13	14	16	13.6
F	14	12	12	14	13	13
F-G	12	16	13	13	13	13.4
G	18	18	18	17	16	17.4
G-H	19	19	19	19	19	19
H	24	20	23	21	25	22.6
H-I	20	21	20	20	20	20.2
I	22	22	23	20	20	21.4
I-I.II	20	21	19	18	18	19.2
I.II	22	21	22	21	20	21.2
J	23	20	24	24	25	23.2
J-K	16	23	23	23	23	21.6
K	24	20	22	22	24	22.4
K-L	25	24	22	23	23	23.4
L	19	19	19	18	19	18.8
L-M	18	19	19	18	20	18.8
M	19	19	19	18	19	18.8
M-N	20	16	18	20	20	18.8
N	20	21	18	19	19	19.4
N-O	18	17	19	18	18	18
O	19	20	22	22	22	21
O-P	16	16	14	16	16	15.6
P	17	17	18	18	17	17.4
P-Q	16	16	17	18	18	17
Q	15	17	15	18	18	16.6
Q-R	20	20	19	19	18	19.2
R	18	20	20	20	18	19.2
R-S	16	14	12	12	18	14.4
S	17	18	18	19	18	18
Base Sand	16	18	18	17	18	17.4

TABLE 21: SUMMARY OF GRAIN-SIZE DISTRIBUTIONS OF SILTSTONES, SANDSTONES AND FAULT ROCK SAMPLED FROM RAPANUI A FAULT.

| Rapanui A | | |

TABLE 22: SUMMARY OF GRAIN-SIZE DISTRIBUTIONS OF SILTSTONES, SANDSTONES AND FAULT ROCK SAMPLED FROM TONGAPORUTU A FAULT (CONTINUED ON FOLLOWING PAGE).

	Grainsize (um)		Siltstone Grainsize Volume											Sandstone Grainsize Volume										
			A	B	C	D	E	F	G	H	I	J	K	Top Sand	A-B	B-C	C-D	D-E	E-F	F-G	G-H	H-I	I-J	J-K	Base Sand
Tongaporutu A	crs sand upper	840	0	0	0	0	0	0	0	0	0	0	0	0	0	0	0	0	0	0	0	0	0	0	0
	crs sand middle	710	0	0	0	0	0	0	0	0	0	0	0	0	0	0	0.100888	0	0	0	0	0	0	0	0
	crs sand lower	500	0	0	0	0	0	0	0	0	0	0	0	0.519574	0.804692	0.039979	0.227343	0	0.155624789	0.004926	0	0	0	6.16452E-19	0
	med sand upper	355	0	0	0	0	0	0	0	0	0	0	0	9.32455	2.757108	0.0339	0.211682	0.707237	0.658136525	1.418011	1.814404989	2.580243	0.813590483	2.497340483	0.092945347
	med sand lower	250	0	0.48	0.08	1.94	0.04	0.29	0	0.77	0	0.19	0.64	8.555518	7.217942	5.377383	7.478924	7.299068	9.267762933	6.481555	8.279539511	3.532941222	9.32780885	9.727161183	5.117530153
	fine sand upper	180	0.13	1.52	1.43	7.03	0.91	1.22	0.08	2.25	0.36	2.52	2.6	24.23607	22.20045	29.51804	28.87213	21.88679	26.17733796	28.25838	26.17155772	5.355203556	26.64586956	27.76413278	27.5639295
	fine sand lower	125	1.2	1.12	2.6	5.81	1.8	1.85	1.23	2.53	0.93	3.66	2.62	12.04334	13.03666	17.05235	14.63634	13.9763	11.28737835	18.5901	14.54585722	7.262191667	15.39247111	14.45630333	15.82259056
	v fine sand upper	90	2.82	2.19	8.34	7.1	3.81	5.52	3.75	7.08	3.38	10.91	6.33	10.33535	11.8488	11.98319	11.97441	15.53168	8.705744056	13.12274	12.01643833	16.01706389	12.43553833	11.61266667	13.42188111
	v fine sand lower	63	3.02	2.52	9.03	5.21	4.22	5.73	4.68	7.64	5.71	9.92	6.88	5.653345	6.692079	6.141791	7.476963	9.014223	6.1810535	5.866126	6.002052778	11.93290444	5.894933889	5.494142778	6.7948
	v crs silt upper	45	6.84	6.53	12.71	7.29	7.66	9.72	9.14	12.31	11.64	12.27	11.03	5.63567	6.278551	5.992905	7.441107	7.340266	6.969014167	5.194181	5.494343333	10.70915167	5.209231111	4.894502778	5.77329
	v crs silt lower	32	10.92	10.63	12.67	8.94	11.04	12.89	11.81	13.27	15.56	11.6	12.75	4.303149	5.042439	4.654727	5.211149	4.899052	5.787812056	4.016176	4.332871111	7.706923889	4.142102778	3.898352778	4.371106111
	crs silt upper	22.4	12.27	11.87	11.71	9.73	11.85	13.11	11.57	11.91	14.96	10.33	12.23	4.095391	5.073431	4.03486	3.869914	4.245208	5.157502889	3.733845	4.334852778	6.806076111	4.172276667	4.009306111	4.21963
	crs silt lower	16	15.78	15.24	11.84	11.24	13.76	13.62	13.67	11.74	14.71	10.17	12.66	3.456362	4.112828	3.39736	3.007374	3.484968	4.740540444	3.052492	3.680981667	6.310375	3.531499444	3.351438889	3.542028889
	med silt upper	11.2	10.91	10.68	7.49	8.12	9.39	8.69	9.46	7.45	8.97	6.69	8.16	2.76816	3.394666	2.664451	2.195308	2.738949	3.622630722	2.394868	3.039175	4.950815	2.873801111	2.808030556	2.94379
	med silt lower	8	8.97	9.52	5.53	6.5	8.04	6.7	8.13	5.79	6.36	5.2	6.12	2.019388	2.496952	1.944819	1.495179	1.938622	2.551625556	1.690915	2.181945	3.56835	2.076282778	2.002375	2.147162222
	fine silt upper	5.6	6.51	6.73	3.94	5.03	6.27	4.94	6.26	4.12	4.41	3.86	4.35	1.590613	2.017261	1.553544	1.227314	1.498949	2.008101111	1.346366	1.768468889	2.923102778	1.639817222	1.630410556	1.796667778
	fine silt lower	4	7.16	7.31	4.3	5.51	7.38	5.28	7.14	4.41	4.52	4.24	4.65	1.833031	2.361782	1.808655	1.415903	1.788522	2.274486444	1.556914	2.069373333	3.442643889	1.942298889	1.913304444	2.063507778
	v fine silt upper	2.8	3.81	3.91	2.22	2.97	4.04	2.88	3.85	2.36	2.3	2.29	2.47	0.953926	1.239224	0.995505	0.783292	0.960613	1.189336056	0.831855	1.118996111	1.849042222	1.034498333	1.037781111	1.136774444
	v fine silt lower	2	4	4.06	2.4	3.09	4.23	3.02	3.97	2.54	2.42	2.45	2.64	1.070026	1.349582	1.102862	0.897549	1.042547	1.263598611	0.951937	1.231947222	2.033895	1.125735	1.123609444	1.257491667
		1.4	2.62	2.65	1.77	2.15	2.67	2.14	2.55	1.83	1.74	1.78	1.85	0.856333	0.962221	0.828456	0.695096	0.833385	0.927295778	0.77506	0.891782222	1.499352778	0.891917778	0.832669444	0.938788889
		1	1.23	1.22	0.68	0.83	1.19	0.86	1.1	0.73	0.7	0.67	0.74	0.161059	0.392982	0.30807	0.283374	0.234132	0.375517556	0.168396	0.351989444	0.536483333	0.233251111	0.333817778	0.371158889
		0.71	1.79	1.82	1.24	1.51	1.68	1.54	1.59	1.26	1.28	1.24	1.27	0.589155	0.599727	0.534084	0.439352	0.579492	0.650030556	0.539176	0.569655556	0.983240556	0.604029444	0.526422778	0.586946111
		0.5	0.02	0.01	0.01	0	0.01	0.01	0.01	0.01	0.04	0	0.01	0	0	0.004602	0.014945	0	0.008054611	0	0	0	0	0	0.003277778
	clay	0.355	0	0	0	0	0	0	0	0	0	0	0	0	0	0	0	0	0	0	0	0	0	0	0
		0.25	0	0	0	0	0	0	0	0	0	0	0	0	0	0	0	0	0	0	0	0	0	0	0
		0.18	0	0	0	0	0	0	0	0	0	0	0	0	0	0	0	0	0	0	0	0	0	0	0
		0.125	0	0	0	0	0	0	0	0	0	0	0	0	0.006152	0.002074	0.000911	0	0.001247722	3.91E-05	0.005551667	0	0.000265	0.004322222	0.000747222
		0.09	0	0	0	0	0	0	0	0	0	0	0	0	0.058391	0.014315	0.019705	0	0.019108444	0.002592	0.049972778	0	0.005684444	0.04129	0.015411667
		0.063	0	0	0	0	0	0	0	0	0	0	0	0	0	0	0	0	0	0	0	0	0	0	0

	Fault Rock					
	K Shale Smear	J-K Cataclasis	G-H Cataclasis	H Shale Smear	Base Sand Cataclasis	
	0	0	0	0	0	
	0	0	0	0	0	
	0	0	0	0	0	
	0	0	0	0	0	
	1.554123	0.24402065	0.16268043	1.26607775	0.24402065	
	5.901163	6.93340835	6.02399523	5.02840575	6.93340835	
	4.203374	7.606371	6.80808733	3.7711785	7.606371	
	4.56359	7.48638	6.82526033	4.901488	7.48638	
	3.46459	3.63232	3.32145	3.74148	3.63232	
	5.00254	5.152195	5.03745333	5.23851	5.152195	
	6.66041	4.56684	4.64232	7.136615	4.56684	
	6.85032	3.51276	3.60899333	7.55433	3.51276	
	10.31784	6.46556	6.86677	11.301935	6.46556	
	9.24623	6.73018	6.94793667	9.748035	6.73018	
	7.90419	4.351375	4.73834333	8.29081	4.351375	
	7.44006	7.001445	7.10886333	7.341875	7.001445	
	9.28473	10.49787	10.7937267	8.74182	10.49787	
	5.33331	7.04135	7.30430667	4.86681	7.04135	
	5.48793	8.207375	8.63245667	4.902585	8.207375	
	3.3578	5.170375	5.46556	3.014315	5.170375	
	1.55387	2.622325	2.80674	1.37726	2.622325	
	1.87393	2.76456	2.88704	1.775065	2.76456	
	0	0.01329	0.01811667	0.001405	0.01329	
	0	0	0	0	0	
	0	0	0	0	0	
	0	0	0	0	0	
	0	0	0	0	0	
	0	0	0	0	0	
	0	0	0	0	0	

TABLE 23: SUMMARY OF GRAIN-SIZE DISTRIBUTIONS OF SILTSTONES AND SANDSTONES SAMPLED FROM TONGAPORUTU B FAULT.

	Grainsize (um)		Siltstone Grainsize Volume							Sandstone Grainsize Volume							
			A	B	C	D	E	F	G	Top Sand	A-B	B-C	C-D	D-E	E-F	F-G	Base Sand
Tongaporutu B	crs sand upper	840	0	0	0	0	0	0	0	0	0	0	0	0	0	0	0
	crs sand middle	710	0	0	0	0	0	0	0	0	0	0	0.162029	0.47972	0	0	0
	crs sand lower	500	0	0	0	0	0	0	0	0.015494	0.001443505	0.118857	0.536258	6.827255	0.158318	0.014646	8.05E-05
	med sand upper	355	0	9.912896	0	3.082741	8.379397	16.75879	0	5.787223	0.40801821	0.033909	0.250534	14.6256	1.254098	0.069845	1.056174
	med sand lower	250	0	4.345878	1.127997	2.674535	2.541248	5.021981	0.060515	16.1885	6.777151674	6.138342	11.35736	11.72467	14.97285	6.284458	8.085398
	fine sand upper	180	0.032115	0.962523	0.802541	1.374262	1.025466	0.621061	1.429872	32.77124	34.01834106	35.14917	43.101	32.46799	38.6974	33.80115	32.36152
	fine sand lower	125	0.835242	0.580713	1.53304	1.770237	0.898119	0.094679	1.701558	13.58251	20.607905	21.80067	18.98107	13.48391	15.00177	21.63673	18.18856
	v fine sand upper	90	3.969318	3.047184	4.800501	5.958509	3.398576	2.605893	4.191259	8.598338	12.36642667	13.09165	9.615965	6.625693	7.392949	13.00478	10.79258
	v fine sand lower	63	5.029849	3.943318	6.193806	7.377683	4.65159	3.808439	5.494741	3.733023	4.784573333	5.009078	3.493657	2.510395	3.19634	5.037348	4.930879
	v crs silt upper	45	9.224572	8.484983	10.91835	12.56043	8.665439	7.946103	9.384774	3.436857	4.184094444	4.183138	2.871389	2.403011	3.270572	4.363481	4.763947
	v crs silt lower	32	13.54237	10.9618	12.90397	13.48266	11.82373	10.76366	12.8838	2.90571	3.339565	3.057354	2.172643	1.905539	2.948411	3.324236	3.792582
	crs silt upper	22.4	13.93294	12.34363	12.61927	12.5773	12.54039	12.06369	13.01709	2.968028	3.120166111	2.701944	1.964099	1.806013	3.073418	2.985125	3.618818
	crs silt lower	16	15.05399	12.17245	13.44906	11.22264	12.72256	11.1558	14.28932	2.447439	2.536965556	2.088354	1.441997	1.311856	2.460014	2.348554	2.801449
	med silt upper	11.2	9.568328	8.562061	8.944279	7.297977	8.444093	7.686372	9.201814	1.866918	1.917877222	1.611607	1.040969	0.979412	1.85777	1.756317	2.234971
	med silt lower	8	7.622663	6.331788	6.822569	5.240713	6.462699	5.527237	7.398161	1.334529	1.348735	1.095153	0.642997	0.605957	1.273649	1.189639	1.495566
	fine silt upper	5.6	5.426767	4.586983	4.973856	3.79113	4.653617	4.049501	5.257733	0.997874	1.008268333	0.803473	0.480873	0.485764	0.974159	0.933592	1.29597
	fine silt lower	4	5.829439	4.932071	5.234671	4.14403	4.956716	4.261436	5.651997	1.097734	1.145470556	0.957794	0.545098	0.529111	1.135543	1.008993	1.423755
	v fine silt upper	2.8	2.953966	2.468341	2.707413	2.08748	2.579424	2.182103	2.976746	0.562787	0.604151667	0.523433	0.296459	0.278698	0.585359	0.541824	0.780103
	v fine silt lower	2	2.955931	2.600338	2.80867	2.173067	2.60158	2.209044	2.994117	0.650108	0.693302222	0.570537	0.354661	0.331306	0.629791	0.637831	0.90892
		1.4	1.933283	1.836919	1.960083	1.544103	1.734169	1.528334	1.940003	0.525946	0.559248333	0.493223	0.355351	0.307849	0.499949	0.543931	0.706794
		1	0.774997	0.637692	0.774823	0.53201	0.69343	0.581518	0.805341	0.126386	0.145779444	0.140484	0.050496	0.119206	0.198371	0.099121	0.245793
		0.71	1.206408	1.288438	1.374571	1.090283	1.177043	1.079991	1.274094	0.371868	0.405927778	0.345857	0.267222	0.184159	0.334422	0.400611	0.453532
		0.5	0.107821	0	0.011918	0.0182	0.023529	0	0.047058	0	0	0.001351	0.001878	0	0	0	0
	clay	0.355	0	0	0	0	0	0	0	0	0	0	0	0	0	0	0
		0.25	0	0	0	0	0	0	0	0	0	0	0	0	0	0	0
		0.18	0	0	0	0	0	0	0	0	9.44444E-05	0	0	0	0	0	0
		0.125	0	0	0	0	0	0.00043	0	0.001762	0.004041667	0.006166	8.33E-05	0	0.001429	0.000116	0.002298
		0.09	0	0	0	0	0	0.021427	0	0.015498	0.013263889	0.042558	0.006864	0.002774	0.037804	0.007706	0.029822
		0.063	0	0	0	0	0	0	0	0	0	0	0	0	0	0	0

TABLE 24: SUMMARY OF GRAIN-SIZE DISTRIBUTIONS OF SILTSTONES, SANDSTONES AND FAULT ROCK SAMPLED FROM PUKEARUHE A FAULT.

	Grainsize (um)		Siltstone Grainsize Volume								Sandstone Grainsize Volume									Fault Rock Grainsize Volume			
			A	B	C	D	E	F	G	H	Top Sand	A-B	B-C	C-D	D-E	E-F	F-G	G-H	Base Sand	D Shale Smear	E Shale Smear	C-D Cataclasis	E-F Cataclasis
Pukearuhe A	crs sand upper	840	0	0	0.619519	0	0	0	0	0	0	0	0	0	0	0	0	0	0	0	0	0	0
	crs sand middle	710	0	0	2.02905	0	0	0	0	0	0	0	0	0	0	0	0	0	0	0	0	0	0
	crs sand lower	500	0	0	0.851122	0	0	0	0	0	0.043596295	2.76E-19	0.010681	0.386363	0.000709	0	0.078641	1.449956	0.038787578	0	0	0	0
	med sand upper	355	0	0	1.94288	0.009373	0	0	0	0	1.140943938	6.455123	0.424589	3.09433	0.065422	0.027437	1.914799	3.61036	2.009485767	0	0.6843715	8.164856667	12.82625
	med sand lower	250	0.153513	0.057944	0	0.817295	0.517212	0.014416	0	0.013224	3.198374322	5.036899	1.089068	3.382743	1.467514	0.678477	3.263608	3.925174	5.340710822	0	1.567877	2.871996667	4.7588675
	fine sand upper	180	1.936227	2.165577	0	8.223229	5.817607	1.63234	0.649137	0.816338	18.49411822	17.05038	10.73165	22.28617	23.23818	4.8665	13.51857	20.62992	28.76895861	0.5147321	1.276918	1.1020214	1.06733855
	fine sand lower	125	3.409632	4.439518	0.475838	8.921374	6.008571	3.731393	2.730632	1.951649	22.80302	15.99881	14.81551	22.79539	24.02838	7.30113	13.79057	17.54758	23.52618833	3.9175574	3.64046125	4.334158267	4.0983262
	v fine sand upper	90	12.446	11.33546	3.917994	13.29926	9.35782	12.5233	9.083941	8.302628	23.70207833	15.33018	20.50671	17.53325	19.25261	18.58348	15.04822	13.70332	13.78574444	8.1373705	6.88704025	7.531710333	6.93220275
	v fine sand lower	63	12.81321	12.29363	4.852149	11.26857	7.632572	13.40345	11.55945	10.98866	9.337872222	7.273596	11.74865	6.366705	7.019608	17.12372	10.08431	6.76375	4.408102222	6.71308	4.1983825	5.66114	4.9758
	v crs silt upper	45	15.24863	14.99572	8.668547	14.25625	10.68967	16.09033	15.98558	16.34395	5.780357222	5.699184	9.096953	4.979722	5.014145	15.57761	9.543742	6.355721	3.622788889	8.90761	4.2836895	7.558183333	6.7877825
	v crs silt lower	32	11.93145	11.90842	9.239662	10.99725	10.96969	11.66396	13.51532	14.07982	3.22	4.011267	6.169016	3.564101	3.646178	8.374737	6.437086	4.657783	2.714023333	9.265155	4.73423	7.13314	5.871315
	crs silt upper	22.4	9.367414	9.602736	7.891289	8.220986	10.21138	8.869161	10.1755	10.4324	2.644378889	3.994537	5.063326	3.353043	3.361003	5.495583	5.82121	4.545948	2.927005	8.1817	4.92647	7.00805	6.30208
	crs silt lower	16	8.598139	8.755523	7.55326	6.640876	10.26217	8.227166	9.555413	9.629963	1.887232778	3.340558	4.407894	2.683485	2.751331	4.546057	4.402901	3.450302	2.394677222	10.15193	7.80873	8.039043333	6.8724375
	med silt upper	11.2	5.638781	5.940674	5.010631	4.230757	6.907959	5.496911	6.377265	6.322282	1.688336111	3.245271	3.464194	2.166943	2.280995	3.749571	3.708291	3.034592	2.236624444	8.243745	8.578415	7.296873333	6.84344
	med silt lower	8	4.370277	4.395173	3.770076	3.070932	5.299391	4.451004	4.878446	5.038813	1.083067222	2.366509	2.5279	1.514838	1.580968	2.668116	2.484375	2.027804	1.553350556	6.30688	6.590455	5.41487	4.8335025
	fine silt upper	5.6	3.28041	3.345176	2.840475	2.299373	3.896129	3.266223	3.782725	3.806954	0.930447778	2.111917	2.113203	1.262412	1.342072	2.339936	2.110883	1.758476	1.396983333	6.27416	7.963115	5.582143333	5.2476475
	fine silt lower	4	3.644898	3.649721	3.109698	2.538935	4.251799	3.602325	4.181641	4.183682	1.196403889	2.656231	2.539082	1.466338	1.512463	2.819401	2.542302	2.118049	1.663756111	7.88424	11.10032	7.281073333	7.0753025
	v fine silt upper	2.8	1.947896	1.952003	1.649042	1.340672	2.281172	1.913703	2.136731	2.279983	0.658062778	1.474572	1.393292	0.811972	0.859577	1.532696	1.348696	1.124139	0.930843889	4.45206	6.976085	4.20757	4.22163
	v fine silt lower	2	2.109243	2.091163	1.767065	1.496491	2.411578	2.048685	2.212648	2.393251	0.815443889	1.595723	1.562076	0.888294	0.962635	1.703206	1.502636	1.238927	1.025101111	4.799235	7.94979	4.65448	4.791875
		1.4	1.511536	1.511476	1.223434	1.143416	1.69252	1.473253	1.533827	1.659479	0.680895	1.155439	1.125992	0.705038	0.723111	1.267811	1.087362	0.912985	0.795324444	3.01962	5.163955	3.037046667	3.20792
		1	0.609363	0.57314	0.553016	0.408916	0.645291	0.576867	0.607949	0.645552	0.188378333	0.418851	0.432503	0.206318	0.28599	0.477747	0.424286	0.351654	0.267651667	1.42743	2.524455	1.33246	1.3929925
		0.71	0.972508	0.982291	0.823474	0.801533	1.146544	1.006728	0.953837	1.108493	0.485112222	0.778786	0.718535	0.493799	0.470985	0.85258	0.732783	0.605182	0.577441111	1.78403	3.035435	1.776206667	1.8835575
		0.5	0.008659	0.00465	0.01747	0.011797	0.000917	0.008785	0.079959	0.002873	0.000141667	0	0.002191	0	0	0.014207	0	0	0	0.019465	0.109805	0.012976667	0.0097325
	clay	0.355	0	0	0	0	0	0	0	0	0	0	0	0	0	0	0	0	0	0	0	0	0
		0.25	0	0	0	0	0	0	0	0	0	0	0	0	0	0	0	0	0	0	0	0	0
		0.18	0	0	0	0	0	0	0	0	0.000297222	0	0	0	0	0	0	0	0	0	0	0	0
		0.125	0	0	0	0	0	0	0	0	0.004038889	0	0.003997	0.003153	0.007075	0	0.008818	0.009286	0.000696667	0	0	0	0
		0.09	0	0	0	0	0	0	0	0	0.010538889	0.002272	0.027904	0.028568	0.065594	0	0.075239	0.091484	0.007975	0	0	0	0
		0.063	0	0	0	0	0	0	0	0	0	0	0	0	0	0	0	0	0	0	0	0	0

TABLE 25: SUMMARY OF GRAIN-SIZE DISTRIBUTIONS OF SILTSTONES, SANDSTONES AND FAULT ROCK SAMPLED FROM PUKEARUHE B FAULT.

	Grainsize (um)		Siltstone Grainsize Volume								Sandstone Grainsize Volume									Fault Rock
			A	B	C	D	E	F	G	H	Top Sand	A-B	B-C	C-D	D-E	E-F	F-G	G-H	Base Sand	Base Sand Cataclasis
Pukearuhe B	crs sand upper	840	0	0	0	0	0	0	0	0	0	0	0	0	0	0	0	0	0	0
	crs sand middle	710	0	0	0	0	0	0	0	0	0	0	0	0	0	0	0	0	0	0
	crs sand lower	500	0	0	0	0	0	0	0	0	0	0	0	0.200367	0	0	0	0	0	0.02
	med sand upper	355	0	0	0	0	0	0	0	0.08	0	0	0	1.587196	0	0	0.000167	0	0.038072039	0.99
	med sand lower	250	0.00447	0.15	0	0	0	0.01	0.01	0.27	1.923333444	0.825194	0.014144	1.836392	1.217015	0.117921	0.622479	0.638149	3.994939906	2.44
	fine sand upper	180	0.708235	2.18	0	0.33	0.65	0.81	1.09	3.01	26.316146	18.94839	5.762121	13.02775	10.03061	5.177689	8.549613	11.50647	27.36390583	17.71
	fine sand lower	125	2.321511	3.88	0.76	1.87	2.61	1.81	3.09	4.42	22.672055	21.73871	13.12423	14.02141	14.37343	9.393649	13.66645	17.63124	25.611895	19.02
	v fine sand upper	90	9.791713	13.19	5.97	7.31	7.61	8.83	10.19	9.63	16.04283056	20.91448	20.08433	12.4219	21.11264	18.13183	17.5485	24.60312	18.73000889	17.26
	v fine sand lower	63	11.61752	13.45	7.61	9.45	9.32	11.91	11.62	9.91	6.847190556	9.458572	13.08273	5.147809	12.60485	13.69483	8.253604	12.58483	6.544045	7.18
	v crs silt upper	45	16.0923	15.93	13.67	15.19	15.2	16.88	16.07	12.86	5.245347778	6.766811	10.71684	4.046196	10.20478	13.02747	5.345758	8.914157	4.500313889	6.16
	v crs silt lower	32	13.50269	12.07	14.7	15.16	14.84	14.43	14.27	13.03	4.498765	4.908037	8.221516	2.780815	7.475473	10.08031	3.413733	6.077888	3.302996667	4.99
	crs silt upper	22.4	10.14506	9.05	12.49	12.46	11.96	10.78	11.23	11.08	4.338306667	4.2959	6.70632	2.466122	6.495778	7.714146	2.787359	5.178859	3.009146111	5
	crs silt lower	16	9.256731	7.95	12.06	11.16	10.91	9.48	9.59	9.84	3.392937778	3.434504	6.972429	2.018263	5.185501	7.473015	1.995111	4.007442	2.07579	4.39
	med silt upper	11.2	6.122283	5.37	7.94	6.69	6.64	6.13	5.67	6.43	1.527456667	1.522596	2.734984	1.599642	2.185703	2.927277	0.839912	1.733912	0.91661	3.45
	med silt lower	8	4.753502	3.89	5.95	4.94	4.98	4.47	4.03	4.57	2.726479444	2.792778	4.809703	1.135931	3.603158	4.53409	1.436511	2.965001	1.414146111	2.57
	fine silt upper	5.6	3.608874	2.96	4.48	3.57	3.55	3.32	2.93	3.44	1.219050556	1.137335	2.343128	0.9369	1.457366	2.335904	0.641822	1.124759	0.792095556	1.96
	fine silt lower	4	3.92933	3.26	4.86	3.91	3.84	3.6	3.18	3.87	1.693092778	1.684149	2.380853	1.090956	2.061206	2.271291	0.790008	1.579162	0.849964444	2.3
	v fine silt upper	2.8	2.160605	1.76	2.6	2.09	2.09	1.97	1.78	1.99	0.074572222	0.068756	0.473447	0.601911	0.125996	0.492935	0.020939	0.052429	0.027925	1.18
	v fine silt lower	2	2.377658	1.96	2.76	2.31	2.27	2.18	2.07	2.23	1.292808889	1.312476	2.321597	0.668395	1.649521	2.341001	0.663439	1.250369	0.711840556	1.26
		1.4	1.761566	1.43	1.96	1.71	1.68	1.63	1.48	1.6	0	0	0	0.523115	0	0	0	0	0	0.91
		1	0.714355	0.54	0.83	0.68	0.68	0.65	0.56	0.67	0.189626667	0.191306	0.251638	0.160868	0.216981	0.286652	0.091264	0.152211	0.116305	0.36
		0.71	1.119574	0.97	1.32	1.17	1.15	1.09	1.09	1.06	0	0	0	0.36634	0	0	0	0	0	0.66
		0.5	0.012027	0.01	0.03	0.02	0.02	0.02	0.04	0.03	0	0	0	0.001275	0	0	0	0	0	0
	clay	0.355	0	0	0	0	0	0	0	0	0	0	0	0	0	0	0	0	0	0
		0.25	0	0	0	0	0	0	0	0	0	0	0	0	0	0	0	0	0	0
		0.18	0	0	0	0	0	0	0	0	0	0	0	0	0	0	0	0	0	0
		0.125	0	0	0	0	0	0	0	0	0	0	0	0.001399	0	0	0	0	0	0.02
		0.09	0	0	0	0	0	0	0	0	0	0	0	0.013116	0	0	0	0	0	0.09
		0.063	0	0	0	0	0	0	0	0	0	0	0	0	0	0	0	0	0	0

TABLE 26: SUMMARY OF GRAIN-SIZE DISTRIBUTIONS OF SILTSTONES, SANDSTONES AND FAULT ROCK SAMPLED FROM PUKEARUHE C FAULT (CONTINUED ON THE FOLLOWING TWO PAGES).

	Grainsize (um)		Siltstone Grainsize Volume																			
			A	B	C	D	E	F	G	H	I	I.II	J	K	L	M	N	O	P	Q	R	S
Pukearuhe C	crs sand upper	840	0	0	0	0	0	0	0	0	0	0	0	0	0	0	0	0	0	0	0	0
	crs sand middle	710	0	0	0	0	0	0	0	0	0	0	0	0	0	0	0	0	0	0	0	0
	crs sand lower	500	0	0	0	0	0	0	0	0	0	0	0	0	0	0	0	0	0	0	0	0
	med sand upper	355	0	0	0	0	0.040954	0	7.28E-20	0	0	0	0	0	1.25E-19	0	0	0	0	0	0.228912	4.01802E-05
	med sand lower	250	0.021562	0.048072	0.072436	0	1.481541	0.097641	0.500251	0	0.160373	0.004681312	0.00702	0.001232	0.509152	0	0.006493	0	0.057025	0.006711766	0.919851	0.19944862
	fine sand upper	180	2.115236	3.566706	0.768182	0.093349	9.418714	4.744101	5.144128	0.389846	1.639171	1.25291391	0.939919	0.96998	2.917188	0.222746	3.023789	0.657791	0.823786	3.007428512	3.087344	3.291143478
	fine sand lower	125	4.050718	6.075584	1.878775	1.362411	10.69939	6.532445	6.988935	2.067672	3.318587	3.315631667	2.622498	2.674787	4.996879	1.593334	4.983481	2.073097	2.63529	5.788966389	3.932996	5.104401833
	v fine sand upper	90	10.41661	11.7799	5.505737	6.974711	12.82484	9.875359	9.660249	8.462221	9.184651	9.681400333	10.66151	5.83271	10.33308	6.294639	8.393239	6.308645	11.04828	14.82979556	12.98788	13.39151478
	v fine sand lower	63	10.72595	10.12453	6.779084	9.077442	6.808044	8.370272	7.363789	10.11976	9.181106	10.30325611	13.00699	5.99641	8.607252	7.470513	7.814519	7.824831	12.36942	14.84200667	13.12185	13.36300944
	v crs silt upper	45	12.67624	11.2928	11.41641	12.67619	8.799089	10.84979	9.563419	14.08468	11.2177	13.03357611	15.60102	9.124739	11.6212	10.98002	10.43334	12.07425	15.61769	15.48634556	16.14304	14.92519278
	v crs silt lower	32	11.12673	9.596208	12.68611	12.5011	8.648328	10.90539	10.0827	11.87491	11.09882	12.21795444	12.05956	11.46629	11.24761	12.40457	10.84571	13.56786	12.22611	10.62107111	12.21499	10.98349
	crs silt upper	22.4	8.973121	8.045445	11.57305	10.13091	8.107301	9.619081	9.175258	9.026051	9.749207	10.09107889	8.7143	11.33166	10.17878	11.1329	9.537109	11.85349	9.16997	7.548965	8.861882	7.719975
	crs silt lower	16	8.905818	8.509389	12.42128	10.36128	7.84287	9.476152	9.642651	9.413436	10.27251	9.877006667	8.276019	12.71024	10.10871	11.67679	10.01416	11.68844	8.582782	6.574509444	7.273819	6.933306111
	med silt upper	11.2	6.258093	6.319614	8.154203	7.252757	5.637742	6.451911	6.792622	6.748157	7.134217	6.632652778	5.774469	8.556353	6.720401	7.793137	7.177588	7.519432	5.89904	4.554251667	4.731603	4.993553889
	med silt lower	8	5.171818	5.317461	6.63131	5.786332	4.152583	4.977657	5.495961	5.478614	5.920626	5.205462778	4.590053	7.211704	5.130544	6.515484	6.025593	6.017844	4.564304	3.517319444	3.373746	4.045728333
	fine silt upper	5.6	4.169531	4.315907	4.985608	4.824463	3.401529	3.951853	4.286049	4.691977	4.648952	4.020005	3.714794	5.396044	3.975507	5.110408	4.757628	4.65457	3.727512	2.819836111	2.764877	3.23353
	fine silt lower	4	5.046111	5.0006	5.772906	5.975657	3.994057	4.697783	5.087094	5.700564	5.47836	4.626087222	4.407582	6.238258	4.589142	6.113486	5.536484	5.290736	4.439807	3.35143	3.285985	3.768543333
	v fine silt upper	2.8	2.885539	2.815125	3.242448	3.487048	2.294124	2.612625	2.867093	3.357463	3.084828	2.612067778	2.538542	3.493312	2.555127	3.507713	3.133605	2.909184	2.482491	1.864880556	1.902155	2.106192222
	v fine silt lower	2	3.147627	3.037881	3.481123	3.918362	2.477215	2.858367	3.103122	3.656288	3.337379	2.882471667	2.859163	3.797313	2.748501	3.840201	3.447421	3.147782	2.684941	2.094431667	2.116487	2.374747778
		1.4	2.110418	2.035081	2.277856	2.653002	1.68963	1.936856	2.056311	2.422772	2.221892	2.000617222	2.033539	2.494163	1.881412	2.554172	2.318116	2.099829	1.830065	1.487066111	1.500917	1.674315556
		1	0.923786	0.890968	0.993794	1.264441	0.666063	0.842948	0.930502	1.067452	0.997087	0.943467778	0.914802	1.171791	0.722636	1.212434	1.061708	0.944158	0.740055	0.633822778	0.601824	0.67503
		0.71	1.254079	1.216198	1.355622	1.601183	1.015771	1.168876	1.236882	1.434949	1.332656	1.240476667	1.238606	1.505789	1.156394	1.541776	1.461226	1.312389	1.096584	0.920572222	0.930532	1.031916111
		0.5	0.021022	0.012534	0.004072	0.059361	0.000214	0.030894	0.022983	0.003189	0.021884	0.059191667	0.039613	0.027231	0.000489	0.03569	0.028793	0.055687	0.004846	0.050589444	0.019306	0.010387222
	clay	0.355	0	0	0	0	0	0	0	0	0	0	0	0	0	0	0	0	0	0	0	0
		0.25	0	0	0	0	0	0	0	0	0	0	0	0	0	0	0	0	0	0	0	0
		0.18	0	0	0	0	0	0	0	0	0	0	0	0	0	0	0	0	0	0	0	0
		0.125	0	0	0	0	0	0	0	0	0	0	0	0	0	0	0	0	0	0	0	0
		0.09	0	0	0	0	0	0	0	0	0	0	0	0	0	0	0	0	0	0	0	0.026675
		0.063	0	0	0	0	0	0	0	0	0	0	0	0	0	0	0	0	0	0	0	0

									Sandstone Grainsize Volume											
Top Sand	A-B	B-C	C-D	D-E	E-F	F-G	G-H	H-I Sand	I-I.II	I.II-J	J-K	K-L	L-M	M-N	N-O	O-P	P-Q	Q-R	R-S	Base Sand
0	0	0	0	0	0	0	0	0	0 n/a		0	0	0	0	0	0	0	0	0	0
0	0	0	0	0	0	0	0	0	0 n/a		0	0	0	0	0	0	0	0	0	0
0	0	0	0	0	0	0	0	0	5.86747E-18 n/a		0	1.142192	0	0	0.254756	6.13E-18	0	0.497428	0	0.071757019
0.162098438	0	0	4.287926011	0	0	0.673925733	0.657125733	0.226771311	4.212625611 n/a		2.310464	15.64041	0.00718	0	0.254927	7.708971	1.264356	1.464988	0.163666	0.976108073
3.471939118	0.002528854	0.00898381	3.974731333	1.167326361	1.500138278	3.052592156	3.035792156	5.341173856	2.005463333 n/a		1.947178	4.469567	1.543497	1.233711	2.092234	0.305248	1.351162	9.989107	1.456939	3.923383764
24.29684633	4.697426868	4.46974919	23.08570072	22.66333697	23.34462228	24.41496933	24.39816933	27.44768428	10.92892661 n/a		5.352573	16.45892	15.72803	24.10989	19.27758	11.17847	18.95501	29.91804	18.934	24.34623792
24.53641111	7.925697611	10.95014089	22.7729933	22.83013778	22.13857278	23.933855	23.917055	24.4665222	15.69354 n/a		7.885903	15.55999	20.16183	20.9243	22.27199	19.29609	21.09372	20.9312	22.32485	23.13079778
18.43973944	16.01235611	21.12000167	15.34344722	17.33103389	17.03531167	17.23475333	17.21795333	16.05691944	21.06259444 n/a		13.74505	12.30132	21.80395	15.20452	19.44187	18.82151	17.44445	12.8142	20.35904	17.10981683
6.172837222	12.35407278	13.69891	5.317843333	6.457149444	6.446498889	5.931973333	5.915173333	5.531093333	11.23402278 n/a		11.48833	5.430998	9.625421	6.26742	7.757054	8.037357	7.593842	4.657214	7.839288	6.073078889
4.590891111	11.60478556	11.104825	4.559844444	5.095876667	5.242350556	4.585622222	4.568822222	4.252897222	8.531070556 n/a		12.38015	5.486067	7.105579	5.532548	5.933294	6.766444	6.258046	4.007441	6.09015	4.627334056
3.33574	8.767356667	7.552025556	3.550509444	4.191911667	4.131474444	3.549326111	3.532526111	3.244181111	5.234496667 n/a		8.959553	4.293383	4.789607	4.561186	4.155947	4.843241	4.798987	3.060346	4.259518	3.287257778
3.178397778	7.109203333	6.076897778	3.532230556	4.084792222	4.104370556	3.417826667	3.401026667	2.995732222	4.485680556 n/a		7.278344	4.094129	4.277706	4.439848	3.927354	4.524709	4.579389	3.101957	4.001313	3.268501944
2.562875	6.860776667	5.513502222	2.892163889	3.511377222	3.410658889	2.865951111	2.880651111	2.340467222	3.640716667 n/a		6.186986	3.455004	3.419722	3.856082	3.057809	3.840135	3.734216	2.168722	3.281834	2.634230444
2.090332778	5.298878333	4.264056111	2.343836111	2.855518333	2.843881111	2.353794444	2.368494444	1.842565	2.911445556 n/a		4.780079	2.667189	2.678006	3.144041	2.607137	3.250424	2.965114	1.788649	2.609557	2.313139
1.467656667	3.979156667	3.204533333	1.651389444	2.068512222	2.028127778	1.661536667	1.676236667	1.264280556	2.025217222 n/a		3.380951	1.885051	1.878086	2.334546	1.814482	2.389539	2.161365	1.067282	1.872326	1.623852444
1.151872222	3.408670556	2.624416111	1.372633889	1.670948333	1.684872778	1.387396667	1.402096667	1.005496667	1.695987778 n/a		2.89558	1.564726	1.548014	1.843188	1.508763	1.966879	1.707118	0.963999	1.495236	1.408187944
1.417123333	3.900862778	3.117676667	1.601396667	1.922332778	1.972206111	1.585436667	1.600136667	1.21747	1.978320556 n/a		3.594961	1.79732	1.74294	2.187558	1.801684	2.358351	2.037531	1.129944	1.708027	1.637558
0.759644444	2.276725	1.705427222	0.871078889	1.085435	1.065170556	0.891750556	0.906450556	0.649963889	1.116108333 n/a		2.044149	0.998823	0.96277	1.208528	0.980803	1.231237	1.085377	0.62396	0.930673	0.918369556
0.847006111	2.413131667	1.888388889	0.952525	1.159190556	1.197885	0.983063333	0.997763333	0.739298333	1.250003889 n/a		2.315493	1.081124	1.067016	1.26926	1.101792	1.392548	1.193782	0.664791	1.018237	0.999082278
0.632136667	1.677520556	1.343476667	0.733061111	0.787801667	0.892215556	0.733771667	0.748471667	0.590698889	0.996855 n/a		1.706931	0.777285	0.798052	0.933514	0.792153	1.054938	0.889902	0.502726	0.742449	0.764440889
0.2658	0.673053889	0.502248889	0.225571667	0.403893333	0.292397778	0.218405556	0.233105556	0.203064444	0.27835 n/a		0.648402	0.298716	0.284402	0.330788	0.337656	0.316426	0.272568	0.210862	0.307916	0.27553655
0.419658333	1.033781111	0.848888889	0.499716667	0.483947222	0.585098889	0.511536111	0.526236111	0.404541667	0.710767778 n/a		1.096502	0.511154	0.539422	0.613709	0.521056	0.690911	0.610549	0.320934	0.487052	0.537297611
0	0.004015	0.005851111	0	0	0	0	0	0	0 n/a		0.002429	0	0.004944	0.000887	0.005453	0	0	0.025832	0.003764	0
0	0	0	0	0	0	0	0	0	0 n/a		0	0	0	0	0	0	0	0	0	0
0	0	0	0	0	0	0	0	0	0 n/a		0	0	0	0	0	0	0	0	0	0
0	0	0	0	0	0	0	0	0	0 n/a		0	0	0	0	0.004919	0	0	0	0	0
0	0	0	0	0	0	0	0	0	0 n/a		0	0	0	0	0	0	0	0	0	0
0.014243333	0	0	0.005823333	0.012616667	0.001692778	0.0009	0.001341111	0.011110556	0.000388889 n/a		0	0.002693	0.00202	0	0.022368	0.001411	1.11E-05	0.003762	0.009957	0.004834611
0.09929444	0	0	0.051976667	0.109004444	0.037412778	0.0029	0.008258889	0.087448889	0.00373 n/a		0	0.040399	0.016426	0.001099	0.047443	0.012753	0.001354	0.044338	0.056266	0.036045667
0	0	0	0	0	0	0	0	0	0 n/a		0	0	0	0	0	0	0	0	0	0

Fault Rock					
I Shale Smear	J Shale Smear	S Shale Smear	H-I Cataclasis	Q-R Cataclasis	
0	0	0	0	0	
0	0	0	0	0	
0	0	0	0	0	
13.820518	13.8524975	18.22037	0	11.149615	
7.928172	5.77598525	7.36102	0	5.877256	
2.042606667	0.808649975	2.01768	1.768458667	3.934055	
3.956126667	1.09532375	4.51964	8.212324333	4.1137585	
5.690396667	3.12991	6.97475	12.8902581	6.15707	
3.89206	3.819725	4.62732	6.212746111	4.92149	
5.61266	6.414177	6.07106	6.351144444	6.59596	
4.88996	6.758255	5.3382	7.715024444	5.685635	
6.300826667	8.6636075	6.92074	5.470928889	6.74375	
5.665736667	9.2141875	5.3753	10.03422889	6.7901	
6.69162	8.0728675	5.83799	8.085411111	7.136035	
4.627366667	6.243565	3.76452	5.676785556	5.09295	
5.171176667	5.5487	4.15696	10.03090167	5.1986	
7.364566667	7.06417	5.7017	4.839176667	6.87508	
4.52629	4.01457	3.48908	1.848488889	4.05335	
5.133136667	4.30531	4.0467	8.063357778	4.460475	
3.403583333	2.831185	2.75777	1.500353889	2.934555	
1.417766667	1.193525	1.16937	1.300410556	1.18399	
1.850913333	1.629757	1.60628	0	1.6373	
0	0.001765	0	0	0	
0	0	0	0	0	
0	0	0	0	0	
0	0	0	0	0	
0	0	0	0	0	
0	0	0	0	0	
0.004076667	0	0.01223	0	0	
0	0	0	0	0	

TABLE 27: SUMMARY OF SHALE SMEAR VALUES (SSF, CSP AND SGR) FOR RAPANUI A, TONGAPORUTU A AND B, AND PUKEARUHE A, B AND C FAULTS. GREEN INDICATES SMEAR AND RED INDICATES NO SMEAR.

	Displacement (mm)	Smear (Y/N)	Smear length (mm)	Smear Thickness (mm)	SGR (%)	CSP	SSF	Fault-rock thickness (mm)	Fault-zone thickness (mm)	Comments	Fault	Smear Continuity	Bed
Rapanui A	25	Y	25		80	16	1.25	2.5	10	Continous Smear	Rapanui A	100	a
	23	Y	5		43.47826087	4.347826087	2.3	2.5	4	smear from FW	Rapanui A	21.73913043	b
	25	Y	25		72	12.96	1.388888889	3	7	slicing and msear from FW and HW	Rapanui A	100	c
	25	Y	15		48	5.76	2.083333333	1.5	2.5	smear from FW and HW	Rapanui A	60	d
	24	Y	2		41.66666667	4.166666667	2.4	2	5	smear from HW	Rapanui A	8.333333333	e
	23	Y	7		78.26086957	14.08695652	1.277777778	3.5	6	Slice from FW	Rapanui A	30.43478261	f
	26	N	0	0	65.38461538	11.11538462	1.529411765	1.5	4		Rapanui A		g
	23	N	0	0	56.52173913	7.347826087	1.769230769	2	3.5		Rapanui A		h
	22	N	0	0	54.54545455	6.545454545	1.833333333	1	1		Rapanui A		i
	20	N	0	0	50	5	2	0.5	0.5		Rapanui A		j
	20	N	0	0	90	16.2	1.111111111	1	2.25		Rapanui A		k
Tongaporutu A	100	Y	40	10	33	10.89	3.03030303	5	15	sliced	Tongaporutu A	40	a
	115	Y	35	5	30.43478261	10.65217391	3.285714286	6	40	15mm from HW 20mm sliced FW, tapers from 10mm to 1mm thick	Tongaporutu A	30.43478261	b
	115	Y	30	5	15.65217391	2.817391304	6.388888889	2	4	sourced from FW	Tongaporutu A	26.08695652	c
	115	Y	30	5	34.7826087	13.91304348	2.875	2	5		Tongaporutu A	26.08695652	d
	160	Y	20	7	8.75	1.225	11.42857143	2	8	sliced from FW	Tongaporutu A	12.5	e
	160	Y	15	2.5	21.875	7.65625	4.571428571	2	15	10mm from HW 5mm FW drag	Tongaporutu A	9.375	g
	130	Y	7	3	15.38461538	3.076923077	6.5	3	3	FW drag only	Tongaporutu A	5.384615385	h
	130	Y		40	7.692307692	0.769230769	13	1	10	sliced HW	Tongaporutu A	0	i
	100	Y	90	4	30	9	3.333333333	2	5	drag from HW	Tongaporutu A	90	k
	160	N	0	0	23.75	9.025	4.210526316	1	4		Tongaporutu A		f
	130	N	0	0	6.923076923	0.623076923	14.44444444	5	7		Tongaporutu A		j
Pukearuhe A	120	Y	11	3.5	41.66666667	20.83333333	2.4	1.5	3.5	10mm HW drag 1mm FW drag	Pukearuhe A	9.166666667	e
	110	Y	1	1	36.36363636	14.54545455	2.75	2	2	1mm drag HW	Pukearuhe A	0.909090909	f
	130	N	0	0	15.38461538	3.076923077	6.5	2	3		Pukearuhe A		a
	125	N	0	0	7.2	0.648	13.88888889	1	2		Pukearuhe A		b
	120	N	0	0	66.66666667	53.33333333	1.5	3.5	4		Pukearuhe A		c
	120	N	0	0	58.33333333	40.83333333	1.714285714	0.5	0.5		Pukearuhe A		d
Pukearuhe B	280	Y	20	3	19.64285714	10.80357143	5.090909091	3	12	drag from HW	Pukearuhe B	7.142857143	a
	265	Y	1	1	12.0754717	3.864150943	8.28125	5	12	drag from FW	Pukearuhe B	0.377358491	e
	255	Y	10	3	13.7254902	4.803921569	7.285714286	2	3	drag from HW	Pukearuhe B	3.921568627	g
	290	Y	15	12	15.17241379	6.675862069	6.590909091	4	15	sliced from HW	Pukearuhe B	5.172413793	h
	280	N	0	0	33.92857143	32.23214286	2.947368421	8	40		Pukearuhe B		b
	265	N	0	0	19.62264151	10.20377358	5.096153846	2.5	5.5		Pukearuhe B		c
	260	N	0	0	17.30769231	7.788461538	5.777777778	3	7		Pukearuhe B		d
	265	N	0	0	14.33962264	5.449056604	6.973684211	2	4		Pukearuhe B		f
Pukearuhe C	165	Y	1	1	32.72727273	17.67272727	3.055555556	4	5		Pukearuhe C	0.606060606	a
	155	Y	135	13.5	37.09677419	21.33064516	2.695652174	3.5	14		Pukearuhe C	87.09677419	d
	155	Y	5	1	12.90322581	2.580645161	7.75	2	3		Pukearuhe C	3.225806452	f
	155	Y	3	12.5	21.93548387	7.458064516	4.558823529	4	18		Pukearuhe C	1.935483871	h
	155	Y	1	1	15.48387097	3.716129032	6.458333333	1	1	drag from hw	Pukearuhe C	0.64516129	k
	150	Y	11	5	13.33333333	2.666666667	7.5	2	6.5	drag from hw	Pukearuhe C	7.333333333	m
	165	Y	44	10	18.18181818	5.454545455	5.5	3	5	20mm fw 24mm HW	Pukearuhe C	26.66666667	o
	135	Y	2	10	14.81481481	2.962962963	6.75	1.5	3	2mm drag FW, 10mm slice HW	Pukearuhe C	1.481481481	p
	135	Y	1	1	25.92592593	9.074074074	3.857142857	2	7	slice HW	Pukearuhe C	0.740740741	q
	150	Y	1	1	38	21.66	2.631578947	2	4	drag HW	Pukearuhe C	0.666666667	r
	165	N	0	0	23.03030303	8.751515152	4.342105263	2	6		Pukearuhe C		b
	165	N	0	0	18.18181818	5.454545455	5.5	2	18		Pukearuhe C		c
	160	N	0	0	18.75	5.625	5.333333333	2.5	9		Pukearuhe C		e
	155	N	0	0	12.90322581	2.580645161	7.75	1.5	2.5		Pukearuhe C		g
	160	N	0	0	71.875	82.65625	1.391304348	3	13		Pukearuhe C		i
	155	N	0	0	19.35483871	5.806451613	5.166666667	1	1		Pukearuhe C		j
	155	N	0	0	35.48387097	19.51612903	2.818181818	1	1		Pukearuhe C		l
	130	N	0	0	15.38461538	3.076923077	6.5	2	3		Pukearuhe C		n
	150	N	0	0	60	54	1.666666667	1	1		Pukearuhe C		s